Wrocław University of Technology
Centre of Advanced Materials and Nanotechnology

Materials Science
Poland

Vol. 25 • No. 1 • 2007

Oficyna Wydawnicza Politechniki Wrocławskiej

From the Workshop Organizers

The joint events *Silesian–Saxony Workshop on Synthesis and Analysis of Nanomaterials and Nanostructures* and *III Czech-Silesian-Saxony Mechanics Colloquium* were organized by the Centre of Excellence "Sol-Gel Materials and Nanotechnology" located at Wrocław University of Technology and AMD Saxony LLC & Co. KG, Dresden, Germany. The workshop was a unique event in more than one aspect. It bridged apparently divergent topics: sol-gel chemistry, materials characterization, as well as various aspects of electronic and optical devices (material, mechanical, etc.) and brought together specialists of various backgrounds (physicists, chemists, material scientists), affiliations (academia and industry) and countries. The latter aspect is worth commenting. Participants came from 3 cities such as Dresden, Prague, and Wrocław, forming a regular triangle on the map. These three cities are very close to each other, not only geographically. Their populations share the same region of Europe as well as very similar challenges, hopes, and problems. We are convinced that meetings like this one will help to stimulate both pan-border research (fundamental and applied) and transfer of results to the industries of the countries involved.

Krzysztof Maruszewski
SGM&N Centre of Excellence,
Wrocław University of Technology, Wrocław, Poland

Ehrenfried Zschech
Materials Analysis Department,
AMD Saxony, Dresden, Germany

CONTENTS

Materials Science-Poland, Vol. 25, No. 1, 2007

Strain state in silicon structures for microprocessor technology*

M. HECKER**, H. GEISLER

AMD Saxony LLC & Co. KG, Materials Analysis Department,
Wilschdorfer Landstrasse 101, D-01109 Dresden, Germany

A promising approach to improve the performance of present CMOS devices is to introduce mechanical strain into the channel regions below the transistor gates. Strain can be generated as global strain on the whole wafer level (e.g., by growing strained silicon films on strain-relaxed silicon–germanium (SiGe) alloy layers or by using strained silicon films on an insulator), or as local strain on the transistor scale by applying specific technology processes (e.g., making use of embedded SiGe source-drain regions). The detection of strain in very thin silicon films requires sophisticated techniques with high depth sensitivity, whereas the measurement of the local strain state in thin Si structures with small lateral dimensions below 50 nm – such as the channels of current CMOS transistors – still remains to be mastered. A technique possessing the potential for solving this problem is Raman spectroscopy, where the diffraction limit for lateral resolution can be bypassed by near-field approaches. In the present paper, the occurrence of large strains in SiGe films and corresponding stresses in the GPa range are demonstrated by Raman spectroscopy, utilizing a simple approach for determining strain and composition separately. To estimate the strain distribution in a silicon channel structure due to embedded SiGe source–drain regions, a silicon strain calculation is applied based on a continuum-mechanical model utilizing a continuous distribution of virtual dislocations along the Si–SiGe boundaries. Within the framework of this model, the stress state in a 2D approximation is obtained by analytical expressions. Thus, the spatial distribution of channel strain and the impact of geometry on the strain state are obtained in a straightforward way.

Key words: *strain; silicon–germanium; Raman spectroscopy; stress modelling*

1. Introduction. Strained Si films for CMOS devices

Strained silicon thin films have not only been the focus of basic research during the last years, but nowadays are also used in the production process of microprocessor devices. On one hand, strain and corresponding stress in microelectronic systems are

---

*Presented at the joint events 1st Workshop "Synthesis and Analysis of Nanomaterials and Nanostructures" and 3rd Czech-Silesian-Saxony Mechanics Colloquium, Wrocław, Poland, 21–22 November, 2005.

**Corresponding author, e-mail: michael.hecker@amd.com

often a reliability issue, e.g. in interconnect lines and dielectric films where effort is made to avoid undesired stress. On the other hand, positive effects of strain are employed in CMOS transistor technology. The reason is a significant performance gain achievable by introducing strained films into active transistor regions [1, 2] which will become more important as the long-term scaling of device dimensions cannot be continued in the future without changing materials and technology. Issues connected with other performance enhancement steps, for example carrier mobility degradation observed due to new high-k gate oxides, can be partially compensated by introducing strain, thus making it a key approach for extending CMOS to the next technology nodes [3].

The effect of strain on device performance is caused by an enhanced mobility of electrons or holes in the strained silicon regions which results from a modification of the silicon band structure. Strain can suspend the degeneracy of different valence bands, modify the band gap and band curvature, yielding a decrease of inter-valley scattering and a reduction of the effective charge carrier mass m^* [3]. Therefore, the mobility of the charge carriers $\mu \sim 1/m^*$ increases, which in turn leads to a reduction in the resistance part of the transistor RC-delay and enables higher transistor frequencies.

Strain can be introduced into thin silicon film structures by several methods, e.g. employing different coefficients of thermal expansion for adjacent materials in combination with thermal treatments, or making use of lattice mismatch for epitaxially grown films. For the latter method, materials with similar crystallographic structure and deviating lattice parameters are needed, for example diamond being the material with the smaller lattice parameter and germanium the material with the larger lattice parameter (Table 1). Since the lattice misfit of these materials with respect to silicon is too large to obtain coherent growth of films with reasonable thickness, it is important that these materials show solubility in silicon and allow the fabrication of alloys with tuneable lattice constants. In particular, silicon–germanium alloys (SiGe) have been used to generate strain in Si films for improved CMOS performance [4].

Table 1. Lattice parameter a_0, mismatch strain ε_m (for a layer coherently on Si), elastic constants C_{ij} (Voigt's notation) for (001) oriented crystals, and corresponding charge carrier mobility for electrons (μ_e) and holes (μ_h) in silicon (Si), germanium (Ge), and diamond (C) [5, 6]

	Si	Ge	C
a_0 [nm]	0.5431	0.5657	0.3567
$\varepsilon_m = (a_{Si} - a_0)/a_0$	0	–4%	52%
C_{11} [GPa]	165.7	128.4	1076.4
C_{12} [GPa]	63.9	48.2	125.2
C_{44} [GPa]	79.6	66.6	577.4
μ_e [cm²/Vs]	1500	3900	1800
μ_h [cm²/Vs]	450	1900	1600

In order to apply these materials to strain the silicon lattice, they must be either in a nearly strain-free state or strained in such a way that a certain lattice mismatch with

respect to bulk silicon is maintained at the interface between these materials and silicon. A customary method of achieving this is to deposit a composition-graded SiGe film on top of silicon, which contains lattice defects to compensate the strain mismatch, and to cap this film by an almost defect-free SiGe film with a lattice parameter corresponding to its constant chemical composition, i.e. in a strain relaxed state. A layer of silicon deposited on top of this stack will then become biaxially tensile strained according to the smaller lattice parameter of Si compared to the alloy (Fig. 1a). Since this technique provides a strained silicon film on the whole wafer level, it is known as the global strain technique.

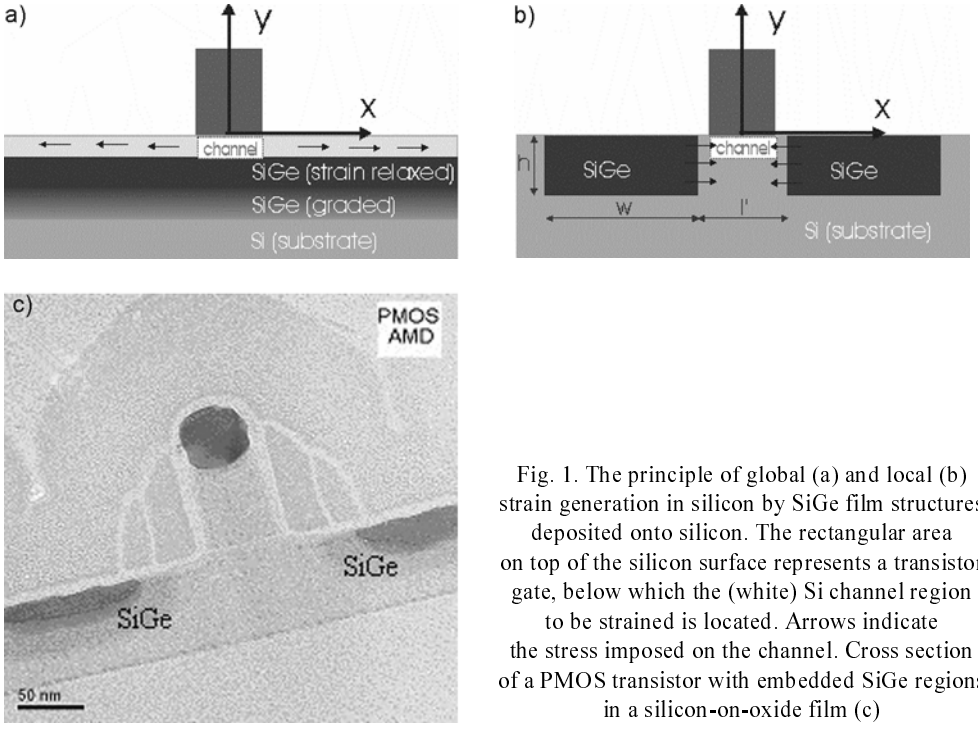

Fig. 1. The principle of global (a) and local (b) strain generation in silicon by SiGe film structures deposited onto silicon. The rectangular area on top of the silicon surface represents a transistor gate, below which the (white) Si channel region to be strained is located. Arrows indicate the stress imposed on the channel. Cross section of a PMOS transistor with embedded SiGe regions in a silicon-on-oxide film (c)

If a biaxial tensile strain of ~1 GPa is reached in the top silicon film, the electron mobility can be improved by ~50% [7], thus yielding an enormous performance gain for NMOS transistors. On the other hand, an increased mobility of holes determining the switching speed of PMOS transistors requires compressive strain which can be achieved by using $Si_{1-x}C_x$ alloy layers instead of SiGe films. To tune the speed of both transistor types independently on a wafer, a local approach is needed (Fig. 1b). By depositing a SiGe alloy into etched Si cavities, a highly selective epitaxial SiGe growth with coherent interfaces to the surrounding silicon can be achieved, resulting in compressive strain within the SiGe region [3]. Depending on the geometry, this strain is also partially transferred to the surrounding silicon, yielding a compressive strain state in channel regions between the SiGe cavities and thus improving the per-

formance of the corresponding PMOS transistors. Usually, the strain state in the channel is denoted as uniaxial [3]. As will be shown in Section 3, the strain is non-uniform inside the channel, and the distribution between the strain components appearing to depend strongly on the given geometry. For advanced CMOS technologies, several methods to induce channel strain, such as embedded SiGe deposition, compressively and tensile stressed cap films (liners), and stress memorization techniques, are combined [8]. Moreover, combinations of global and local strain generation are expected to boost CMOS performance [9]. Thus, both the measurement and calculation of strain in such structures is required to achieve a better understanding of the strain state and its dedicated improvement of technological progress.

2. Strain measurement of SiGe films by Raman spectroscopy

To determine strain on non-patterned silicon film stacks, several methods, including high-resolution X-ray diffraction, wafer-curvature measurements by light deflection techniques, and Raman spectroscopy, can be applied. Among these, Raman spectroscopy has not only an excellent lateral resolution reaching the sub-micron scale, but has the potential to be scaled down to the nm-range by combining it with near-field optical techniques. The experimental challenges of making the so-called nano-Raman technique available for strained silicon analysis with high spatial resolution are discussed in [10]. With the common ~1 μm lateral resolution of confocal micro-Raman microscopes, Raman spectroscopy is already a precise strain measurement technique, with the additional advantage of high sample throughput due to short measurement time.

Nonetheless, simultaneous analysis of chemical composition and strain in thin films is difficult by Raman spectroscopy, since the Raman frequencies used for evaluation are sensitive to both, and the intensity from very thin films is weak. In principle, the different dependences of Raman peak positions on composition and strain in certain ranges of film thickness and composition can be utilized. In the following it will be shown that for epitaxial SiGe films in the range of the germanium content x between 10 at. % and 50 at. %, the separation of both effects can be achieved by determining the frequency of the Si–Si and Si–Ge phonon modes of the films, and that huge strains in the GPa range are accessible.

The instrument used was a Jobin Yvon Micro-Raman confocal microscope with a 488 nm wavelength Ar laser and ca. 1 μm spot size. Figure 2 shows the results of measurements for two SiGe films epitaxially grown on (001) silicon. Apart from the silicon bulk signal emerging at the wavenumber $\omega = 521$ cm^{-1}, characteristic peaks of the film appear corresponding to the excitations of Si–Si, Si–Ge, and Ge–Ge lattice phonons. In particular, the observation of the latter two modes is a challenge in the case of thin silicon-rich films.

In addition to the Si–Si phonon mode of the SiGe film, the Si–Ge mode was also evaluated, whereas the Ge–Ge phonon mode is very weak, especially for the low content range of Ge.

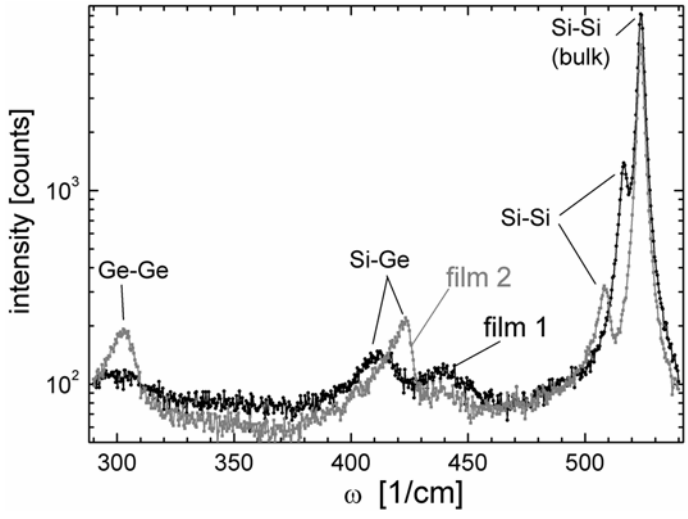

Fig. 2. Raman measurements of two $Si_{1-x}Ge_x$ films grown coherently on (001)-Si. The parameters t for film thickness and x for Ge content as determined by high-resolution X-ray diffraction are $t_1 = 57$ nm, $x_1 = 22.2$ at. % and $t_2 = 18$ nm, $x_2 = 46.8$ at. % for film 1 and film 2, respectively

Figure 3 suggests a linear composition dependence for the peak position of the strained films (in a certain composition range). A linear dependence with a different slope was obtained for strain-relaxed SiGe alloys [11], suggesting a general dependence of the following type:

$$\Delta\omega = \omega - \omega_0 = \alpha x + \beta x \frac{\varepsilon_{\parallel}}{\varepsilon_{\parallel,\max}} \tag{1}$$

where ω_0 is the Raman wavenumber for the strain-free state with vanishing Ge content (x –> 0), α and β are constants, $\varepsilon_{\parallel}$ is the in-plane strain of the SiGe film, and $\varepsilon_{\parallel,\max}$ is the maximum in-plane SiGe strain achievable for the given composition x assuming fully coherent film growth, i.e.

$$\varepsilon_{\parallel,\max} = \frac{a_{Si} - a_{SiGe}}{a_{SiGe}} \tag{2a}$$

and a_{SiGe} is the strain-free alloy lattice parameter determined for the Dismuke's law [12]:

$$a_{SiGe} = a_{Si} + a'x + a''x^2 \tag{2b}$$

with $a' = 0.01992$ nm and $a'' = 0.002733$ nm. The ratio $\varepsilon_{\parallel}/\varepsilon_{\parallel,\max}$ is a measure of the film strain degree and equals $1 - R$, with R being the usual relaxation degree of an epitaxial film. Considering a range of values for α (e.g., α_{Si-Si} from –62 cm^{-1} to –70 cm^{-1}) [11, 13]) for both the Si–Ge and Si–Si modes, from Fig. 3a, b it results that $\beta_{Si-Ge} \sim \beta_{Si-Si} = \beta \sim 30$. Within this approximation, the Ge content x and in-plane

strain $\varepsilon_{\|}$ can be derived from the measurement of the peak shifts $\Delta\omega_{\mathrm{Si–Si}}$ and $\Delta\omega_{\mathrm{Si–Ge}}$ using Eq. (1) for the Si–Si and Si–Ge modes, which yields:

$$x = \frac{\Delta\omega_{\mathrm{Si–Si}} - \Delta\omega_{\mathrm{Si–Ge}}}{\alpha_{\mathrm{Si–Si}} - \alpha_{\mathrm{Si–Ge}}} \tag{3a}$$

$$\varepsilon_{\|} = \frac{\Delta\omega_{\mathrm{Si-Si}} - x\alpha_{\mathrm{Si-Si}}}{x\beta} \qquad \varepsilon_{\|,\,\mathrm{max}} = -\frac{\Delta\omega_{\mathrm{Si-Si}} - x\alpha_{\mathrm{Si-Si}}}{\beta}\,\frac{a' + a''x}{a_{\mathrm{Si}} + a'x + a''x^2} \tag{3b}$$

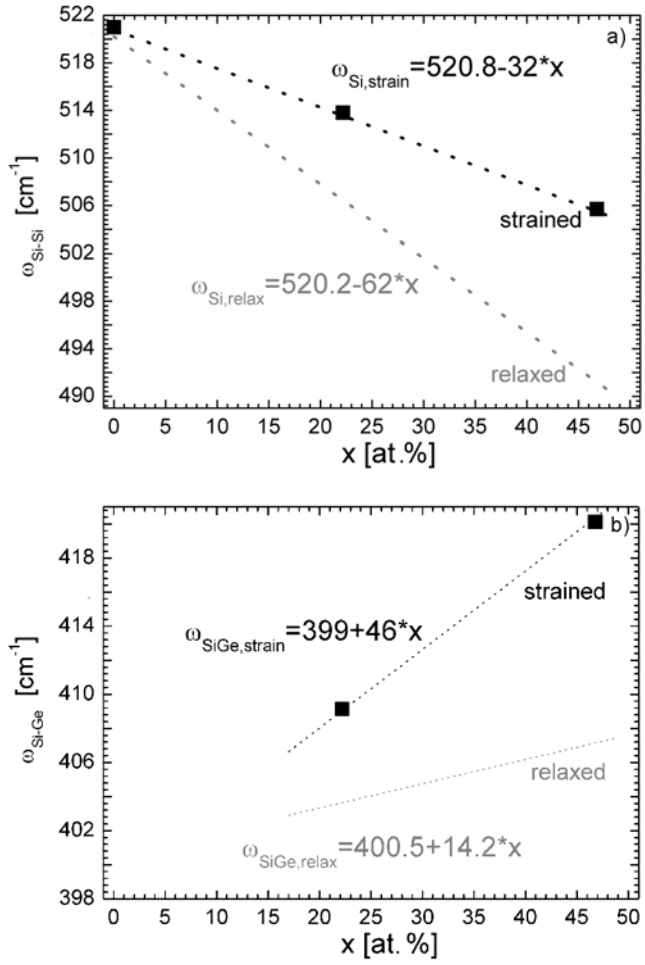

Fig. 3. Raman peak position of the Si–Si mode (a) and of the Si–Ge mode (b) for the measurements shown in Fig. 2, compared to data for bulk (strain relaxed) SiGe [11]

These relations provide an easy and straightforward way of determination of strain and composition in SiGe films with $0.2 < x < 0.5$. The observation of similar strain-

shift coefficients for both phonon modes is a rough approximation but it agrees with the measurements of Lockwood et al. [14]. Also, the dependence of the strain induced part of the Raman shift $\Delta\omega_\varepsilon$ and the in-plane strain $\varepsilon_\parallel$, written as $\Delta\omega_s = b\varepsilon_\parallel$ [14] can be derived. For vanishing Ge content, from Eq. (1):

$$b\,(x=0) = -\frac{a_{\mathrm{Si}}}{a'}\,\beta \tag{4}$$

with the value of $b \sim -820$ cm^{-1} inferred, which is in the reported range –(715–832) cm^{-1} (cf. [14]). Further measurements to improve the precision of these evaluations and to refine Eq. (3) are ongoing.

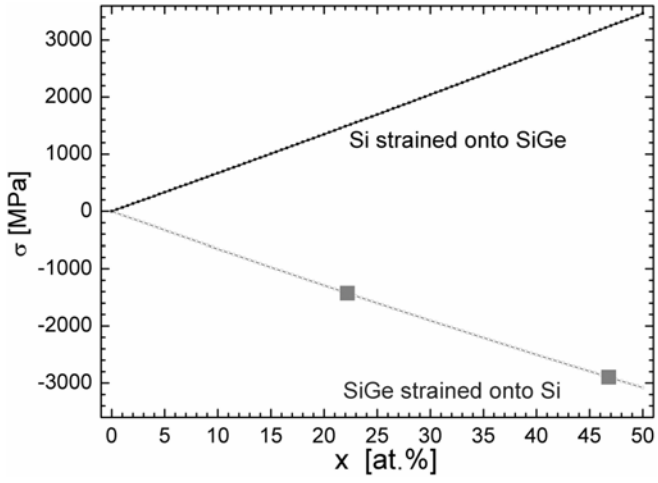

Fig. 4. Biaxial film stress of a $Si_{1-x}Ge_x$ film deposited in a fully strained state onto Si (lower line) with the two data points corresponding to Fig. 2, and the film stress of a Si film fully strained on a $Si_{1-x}Ge_x$ substrate (upper line)

The stress σ_{ij} in the SiGe films is obtained via Hooke's law:

$$\sigma_{ij} = C_{ijkl}\,\varepsilon_{kl} \tag{5}$$

(C_{ijkl} – elastic constants of the SiGe film, ε_{kl} – elastic film strain components), assuming linear elasticity. For the presupposed biaxial strain state:

$$\varepsilon_{11} = \varepsilon_{22} = \varepsilon_\parallel, \qquad \varepsilon_{33} = \varepsilon_\perp, \qquad \varepsilon_{ij} = 0\ (i \neq j) \tag{6a}$$

with vanishing stress normal to the free surface

$$\sigma_{33} = 0 \tag{6b}$$

resulting from Eq. (5) for the biaxial stress $\sigma = \sigma_{11} = \sigma_{22}$ in a (001)-oriented film

$$\sigma = \left(C_{11} + C_{12} - 2\frac{C_{12}^2}{C_{11}} \varepsilon_{\parallel} \right) \tag{7}$$

where the elastic constants C_{ij} of the SiGe alloy can be approximated by the linear rule of mixtures from those of Si and Ge [15]

$$C_{ij} = xC_{ij,\mathrm{Ge}} + (1-x)C_{ij,\mathrm{Si}} \tag{8}$$

Figure 4 shows the degree of stress attainable in strained SiGe films, calculated according to Eq. (4) with values corresponding to the measurement results given in Figs. 2 and 3. If in turn a Si film can be grown coherently on top of a defect-free unstrained SiGe substrate, stresses of similar magnitude but opposite in sign arise in the silicon (Fig. 4, upper curve).

3. Model calculations for strained Si regions between SiGe cavities

The strain in a coherently grown film with a given lattice mismatch to the substrate, as represented in Fig. 1a, can be directly determined from Eq. (7) as a homogeneous number within the film, whereas a strain or stress distribution has to be considered for patterned structures as in local strain generation (Fig. 1b). A detailed estimation of the strain state requires many structural details to be considered and is usually achieved by numerical methods such as FEM simulations [7]. Some basic aspects of the impact of geometry on the local strain state can also be derived analytically. In the following, a simple two-dimensional approach is discussed, considering SiGe regions as coherent inclusions in the sense of Eshelby [16] with a stress-free strain ε^* according to the lattice mismatch to Si, embedded in an isotropic Si matrix. The strain determined by an inclusion approach can be alternatively formulated using the model of continuously distributed virtual surface dislocations, as utilized in [17, 18] for modelling cubic and prismatic precipitates. Figure 5 represents the principle of virtual edge dislocations distributed along SiGe cavity interfaces. The defects are described by the ratio s between the Burgers vectors b_e of the edge dislocations and their separation distance l_e, corresponding to the stress-free strain:

$$\varepsilon^* = \frac{a_{0,\mathrm{SiGe}} - a_{\mathrm{Si}}}{a_{0,\mathrm{SiGe}}} = s = \frac{b_e}{l_e} \tag{9}$$

As pointed out in [16–18], the distribution of continuous dislocation can be considered to be equivalent to two-dimensional defects, conveniently described as Somigliana dislocations [19]. Figure 5a illustrates that each component ε_{11}^* and ε_{22}^* of the stress-free strain corresponds to two dipoles of Somigliana dislocations (SDs), introduced along the four interfaces of a rectangular SiGe region. Each SD thus corresponds to a semi-infinite distribution of edge dislocations (Fig. 6).

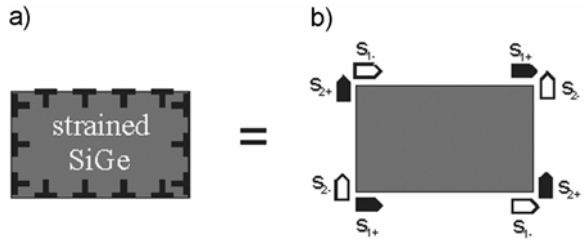

Fig. 5. Modelling of a strained SiGe region by a continuous distribution of virtual interface dislocations (a). Filled and empty symbols (b) represent SDs with positive and negative strengths s_+ and s_- in an equivalent description by pairs of SD dipoles

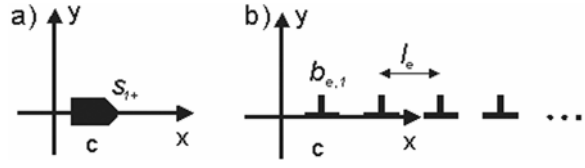

Fig. 6. SD s_{1+} (a) located at a distance c from the origin of the x-axis, according to a semi-infinite row of continuously distributed edge dislocations (b), with the defect strength parameter $s_1 = b_{e,1}/l_e$. A defect s_{1-} corresponds to a semi-infinite row of edge dislocations with the opposite Burgers vectors distributed along the x-axis, and SDs s_2 are obtained by a distribution of edge dislocations parallel to the y-axis with the Burgers vector $b_{e,2}$

The elastic fields for both orientations of the SDs within the xy-plane, described by indices 1 and 2 as the components of the Burgers vectors in the x- and y-directions, respectively, can be obtained by integrating the elastic fields of the equivalent edge dislocations [18], resulting in the following non-vanishing stress components for a defect s_{1+} (cf. Fig. 6a):

$$\sigma_{xx} = \frac{Gs_1}{2\pi(1-\nu)}\left\{\frac{(x-c)\,y}{(x-c)^2+y^2} - 2\arctan\frac{(x-c)}{y} - \pi\,\mathrm{sgn}\,y\right\} \tag{10a}$$

$$\sigma_{yy} = -\frac{Gs_1}{2\pi(1-\nu)}\,\frac{(x-c)\,y}{(x-c)^2+y^2} \tag{10b}$$

$$\sigma_{xy} = \frac{Gs_1}{2\pi(1-\nu)}\left\{\frac{1}{2}\ln\left[(x-c)^2+y^2\right] + \frac{y^2}{(x-c)^2+y^2}\right\} \tag{10c}$$

$$\sigma_{zz} = \nu\,(\sigma_{xx} + \sigma_{yy}) \tag{10d}$$

with the shear modulus G and Poisson's ratio ν, related to C_{ij} for a (001)-orientation by:

$$G = C_{44}\,, \qquad \nu = \frac{C_{12}}{C_{11}+C_{12}} \tag{11}$$

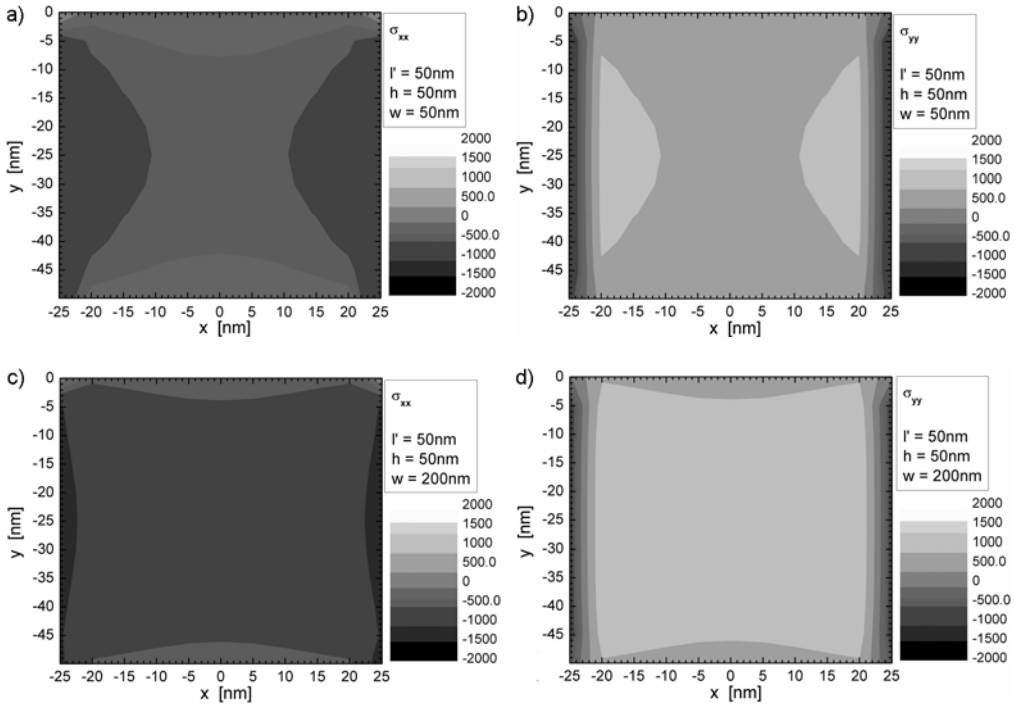

Fig. 7. Distributions of the stress components σ_{xx} (a, c) and σ_{yy} (b, d) in the channel region between two SiGe cavities with a square cross sections ($w = h = 50$ nm, a, b) and rectangular cross sections ($h = 50$ nm, $w = 200$ nm, c, d). The scale is given in MPa. The assumed lattice misfit of 1% corresponds to $x = 26.6$ at. % according to (2b). In a planar Si film fully strained on a SiGe substrate with this misfit, stresses of ~1800 MPa would arise

The corresponding fields of SDs s_2 can be obtained by coordinate transformation. Isoline maps of the 2D-stress fields obtained after summing up fields according to Figs. 1b and 5b are represented in Fig. 7. In these maps, two SiGe cavities are considered, with channel boundaries at $x = \pm 25$ nm and in the y-range between 0 and –50 nm. The gate structure, the lower elastic constants of SiGe (~94% of the Si constants for the given concentration), and the surface on top are neglected in this approach. In particular, the upper surface should modify the stress distribution within the channel. Nevertheless, some general tendencies for the impact of geometry on the stress state can be derived already from this simple approach. The stress state within the channel is thus not really uniaxial and restricted to the component σ_{xx}, but a perpendicular stress component of opposite sign occurs. Both local distribution and mean stress within the channel region depend on the cavity geometry. Figures 7c, d show, in comparison to Figs. 7a, b, that an elongation of the SiGe regions in the x-direction with unchanged channel structure yields a significant increase in the magnitude of both channel stress components. This tendency is also reflected in Fig. 8 for the central line $x = 0$ between the SiGe regions, showing a stress reduction of ~200 MPa for a change from the elongated cavity cross section to a square-like one. Furthermore, Figure 8 shows how an

increase of the stress component σ_{xx} can be achieved by reducing the distance l' between the cavities or by increasing their height h (cf. Fig. 1b).

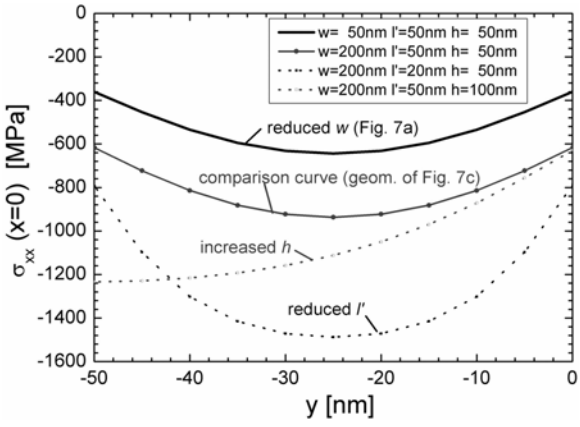

Fig. 8. Distribution of the stress σ_{xx} along a line in the channel centre (x = 0 nm) between SiGe regions with different geometric parameters for a lattice misfit of 1%

These results show that the geometry of SiGe cavities has an important impact on the stress component σ_{xx} which is directly related to the charge carrier mobility in the x-direction according to the piezoelectric tensor of Si [20]. For a detailed discussion of the distribution of all stress components, a subsequent refinement of the present approach is necessary, taking into account different elastic properties in the SiGe cavities and in the surface on top of the cavities. The approach can be based on stress fields of virtual dislocations at interfaces of isotropic media [21], considering the impact of a surface on the SD stress fields [22].

4. Conclusions

In summary, the problem of local stress in silicon structures used for CMOS technology was approached both experimentally and by modelling. It was shown that Raman spectroscopy is an appropriate technique to derive SiGe film stress and composition. For that purpose, a simple relationship between the Raman shifts of two phonon modes, composition, and stress was derived. High stress levels in strained SiGe films were obtained. Though the Raman measurements were performed with a spatial resolution of only ~ 1μm, highly improved lateral resolution can be obtained by combining a near-field Raman approach with AFM techniques. The need for higher strain resolution is motivated by the requirement to understand stress state on the device scale in present and future CMOS technologies. A link between strain measurements and technology development can be provided by modelling on the device scale, which requires close feedback to measurements. To estimate the local stress state in patterned silicon structures, an analytic approach for calculating the local distribution is

introduced, which can yield general tendencies important for understanding the mechanisms and for further improving the performance of devices. According to calculation results, effective methods for increasing the magnitude of the (compressive) channel stress σ_{xx} should be elongating the SiGe cavities in the x-direction and reducing their distance l'. Within the framework of the used analytic approach, the implementation of different elastic moduli of Si and SiGe, of surface effects, and of the 3D shape of strained regions, as considered in [17, 21, 22], is possible.

Acknowledgements

Valuable discussions with Ehrenfried Zschech, AMD Saxony, Dresden (Germany), are gratefully acknowledged. For TEM we are grateful to Hans-Jürgen Engelmann, also with AMD Saxony, Dresden (Germany).

References

[1] WELSER J., HOYT J.L., TAGAKI S., GIBBONS, F.J., IEDM Tech. Dig., 1994, 373.
[2] HOYT J.L., NAYFEH H.M., EGUCHI S., ABERG I., XIA G., DRAKE T., FITZGERALD E.A., ANTONIADIS D.A., IEDM Tech. Dig., 2002, 23.
[3] MOHTA N., THOMPSON S.E., IEEE Circuits Dev. Mag., 9/10 (2005), 18.
[4] LEE M.L., FITZGERALD E.A., BULSARA M.T., CURRIE M.T. LOCHTEFELD A., J. Appl. Phys., 97 (2005), 011101.
[5] EBERL K., SCHMIDT O.G., DUSCHL R., [in:] *Properties of Silicon Germanium and SiGe: Carbon*, E. Kasper, K. Lyutovich (Eds.), INSPEC London (2000), p. 75.
[6] ANASTASSAKIS E., SIAKAVELLAS M., J. Appl. Phys., 90 (2001), 144.
[7] MOROZ V., XU X., PRAMANIK D., NOURI F., KRIVOKAPIC Z., Sol. State Techn., 7 (2004), 49.
[8] HORSTMANN M., WEI A., KAMMLER T., HÖNTSCHEL J. BIERSTEDT H., FEUDEL T., FROHBERG K., IEDM Tech. Dig. (2005), 243.
[9] IRISAWA T., NUMATA T., TEZUKA T., USADA K., NAKAHARAI S., HIRASHITA N., SUGIYAMA N., TOYODA E., TAGAKI S., IEDM Tech. Dig. (2005), 727.
[10] ZHU L., ATESANG J., DUDEK P., HECKER M., RINDERKNECHT J., RITZ Y., GEISLER H., HERR U., GEER R., ZSCHECH E., Mater. Sci.-Poland, 27 (2007), 19.
[11] TSANG J.C., MOONEY P.M., DACOL F., CHU J.O., J. Appl. Phys., 75 (1994), 8098.
[12] DISMUKES J.P., EKSTROM L., PAFF R.J., J. Phys. Chem., 68 (1964), 3021.
[13] ALONSO M.I., WINER K., Phys. Rev. B, 39 (1989), 10056.
[14] LOCKWOOD D.J., BARIBEAU J.M., Phys. Rev. B, 45 (1992), 8565.
[15] FLORO J.A., CHASON E., LEE S.R., PETERSEN G.A., Appl. Phys. Lett., 71 (1997), 1694.
[16] ESHELBY J.D., Proc. Royal Soc., A241 (1957), 376.
[17] KROUPA F., LEJCEK L., Czech. J. Phys., B20 (1970), 1063.
[18] BONNET R., MARCON G., ATI A., Phil. Mag (A), 51 (1985), 429.
[19] SOMIGLIANA, C., Atti. Accad. Naz. Lincei Rc., 23 (1914) 463.
[20] SMITH C.S., Phys. Rev. B, 94 (1954), 42.
[21] NAKAHARA S., WU J.B.C., LI J.C.M., Mat. Sci. Engn., 10 (1972), 291.
[22] ROMANOV A.E., HECKER M., phys. stat. sol. (a), 115 (1989), K159.

Received 3 January 2006
Revised 28 May 2006

Materials Science-Poland, Vol. 25, No. 1, 2007

Experimental challenges for approaching local strain determination in silicon by nano-Raman spectroscopy*

L. ZHU[1,2], J. ATESANG[1,3], P. DUDEK[1,4], M. HECKER[1**], J. RINDERKNECHT[1], Y. RITZ[1], H. GEISLER[1], U. HERR[2], R. GEER[3], E. ZSCHECH[1]

[1]AMD Saxony LLC & Co. KG, Materials Analysis Department, Wilschdorfer Landstrasse 101, D-01109 Dresden, Germany

[2] University of Ulm, Materials Department, Albert-Einstein-Allee 47, D-89081 Ulm, Germany

[3] University at Albany-SUNY, College of Nanoscience and Engineering, NanoFab 300 South, 255 Fuller Rd. Albany NY 12203, USA

[4] Wrocław University of Technology, Faculty of Microsystem Electronics and Photonics, ul. Janiszewskiego 11/17, 50-372 Wroclaw, Poland

Raman intensity enhancement induced by nanoprobes (metal particles and metallised tips) approached to a strained silicon sample surface is reported. With silver nanoparticles deposited onto a silicon surface, high enhancements in the vicinity of particles were observed. Furthermore, metallised tips were scanned inside the spot of the laser used for Raman measurements. Both silver-coated and pure silver tips, mounted onto a tuning fork, indicated high Raman signal enhancement for optimised tip position within the laser spot. Atomic force microscopy was performed on a structured sample to investigate the stability of these tips. Focused ion beam was utilized to refine and to re-sharpen pure silver tips after the measurements. Complementary measurements were performed using pure tungsten tips. Due to the high hardness of W wires, a special pre-etching technique was applied in this case.

Key words: *Raman scattering; strained silicon; Ag particles; tip enhanced Raman spectroscopy*

1. Introduction

Increasing product performance and achieving a continuous cost reduction per function have been for several decades the driving forces for scaling down CMOS device dimensions. Traditional scaling of the device structures alone, however, will

---

* Presented at the joint events 1st Workshop "Synthesis and Analysis of Nanomaterials and Nanostructures" and 3rd Czech-Silesian-Saxony Mechanics Colloquium, Wrocław, Poland, 21–22 November, 2005.

** Corresponding author, e-mail: michael.hecker@amd.com

not be sufficient to meet future performance goals. New materials and "non-classical" devices are developed and implemented, resulting in new challenges for the device metrology. Strain engineering has become an important tool; for example, strained silicon has been used to affect the electronic band structure and to increase charge carrier mobility in the channel region of MOSFET devices. New analytical techniques for high-resolution strain measurement at transistor cross-sections and new metrology strategies to monitor non-destructively strain variations are needed to optimise and control the variety of processes, including those for strained silicon substrates and for utilizing process-induced local strain.

The potential for measuring local strain in the transistor channel with high spatial resolution is limited to a few techniques. Techniques based on transmission electron microscopy (TEM) such as convergent beam electron diffraction (CBED), nanobeam diffraction (NBD), and high-resolution TEM (HRTEM) [1, 2], as well as nano-Raman spectroscopy [3, 4] are currently being evaluated for their applicability to measure strain with a spatial resolution in the 10 nm range. In particular, approaches based on Raman spectroscopy are promising due to fewer preparation issues and higher sample throughput. They have been proven to be well suited to strained silicon problems on the μm scale [5].

Since the first report of Anastassakis et al. [6] related to the effect of strain on the Raman peak position, Raman spectroscopy has been widely applied as a stress sensor. The Raman signal, however, is intrinsically weak (less than 1 in 10^7 photons), and its spatial resolution is limited by the optical diffraction limit. This resolution limit can be overcome by scanning near field microscopy (SNOM) utilizing an apertured fibre tip, however the intensity issue becomes even worse [7]. After the discovery of significantly enhanced Raman signals of pyridine molecules due to rough silver electrodes by Fleischmann et al. [8], Jeanmaire and van Duyne found that the differential Raman cross section of molecules in liquid or gaseous phases receives a huge enhancement upon adsorption on rough noble metal surfaces [9]. The so-called surface enhanced Raman spectroscopy (SERS) can be applied not only to bulk metallic materials, but also to metal nanoparticles, and even evaporated thin silver films [10]. The limitation of the nanoparticle approach is that the particles should be deposited exactly in the region of interest. As an alternative, an apertureless approach is to utilize metal tips, employing the tip enhanced Raman spectroscopy (TERS) effect, which can increase the Raman intensity by several orders of magnitude [11, 12]. In this case, the signal enhancement is due to the enhancement of the electromagnetic field in the vicinity of a sharply pointed tip, resulting from the excitation of surface plasmons by the incident laser beam. Metallic tips can be made of or coated with certain metals (e.g. Ag, Au), or nanoparticles can be attached to the tip. It has been reported that parallel silicon lines with 300 nm line-widths, separated by 380 nm SiO_2 lines, can be resolved utilizing a metal-coated fibre tip [13]. The near field approach, TERS, seems to allow a spatial resolution of the Raman signal well below 100 nm to be reached.

In this paper, experimental challenges are described for obtaining the silver-based SERS/TERS effect using nanoparticles and shape-optimised pure silver and silver-coated tips.

2. Experimental

2.1. Measurement set-up

The measurement system consists of a Renishaw spectrometer with a confocal microscope for Raman measurements [14], combined with a Nanonics Atomic Force Microscopy (AFM) system for navigating a metallic tip close to the sample surface inside the laser spot. The integration of these two systems is controlled by dynamic data exchange software allowing the system to acquire simultaneously AFM data and Raman spectra.

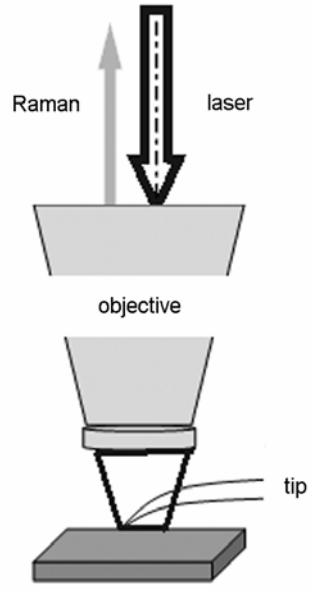

Fig. 1. Schematic set-up diagram of tip enhanced Raman scattering. The tip was positioned inside the laser spot between the objective lens and the sample surface. The Raman light is backscattered through the same objective lens to the grating and detector

For the AFM part, a cantilevered tip, fixed to a tuning fork, is used (Fig. 1). The tip can be controlled both when it is approached to the surface below the objective lens ("in feedback", distance to surface being several nanometers) and when it is "retracted" (distance to surface several μm).

The Raman system is equipped with a Leica microscope and a motorized stage placed in an enclosure chamber. The 50× objective (numerical aperture 0.45, working distance 1 cm) used in our experiments focuses the laser to a spot size of about 3 μm and has a convergence angle of 26°. This facilitates adequate access of the laser to the tip below the objective. The collected signal is detected by a charge coupled device (CCD) cooled by a Peltier cooling system. The spectrometer uses several gratings, from which one can be selected for spectra acquisition for different laser wavelengths. For the measurements presented here, Ar-ion lasers with 488 nm and 514 nm wavelengths were used.

2.2. Tip preparation

Tip preparation is crucial for TERS measurements, because the radius, shape, and material of the tip determine the enhancement factor and spatial resolution. To obtain a highly localized field enhancement, a tip with a small diameter and sharp end should be used for TERS. Pure metallic tips were prepared using electrochemical etching of silver and tungsten wires. This preparation technique provides good quality tips in a reproducible and reliable way [15, 16]. The principal set-up for etching both kinds of tips is based on a commonly used configuration [17], as shown in Fig. 2. For our experiments, an aqueous solution with approximately 60% perchloric acid and ethanol (1:2 or 1:3), and an applied voltage from 1.5 V to 1.8 V, were selected for silver tip etching [18]. A diluted KOH solution (3 mol/dm^3: 56 g KOH in 333 ml of water) and an applied voltage between 1.8 V and 2.1 V were chosen for tungsten tip etching [19].

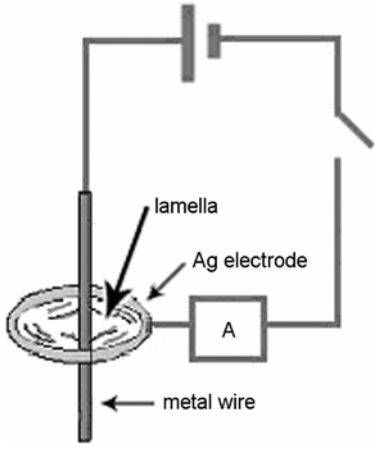

Fig. 2. Schematic diagram of electrochemical etching. The metal wire (anode) is situated in the middle of the lamella inside a silver ring that acts as a cathode during etching

Since a tungsten wire is much harder and stiffer than a silver one, it is much more difficult to cut the etched tungsten tips to a proper length with a wire cutter. Therefore, an additional process called "pre-etching" was developed. Prior to the actual tungsten tip etching, the tungsten wire was etched at a specific position to generate a "pre-determined breaking point". Subsequently, the tungsten wire was finally etched and separated. The scanning electron microscopy (SEM) picture of a tungsten tip after "pre-etching" (Fig. 3) clearly shows that the thinner part originating from the "pre-etch" can be cut later in a well-defined way. Furthermore, the length of the tip after the final cut can also be controlled by the position of the "pre-etch".

The mounting of the tips to the tuning fork (Fig. 4) was done in such a way that the total mass of tip and glue added onto the tuning fork was as small as possible. This method should minimize the damping of the tuning fork resonance frequency and, consequently, enables a high sensitivity to be maintained during feedback. Epoxy (Epo-Tek 375) was used to glue the tip to the tuning fork. The epoxy was cured at 90 °C for 90 minutes. It showed excellent adhesion between the tip and tuning fork.

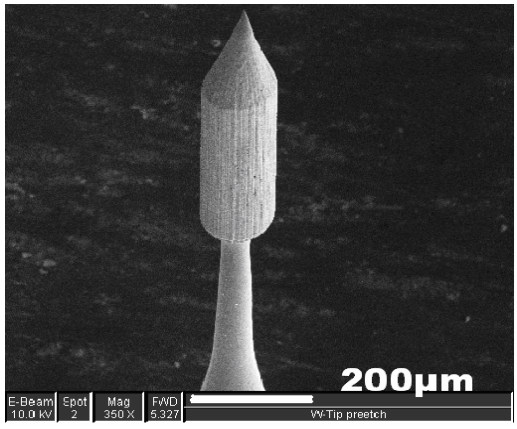

Fig. 3. SEM image of a tungsten tip after a "pre-etch" treating for local thinning below the tip apex

Fig. 4. Schematic picture showing a tip mounted to a normal tuning fork

By using a 45° mounting angle, a good compromise to minimize the laser and Raman light shadowing and to maximize the enhancement effect was achieved.

2.3. Preparation by FIB

The Focused Ion Beam (FIB) technique [20] was used combined with micromanipulators for target cross-section preparation of samples subsequently imaged by

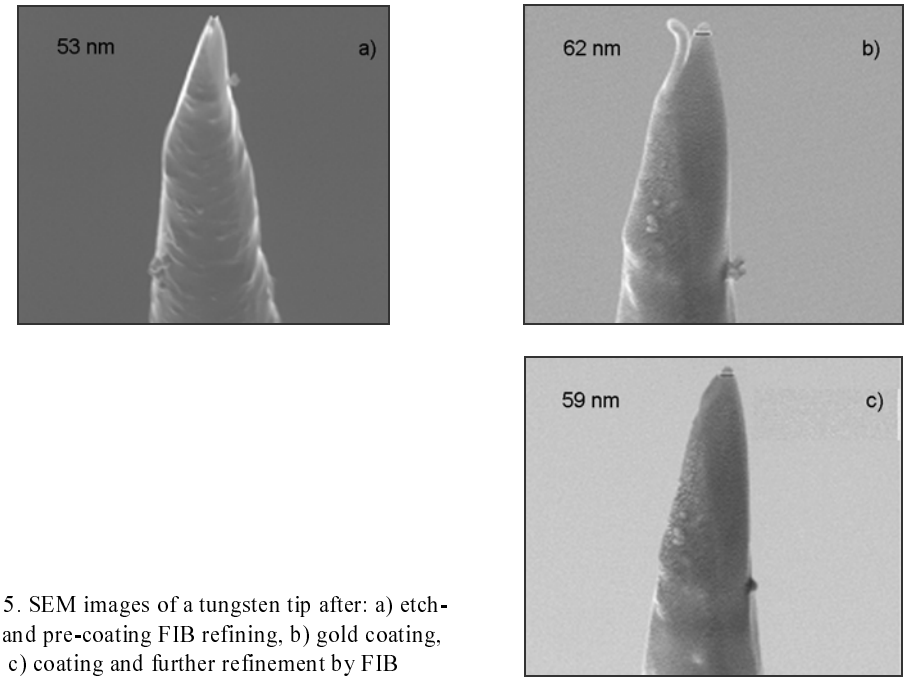

Fig. 5. SEM images of a tungsten tip after: a) etching and pre-coating FIB refining, b) gold coating, c) coating and further refinement by FIB

lamella can be prepared by the lift-out technique directly from the region of interest of the sample, which is lifted using a needle manipulator [21, 22]. This method is also an attractive technique for fabrication and modification of metallic nanostructures. In our application, the FIB technique was used to refine or re-sharpen metallised tips. A FEI dual-beam FIB (Strata 235), with a built-in needle Omniprobe manipulator, was applied to modify the tips. For example, after etching, a pure W tip was refined and milled by FIB as shown in Fig. 5a. After subsequent gold coating, a defect in the gold capping was found (Fig. 5b). Finally, this gold coated W tip was re-sharpened to achieve a diameter of about 60 nm (Fig. 5c). This refinement technique is limited to a maximum rotation of 66^{o} (from $-12°$ to $54°$) of the tip itself, which determines the type of tips that can be prepared or modified using the FIB technique without readjusting the tips.

3. Results of measurement and discussion

Bulk Si samples are often used for TERS measurement [13], whereas in our application a special film stack was utilized, consisting of a 70 nm strained Si layer on top of 150 nm thick SiO_2 and the Si substrate. Since the penetration depth of 488 nm laser light in Si is about 500 nm, a two-peak spectrum was obtained for the first-order Si–Si phonon modes, which can be well fitted with two Lorentzian curves. The lower frequency at about 516 cm^{-1} represents a strained Si peak, and the peak appearing at 521 cm^{-1} corresponds to the Si bulk peak. Monitoring the intensity ratio between these two peaks allows us to distinguish between conventional (far field) Raman measurements, shadowing effects, and enhancement effects. Moreover, information regarding the penetration depth related to the near field can be derived from measuring layer stacks.

3.1. Enhanced Raman scattering intensity close to silver particles

Nanoparticles of noble metals such as Ag or Au deposited onto the surface of a Raman active sample potentially lead to a Raman signal enhancement caused by SERS. The described particles were obtained from a solution containing Ag nanoparticles with sizes ranging from 20 nm to 300 nm. A droplet of a mixture of this solution and deionised water (volume ratio 1:4) was deposited on the sample surface with a pipette and evaporated at room temperature. SEM was used to characterize the deposited silver as shown in Fig. 6a. Subsequently, a Raman mapping with a step size of 0.1 μm in both x and y directions utilizing the 488 nm laser was conducted. The mapped intensity at wavenumber 516 cm^{-1} (Fig. 6b) corresponding to the position of the strained Si film peak exhibits high enhancement effects. A comparison with the spectrum taken from the bottom part of the Raman mapping and far from the particles reveals an enhancement of the strained Si peak intensity by around 75% without sig-

nificant change of the Si bulk peak intensity and background signal (Fig. 7). This example of the strong amplification of the evanescent near field close to a nanoparticle reflects the high depth resolution that can be achieved utilizing the SERS effect compared to the far field signal which is related to the normal penetration depth of the incident laser.

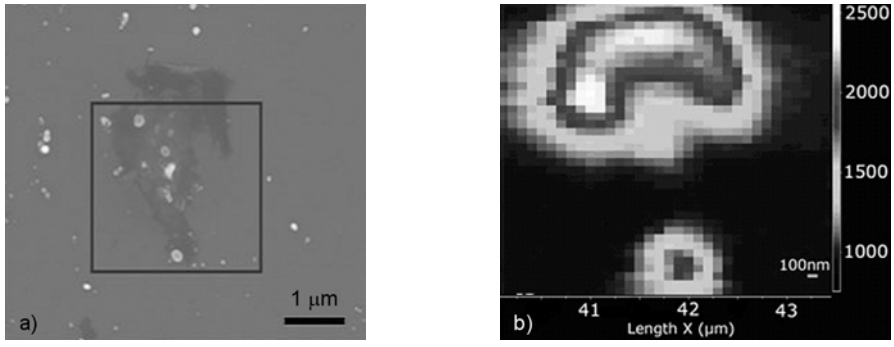

Fig. 6. SEM image with the size of 6.5×6.5 μm^2 (a), and Raman mapping utilizing the 488 nm laser (b) with the size of 3.5×3.5 μm^2. The grey scale indicates the intensity of the strained silicon film peak at the wavenumber of 516 cm^{-1}

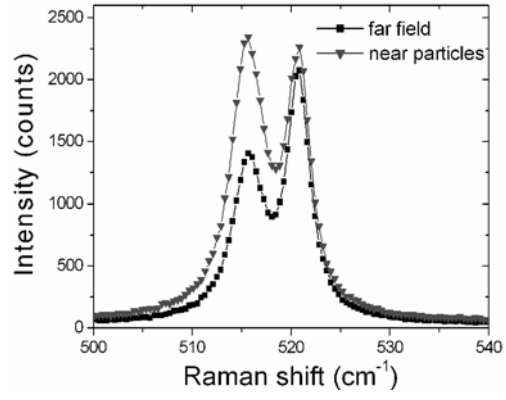

Fig. 7. Spectra obtained at a sample position far from particles (far field) and close to particles, utilizing the 488 nm laser

From the SEM picture shown in Fig. 6a and the Raman map in Fig. 6b taken at the same area it is possible to correlate the bottom part of the Raman map to the single particle shown in the SEM picture. Due to the selected deposition procedure, there are also regions such as those in the top parts of both pictures, where no exact correlation was obtained because of high particle density.

3.2. Tip enhanced Raman scattering with silver tips

As discussed in Section 2, pure silver tips were produced by an electrochemical etching method. The Ag tips, properly etched and mounted to a tuning fork, were carefully approached to the sample surface by the AFM table located below the objective lens and then slightly retracted (to a distance of several hundred nm). Raman

spectra of the sample below the tip as shown in Fig. 8 were measured under this condition and compared with a measurement obtained with the tip far away from the laser spot ("far field" measurement).

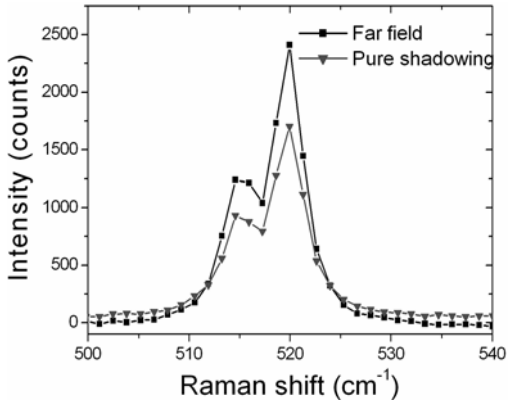

Fig. 8. Spectra taken without the tip (far field) and with the tip slightly retracted, showing the shadowing effect of the tip. The laser wavelength of 488 nm was used

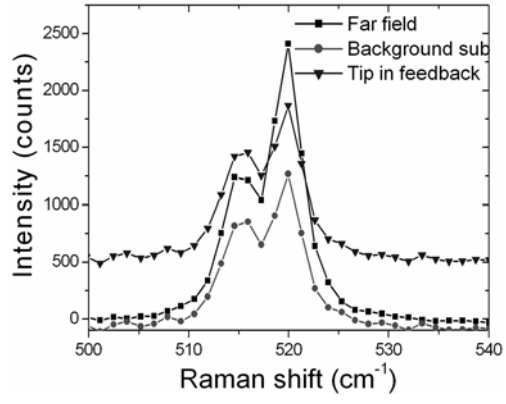

Fig. 9. Spectra obtained without the tip (far field), with the tip in feedback, and background subtracted, utilizing the 488 nm laser

After curve fitting, the intensity ratio between both peaks was found to be unchanged for these two spectra. Furthermore, both peak intensities are lower for the tip in feedback, indicating a pure shadowing effect. After this measurement, the tip was approached to the sample surface again and navigated inside the laser beam to obtain enhanced intensities. Enhancement effects as shown in Fig. 9 were obtained only in a small *xy* range inside the laser beam. A high background, which might arise from a contamination on the tip surface, was subtracted for curve fitting. After this subtraction, no increment for the strained Si peak intensity due to the approached tip was obtained. This result may be related to the high background and strong shadowing effect by the tip. However, an enhancement effect can be derived from the change of the intensity ratio between the Si bulk peak and the strained Si peak. According to Fig. 9, this ratio changed from 2.1 for the far field measurement to 1.4 for the tip in feedback. Possibly, an additional cleaning procedure of the silver tips could reduce the background signal.

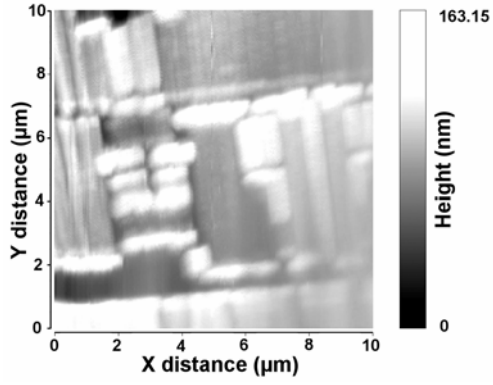

Fig. 10. AFM mapping graph of a structured sample using a silver tip

AFM scanning of the region of interest is necessary to characterize laterally structured samples by such tips and to correlate surface morphology to measured Raman features. Figure 10 shows an example obtained with the Ag tip used in Fig. 9, which demonstrates the principal possibility of obtaining AFM scans by these tips. After scanning, however, most of the self-prepared silver tips were bent, apparently because silver is very ductile compared to other AFM tip materials. One possibility to overcome this problem is to use FIB preparation to re-sharpen the bent tips. With FIB, tips of good quality with the diameter of approximately 40 nm were obtained. Another possibility to combine AFM mappings and Raman enhancement experiments is to use W tips coated with Ag or Au. FIB was used to sharpen and refine tips before and after coating, too. A third way, utilizing metal coated quartz tips, is discussed below.

3.3. TERS measurements with silver coated quartz tips

As observed for pure Ag tips, Raman enhancement effects are obtained only for a certain position of the tip inside the laser spot. For a more systematic study, measurements were performed by *xy* scanning the tip in the feedback mode inside the 514 nm laser spot, with fixed positions of the laser spot and sample. During such AFM scans, Raman spectra were acquired at specific positions, thus yielding Raman maps for tip positions inside the whole defined area. After curve fitting, the Raman intensities related to the Si bulk peak and to the strained Si peak are shown separately in Fig. 11. The left Raman mapping showing the Si bulk peak intensity clearly indicates a gradual shadowing effect. During tip scanning, an increasing part of the tip inhibits laser light from illuminating the sample surface, leading to a decrement of the overall bulk Raman signal. Raman mapping of the strained Si peak intensity shows that there is a large enhancement without increased background inside the area where shadowing effects for the Si bulk peak intensity occur. As a reference, a spectrum was also recorded with the tip outside the laser spot. Both spectra in Fig. 12 were fitted using the Lorentzian function. The enhancement for the strained Si peak is 48%, and the decrement of the Si bulk peak intensity is about 7% as compared to the “far field”

spectrum. This result should be referred to a local field enhancement close to the tip and restricted to the strained Si layer, not propagating into the Si bulk.

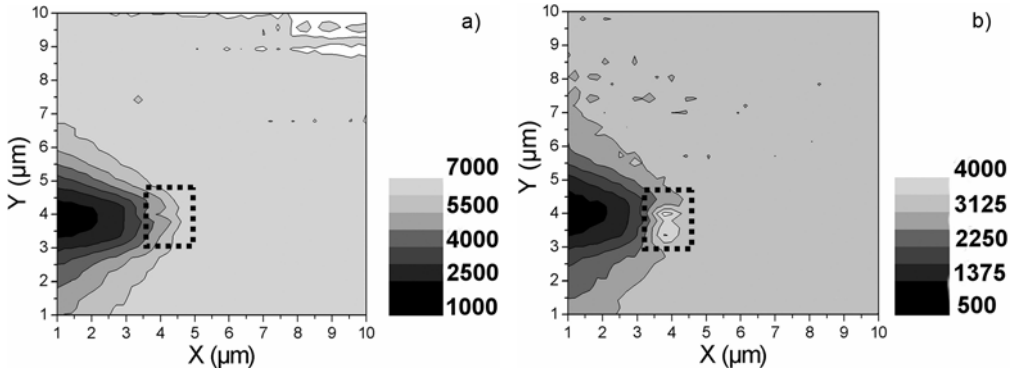

Fig. 11. Raman mapping of: a) Si bulk intensity (521 cm^{-1}) utilizing a 514 nm laser, b) strained Si layer intensity (516 cm^{-1}) utilizing a 514 nm laser. The sizes of both mappings are 10×10 μm^2

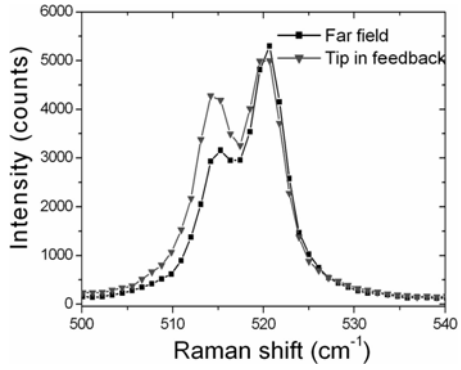

Fig. 12. Raman spectra obtained from tip scanning utilizing a 514 nm laser. "far field" spectrum denotes a spectrum taken with the tip outside the laser spot

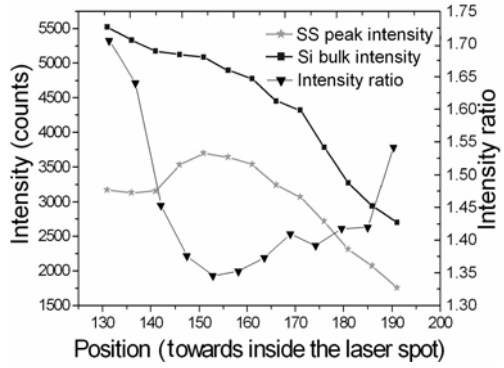

Fig. 13. Curves of strained Si peak intensity I_{sSi}, Si bulk peak intensity I_{Si} and intensity ratio I_{Si}/I_{sSi} for the tip scanning the laser spot utilizing a 514 nm laser

The enhancement was verified by navigating the tip manually inside the 514 nm laser spot. First, for the tip positioned outside the laser spot, a spectrum was acquired. Subsequently, the tip was moved inside the laser spot with a step size of 125 nm. The Si bulk peak intensity curve shown in Fig. 13, with the tip successively approaching the laser spot, indicates that the shadowing effect increases while moving the tip towards the centre of laser spot. At specific positions within the spot, the strained Si peak intensity is increased. This observation can be seen more clearly in the intensity ratio curve (Fig. 13). The spatial extension of the region with low intensity ratio, i.e. an enhancement of the strained Si layer intensity, was found to be sensitive to the tip properties. As a consequence, in order to avoid strong shadowing effects and achieve high enhancement at the same time, the tip position should be near the edge of the laser spot.

In order to confirm the TERS effect from these tips, a "two-point" mapping was performed, i.e. two spectra were taken at each point, one for the tip in feedback and one for the tip retracted by about 8 μm from the sample surface. Furthermore, the difference between these two spectra was calculated for every scanning point. The mapping of the difference spectrum at the wavenumber 516 cm^{-1} (Fig. 14) clearly shows that besides the "island", i.e. the enhancement area, all other regions show a small or almost no difference signal.

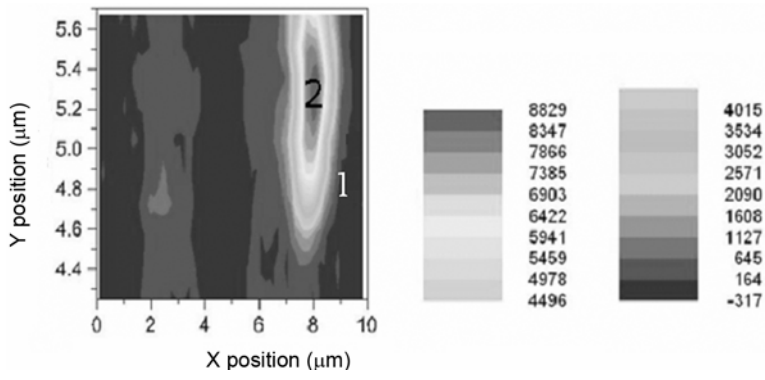

Fig. 14. Raman mapping of the difference spectrum at 516 cm^{-1} utilizing a 514 nm laser

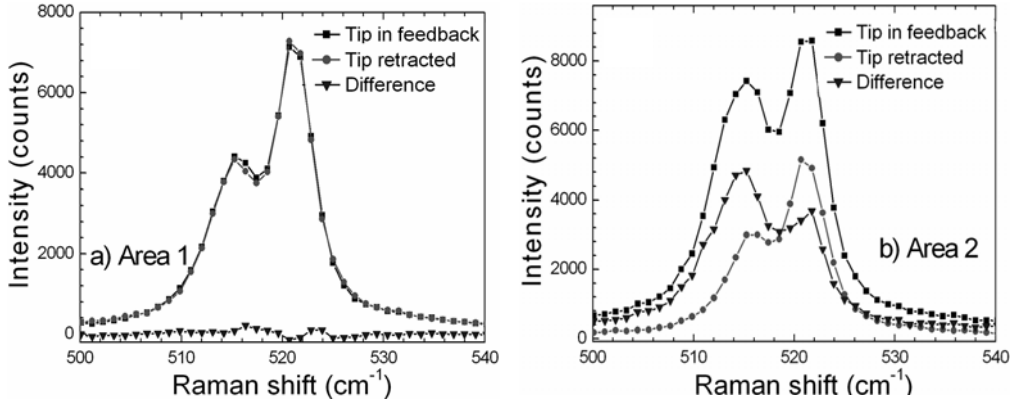

Fig. 15. Spectra obtained from areas 1 and 2 in Fig. 14, corresponding to the tip being retracted (about 8 μm), the tip in feedback, and the difference between the two spectra, utilizing a 514 nm laser

In area 1 of Fig. 14, there is almost no difference between the spectra taken with the tip in feedback and with a retracted tip (Fig. 15a), which means that the tip was totally outside the laser spot. Therefore the spectra taken inside area 1 can be regarded as "far field", i.e. spectra acquired without a tip or any influence of the tip. Within area 2, a high enhancement was achieved (Fig. 15b). Upon retraction, the tip moved towards the centre of the laser spot causing increased shadowing. Therefore, "far field" spectra obtained inside area 1 should be used for direct comparison with the

enhanced spectra acquired inside area 2, if the shadowing effect is not considered thoroughly. From curve fitting an enhancement for the strained Si peak intensity of 93% and a slight intensity increment for the Si bulk peak intensity of 8% was obtained. Note that inside the mapping shown in Fig. 14, the positions of area 1 and area 2 are rather close. Since area 1 is the area where the tip was outside the laser spot, in area 2 the tip should be close to the edge of the laser spot. This result confirms the proposed optimum tip position for highest enhancement. From the mapping data in Fig. 14, the size of the area in which high enhancement is achieved is about 500×500 nm^2.

4. Conclusions

To investigate the surface enhanced Raman scattering of strained silicon samples, both silver nanoparticles and metallised AFM tips were approached to the surface of a silicon layer stack. The top silicon layer was strained, enabling the enhancement effects close to the surface and in the bulk of the sample to be observed separately.

For silver nanoparticles deposited on the layer stack, a high enhancement of the strained Si intensity (~ 75%) was observed. The locations of the enhanced Raman signal were correlated to the particles using SEM. In contrast to the signal from the top layer about 70 nm thick, no significant enhancement of the Si bulk peak occurred.

Pure silver tips etched by an electrochemical method were mounted to an AFM tuning fork for measuring enhanced Raman signals. Clear enhancement effects were observed, and the potential of such tips for AFM scanning was proven. The use of such tips, however, is limited by bending effects occurring during AFM scanning. The possibility of re-sharpening bent tips by FIB was verified. An improvement of tip stability is expected for tungsten tips prepared by electrochemical etching, which can be coated by a SERS inducing metal film.

With silver coated quartz tips, Raman peak enhancement of the strained silicon film up to 50% was achieved by navigating the tip inside the laser spot and moving it to an optimised position. This was achieved by performing tip scans with the tip in feedback, and by "two-point" tip mappings, i.e. measurements of two Raman spectra at each point. These experiments indicate that the optimal tip position for highest enhancement is close to the edge of the laser spot.

The experiments performed with metallised tips are promising for achieving high local strain resolution in patterned Si structures by utilizing the described difference measurements ("two-point mappings") in TERS experiments. Further efforts are necessary to prevent the oxidization of the silver coating, and to achieve long-term stability of both the tip itself and enhancement effect.

Acknowledgements

The authors would like to thank Boleslaw Mazurek, Wrocław University of Technology (Poland) for providing the Ag particle solution, Petra Hofmann, AMD Saxony LLC & Co. KG (Germany) for SEM support, as well as Hartmut Prinz, also with AMD Saxony LLC & Co. KG, and Othmar Marti, University of Ulm (Germany) for their helpful discussions.

References

[1] MORNIROLI J.P., ALBAREDE P.H., JACOB D., [in:] E. Zschech, C. Whelan, T. Mikolajick (Eds.), *Materials for Information Technology*, Springer, London, 2005, p. 99.
[2] FORAN B., LIAN G., CLARK M.H., Future Fab. Intl. 20 (2006), 127.
[3] ATESANG J., GEER R.E., [in:] R.E. Geer, N. Meyendorf, G.Y. Baaklini, B. Michel (Eds.), SPIE Proc., 2005, p. 134.
[4] PRIKULIS J., MURTY K.V.G.K., OLIN H., KÄLL M., J. Microscopy, 210 (2003), 269.
[5] HECKER M., GEISLER H., Mater. Sci.-Poland, 25 (2007), 7.
[6] ANASTASSAKIS E., PINCZUK A., BURSTEIN E., POLLAK F.H., CARDONA M., Solid State Commun., 8 (1970), 133.
[7] LEWIS A., TAHA H., STRINKOVSKI A., MANEVITCH A., KHATCHATOURIANTS A., Nature Biotechn., 21 (2003), 11.
[8] FLEISCHMANN M., HENDRA P.J., MCQUILLAN A.J., Chem. Phys. Lett., 26 (1974), 163.
[9] JEANMAIRE D.L., VAN DUYNE R.P., J. Electroanal. Chem., 84 (1977), 1.
[10] HAYAZAWA N., MOTOHASHI M., SATIO Y., KAWATA S., Appl. Phys. Lett., 86 (2005), 263114.
[11] MEHTANI D., LEE N., HARTSCHUH R.D., KISLIUK A., FOSTER M.D., SOKOLOV A.P., MAGUIRE J.F., J. Raman Spectrosc., 36 (2005), 1068.
[12] PETTINGER B., REN B., PICARDI G., SCHUSTER R., ERTL G., Phys. Rev. Lett., 92 (2004), 096101.
[13] SUN W.X., SHEN Z.X., Mater. Phys. Mech., 4 (2001), 17.
[14] Available online at: http://www.renishaw.com/client/product/UKEnglish/PRD-1027.shtml
[15] GUISE O.L., AHNER J.W., JUNG M.C., GOUGHNOUR P.C., YATES J.T., Jr., Nano Lett., 2 (2002), 191.
[16] KLEIN M., SCHWITZGEBEL G., Rev. Sci. Instrum., 68 (1997), 3099.
[17] REN B., PICARDI G., Rev. Sci. Instrum., 75 (2004), 4.
[18] IWAMI M., UEHARA Y., USHIODA S., Rev. Sci. Instrum., 69 (1998), 4010.
[19] ITO T., BUEHLMANN P., UMEZAWA Y., Anal. Chem., 70 (1998), 255.
[20] GIANUZZI L.A., STEVIE F.A. (Eds.), *Introduction to Focused Ion Beams*, Springer, New York, 2004.
[21] ALTMANN F., Pract. Metallography, 40 (2003), 175.
[22] RITZ Y., STEGMANN H., ENGELMANN H.J., ZSCHECH E., Pract. Metallography, 41 (2004), 180.

Received 3 January 2006
Revised 28 May 2006

Materials Science-Poland, Vol. 25, No. 1, 2007

Scaling of nonvolatile memories to nanoscale feature sizes*

T. MIKOLAJICK**, N. NAGEL, S. RIEDEL, T. MUELLER, K.-H. KÜSTERS

Qimonda Dresden GmbH & Co. OHG, Technology Center flash QD TC FL, Dresden, Germany

The market for nonvolatile memory devices is growing rapidly. Today, the vast majority of nonvolatile memory devices are based on the floating gate device which is facing serious scaling limitations. Material innovations currently under investigation to extend the scalability of floating gate devices are discussed. An alternative path is to replace the floating gate by a charge trapping material. The combination of charge trapping and localized channel hot electron injection allows storing two physically separated bits in one memory cell. The current status and prospects of charge trapping devices are reviewed, demonstrating their superior scalability. Floating gate as well as charge trapping memory cells suffer from severe performance limitations with respect to write and erase speed and endurance driving system overhead. A memory that works like random access memory and is nonvolatile would simplify system design. This, however, calls for new switching effects that are based on integrating new materials into the memory cell. An outlook to memory concepts that use ferroelectric switching, magnetic switching, phase change, or other resistive switching effects is given, illustrating how the integration of new materials may solve the limitations of today's semiconductor memory concepts.

Key words: *nonvolatile memories; flash memories; NAND; NOR; organic memories; molecular memories*

1. Introduction

Driven by the demand in mobile devices, the market for nonvolatile memories is growing rapidly [1]. Figure 1 shows the market development expected until 2010. In recent years, floating gate flash memories have evolved as the mainstream nonvolatile memory solution. Traditionally, the flash market is divided into two parts. In code flash it is important to execute software directly from the flash memory, therefore fast random access is required. Typical applications for such memories are cellular phones, where the software of the phone as well as user data can be stored on the

---

*Presented at the joint events 1st Workshop "Synthesis and Analysis of Nanomaterials and Nanostructures" and 3rd Czech-Silesian-Saxony Mechanics Colloquium, Wrocław, Poland, 21–22 November, 2005.

**Corresponding author, e-mail: Thomas.Mikolajick@esm.tu-freiberg.de

same flash device. In the data flash arena large amounts of data are transferred between the memory and system. Performance is therefore achieved by handling large amounts of data in parallel.

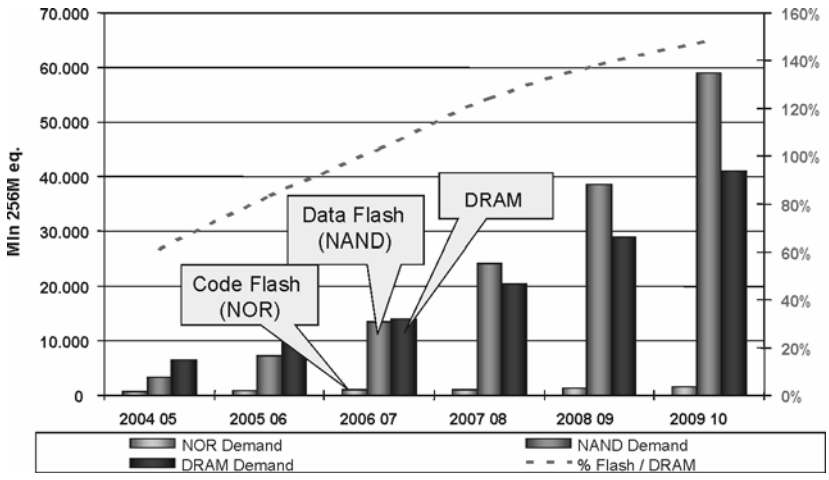

Fig. 1. Market development in terms of bit consumption for code and data flash memories in comparison to DRAM memories for the years 2004–2010

Typical applications here are memory cards for digital still cameras or USB sticks. Dynamic random access memories were traditionally used as the technology driver for the semiconductor industry. Since the 1Gb generation, data flash memories have caught up with DRAM and recently data flash is scaling ahead of DRAM in terms of density as well as minimum feature size [2]. To achieve the required 10 years of retention, however, the tunnel oxide cannot be scaled below 6 nm. Moreover, the coupling between floating gates will narrow down the available window between different states of a memory cell. These effects will limit further scaling of floating gate devices, which is today's workhorse of nonvolatile memories. This paper discusses the scaling down of nonvolatile memory cells, with focus on material innovations essential for extending nonvolatile memory scalability down to a feature size of tens of nanometers.

2. Floating gate devices

In Figure 2, basic structures of a floating gate memory cell are shown together with a brief explanation of the cell operation as well as main programming and erase mechanisms. The amount of charge present on a floating gate determines the threshold voltage of the transistor. By sensing the current at an appropriate gate voltage, two states of the cell can be discriminated according to the current that will flow through the cell. Electrons can be transferred to the floating gate using either channel hot electron injection or Fowler–Nordheim tunnelling. In channel hot electron programming, the current is passed trough the channel by applying both a high drain as well as

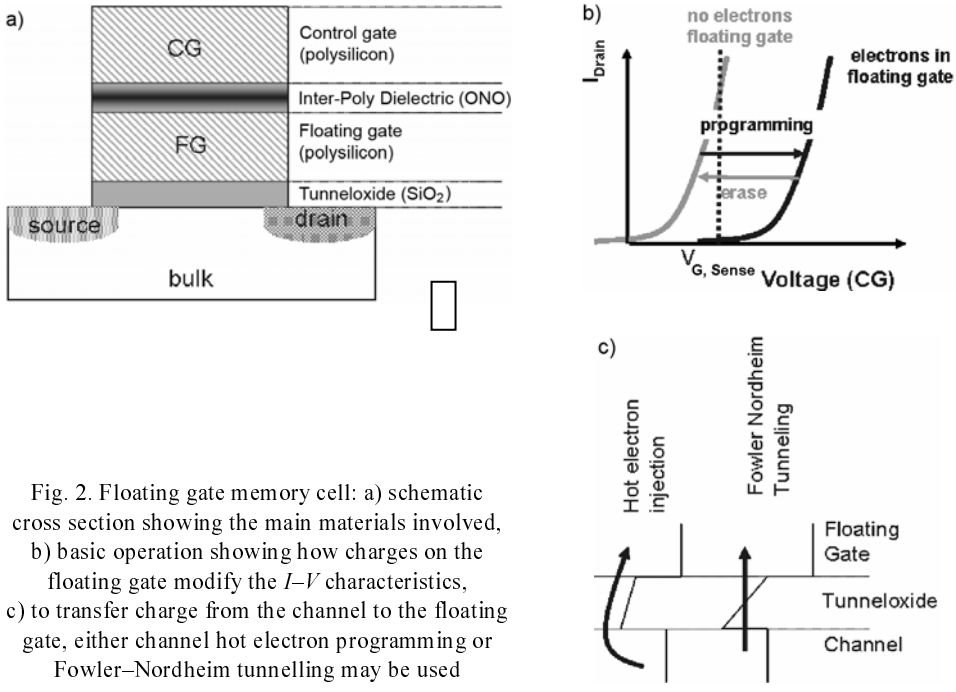

Fig. 2. Floating gate memory cell: a) schematic cross section showing the main materials involved, b) basic operation showing how charges on the floating gate modify the *I–V* characteristics, c) to transfer charge from the channel to the floating gate, either channel hot electron programming or Fowler–Nordheim tunnelling may be used

a high gate voltage with respect to the source. At the drain side of the device, some of the electrons may have enough energy to surmount the potential barrier between the silicon and tunnel oxide and can be injected into the floating gate. In Fowler–Nordheim tunnelling, a high field is applied between the channel and floating gate, leading to the reduction of the effective barrier for electrons.

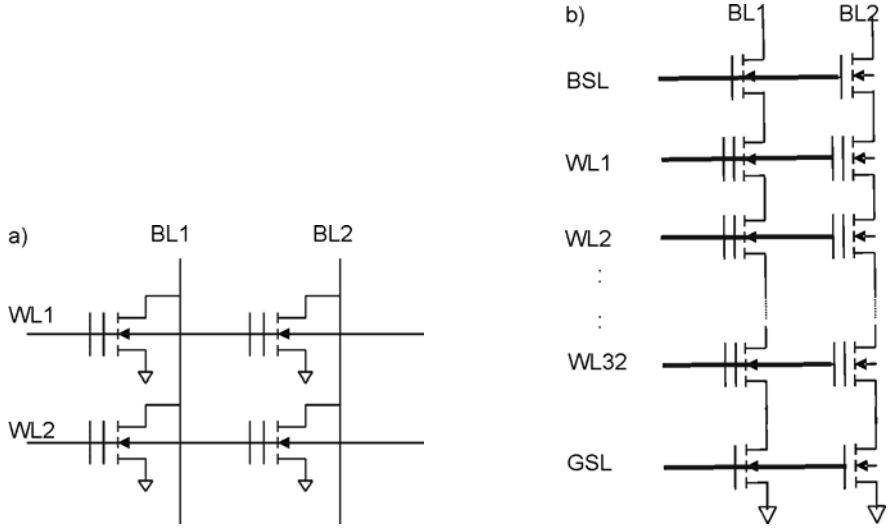

Fig. 3. Basic architectures for flash memory arrays: a) NOR, b) NAND

Figure 3 shows the main array architectures which can be implemented in this basic cell [3]. In the NOR architecture, each cell is connected to a separate bitline by a bitline contact. This allows fast random access. In the NAND architecture, however, an individual cell is connected to the bitline through a string of 16 or 32 cells. This leads to a very small physical cell size, since contacts to the source and drain regions are shared between all 16 or 32 cells of one NAND string. The high series resistance created by the series connection of the cells leads to slow random access, which has to be compensated by massive parallelisation.

Looking into the future, floating gate memories are facing serious scaling limitations. A general issue is the non-scalability of the tunnel dielectric. To maintain the required nonvolatile retention, the tunnel dielectric has to be thicker than 6 nm [4]. Further scaling can only be obtained by radically reengineering the tunnel barrier. Materials with a higher electric permittivity constant, such as HfO_2, ZrO_2, etc., which are currently investigated in logic transistors, could help. Crested barriers [5] could further improve the basic memory cell by increasing the ratio between on and off currents, leading to much faster write times as well as lower programming voltages.

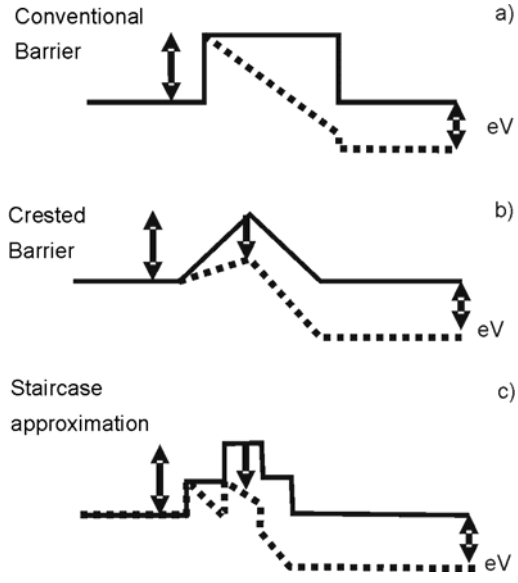

Fig. 4. Schematic presentation of crested barriers: a) conventional barrier, b) crested barrier, c) an approximation of a crested barrier by a staircase function

Figure 4 shows the principle of such an approach. Since a crested barrier is not achievable with materials having the required barrier heights, a staircase approximation using three layers with different band offsets as well as different electric permittivities is a reasonable approach. In the optimum structure, the centre layer would have a high band offset and a high electric permittivity and the surrounding layer a lower band offset as well as a lower electric permittivity. In most materials, how-

ever, a high band offset is correlated with a low electric permittivity and vice versa, making the optimum choice very difficult. A stack consisting of $Si_3N_4/Al_2O_3/Si_3N_4$ could be a reasonable and producible compromise [6]. Another serious constraint is that in the current cell architecture, the inter-poly dielectric together with the wordline has to fit into the space between two floating gates (see Fig. 5a).

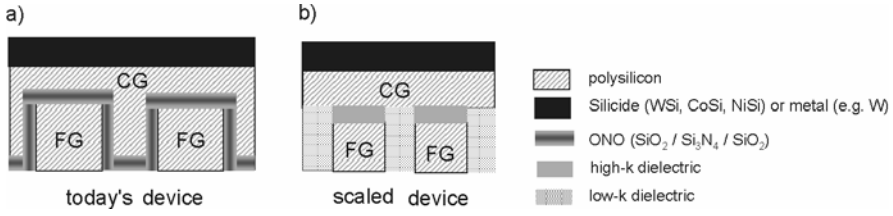

Fig. 5. Cross section of a floating gate cell along the wordline: a) today's solution with an ONO interpoly-dielectric, b) scaled down version with a high-*k* interpolydielectric and low-*k* decoupling dielectric

With the currently used triple dielectric consisting of $SiO_2/Si_3N_4/SiO_2$, with a total thickness of about 15–20 nm, this will limit cell scaling. Without using the floating gate sidewalls a high-*k* dielectric will be required to achieve the necessary coupling between the control gate and floating gate. Furthermore, a low-*k* dielectric will be necessary to decouple two neighbouring floating gates (see Fig. 5b). Typical materials are very similar to the ones discussed for gate dielectrics in conventional MOS transistors, including HfO_2 and Hf/Al microlaminates [7]. While scaling down the floating gate device, the spacing between floating gates will continuously decrease. This leads to a higher capacitive coupling between floating gates, resulting in cross talk between cells. This calls for a material with a lower electric permittivity between the floating gates, like that already shown in Fig. 5b, which also has to be implemented in the area between the word lines. Replacing the silicon nitride spacer of the cell transistor by a silicon dioxide spacer as shown in [8] may already help to significantly reduce the effect. In the long term, real low-*k* materials will be necessary.

3. Charge trapping devices

A natural way to extend the scalability of a floating gate device is to replace the charge storing floating gate by a dielectric material, in which the charges are stored in deep traps. The main drawback of this approach is that electrons that are erased via the bottom oxide by either electron or hole tunnelling may be replaced by electrons tunnelling from the control gate trough the top oxide to the nitride. This will lead to erase saturation, which limits the erase speed at a given thickness of the bottom oxide. A very thin bottom oxide of the order of 1 nm is not practical, since the retention requirement cannot be achieved. This was the biggest obstacle for the commercial success of charge trapping devices. New materials can greatly help improve this issue. A high-*k* top oxide can reduce the voltage drop across the top oxide and a high work

function gate can increase the potential barrier for electrons that travel across the top oxide. For the top oxide, Al_2O_3 or a combination of Al_2O_3 and HfO_2 are the best candidates [9], and As gate electrodes p^+ have the potential of drastically improving the situation [10]. Poly-depletion, however, may limit the actual gain in this approach. Since materials like Pt or Ir, which would be very well suited from a work function point of view, are hard to integrate into a CMOS flow, TaN seems to be a very good choice [11]. The combination of both approaches allows for an erase speed like in charge trapping memory cells similar to tht in NAND flash [12]. For the charge trapping material itself, silicon nitride has been well established for many years. Silicon oxinitride [13] as well as hafnium oxide and aluminium oxide [14], however, are possible alternatives with potential benefits.

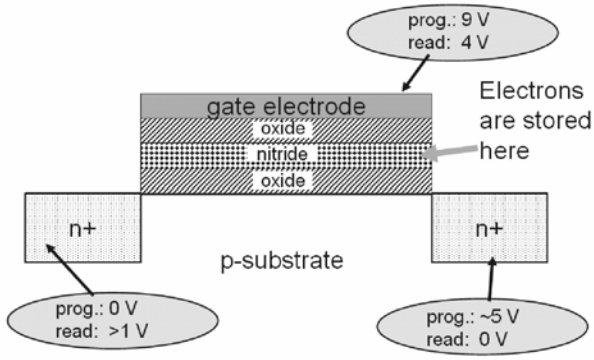

Fig. 6. Schematic of a multi-bit charge trapping memory cell illustrating the programming, erase, and read operations

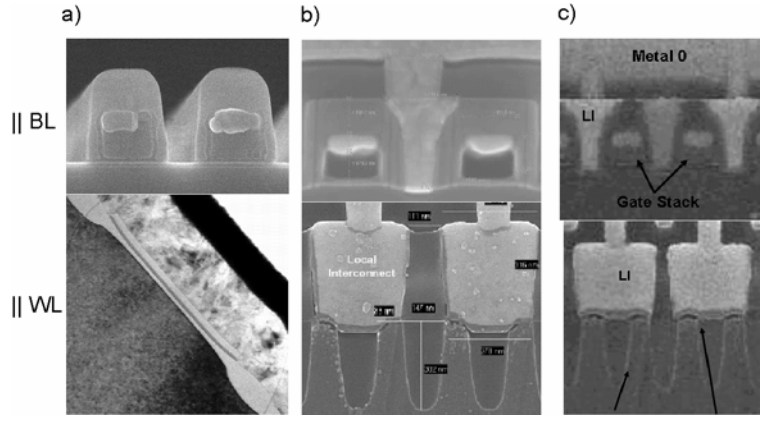

Fig. 7. Cross section parallel to bitline (top row) and parallel to WL (bottom row) of TwinFlash memory cells of the: a) 170 nm, b) 110 nm, and c) 90 nm generations

Another way of solving the erase saturation issue is to change the erase mechanism to hot hole injection [15]. If hot electrons are used for the programming, then

two bits can be stored and physically separated in a single cell [16]. Figure 6 illustrates such a multi-bit charge trapping memory cell as well as its basic programming, erase and read functions. Figure 7 shows the real cross sections of three generations of TwinFlash, which is an advanced version of the multi bit charge trapping concept [17, 18].

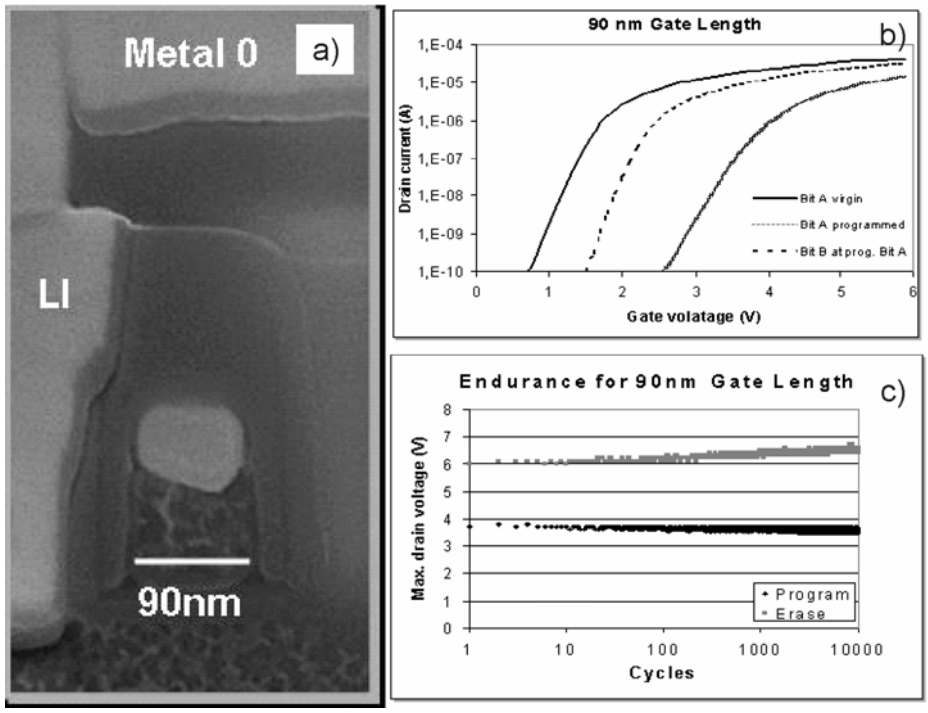

Fig. 8. TwinFlash memory cell from the 60 nm generation: a) SEM cross section, b) *I–V* characteristics of native and programmed cell, c) cycling behaviour

Figure 8 demonstrates the scalability of this type of cell down to the 60 nm node. Further scaling down to about 40 nm groundrules is possible using standard approaches [18]. For even smaller groundrules, 3D devices can help overcome the scaling issues [19]. Again, high-*k* materials that replace existing charge trapping and barrier materials may further extend the scalability of also this type of device [20].

4. Alternative memories

All charge-based nonvolatile memories described in the previous chapters suffer from the fact that a high potential barrier is needed to achieve nonvolatile retention. The barrier, however, has to be overcome by charges during programming and erasing operations. This contradiction leads to severe performance drawbacks of all charge-

based memory concepts that include the necessity for high programming and erase voltages (in the range 10–20 V), slow write and erase times (from μs up to seconds in contrast to ns, which are common in random access memories), and very limited endurance (typically up to 10^6 cycles; 10^{16} cycles are required for a random access memory). From a system point of view, a random access type of memory that is nonvolatile would be of great benefit. To achieve such a memory, new switching effects realized in new materials are required [21].

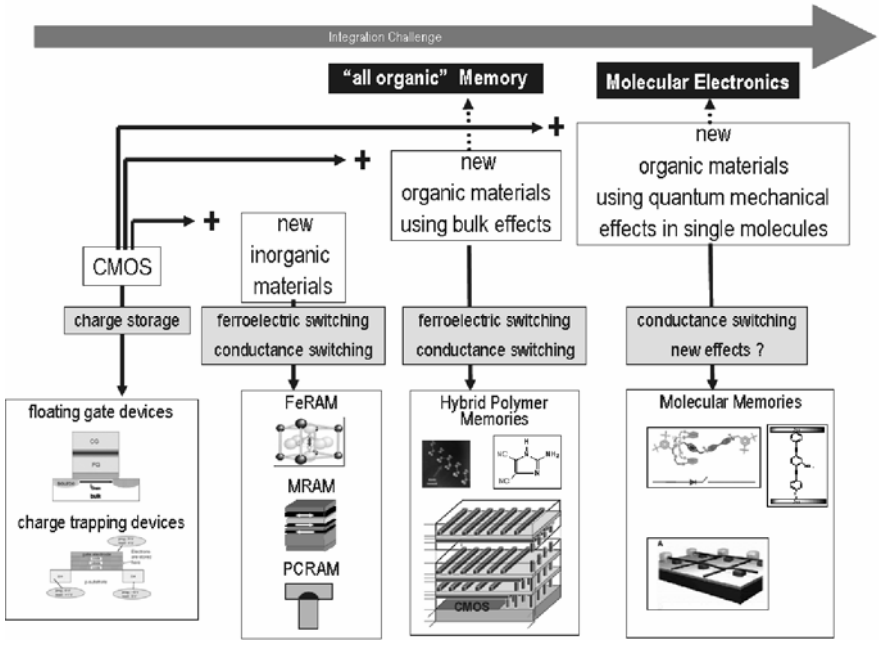

Fig. 9. Hierarchy of alternative nonvolatile memories from a materials perspective

Figure 9 gives an overview over a number of concepts discussed in the literature from a material point of view. In general, the concepts can be classified [22] into concepts that use switching in inorganic materials, concepts that use bulk effects in organic materials (referred to as organic memories in this overview), and concepts that use quantum mechanical effects in single molecules (referred to as molecular memories). Due to a scaling potential down to the molecular level, memories based on carbon nanotubes are included in the later class. A detailed overview of the material aspects of many possible options can be found in Chapter 3 of [22]. Due to their similarity to CMOS processing, the concepts that use inorganic switching materials are the most advanced. Among them ferroelectric memories (FeRAM), magnetoresistive memories (MRAM), and phase change memories (PCRAM) are close to production or already in production for niche applications. FeRAM [23, 24] uses the switchable electrical polarization of ferroelectric materials such as lead-zirconium titanate (PZT) and strontium-bismut tantalate (SBT) to store information. The main

challenge is the material integration of the ferroelectric material and electrodes. Since the ferroelectric has to maintain the right phase, high temperature annealing is necessary and exposure to hydrogen needs to be avoided. Moreover, since the charge transferred during polarization switching is detected, a three dimensional structure is necessary in order to maintain a minimum sensed charge when the device is scaled to nanometer dimensions [25]. In MRAM [26], tunnel magnetoresistance is used to distinguish between different states. This approach consists of a thin tunnelling dielectric like Al_2O_3 or MgO placed between two ferromagnetic electrodes. One of the two ferromagnetic electrodes is pinned to an antiferromagnetic layer to define a reference. The resistance of the stack then depends on the orientation of the magnetization in both electrodes with respect to one another. A resistance ratio of 50-200% can be obtained when the magnetizations of the two layers are parallel (lower resistance case) or when they are antiparallel (higher resistance case). Writing is traditionally done by passing current through the word and digit lines, leading to a situation where the superposition of the two magnetic fields at the intersection of both lines is high enough to switch one of the two ferromagnetic layers, while the field generated by each of the lines separately is not high enough to change the magnetization state. This approach, however, requires high currents (in the mA range) to be passed trough the lines, and is therefore a major scaling limitation. Spin transfer switching, where a current is passed trough the tunnelling barrier, has recently been proposed to overcome this issue [27]. Even in this approach the required switching current has to be further reduced. PCRAM is based on the reversible phase change of chalcogenide materials such as $Ge_2Se_2Te_5$ between high resistive amorphous and low resistive crystalline phases [28]. Integration as well as scalability is much simpler than in FeRAM and MRAM. Some issues remain, however, the most prominent one being the reset current that is required to melt the material in the process of transforming the crystalline phase to an amorphous one. Other issues are the asymmetric write/erase as well as the still limited endurance. Recently, a 64Mb memory was demonstrated using 0.12 μm technology [29].

More challenging than the integration of inorganic materials is the integration of organic materials. Here, a wide variety of concepts have been shown in literature [30–32]. Polymer ferroelectrics seem to be the most advanced. Nonetheless, resistive switching devices promise better scalability.

Switching in single molecules directly paves the way to the nanoscale world. Rotaxane [33], porphyrines [34], and phenyl-based molecules with attached nitro-redox centres [35] are among the most prominent molecules that show promising switching effects. In all these, however, the defined contact with the outside world and integration with CMOS logic are challenges that remain to be solved. An alternative path to molecular memories is the utilization of carbon nanotubes. A mechanical memory based on a cross bar arrangement of nanotubes, separated by support pillars and switched by electrostatic forces, is among the most frequently discussed concepts in this direction [36]. An alternative is the implementation of a charge trapping device using a carbon nanotube transistor. Carbon nanotubes, however, have basic uncertainties with respect to reproducible mass production.

5. Summary and conclusions

Driven by the demand for more mobile electronic devices, the market for nonvolatile memories is growing rapidly. Today, floating gate flash is the mainstream solution for nonvolatile memories. Floating gate devices face serious scaling limits in the sub 50 nm region, however, and new materials will be required to scale below 50 nm, especially high-*k* dielectrics to increase coupling and low-*k* dielectrics to reduce unwanted coupling between neighbouring cells. Charge trapping devices are an alternative that have developed very rapidly in the past few years. Especially the multibit charge trapping concept has appeared in significant production volumes for both code and data flash products. The scaling of this type of device will continue to the 40 nm generation without major material innovations. In order to overcome the basic limitations of all charge-based nonvolatile memories, new switching materials have to be integrated into the CMOS process flow. Inorganic approaches such as ferroelectrics, magnetoresistive switching, as well as material phase change, are in advanced development stages. They are all, however, far from reaching the small cell size benchmark set for data flash memories. Therefore, they will appear where their performance advantage comes into play or as an alternative to code flash or SRAM memories. For the long-term scalability, organic as well as molecular memories promise to extend nonvolatile memories beyond classical CMOS scaling. Hybrid memories that combine CMOS with organic or molecular memory cells, as well as memories where even the necessary electronic circuits are replaced by organic or molecular circuits, can be envisioned as two possible development steps on the long-term roadmap as indicted in Fig. 9. In the short to mid term, classical charge-based memories fabricated with the CMOS technology will continue to dominate the market, especially in data flash devices.

References

[1] NIEBEL A., Proc. of the 20th Nonvolatile Semiconductor Memory Workshop, Monterey, California (2004), p. 14.
[2] BYEON D.-S., LEE S.-S., LIM Y.-H., PARK, J.-S., HAN W.-K., KWAK P.-S., KIM D.-H., CHAE D.-H., MOON S.-H., LEE S.-J., CHO H.-C., LEE J.-W., KIM M.-S., YANG J.-S., PARK Y.-W., BAE D.-W., CHOI J.-D., HUR S.-H., SUH K.-D., Proc. Int. Solid State Circuits Conference, IEEE, San Francisco (2005), p. 46.
[3] PAVAN P., BEZ R., OLIVO P., ZANONI E., Proc. IEEE, 85 (1997), 1248.
[4] LAI S., Proc. Seventh Biennial International Nonvolatile Memory Technology Conference, IEEE, Albuquerque (1998), p. 6.
[5] LIKHAREV K., Appl. Phys. Lett., 73 (1998), 2137.
[6] CASPERSON J., J. Appl. Phys., 92 (2002), 261.
[7] LEE W.-H., CLEMENS J.T., KELLER R.C., MANCHANDA L., VLSI Technology Digest of Technical Papers (1997), p. 117.
[8] LEE J.-D., SUNG-HOI H., CHOI J.-D., IEEE Electr. Device Lett., 23 (2002), 264.
[9] CHOI S., CHO M., HWANG H., KIM J.W., J. Appl. Phys., 94 (2003), 5408.
[10] BACHHOFER H., REISINGER H., BERTAGNOLLI E., VON PHILIPSBORN H., J. Appl. Phys., 89 (2001), 2791.
[11] LEE C.-H., PARK K.-C., KIM K., Appl. Phys. Lett., 86 (2005), 73510.

[12] SHIN Y., CHOI J., KANG C., LEE C., PARK K.-T., LEE J.-S., SEL J., KIM V., CHOI B., SIM J., KIM D., CHO H.-J., KIM K., IEDM Digest Techn. Papers, IEEE (2005), p. 327.
[13] ISHIMARU T., MATSUZAKI N., OKUYAMA Y., MINE T., WATANABE K., YUGAMI J., KUME H., ITO F., KAWASHIMA Y., SAKAI T., KANAMARU Y, ISHII Y., MIZUNO M., ISHII Y., MIZUNO M., KAMOHARA S., HASHIMOTO T., OKUYAMA K., KURODA K., KUBOTA K., IEDM Digest Techn. Papers. IEEE (2004), p. 885
[14] TAN Y.-N., CHIM W.-K., BYUN J.C., WEE-KIONG C., IEEE Trans. Electr. Devices 51 (2004), 1143.
[15] CHAN T.Y., IEEE Electr. Device Lett., 8 (1987), 93.
[16] EITAN B., PAVAN P., BLOOM I., ALONI E., FROMMER A., FINZ D., IEEE Electr. Device Lett., 21 (2000), 543.
[17] NAGEL N., OLLIGS, D., POLEI, V., PARASCANDOLA S., BOUBEKEUR H., BACH L., MULLER T., STRASSBURG M., RIEDEL S., KRATZERT P., CASPARY D., DEPPE J., WILIER J., SCHULZE J., SCHULZE N., MIKOLAJICK T., KUSTERS K.-H., SHAPPIR A., REDMARD E., BLOOM I., EITAN B., VLSI Techn. Digest Techn. Papers, Kyoto (2005), p. 120.
[18] STEIN V., KAMIENSKI E.G., ISLER M., MIKOLAJICK T., LUDWIG C., SCHULZE N., NAGEL N., RIEDEL S., WILLER J., KÜSTERS K.-H., Proc. Non-Volatile Memory Technology Symposium, Dallas, 2005, p. 5.
[19] WILLER J., LUDWIG C., DEPPE J., KLEINT C., LAU F., PALM H., EITAN B., BLOOM I., Proc. 19th Non-volatile Semiconductor Memory Workshop, Monterey, California (2003), p. 42.
[20] SUGIZAKI T., KOBAYASHI M., ISHIDAO M., MINAKATA H., YAMAGUCHI M., TAMURA Y., SUGIYAMA Y., NAKANISHI T., TANAKA H., VLSI Techn. Digest Techn. Papers, Kyoto (2003), p. 27.
[21] PINNOW C.-U., MIKOLAJICK T., J. Electrochem. Soc., 151 (2004), K1.
[22] *Materials for Information Technology*, E. Zschech, C. Whelan, T. Mikolajick (Eds.), Springer, London, 2005, p. 112.
[23] MIKOLAJICK T., DEHM C., HARTNER W., KASKO I., KASTNER M.J., NAGEL N., MOERT M., MAZURE C., Microelectronics Reliability, 41 (2001), 947.
[24] LEE S.Y., Extended Abstracts of the International Conference on Solid State Devices and Materials, Kobe, Japan (2005), p. 1026.
[25] KOO JU.M., SEO B.-S., KIM S., SHIN S., LEE J.-H., BAIK H., LEE.J.-H., LEE J.H., BAE B.-J., LIM. J.-E., YOO D.-C., PARK S.-O., KIM H.-S., HAN H., BAIK S., CHOI J.-Y., PARK Y.J., PARK Y., IEDM Digest Tech. Papers, IEEE (2005), p. 4.
[26] GALAGHER W.J., IEEE VLSI-TSA Int. Symp. VLSI Technology, Kyoto, Japan (2005), p. 72.
[27] HOSOMI M., YAMAGISHI H., YAMAMOTO T., BESSHO K., HIGO Y., YAMANE K., YAMADA H., SHOJI M., HACHINO H., FUKUMOTO C., NAGAO H., KANO H., IEDM Digest Techn. Papers, IEEE (2005), p. 459.
[28] HUDGENS S., JOHNSON B., MRS Bull. November (2004), p. 829.
[29] OH H.-R., IEEE J. Solid State Circuits, 41 (2006), 122.
[30] SECZI R., WALTER A., ENGL R., MALTENBERGER A., SCHUMANN J., KUND M., DEHM C., IEDM Digest Techn. Papers IEEE (2003), 10.2.1.
[31] YANG Y., Organic Nonvolatile Memories, in [22], p. 197.
[32] KRIEGER J.H., SPITZER S.M., Proc. Non-Volatile Memory Technology Symposium, Orlando-Florida (2004), p. 121.
[33] LUO Y., COLLIER C.P., JEPPESEN, J.O., NIELSEN K.A., DEIONNO E., HO G., PERKINS J., TSENG H.-R., YAMAMOTO T., FRASER STODDART J., HEATH, J. R., ChemPhysChem, 3 (2002), 519.
[34] ROTH K.M., DONTHA N., DABKE R.B., GRYKO D.T., CLAUSEN C., LINDSEY J.S., BOCIAN D.F., KUHR W.G., J. Vac. Sci. Technol., B 18, (2000), 2359.
[35] REED M. A., CHEN J., RAWLETT A.M., PRICE D.W., TOUR J.M., Appl. Phys. Lett., 78 (2001), 3735.
[36] RUECKES T., KIM K., JOSELEVICH E., TSENG G.Y., CHEUNG C.-L., LIEBER C.M., Science, 289 (2000), 94.

Received 3 January 2006
Revised 28 May 2006

Materials Science-Poland, Vol. 25, No. 1, 2007

Influence of thermo-mechanical properties of polymer matrices on the thermal conductivity of adhesives for microelectronic packaging*

J. FELBA, T. FAŁAT**, A. WYMYSŁOWSKI

Faculty of Microsystem Electronics and Photonics, Wrocław University of Technology,
ul. Janiszewskiego 11/17, 50-372 Wroclaw, Poland

Thermally conductive adhesives are among major concerns of contemporary microelectronics. The main goal of ongoing research is to improve the thermal conductivity of these composites by using a proper filler material and the best shape and size of filler particles. In this work, it has been proven by numerical simulation that the polymer matrix may also play a crucial role, as the contact area between filler particles depends on the stresses that occur due to the shrinkage of the resin during curing. It has been observed that the resins relax with time. The time until the fully relaxed state is reached strongly depends on the temperature at which the system operates. In the considered case, the contact pressure is fully relaxed when it decreases from the initial value of 0.73 GPa to 0.03 GPa. When the temperature is 70 °C, the contact pressure becomes fully relaxed after 10 seconds, but when it is lower than 40 °C, the relaxation is completed after about 10^9 seconds (more than 30 years!). After the relaxation of contact pressure, the thermal conductivity drops by approximately 50% of the initial thermal conductivity of the non-relaxed structure.

Key words: *thermal conductivity; thermally conductive adhesives; polymer matrix; microelectronic packaging*

1. Introduction

The continuous miniaturization of electronic devices and components depends on ever higher packaging densities. This introduces problems with heat transport and heat dissipation, which at present are becoming crucial issues and require the application of materials with high thermal conductivity and novel packaging methods. Thermally conductive adhesives (TCA) seem to be among the most attractive materials for this purpose.

---

*Presented at the joint events 1st Workshop "Synthesis and Analysis of Nanomaterials and Nanostructures" and 3rd Czech-Silesian-Saxony Mechanics Colloquium, Wrocław, Poland, 21–22 November, 2005.

**Corresponding author, e-mail: tomasz.falat@pwr.wroc.pl

Conductive adhesives consist of a polymer base material matrix and a metal filler dispersed randomly. Conduction is provided by metal additives, and high conductivity requires high metallic content, considerably above the percolation threshold. It is believed that at this concentration all conductive particles contact each other and form a three-dimensional network. The expected conductivity is obtained after the curing process due to a better contact between filler particles, resulting from the shrinkage of the polymer matrix. Thermal conductivity is limited by the so-called thermal contact resistance between filler particles. The contact thermal resistance depends on both the material properties and geometric parameters of the contact areas between particles. The geometric parameters are related to the contact pressure within the contact area. TCAs are typically formulated analogously to electrically conductive adhesives with conductive particles (usually silver flakes with average particle dimensions of several micrometers) and a polymer matrix (usually a thermosetting epoxy resin). The thermal conductivity of such composites reaches values lower than 3 W/(m·K) [1]. The conductive particles in adhesives are responsible for thermal contacts, while the polymer matrix mainly provides the mechanical interconnections.

2. The role of the adhesive filler material

The filler material is responsible for heat transport. Thermal conductivity of the bulk material is given by the equation

$$\lambda = \frac{1}{3}\left(c_e \nu_e L_e + c_{ph} \nu_{ph} L_{ph}\right) = \lambda_e + \lambda_{ph} \tag{1}$$

where c_e and c_{ph} are the heat capacities per unit volume [J/(m^3·K)] of electrons and phonons, respectively, ν_e and ν_{ph} are their root-mean-square velocities, and L_e and L_{ph} are their mean free paths. Since λ_e is the dominant part of the thermal conductivity of metals, one can roughly assume that

$$\lambda = \lambda_e \tag{2}$$

In the case of copper at room temperature, $\lambda_e = 380$ W/(m·K) and $\lambda_{ph} = 21$ W/(m·K).

Generally, because of their relatively low cost, pure metals such as copper or silver are the best candidates for TCA fillers. There are also materials with much higher thermal conductivities reching 2000 W/(m·K) for synthetic diamond and up to 3000 W/(m·K) for carbon nanotubes. Carbon nanotubes consist of graphite sheets wrapped into hollow cylinders with the diameters as small as 1 nm and lengths in the micrometer range. Their unique mechanical and thermal properties make them ideal fillers in the development of a new generation of composite materials for, among others, microelectronic packaging. For certain applications, high thermal conductivity and electrical insulating properties are needed. Aluminium nitride particles (7 μm) and whisk-

ers (250 μm) or silicon carbide whiskers could be used as fillers in TCAs for such purposes. [2]

Generally, the filler particles used in thermally conductive adhesives occur in many different shapes, such as spheres, flakes, whiskers, tubes, fibres, etc., and their dimensions vary from micro- to nanometers.

3. The role of contacts between filler particles

Tests with TCAs containing different filler materials show that there is no simple relationship between the conductivities of the bulk material and composite. For example, synthetic diamond powder as the filler reveals a low value of TCA thermal conductivity compared to silver flakes [3]. This is believed to be due to the presence of nitrogen and other impurities in the synthetic diamond, but generally small contact areas between filler particles significantly reduce the thermal conductivity of the adhesive. If contact members are in the form of perfect hard balls, they touch each other at one point (the contact point *A* in Fig. 1). In fact, this point turns into a small area, since the contact materials are deformable.

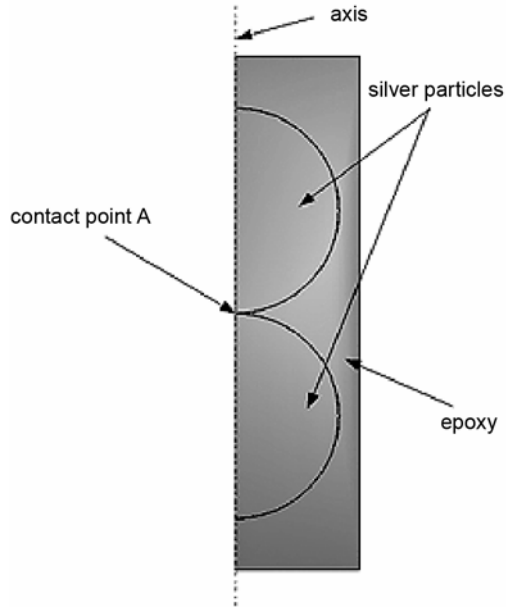

Fig. 1. 2D axis-symmetric model of silver-filled TCA

The thermal contact resistance between particles can be lowered by using mixed filler materials that differ in particle sizes. Composites containing silver particles and nanoparticles improve thermal conductivity even by the factor of 2.55 [4]. Furthermore, the thermal conductivity of TCAs can be improved by using fillers with different particle shapes (e.g., spheres + whiskers) [2, 5]. Both of these techniques are

costly and require a lot of experiments to be performed with various material contents and configurations in order to obtain optimal results.

Therefore, it is worth asking: how does the contact state between particles affect the thermal conductivity of TCA? In order to test this, a numerical modelling of silver-filled TCA was performed. The numerical model was simplified by some assumptions: identical, spherical silver particles were used as the filler, a closely packed (HCP or FCC crystal equivalent) 3D structure was analysed as the unit cell (see Fig. 2), the particles touch each other, and the contact properties were described by contact areas (impurities and roughness were neglected). The closely packed structure was assumed as a consequence of the maximal possible packing efficiency ($V_{\text{filler}}/V_{\text{total}}$ = 74.05%) for the 3D spherical particles.

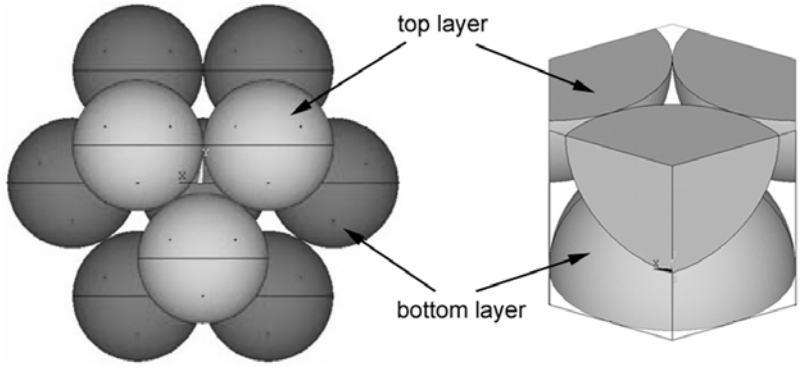

Fig. 2. Closely packed structure (left) and the analysed unit cell (right)

The unit cell shown in Fig. 3 was analysed with ANSYS 8.0 commercial FEM software. Two different contact area radii were taken into account and represented by the r/R relation, where r is the contact area radius and R is the particle radius. The results of the simulation are collected in Table 1.

Table 1. Results of numerical simulation

r/R	λ [W/(m·K)]
0.05	49.12
0.02	26.46

As shown in Table 1, the contact area between the filler particles has a strong influence on the thermal conductivity of TCA. This area depends on the stress between the particles, which occurs due to the shrinkage of the resin during curing. Calculating this stress is quite complex because of its temporal relaxation due to the viscoelastic behaviour of the resin.

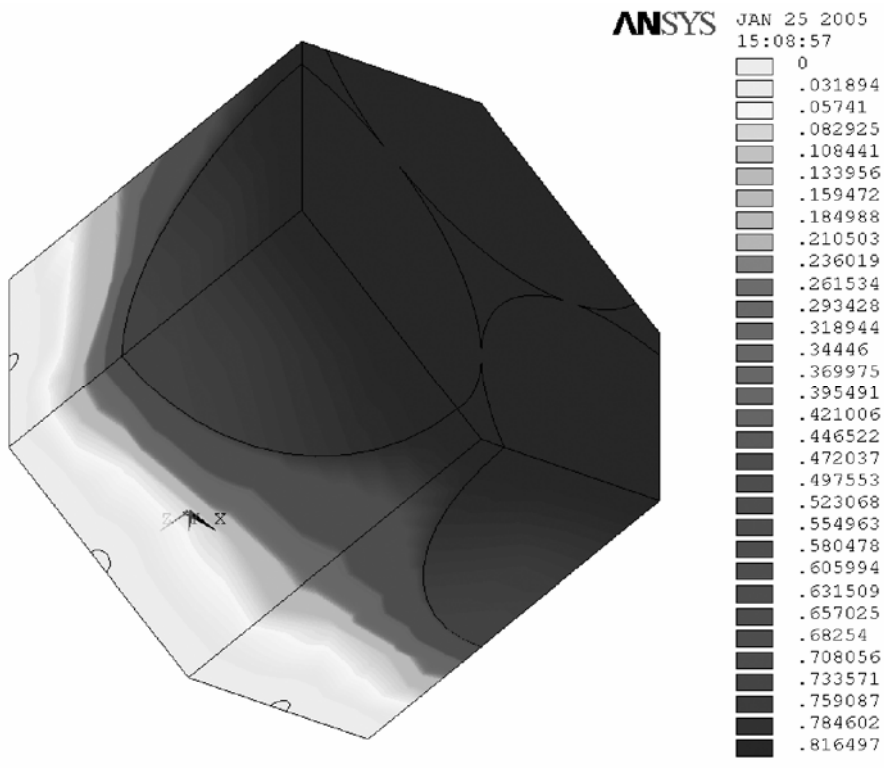

Fig. 3. The unit cell analysed by ANSYS 8.0

4. The role of the polymer matrix

An adhesive matrix is used to form mechanical bonds at interconnections. Polymeric materials have thermal conductivities about 2000 times lower than silver or copper. Thermal conductivities of all polymeric materials, epoxy or other types, thermoset or thermoplastic, range from 0.2 to 0.3 W/(m·K). Nevertheless, the thermomechanical properties of polymer matrices may strongly influence the thermal conductivity of adhesives for microelectronic packaging.

4.1. Viscoelasticity

The general linear viscoelastic equation is the basic equation for modelling the development of viscoelastic stresses (σ_{ij}) as a function of temperature and loading time in fully cured polymer materials:

$$\sigma_{ij}(t,T) = \int_{-\infty}^{t} \left\{ 2G(t-s,T)\dot{\varepsilon}_{ij}^{d} + K(t-s,T)\dot{\varepsilon}_{V}^{\text{eff}} \right\} ds \tag{3}$$

where G and K denote the shear and bulk relaxation moduli, respectively (they are time- (t) and temperature- (T) dependent), and $\dot{\varepsilon}_V^{\text{eff}}$ is the effective strain contribution.

Shear and bulk moduli also depend on the conversion level (degree of cure, α). Therefore, the viscoelastic stress described by Eq. (3) can be written as:

$$\sigma_{ij}(t,T,\alpha) = \int_{-\infty}^{t} \left\{ 2G(t-s,T,\alpha)\dot{\varepsilon}_{ij}^{d} + K(t-s,T,\alpha)\dot{\varepsilon}_V^{\text{eff}} \right\} ds \tag{4}$$

and $\dot{\varepsilon}_V^{\text{eff}}$ consists of mechanical, thermal, and cure shrinkage parts [6, 7]:

$$\varepsilon_V^{\text{eff}} = \varepsilon_V^{\text{mech}} - \varepsilon_V^{\text{cure}} - \varepsilon_V^{T}, \quad \varepsilon_V^{T} = 3\beta_L^{g,r}(T - T_{\text{ref}}) \quad \varepsilon_V^{\text{cure}} = -3\gamma_L(\alpha - \alpha_{\text{ref}}) \tag{5}$$

where β_L^g and β_L^r are the linear coefficients of thermal expansion (CTE) measured below the glass transition temperature T_g (glassy region) and above T_g (rubbery region), respectively, and γ_L is the linear cure shrinkage. The change of the modulus during curing can be explained by the change in the molecular structure of the matrix. Since cure-dependent viscoelasticity is not implemented in commercial FEM software such as ANSYS 8.0 or ABAQUS 6.5, only the results of measurements for fully cured materials were used and the cure dependence of the relaxation modulus was neglected.

If the time is relatively short ($t \to 0$), shear and bulk relaxation moduli are treated as instantaneous shear and bulk moduli G_0 and K_0, respectively, and they can be determined from the values of the instantaneous (obtained from the high-rate tests) elastic (Young) modulus E_0 and Poisson's ratio ν_0:

$$G_0 = \frac{E_0}{2(1+\nu_0)} \quad \text{and} \quad K_0 = \frac{E_0}{3(1-2\nu_0)} \tag{6}$$

Poisson's ratio is often assumed to be time-independent in viscoelastic materials, therefore Eq. (6) can be used for the whole time scale of the shear, bulk, and elastic relaxations up to the point when strains are small. The advantage of such an approach is that when modelling the behaviour of viscoelastic materials only one modulus needs to be measured (e.g., the shear relaxation modulus) and the other can be calculated from Eq. (6).

The effect of temperature in Eq. (3) is usually not included as $G(t,T)$, but as $G(t_{\text{red}}(T))$, where t_{red} is the so-called reduced time scale and $G(t_{\text{red}})$ is referred to as the master curve. The reduced time scale is defined as

$$t_{\text{red}} \equiv \int_0^t a_T \, dt \tag{7}$$

where a_T is the temperature-dependent shift factor, which can be described by the WLF (Williams, Landel, Ferry) equation

$$a_T = \exp\left\{-\frac{C_1\left(T - T_{\text{ref}}\right)}{C_2 + T - T_{\text{ref}}}\right\} \tag{8}$$

T_{ref} is the reference temperature, and C_1 and C_2 are material parameters. The reduced time scale t_{red} can be replaced by the reduced frequency scale $f_{\text{red}} = a_T f$.

4.2. Experimental procedures

The standard way of measuring dynamic changes of the mechanical parameters of shear modulus (for polymeric materials in particular) is a continuous monitoring of the thermo-mechanical properties from the liquid to the fully cured state by applying the liquid compound (e.g. resin + hardener) in small gaps between parallel plates of the shear clamps of a dynamic mechanical analyzer (DMA). The samples are subject to a series of sinusoidal strains or stresses at different frequencies (a frequency sweep). The temperature is then increased by 5–10 °C and another frequency sweep is applied. This procedure is repeated from about 80 °C below the glass transition temperature (T_g) to about 80 °C above it. Far below the glass transition temperature the modulus data (stress amplitude divided by strain amplitude) is frequency independent. This modulus is called the glassy modulus. Far above the glass transition temperature, the material either melts, as is typical of thermoplasts, or displays a nonzero, frequency-independent rubbery modulus of thermosets. In between, in the so-called viscoelastic region, the modulus is frequency-dependent and lies between the glassy and the rubbery values. It is customary to shift the individual modulus vs. frequency curves along the logarithmic frequency axis until they overlap and form a master curve. The shift (a_T) is different for each temperature. The master curve, together with this shift factor, completely describe the temperature and frequency-dependent modulus data and can even be used to predict the mechanical behaviour at time scales and temperatures different from those of the test conditions [8].

4.3. Numerical approach

To study the contact pressure occurring between the filler particles due to the cure shrinkage of the polymer matrix and its influence on thermal conductivity, the model shown in Fig. 1 was implemented by ABAQUS v.6.5 FEM software [9]. It is the 2D axis-symmetric model, which consists of two identical spherical silver particles surrounded by cylindrically shaped epoxy resin. The volume fraction of filler was about 23%. The particles touch each other at one point at the beginning of the simulation. The contact pressure and its change in time after curing at different temperatures were monitored at the contact point A.

Silver (as the filler) is considered to be a linear elastic material with the elastic modulus E = 76 GPa and the Poisson's ratio v = 0.37. The thermal conductivity of silver is 423 W/(m·K).

The tested epoxy resin was delivered by Amepox Microelectronics, Poland. The linear reaction cure shrinkage was assumed at the level of 1×10^{-2} (volume shrinkage $\approx 3\times10^{-2}$). To determine the viscoelastic properties of the fully cured epoxy sample, dynamical mechanical thermal analysis (DMTA) was performed. The DMTA measurements were conducted using a TA Instruments ARES rheometer (the tool: torsion pendular; geometry: rectangle). The dynamic mechanical shear tests were performed to obtain the storage and loss relaxation moduli. The tests were performed in the Fraunhofer Institut für Fertigungstechnik und Angewandte Materialforschung, Bremen, Germany.

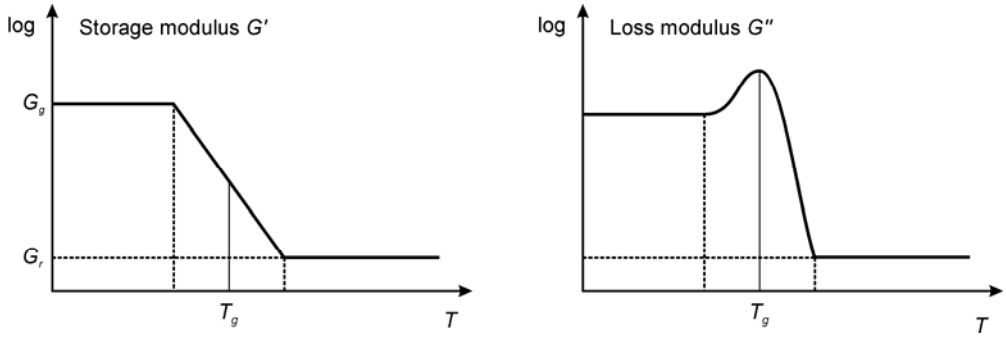

Fig. 4. The storage (G') and loss (G'') shear moduli for the fully cured material vs. temperature

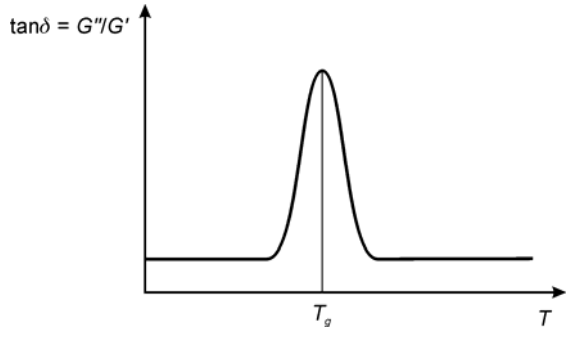

Fig. 5. The loss angle $\tan\delta = G''/G'$ vs. temperature

Figure 4 shows an example of the storage (G') and loss (G'') moduli as functions of temperature. In Figure 5, an example of the temperature dependence of the loss angle $\tan\delta = G''/G'$ is shown. It is possible to deduce the glass transition temperature T_g from these data. The glass transition temperature does not show a sharp transition from one state into another but a gradual change. There appears to be no consensus in the literature on its precise definition [10]. Therefore, the two following criteria are applied for the measurement of T_g: the peak in the loss modulus G'' vs. T and the peak in the loss angle $\tan\delta$ vs. T. The measured T_g values were as follows: $T_g = 55$ °C (for the peak in the loss modulus G'') and $T_g = 68$ °C (for the peak in the loss angle $\tan\delta$).

By measuring the storage modulus G' and loss modulus G'' as a function of frequency at various temperatures, it is possible to construct master curves for the storage and loss moduli. Examples of the master curves are shown in Figs. 6 and. 7.

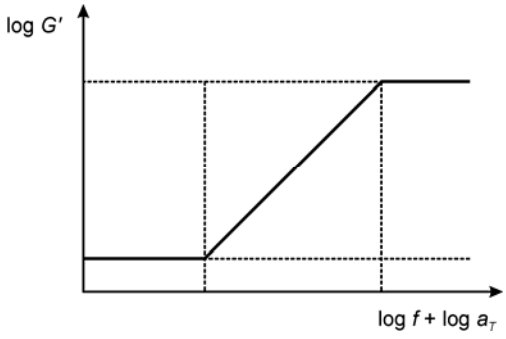

Fig. 6. Master curve of the storage modulus G'

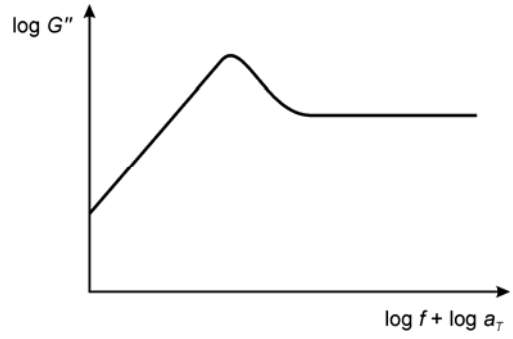

Fig. 7. Master curve of the loss modulus G''

When constructing the master curves, the shift factor a_T has to be evaluated (see Eq. (8)) by estimating the values of the WLF equation parameters. The parameters of the WLF equation for the considered epoxies are collected in Table 2.

The simulation procedure was divided into two steps. In the first step, a steady state analysis was performed to simulate the shrinkage caused by curing the epoxy and to monitor the initial contact pressure between silver particles. In this step, the epoxy resin was treated as an elastic material and the cure dependence and viscoelastic properties were neglected. Since the cure shrinkage is not implemented in ABAQUS v.6.5, it was simulated by using thermal expansion features. The coefficient of thermal expansion (CTE) was fixed at 1×10^{-4} K^{-1} and the temperature was lowered from the initially elevated temperature (T_0 + 100 °C) to the temperature at which the second step was performed (T_0). After this procedure, it was possible to obtain a linear shrinkage of 1×10^{-2}. In the second step, transient analysis was performed and various temperatures (T_0 changes from 40 °C to 70 °C) were applied to observe the temperature dependence of the contact pressure relaxation.

Table 2. Estimated parameters for the WLF equation (Eq. (8))

Parameter	Estimate
T_{ref}	60 °C
C_1	17.66
C_2	80.58 °C

The results of the simulations, i.e. the contact pressures between particles vs. time for different temperatures, are shown in Fig. 8.

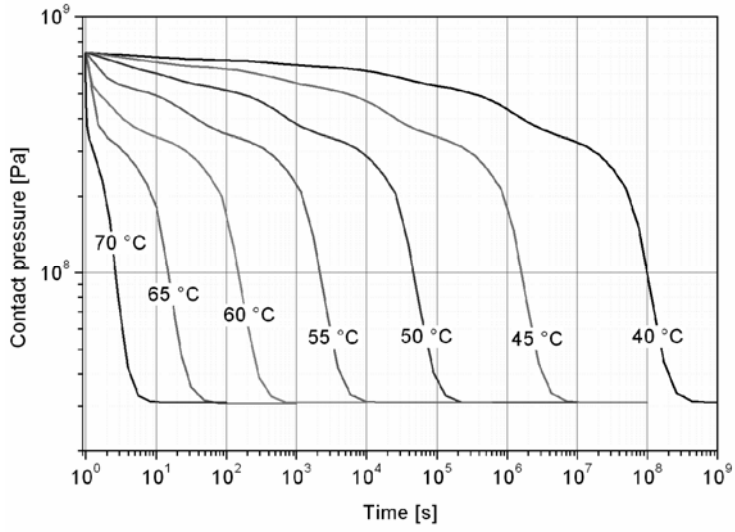

Fig. 8. The results of simulation–contact pressure between the filler particles vs. time for various temperatures

The contact pressure occurring between filler particles due to the cure shrinkage relaxes within time. The time needed to reach the fully relaxed state strongly depends on the working temperature of the system. In the considered case, the contact pressure is fully relaxed when it decreases from an initial value of 0.73 GPa to 0.03 GPa, as shown in Fig. 8. When the temperature is 70 °C, the contact pressure becomes fully relaxed after 10 seconds, but when it is lower (e.g. 40 °C) the full relaxation state is reached after about 10^9 seconds (more than 30 years!).

The thermal conductivities of the tested structures have been calculated (using FEM) before and after relaxation. After the relaxation of the contact pressure, the thermal conductivity drops to around 50% (0.484) of its initial value for the unrelaxed structure.

5. Conclusions

Thermally conductive adhesives consist of a polymer base matrix and a filler, which is mainly responsible for thermal conductivity. Silver in the form of flakes with average particle dimensions of several micrometers is typically used as the filler. Pure metals with thermal conductivity about 400 W/(m·K) can be replaced by much more conductive materials such as synthetic diamond (2000 W/(m·K)) or carbon nanotubes (up to 3000 W/(m·K)). Nevertheless, there is a lack of reports concerning the significant influence of those materials on the thermal conductivity of adhesives for microelectronic packaging. The main reason for the huge differences between the thermal conductivities of bulk materials and composites is due to small contact areas between filler particles. In the case of identical, spherically shaped silver particles, the numerically calculated value of thermal conductivity reaches 26.46 W/(m·K). The particles

are closely packed (HCP or FCC crystal equivalent) with the ratio of particles radius to contact area radius being 0.02. Certainly, such an ideally shaped and closely packed filler is an oversimplification, but it does indicate theoretical limits.

As calculated using the model presented above, the contact area between filler particles has a strong influence on the thermal conductivity of the adhesive. This area depends on the stress between particles, which occurs due to resin shrinkage during curing, indicating that the role of the polymer matrix is more important than only forming mechanical bonds at interconnections. Calculating such a stress is quite complex because of its temporal relaxation due to the viscoelastic behaviour of the resin.

In the simulation procedure, transient analysis was performed in order to observe the temperature dependence of contact pressure relaxation between filler particles. The time needed for it to reach the fully relaxed state strongly depends on the temperature at which the system operates. The contact pressure relaxation time changes from 10 seconds at 70 °C to about 10^9 seconds (more than 30 years) at 40 °C. After relaxation of the contact pressure, the thermal conductivity drops to around 50% (0.484) of its initial value for the unrelaxed structure.

Acknowledgements

Authors would like to thank Mr. Andrzej Moscicki from AMEPOX Microelectronics, Poland for supplying the epoxy resin and Ms. Jana Kolbe from IFAM Fraunhofer Institut fuer Fertigungstechnik und Angewandte Materialforschung, Klebetechnik und Oberflaechen, Germany for the measurements.

References

[1] FAŁAT T., FELBA J., WYMYSŁOWSKI A., Proc. of 28th International Conference of IMAPS Poland Chapter, Wrocław, 2004, p. 219.

[2] XU Y., CHUNG D.D.L., MROZ C., Composites A: Appl. Sci. Manufacturing, 32 (2001), 1749.

[3] BOLGER J.C., *Prediction and measurement of thermal conductivity of diamond filled adhesives*, IEEE Publ. No 0569-5503/92/000-0219, 1992.

[4] UKITA Y., TATEYAMA K., SEGAWA M., TOJO Y., GOTOH H., OOSAKO K., Proc. of IMAPS2004, Long Beach, USA, 2004, WA71.

[5] LI H., JACOB K.I., WONG C.P., IEEE Trans. Adv. Packaging, 26 (2003), 25.

[6] JANSEN K.M.B., WANG L., YANG D.G., VAN 'T HOF C., ERNST L.J., BRESSERS H.J.L., ZHANG G.Q., Proc. of IEEE 2004 Electronic Components and Technology Conference, Las Vegas, Nevada, 2004, p. 890.

[7] JANSEN K.M.B., WANG L., VAN 'T HOF C., ERNST L.J., BRESSERS H.J.L., ZHANG G.Q., Proc. 5th Int. Conf. on Thermal and Mechanical Simulation and Experiments in Micro-electronics and Micro-Systems EuroSimE, Brussels, 2004, p. 581.

[8] MILOSHEVA B.V., JANSEN K.M.B., JANSSEN J.H.J., BRESSERS H.J.L., ERNST L.J., 6th. Int. Conf. on Thermal, Mechanical and Multiphysics Simulation and Experiments in Micro-Electronics and Micro-Systems, EuroSimE, Berlin, 2005, p. 462.

[9] FAŁAT T., WYMYSŁOWSKI K., KOLBE J., Proc. of 5th International IEEE Conference on Polymers and Adhesives in Microelectronics and Photonics Polytronic2005, Wrocław, Poland, 2005, p. 180.

[10] MEUWISSEN M.H.H., DE BOER H.A., STEIJVERS H.L.A.H., SCHREURS P.J.G., GEERS M.G.D., *Microelectronics Reliability*, 44 (2004), 1985.

Received 21 February 2006
Revised 28 May 2006

Materials Science-Poland, Vol. 25, No. 1, 2007

Fabrication of Al–4.5% Cu alloy with fly ash metal matrix composites and its characterization

K.V. MAHENDRA[1*], K. RADHAKRISHNA[2]

[1]Department of Mechanical Engineering, New Horizon College of Engineering, Outer Ring Rd., Panathur Post Bangalore-560087, Karnataka State, India

[2]Mechanical Department BMS College of Engineering, Bangalore-560019, India

Metal matrix composites (MMCs) are engineered materials, formed by the combination of two or more dissimilar materials (at least one of which is a metal) to obtain enhanced properties. In the present investigation, an Al–4.5% Cu alloy was used as the matrix and fly ash as the filler material. The composite was produced using conventional foundry techniques. The fly ash was added in 5%, 10%, and 15 wt. % to the molten metal. The composite was tested for fluidity, hardness, density, mechanical properties, impact strength, dry sliding wear, slurry erosive wear, and corrosion. Microstructure examination was done using a scanning electron microscope to obtain the distribution of fly ash in the aluminium matrix. The results show an increase in hardness, tensile strength, compression strength, and impact strength with increasing the fly ash content. The density decreases with increasing fly ash content. Resistance to dry wear and slurry erosive wear increases with increasing fly ash content. Corrosion increases with increasing fly ash content.

Key words: *wear; metal matrix composite; fly ash; corrosion; aluminium alloy*

1. Introduction

Traditional materials do not always provide the necessary properties under all service conditions. Metal matrix composites (MMCs) are advanced materials resulting from a combination of two or more materials (one of which is a metal and the other a non-metal) in which tailored properties are realized. They have received considerable attention in recent years due to their high strength, stiffness, and low density. Data related to mechanical properties, wear, microstructure, etc., have been cited in the literature. It has been reported that particle size and wear parameters (sliding speed, material property, normal load) influence the wear of the material [1–3]. A variety of particles such as mica, Al_2O_3, graphite, and SiC have been used as reinforcement materials with aluminium alloys [4–8] as the matrices. It appears that stir

*Corresponding author, e-mail: mahendrakv@rediffmail.com

casting is one of the methods for producing composites. The use of fly ash as a reinforcement material [9] results in improvement of mechanical properties of the composite. An extensive review on dry sliding wear characteristics of composites based on aluminium alloy was undertaken by Sannino et al. [10] and of their abrasive wear behaviour by Deuis [11]. Fly ash was separated into cenosphere and precipitator fly ash. The use of precipitator fly ash in aluminium decreases the density of composites and increases their wear resistance [12]. In slurry erosive wear, the effect of the impingement angle and velocity on the erosion rate depends on particle size and amount of particulates. It has been reported that the erosion rate increases with increasing particle size up to a point, beyond which it is not significantly affected by the size. It was reported that corrosion increases with increasing particulates in composites [13]. Bienias et al. [14] reported the pitting corrosion behaviour and corrosion kinetics of Al alloy with precipitator fly ash (9 vol %, 75–100 μm) composites. It was found that fly ash particles lead to an enhanced pitting corrosion of the composite in comparison to unreinforced matrix.

In the present investigation, Al–4.5% Cu alloy with fly ash (as received from a thermal power plant) as particulates were successfully fabricated using the stir casting method. Fluidity, mechanical properties, dry sliding wear, slurry erosive wear, and the corrosion behaviour of the MMCs were investigated.

2. Experimental

Aluminium with 4.5% Cu was selected as the matrix material. The chemical composition, analysed by a Bairdas DV-6S optical emission spectrometer, is given in Table 1. Fly ash was used as the reinforcement and its composition is given in Table 2. The average particle size was found to be 10 μm. The density of fly ash was found to be 2.09 g/cm^3. Fig. 1 shows SEM micrographs of fly ash particulates.

Table 1. Chemical composition of Al–4.5% Cu alloy

Cu	Mg	Si	Fe	Mn	Ni	Pb	Sn	Ti	Zn	Al
4.52	0.066	0.538	0.663	0.131	0.075	0.029	0.021	0.013	0.118	balance

Table 2. Chemical composition of fly ash in weight percentages

Al_2O_3	SiO_2	Fe_2O_3	TiO_2	Loss on ignition
30.40	58.41	8.44	2.75	1.43

The synthesis of the composite was carried out by stir casting. The ingots of Al–4.5% Cu alloy were taken in a graphite crucible and melted in an electric furnace. The temperature was slowly raised to 850 °C. The melt was degassed at 800 °C using a solid dry hexachloroethane (C_2Cl_6, 0.5 wt. %) degasser. The molten metal was stirred to create a vortex and the particulates were introduced. The degassed molten metal was placed below the stirrer and stirred at approximately 600 rpm. The preheated fly ash particles were slowly added into the melt. Small pieces of Mg (0.5 wt. %)

were added to the molten metal to ensure good wettability of particles with the molten metal. The percentage of fly ash added was 5, 10, or 15 wt. %. The stirred dispersed molten metal was poured into preheated S.G. iron moulds 25, 50, or 75 in diameter and 200 mm hight, and cooled to room temperature.

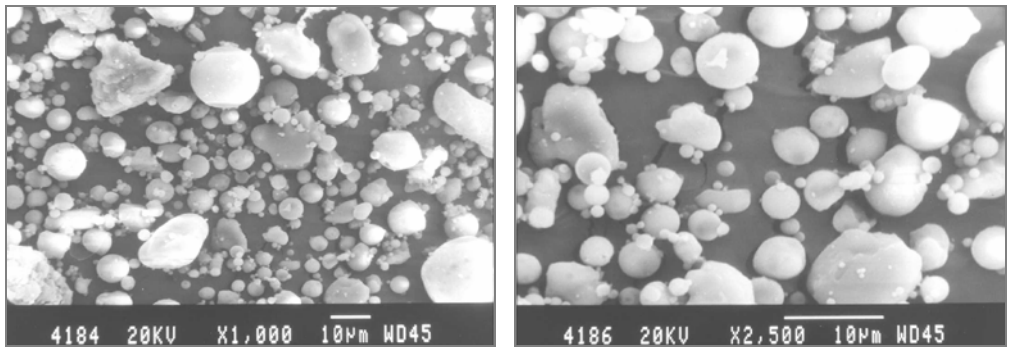

Fig. 1. SEM of fly ash particulates

The flowability characteristic of the molten metal was assessed using two types of fluidity tests, the spiral and strip ones. The total length of the metal flowing inside the mould cavity was taken as a measure of fluidity.

Composites produced were subjected to solutionisation and age hardening (T6). The castings were heated to 525 °C and held for 17 hours, quenched in warm water, then reheated to 175 °C and held for 18 hours. They were sectioned and test samples were prepared for various tests. The densities of the specimens were measured using the Archimedes principle. Their hardness was determined using the Brinnel hardness tester. The load of 500 kg using a 10 mm steel ball indenter was used to measure the hardness. The microstructure of the MMCs was observed under a scanning electron microscope (SEM) at various locations across the specimen to examine the distribution of fly ash in the matrix.

Tensile and compression strengths were determined using a 20 kN computerised UTM with an electronic extensometer as per ASTM E-8 standards. Online plotting of load versus extension was done continuously through a data acquisition system. The impact strength of castings was tested using a standard impact testing machine using Izod and Charpy specimens. The Izod test is carried out by a pendulum-type testing machine, which employs a cantilever test specimen 75 mm long with a 10×10 mm^2 cross section, having a standard 45° notch 2 mm deep. The Charpy test employs a notched specimen $10\times10\times55$ mm^3 in size with a U notch.

Dry sliding wear test. Specimens 5 mm in diameters and 20 mm long were used for the dry sliding wear tests. The tests were carried out using a computerized pin on a disc wear testing machine under ambient temperature conditions on specimens for normal loads of 4.9, 9.8, 14.7, and 19.6 N, and for a constant track velocity of 80 m/sec.A hardened steel disc (60 HRc) was used as the counterface. The wear of the

specimen and friction were measured directly using sensors. The wear tracks on the specimen were observed under a SEM to examine the effect of the percentage of particulate on the wear behaviour of the MMCs.

Slurry erosive wear test. Slurry erosive wear was made using a bolt-shaped specimen7 mm in diameter. A slurry of silica sand and distilled water in the ratio 1:2 with different pH values was used. The bolt specimen was rotated in the slurry at 1170 rpm for 24 hours, then washed, dried, and weighed with a digital balance every 2 hours. The loss of weight was recorded for each time interval. The experiment was repeated for neutral, basic, and acidic conditions of the slurry.

Fog corrosion test. Thin rectangular specimens of 25.4×101.6×6 mm^3 dimensions were exposed to a fog atmosphere of salt solution in a closed chamber. The specimens were prepared with a good surface finish, cleaned and used. The test was carried out as per ASTM B-117 standards. The temperature of the salt bath was maintained at 25 °C and air was bubbled through the bath under the pressure of 0.69 bar. Every 3 hours the specimens were taken out, cleaned, dried, and weighed accurately. The total testing time was 48 hours.

3. Results and discussion

Figure 2 shows the effect of fly ash content on the fluidity of composites. It was observed that with an increasing percentage of fly ash particulates the fluidity length

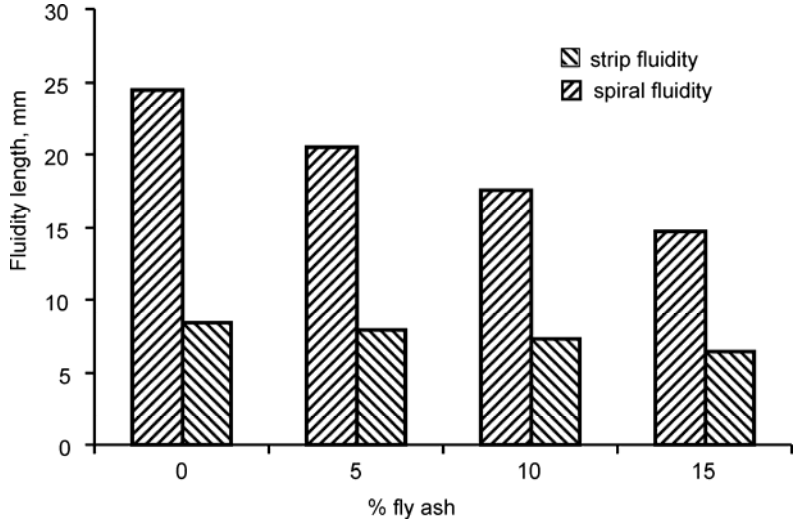

Fig. 2. The effect of fly ash on fluidity of composite

decreases. This may be due to an obstruction to the flow of molten metal by fly ash particulates, in turn due to an increase in the viscosity of the base alloy as a result of

the suspension of fly ash particles. Base metal shows a better fluidity than composites in both strip and spiral fluidity.

The density decreases with an increasing percentage of particulates (Fig. 3). Since the density of fly ash was 2.09 g/cm^3, the overall density of fly ash composite was decreased. The hardness increases with an increasing percentage of particulates. This may be due to the presence of hard fly ash particulates.

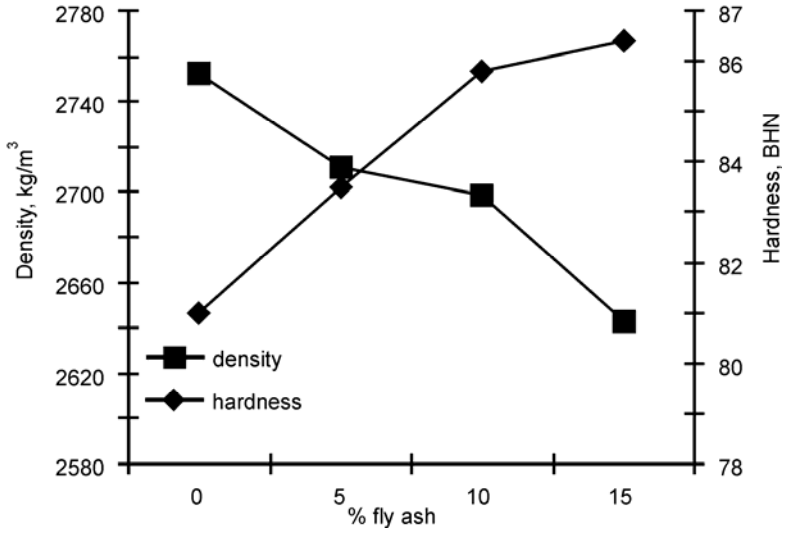

Fig. 3. The density and hardness of composites

The microstructure of MMCs clearly shows a uniform distribution of fly ash in the matrix (Fig. 4), with no void and discontinuities observed. There was good interfacial bonding between the fly ash particles and matrix material. Figure 5 shows a photomicrograph of a single fly ash particle in the matrix, displaying a good bonding.

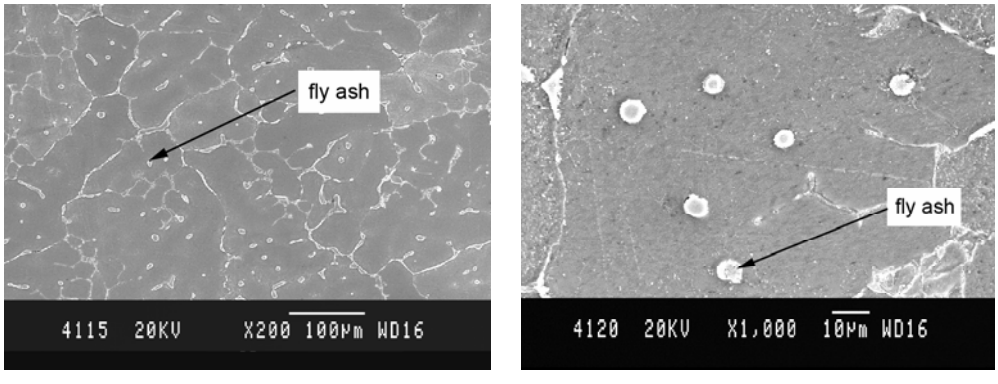

Fig. 4. Photomicrograph of castings 50 mm in diameter with 5% fly ash

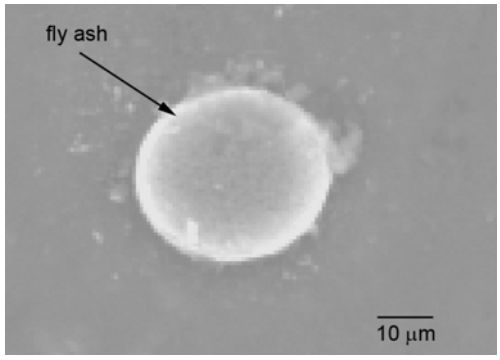

Fig. 5. Enlarged view of a single fly ash particle

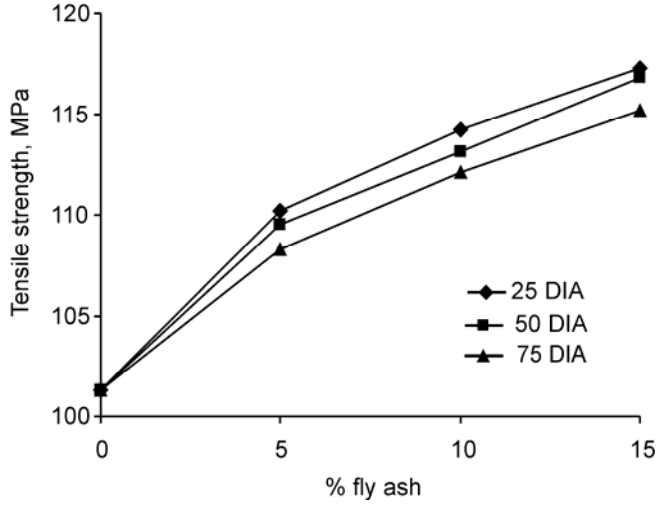

Fig. 6. The tensile strength of composites

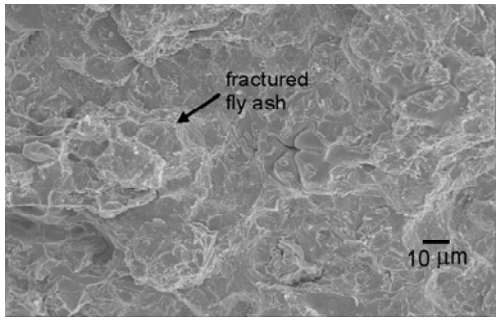

Fig. 7. The tensile fractured surface of the composite

The tensile strength (Fig. 6) increases with an increasing percentage of fly ash particulates. Castings with smaller cross sections exhibit higher tensile strengths than those with larger cross sections. This may be due to a faster heat transfer from the mould, resulting in a finer grain structure of the castings. The fracture of fly ash particulates can be seen in the SEM photomicrograph of 5% fly ash composite (Fig. 7).

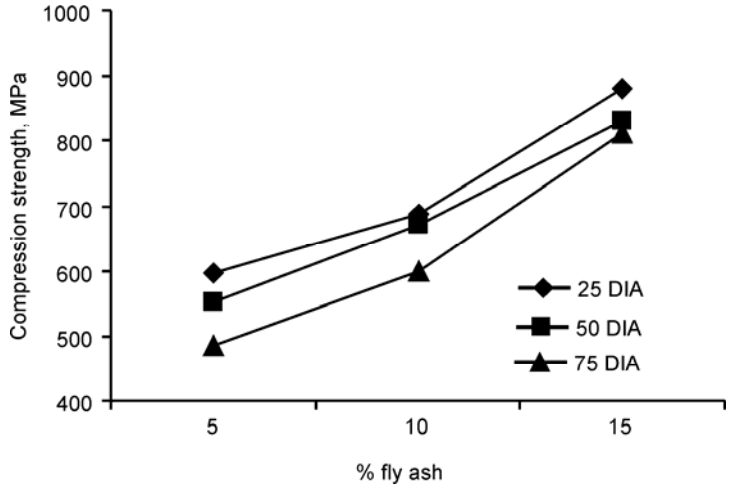

Fig. 8. Compression strengths of composites

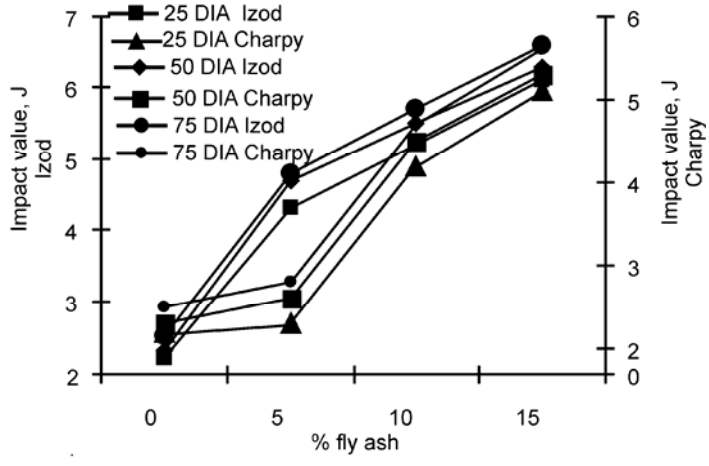

Fig. 9. Izod and Charpy impact strengths of composites

Similarly, compression strength (Fig. 8) increases with increasing percentage of fly ash particulates. This may be due to the hardening of the base alloy by fly ash particulates. The impact strength (Fig. 9) also increases with increasing fly ash content. This may be due to the presence of hard fly ash particulates. The impact strength shows higher values for 10% and 15% fly ash composites than the base alloy.

3.1. Dry sliding wear

Figure 10 shows the results of dry sliding wear behaviour for MMCs with 5, 10, and 15% fly ash content. It was observed that wear decreases with increasing fly ash content. This may be due to the abrasive nature of fly ash. Since the average particle

size of fly ash lies in the range 1–10 μm, the extent of particles pulled out from the surface was smaller. With increasing fly ash content, the amount of particle present strengthens the matrix and hence more wear resistance is observed.

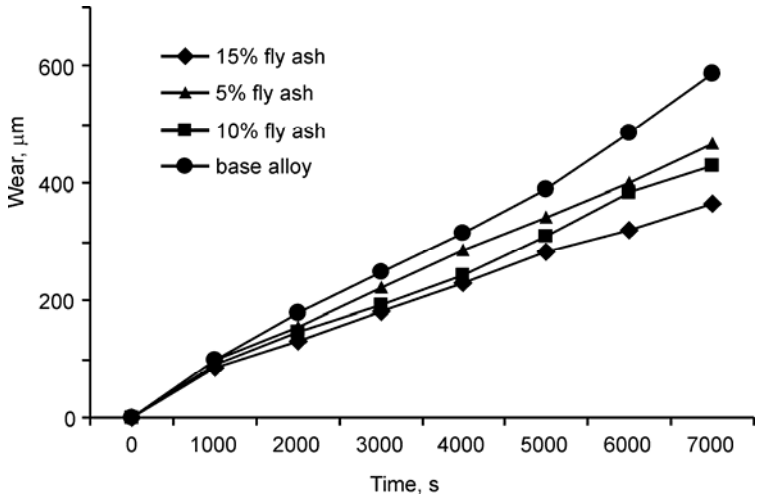

Fig. 10. Wear vs. time at various fly ash percentages at the 4.9 N load of castings 50 mm in diameter.

It was observed that with increasing load wear increases for normal loads of 4.9, 9.8, 14.7, and 19.6 N. Castings with smaller diameters exhibit less wear than castings with the larger ones. It was also observed that with increasing fly ash content there was a decrease in frictional force and the coefficient of friction (Tables 3, 4).

Table 3. Average values of frictional force N for fly ash composites with the addition of particulates, after 120 minutes

Load, N	Fly ash content, %			
	0	5	10	15
4.9	1.8	0.22	0.18	0.11
9.8	3.2	1.9	1.4	1.1
14.7	5.6	4.8	4.1	3.2
19.6	5.9	5.8	5.1	4.6

Table 4. Average values of the coefficient of friction μ for fly ash composites with addition of particulates after, 120 minutes

Load, N	Fly ash content, %			
	0	5	10	15
4.9	0.32	0.28	0.25	0.22
9.8	0.31	0.27	0.23	0.21
14.7	0.3	0.22	0.18	0.16
19.6	0.28	0.12	0.11	0.10

Figure 11 shows the worn surface of 5% fly ash composite (25 mm in diameter) under the normal load of 4.9 N. It can be seen that the ploughing and scoring along the sliding direction is enhanced. When compared to the base alloy, the wear scars are smaller due to the presence of fly ash particulates. This shows that the presence of fly ash in the matrix offers a resistance to wear. The fractured fly ash particles are seen in the SEM photomicrographs.

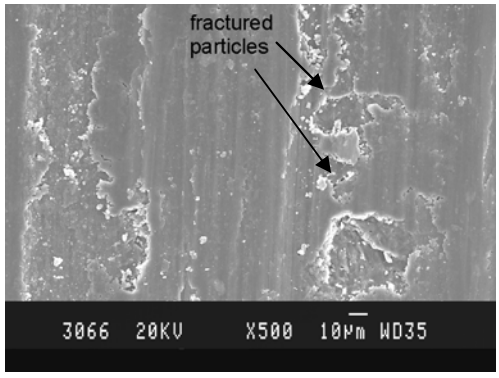

Fig. 11. A worn-out surface of 5% fly ash composite at 4.9 N (25 mm in diameter)

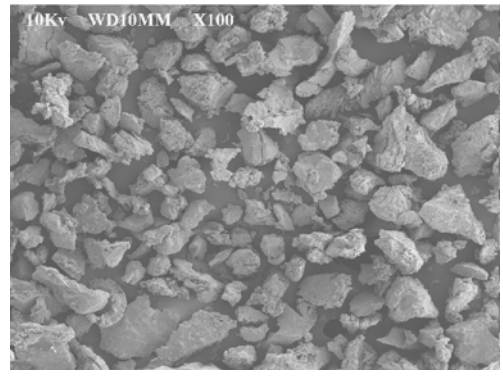

Fig. 12. The wear debris of a composite

The worn debris particles are likely to act as third body abrasive particles. The fly ash particles trapped between the specimen and counterface cause microploughing on the contact surface of the composite. The continuous longitudinal lines parallel to the sliding direction on the worn surfaces of the composites probably result from the ploughing action of the fly ash particles. At higher loads, composites show delamination, due to which the material loss in the form of plate-like debris takes place. The additional abrasive wear (microploughing) component of the sliding wear caused by fly ash particles may be the reason for the marginal decrease in wear rate of 15% fly ash reinforced composites compared to composites reinforced with 10% and 5% fly ash. Figure 12 shows the wear debris of MMCs. The volume of wear debris increases with increasing normal load, resulting in greater wear loss.

3.2. Slurry erosive wear

Figure 13 shows the time dependence of weight loss for erosive wear in an acidic medium. It was observed that with an increasing percentage of fly ash particulates the slurry erosive wear decreases. Erosive wear in the case of a basic medium is larger than in an acidic one. The erosion of MMCs takes place by the impact of abrasives present in the slurry. Initially, the corrosion of the matrix takes place by the oxidation reaction when Al^{3+} ions are released from the matrix to the slurry. Due to this, more

surface area is exposed to the slurry and causes further removal of the matrix and hence a higher loss of weight in the initial stage. Further in time, the slurry adjacent to the specimen surface becomes saturated with Al^{3+}, resulting in a reduction of the pH of the slurry. As a result, the dissolution rate of Al^{3+} in the slurry is reduced and the excess of Al^{+3} ions are deposited over the specimen surface, reacting with OH^- ions to form $Al(OH)_3$. This passive layer slows the rate of weight loss. SEM photomicrographs of slurry abrasive wear specimens show pitting in few places (Fig. 14).

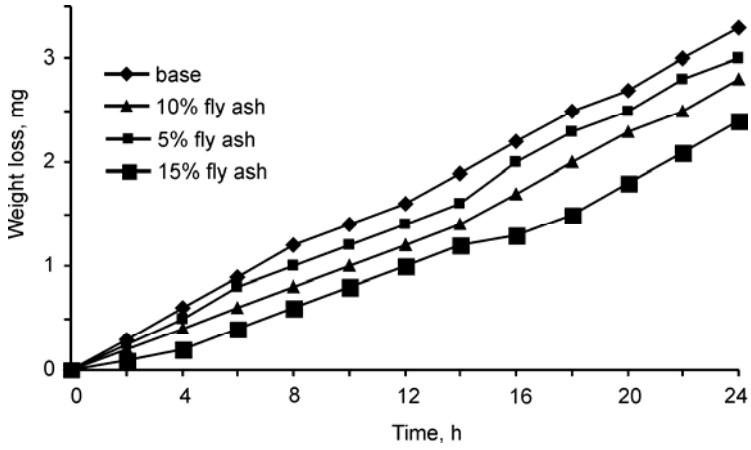

Fig. 13. Slurry erosive wear – acidic medium
(castings 50 mm in diameter)

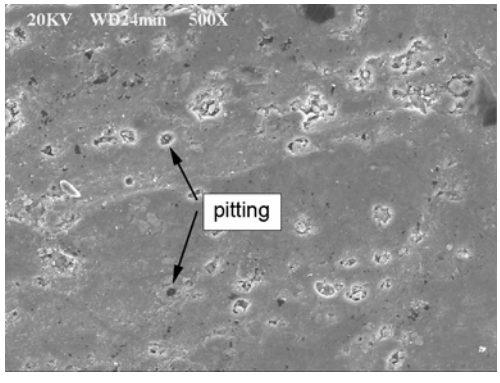

Fig. 14. SEM of the worn surface
of a composite under acidic conditions

3.3. Fog corrosion

Figure 15 shows weight loss versus time for fly ash composites tested at various temperatures for castings 50 mm in diameter. The temperature has an effect on the corrosion. It was observed that with increasing temperature corrosion increases, and the base alloy shows less corrosion than the composites in all the cases. It was also observed that corrosion increases with an increasing percentage of fly ash particu-

lates. The formation of an aluminium oxide layer is visible within 20 hours of commencing the test. Pits were formed in the specimens due to corrosion.

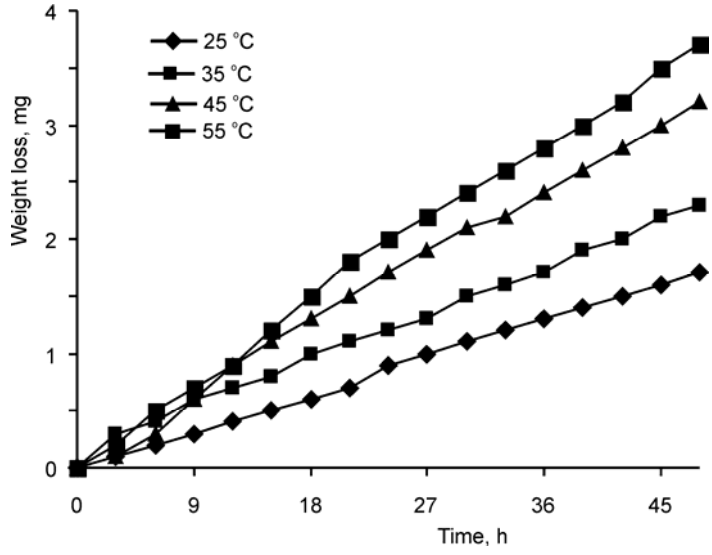

Fig. 15. Weight loss versus time at various temperatures of castings 50 mm in diameter (10% fly ash)

As is evident from the SEM photographs (Fig. 16), there was a build-up of corroded particle debris in the pits. The interfaces between reinforcement and matrix material, where the matrix surface is broken, will act as pit initiators. Since pits initiate at flaws and interfaces between matrix aluminium and reinforced particles are flaws, the metal is pitted by aerated sodium chloride solution.

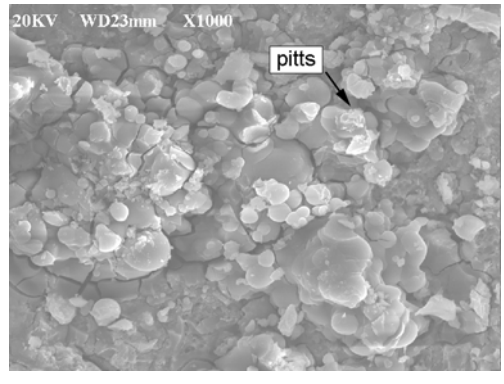

Fig. 16. SEM photomicrograph of a corroded surface (5% fly ash)

The rapid dissolution of aluminium occurs within pits, while oxygen reduction takes place on adjacent surfaces. The rapid dissolution of aluminium within pits tends to produce an excess of positive charge in these areas, resulting in the migration of

chloride ions to maintain electroneutrality. Thus, there will be high concentrations of hydrogen ions in pits as a result of hydrolysis, and this process accelerates with time.

4. Conclusions

MMCs containing up to 15% fly ash particles were easily fabricated. A uniform distribution of fly ash was observed in the matrix. The fluidity and density of the composites decreases, whereas the hardness increases with an increasing percentage of the fly ash particulates. The tensile strength, compression strength, and impact strength increase with an increasing percentage of fly ash particulates. The dry sliding wear resistance increases with an increasing percentage of fly ash. In the slurry erosive wear test, the resistance to wear increases with increasing fly ash content. The wear is enhanced in the case of basic media compared to acidic and neutral media. Corrosion increases with an increasing percentage of fly ash content. The MMC produced can be used for bearing applications, because of its good wear resistance.

References

[1] EYRE T.S., Tribol. Int., (1976), 203.
[2] BHANSALI K.J., MEHRABIAN R., J. Metals, 34 (1982), 30.
[3] HOSKING F.M., PORTILLO F.F., WUNDERLIN R., MEHRABIAN R., J. Mater. Sci., (1982), 477.
[4] DEONATH S.K., BHAT R.T., ROHATGI P.K., J. Mater. Sci., (1980), 1241.
[5] MAJUMDAR B.C., YEGNESHWARAN A.H., ROHATGI P.K., Mater. Sci. Eng., 68 (1984), 885.
[6] POZA P., LLORCA J., Mater. Sci. Eng., A206 (1996), 183.
[7] PRADER P., DEGISCHER H.P., Mater. Sci. Technol., 16(2000), 893.
[8] IAN J.H., Metal Powder Rep., 10(1990), 689.
[9] ROHATGI P.K., GUO R.Q, J. Metall. Mater. Trans. B, 298 (1998), 519.
[10] SANNINO A.P., RACK H.J, Wear, 216 (1995), 1.
[11] DEUIS R.L., SUBRAMANIAN C., YELLUP J.M., Wear, 201 (1996), 132.
[12] GUO R.Q., ROHATGI P.K., Metal. Mater. Trans. B, 29B (1998), 519.
[13] HIHARA L.H., LATANISION R.M, Int. Mater. Rev., 39 (1994), 245.
[14] BIENIAS J., WALCZAK M., SUROWSKA B., SOBCZAK J., J. Optoelectronics Adv. Mater., 5, (2003), 55.

Received 21 July 2005
Revised 22 May 2006

Materials Science-Poland, Vol. 25, No. 1, 2007

Photoinduced degradation in the electrical properties of normally and obliquely deposited As_2Se_3 thin films

P. BHARDWAJ[1*], P. K. SHISHODIA[2], R. M. MEHRA[1]

[1]Department of Electronic Science, University of Delhi South Campus, New Delhi-110021, India

[2]Department of Physics & Electronics, Zakir Husain College, New Delhi-110002, India

Dark conductivity in As_2Se_3 films was measured in the temperature range 300–400 K. It was found to be of the doubly activated type in high- and low-temperature ranges. The experimental results were analysed using the Meyer–Neldel rule. The effect of light soaking on the electrical transport properties of normally and obliquely deposited As_2Se_3 thin films were examined. It has been observed that light soaking results in the degradation of photocurrent, which nearly saturates in an hour. Dark conductivity is found to be smaller after light soaking than without it.

Key words: *chalcogenides; oblique deposition; Meyer–Neldel rule*

1. Introduction

In amorphous chalcogenide films, photostructural transformations have been extensively studied. It is well known that transformations are induced in some materials of the As–Se and As–S systems by band gap illumination, and are associated with certain changes in optical properties, such as the band gap and refractive index. These photoinduced changes can be increased by varying the deposition conditions, mainly the angle of deposition, since obliquely deposited films have a columnar structure and a smaller density of atoms [1]. As a result, large changes have been observed after photoillumination in obliquely deposited chalcogenide films [1–3].

Besides optical properties, various photoinduced phenomena [1, 2] have also been reported for photocurrent in amorphous semiconductors in recent years. Various models have been put forward in support of the observed light-soaked effects on photocurrent [3–5] and the decay of photocurrent [6]. It is well known that amorphous semiconductors undergo photoconductive degradation when exposed to light illumination. Light-induced effects on dark conductivities and photoconductivities in amorphous semiconductors are important subjects from both the fundamental and practical points

*Corresponding author, e-mail: priyam75@yahoo.com

of view [1, 2]. Specifically, the Staebler–Wronski effect, appearing in hydrogenated amorphous Si (a-Si: H) [3], poses serious problems in solar cell applications. Shimakawa et. al. [7] have reported a similar degradation phenomenon of photocurrent in chalcogenide glasses. The mechanisms of these photodegradation phenomena are assumed to be connected to the photoinduced creation of some kinds of defects. The transport properties of oblique films, however, have not been extensively studied, and therefore the purpose of the present paper is to investigate light-induced changes in the transport properties of As_2Se_3 films deposited at oblique incidence and to compare them with films at normal incidence. Thin films are key to exploiting the switching characteristics of chalcogenides. Also, thin films allow a current to flow through the highly resistive amorphous state at relatively low voltages.

2. Experimental details

Normal and oblique films of As_2Se_3 were prepared by the vacuum evaporation technique. The oblique films were deposited at the angle of 80°, this being the angle between the normal to the substrate and the direction of incidence of the evaporated atoms. Optical glass slides were used as the substrate for depositing the films. Evaporation was carried out on the substrates at room temperature in a vacuum of about 10^{-6} Torr from a molybdenum boat heater. A surface profiler (DekTek 3) was used to measure the thickness of the film. The films had thicknesses of the order of 1 μm. Conductivity measurements were done by evaporating aluminium contacts on the film in a coplanar configuration with a spacing of ~ 0.1 cm. The samples were annealed below the glass transition temperature for an hour. A running vacuum of the order of 10^{-3} Torr was maintained throughout the experiment. The temperature dependence of conductivity was measured in the range of 300–400 K. The temperature of the films was varied by inserting a heater into the cryostat and measured using a Chromel–Alumel thermocouple. A constant DC voltage, from a highly stabilized power supply, was applied across the sample, and the current was measured with a Keithly 610C electrometer.

Photocurrent and light soaking measurements were done using a tungsten halogen lamp (100 mW/cm^2). The cryostat had a window facing the film to let light fall on it. Different coloured filters were used to measure the spectral response of photocurrent.

3. Results and discussion

3.1. Dark current

The temperature dependences of dark conductivity for normal and oblique (80°) As_2Se_3 films are shown in Fig. 1. Dark conductivity was measured by warming the samples after rapid and normal cooling. Dark conductivity data can be described well by the standard expression

$$\sigma_{DC} = \sigma_0 \exp\left(\frac{-E_a}{kT}\right) \tag{1}$$

where σ_0 is the preexponential factor, E_a is the activation energy for electrical conduction, k is the Boltzmann constant, and T the absolute temperature. It is clearly seen from the figure that there are two different temperature regions for conductivity.

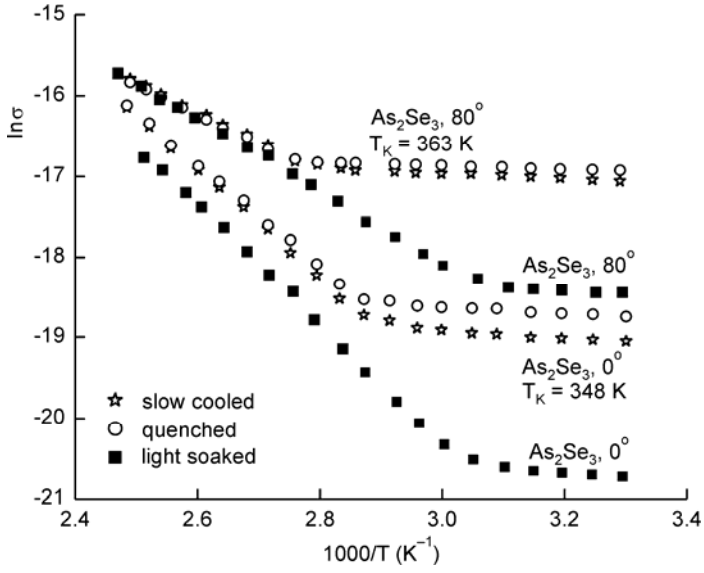

Fig. 1. Temperature dependence of dark conductivity (σ) for various cooling rates in As_2Se_3 normal and oblique films

Table 1. Activation energies and pre-exponential factors at various temperature ranges

Sample[1]	Temperature	E_a (eV)	σ_0
As_2Se_3-0° (NC)	high	0.57	1.47
As_2Se_3-0° (Q)		0.54	0.657
As_2Se_3-80° (NC)		0.31	1.2×10^{-3}
As_2Se_3-80° (Q)		0.29	6.78×10^{-4}
As_2Se_3-0° (NC)	low	0.04	3.54×10^{-7}
As_2Se_3-0° (Q)		0.039	3.24×10^{-8}
As_2Se_3-80° (NC)		0.027	1.08×10^{-7}
As_2Se_3-80° (Q)		0.018	8.9×10^{-8}

[1]NC – normal cooling, Q – quenched.

The activation energies and pre-exponential factors in the high- (360–400 K) and low- (350–300 K) temperature ranges are given in Table 1 for all the samples. The calculated values of activation energy and the pre-exponential factor in the high temperature region suggest that conduction is due to the thermally-assisted tunnelling of

charge carriers in localized states in the band tails [8]. The observed decrease in activation energies in obliquely deposited films entails an increase in the conductivity. At low temperatures, the data suggest that conduction takes place in localized states near the Fermi level. The conductivity and pre-factor data were analysed using the Meyer –Neldel rule (MNR) [9].

According to MNR, the pre-factor σ_0 in Eq. (1) correlates with the activation energy E_a:

$$\sigma_0 = \sigma_{00} \exp\left(\frac{E_a}{E_{MN}}\right) \tag{2}$$

where the pre-factor σ_{00} and the characteristic energy (E_{MN}) are positive constants. The values for E_{MN} in various materials and processes have been reported to be between 25 and 100 meV [10]. A combination of Eqs. (1) and (2) gives a general expression for σ_0:

$$\sigma = \sigma_{00} \exp\left[\left(\frac{1}{E_{MN}} - \frac{1}{kT}\right) E_a\right] \tag{3}$$

This implies a single crossing point for different activation energies at a temperature $T_{MN} = E_{MN}/k$. At this temperature, σ is independent of activation energy. In a plot of $\ln\sigma$ vs. $1/T$, the curves should show one common intersection at T_{MN}. Figure 2 shows the plot of $\ln\sigma_0$ vs. E_a. It can be seen from the figure that the MNR is satisfied for our films. The value of E_{MN} is 32 meV.

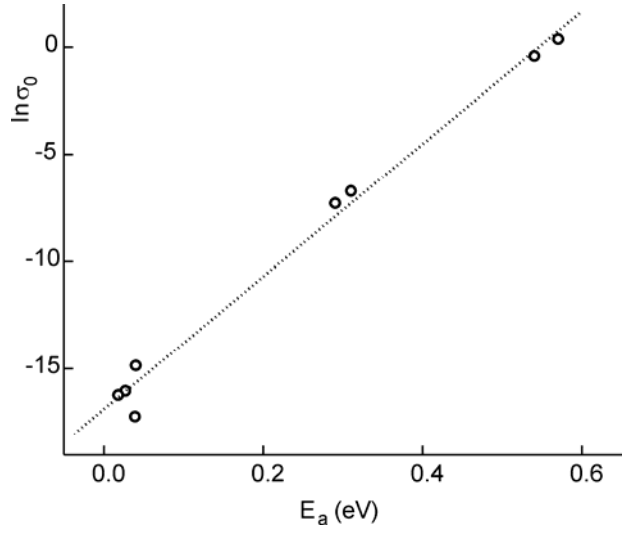

Fig. 2. Plot of $\ln\sigma_0$ vs. E_a of normal and obliquely deposited As_2Se_3 films exhibiting the Meyer–Neldel rule

This type of variation in activation energy with a pre-exponential factor indicates the movement of the Fermi level towards the edge of the valence band with increasing temperature, resulting in an increase in conductivity.

3.2. Photocurrent

The variation of photocurrent I_P with exposure time is shown in Fig. 3. It is observed that I_p initially reduces with time and attains a nearly constant value after 1 hour of exposure in both normal and obliquely deposited films. This feature is qualitatively consistent with previous observations [11]. Obliquely deposited films exhibited a higher value of I_p at all times. In general, photocurrent is directly related to the photoexcitation rate, the change in the lifetime of the carrier, and the change in mobility. Since in the present case both films were exposed to the same light, it is expected that a longer lifetime in obliquely deposited films is responsible for the observed higher photocurrent.

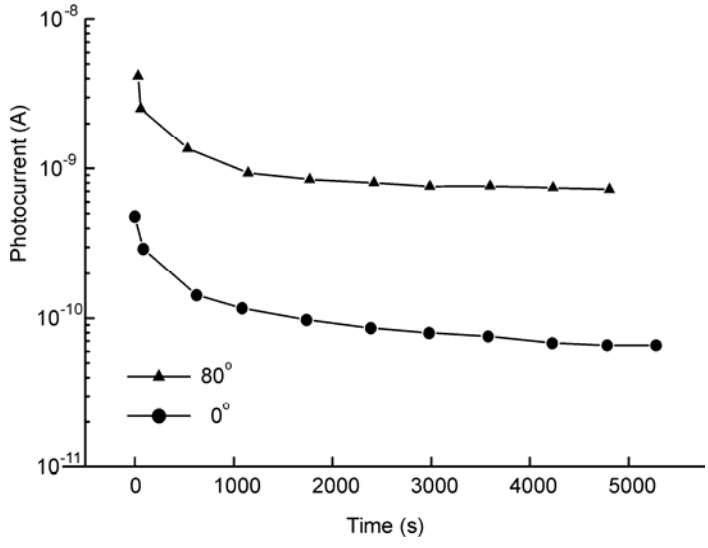

Fig. 3. Photocurrent in normal and obliquely deposited As_2Se_3 films as a function of exposure time

A higher photocurrent degradation rate was observed at an early stage of light soaking, as the defect generation rate is higher initially, but as time passes it decreases and finally becomes constant. The decrease in the rate of degradation with light soaking can be understood in terms of the difference between light-induced defect creation and annihilation. Since the annihilation component is directly dependent on the density of metastable defects, the density of defects increases more quickly initially. These photoinduced changes are reversible and can be annealed out near the glass transition temperature of 423 K.

Figures 4 and 5 show the photocurrent spectra before and after light soaking for an hour in normal and obliquely deposited As_2Se_3 films, respectively. At room temperature, light soaking gives rise to a decrease in the photocurrent over the entire investigated spectral range. It can also be seen from these figures that maximum in the photocurrent (~2 eV) appears at an energy greater than the band gap of the films (~1.79 eV) [12].

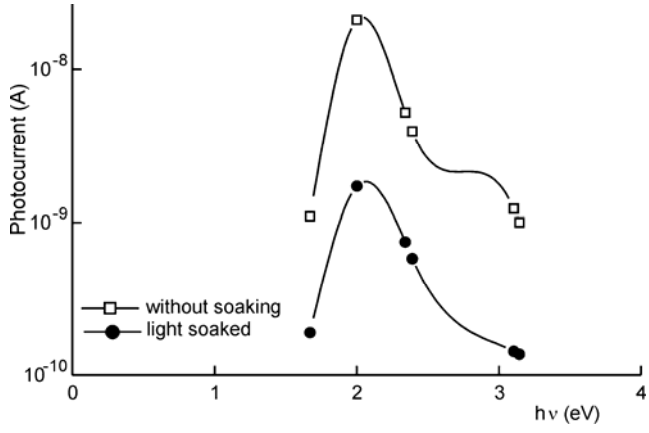

Fig. 4. Spectral dependence of photocurrent for light soaked and without light soaked As_2Se_3 normal films

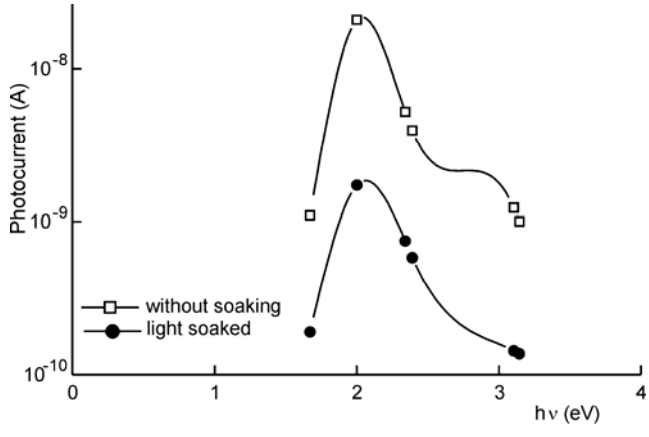

Fig. 5. Spectral dependence of photocurrent for light soaked and without light soaked As_2Se_3 obliged films

The decay of photocurrent in chalcogenide glasses due to light soaking can be understood on the basis of the charged defect model originally proposed by Mott [13]. According to the charged defect model, D^- centres can act as recombination (or trapping) centres for photoexcited holes due to Columbic attractive forces, and accordingly the photocurrent decreases with light soaking at room temperature in a-As_2Se_3,

because new D^- centres (light induced metastable defects (LIMD)) are created by illumination. These photoinduced charged defects are metastable, and can recover to normal bonding structures when annealed at the glass-transition temperature. Shimakawa et al. have also proposed a similar model [7, 14]. The decrease in photocurrent is larger in the case of oblique films, which can be due to the photostructural changes induced by strongly absorbed light [15, 16]. Photo-darkening may accompany the creation of new localized states. It has been suggested [14] that these new localized states are close pairs of the charged D^+ and D^- centres. Thus, the recombination of photoexcited holes will be more intense in oblique films then in normal incidence films.

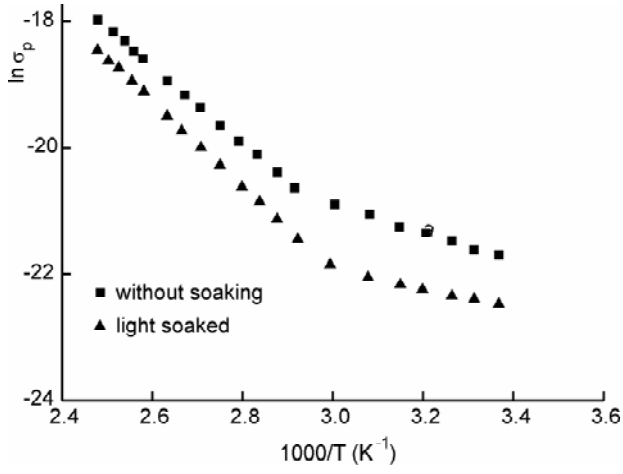

Fig. 6. Temperature dependence of the photoconductivity without light soaking and after light soaking in As_2Se_3 normal films

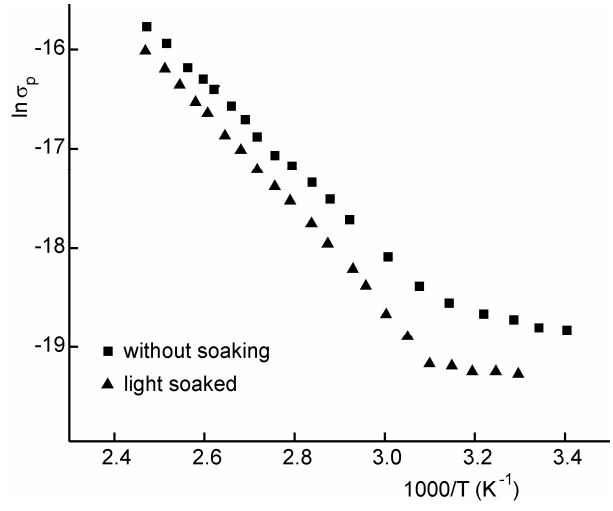

Fig. 7. Temperature dependence of the photoconductivity without light soaking and after light soaking in As_2Se_3 obliged films

The creation of defect states due to light soaking may result in a decrease in dark conductivity. The variation of dark conductivity with temperature is also shown in Fig. 1 for comparison. It is clear from this figure that in the low-temperature range dark conductivity after light soaking is nearly two orders smaller than the conductivity without light soaking, for both normal and obliquely deposited films.

Figures 6 and 7 show the temperature dependences of photoconductivities under the illumination of 100 mW/cm^2 in light-soaked and unmodified a-As_2Se_3 films. A thermally activated behaviour can be observed. Light soaking induces a decrease in photoconductivity. The temperature dependences of photoconductivity in a variety of different IV–V–VI chalcogenide semiconductors can be classified into three types, i.e. (a) type I, (b) type II, and (c) an intermediate between type I and type II. In type I, photoconductivity has a maximum at a specific temperature T_m and generally higher values than the dark conductivity for $T < T_m$ and smaller than dark conductivity for $T > T_m$. Some amorphous materials from the IV–V–VI family show a different temperature dependence of photoconductivity, called type II behaviour, displaying no maximum in photoconductivity, the photoconductivity simply increasing slowly and monotonically with increasing temperature. In general, the photoconductivity is much smaller in this case than the dark conductivity.

In our case, the photoconductivity appears to be somewhat intermediate between type I and type II, as the magnitude of photoconductivity is much smaller than dark conductivity and it is activated in nature. Such a behaviour has been observed in Ge_xAs_{1-x} (x = 0.33, 0.50) and $GeTe_{1-x}$ for $0.3 \le x \le 0.5$ [17].

4. Conclusions

It can be concluded that photodegradation is larger in obliquely deposited films, similar to other photoinduced changes. These photoinduced changes in conductivity have been found to be reversible and can be removed by annealing near the glass transition temperature. Enhanced photodegradation may be due to the creation of new localized states, as is evident from the low value of dark conductivity after light soaking.

References

[1] AOKI T., SHIMADA H., SHENG W.Q., SHIMAKAWA K., Philos. Mag. Lett.,75 (1997), 163.
[2] HAYASHI K., HIKIDA Y., SHIMAKAWA K., ELLIOT S. R., Philos. Mag. Lett., 76 (1997), 233.
[3] MOTT N.F., DAVIS E.A., *Electronic Processes in Non-Crystalline Materials*, 2nd Ed., Clarendon Press, Oxford, 1979.
[4] SHIMAKAWA K., KOLOBOV A., ELLIOT S.R., Adv. Phys., 44 (1995), 475.
[5] WATANABE Y., KAWAZOL H., YAMANE M., Phys. Rev. B, 38 (1988), 5677.
[6] SHIMAKAWA K., J. Non-Cryst. Solids, 77–78 (1985), 1253.
[7] SHIMAKAWA K., Phys. Rev. B, 34 (1986), 8703.
[8] MOTT N.F., DAVIS E.A., *Electronic Processes in Non-Crystalline Materials*, Clarendon Press, Oxford, 1971.
[9] MEYER W., NELDEL H., Zh. Tekh. Fiz., 12 (1937), 588.

[10] WIDENHORN R., MUNDERMANN L., REST A., BODEGOM E., J. Appl. Phys., 89 (2001), 8179.
[11] KOUNAVIS P., MYTILINEOU E., Philos. Mag. Lett., 72 (1995), 117.
[12] BHARDWAJ P., SHISHODIA P.K., MEHRA R.M., J. Mat. Sci., 38 (2003), 937.
[13] BIEGELSEN D.K., STREET R.A., Phys. Rev. Lett., 44 (1980), 803.
[14] SHIMAKAWA K., INAMI S., ELLIOTT S.R., J. Non-Cryst. Solids, 137–138, (1991), 1017.
[15] TANAKA K., J. Non-Cryst. Solids, 35–36 (1980), 1023.
[16] RAJAGOPALAN S., HARSHVARDHAN K.S., MALHOTRA L.K., CHOPRA K.L., J. Non-Cryst. Solids, 50 (1982), 29.
[17] SHIAH R.T.S., BUBE R.H., J. Non-Cryst Solids, 47 (1976), 2005.

Received 18 October 2005
Revised 16 February 2006

Materials Science-Poland, Vol. 25, No. 1, 2007

Microstructure of austenitic steel after the oscillatory compression test

G. NIEWIELSKI, D. KUC*, K. RODAK

Silesian University of Technology, Department of Materials Science,
40-019 Katowice, Krasińskiego 8, Poland

The paper presents the influence of oscillatory torsion on the microstructure of compressed cylindrical samples of austenitic steel. The austenitic steel was deformed at room temperature using a standard compression test and oscillatory torsion test at constant parameters: the torsion angle $\alpha = \pm 5$ and torsion frequency $f_{sk} = 1.8$ Hz. Samples were deformed at strains of $\varepsilon = 4$. Optical observations showed that well-defined slip bands and clusters of slip lines were present in the austenitic steel after two modes of deformation. Specimens deformed during the oscillatory compression test exhibit well-defined deformation twins intersected by shear bands. The structure of shear bands consists of grains between 50 nm and 400 nm in diameter. The analysis of selected diffraction pattern areas has shown that diffraction spots are arranged in rings, indicating that disorientation angles of grain boundaries are higher than 15°. Our investigations constitute a preliminary stage of complex analysis of reactions of metals under diversified process conditions.

Key words: *oscillatory compression test; austenitic steel; substructure; high-angle boundaries*

1. Introduction

Nanocrystalline materials of grain sizes not exceeding 100 nm possess competitive mechanical properties when compared to conventional alloys, and demonstrate much better plastic properties, temperature stability, and corrosion resistance [1]. One of the techniques for producing nanocrystalline materials is the so-called "top-down" method, focused on structure size reduction from the micrometric to nanometric scale. Size reduction may be performed by deformation methods, which allow considerable deformations without losing coherence. Acknowledged plastic deformation methods, which yield nanometric structures include:

- cyclic extrusion compression [2],
- equal channel angular extrusion [3],

*Corresponding author, e-mail: dariusz.kuc@polsl.pl

- high pressure torsion methods [1, 4],
- cumulated plastic deformation [5].

New, unconventional deformation methods such as compression with oscillatory torsion have also been implemented. A device for this purpose was developed by Grosman and Pawlicki [6]. The method offers a lot of possibilities with regard to considerable plastic deformations. Control over the process allows one to adjust the compression rate, torsion frequency, and the amplitude of the torsion angle. The paper presents the influence of compression with oscillatory torsion on the structure of austenitic steel. The results obtained indicate that areas characteristic of nanometric structures are formed.

2. Materials and methods

Hot-rolled bars made of AISI304 austenitic steel with 0.03% C, 18.5% Cr, and 8.9% Ni content were used for specimen preparation. Before plastic deformation, for the purpose of dissolving carbide precipitations and obtaining a uniform austenite structure, the samples were subject to solution heat treatment at the temperature of 1150 °C for 60 minutes. The size of austenite grains after thermal treatment was 60 μm.

The research was conducted by a conventional compression method as well as by applying compression with simultaneous oscillatory torsion under conditions of free radial metal flow, using samples in the form of cylinders with initial dimensions of $\phi 10 \times 15$ mm^2. The torsion angle amounted to ±5°, and the fluctuation frequency for the lower punch was 1.8 Hz. Based on the recorded data, the relationship between average unit pressure and a true draft was determined.

The structures and substructures of the samples after deformation were examined in the centre of their section height, at the distance of the 0.8 external radius of the sample. The examination of the substructure was carried out with a JEM 3010 high resolution transmission electron microscope operating at 300 kV accelerating voltage and by a JEOL 100B transmission microscope with an accelerating voltage of 100 kV.

The grain sizes were measured with a MOP-AMO 3 semi-automatic image analyser using images obtained from the dark field. The measurements were then used to determine the average equivalent diameter (d) as a measure of grain size as well as frequency distributions for the occurrence of grains of specified sizes. By means of diffraction examinations, the value of disorientation between particular crystallites was determined.

3. Results

The influence of the deformation route on the value of mean unit pressure p_{av} and on the structure of the investigated steel is presented in Fig. 1. The application of compression by oscillatory torsion causes a remarkable decrease in unit pressure val-

ues, compared to conventional compression at any phase of the process. The influence of the deformation route enabled cumulating deformation $\varepsilon = 4$ in the material, which has a significant influence on the structure of the steel. In the samples compressed by conventional methods, wide deformation bands were revealed (Fig. 1a). After combined deformation, deformation bands as well as shear microbands can be observed in the steel structure (Fig. 1b).

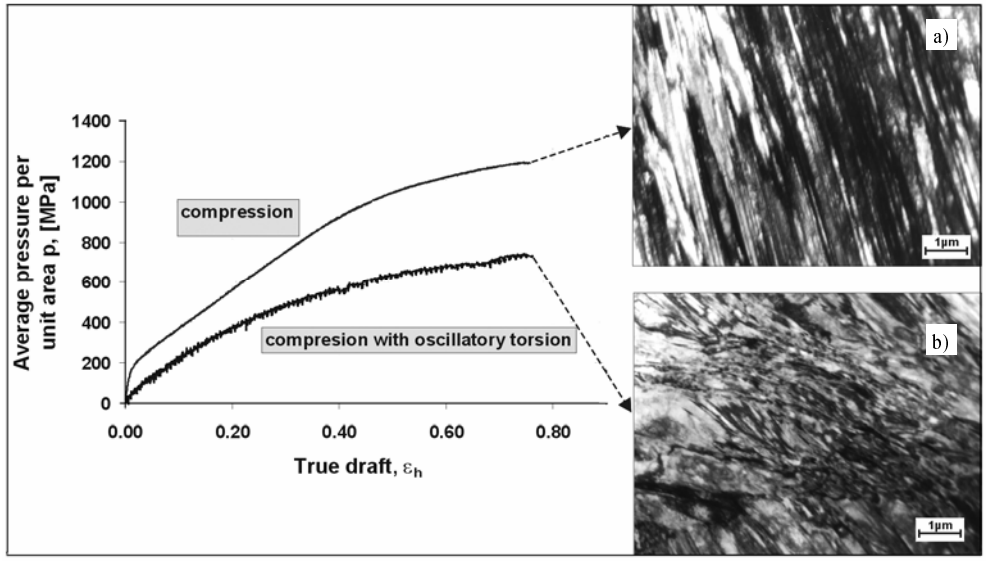

Fig. 1. Influence of conventional compression and compression by oscillatory torsion on mean unit pressure and the structure of the examined austenitic steel

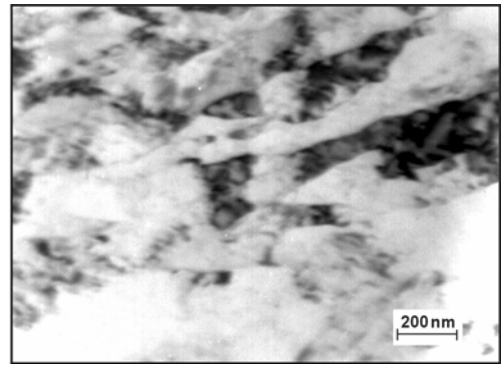

Fig. 2. Nanogranular substructure of austenitic steel after oscillatory compression

A typical substructure created during compression by oscillatory torsion is a band structure running through a number of grains, which indicates that the bands are shear bands. Apart from structures with diverse dislocation densities and indistinct boundaries, structures formed of elongated subgrains occur most often (Fig. 2). Certain areas

are characterised by insignificant dislocation densities inside the subgrains. Such a phenomenon is related to structure reconstruction which takes place when considerable deformations are applied. Diffraction patterns obtained from areas of subgrains formed in this way indicate the occurrence of high angle boundaries (Fig. 3).

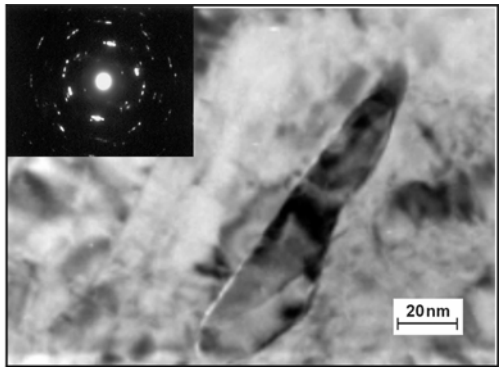

Fig. 3. The area from Fig. 2 in a bright field. Elongated subgrains are visible, with some areas of a reduced defect density. The disorientation calculated from the diffraction pattern amounts to 19°

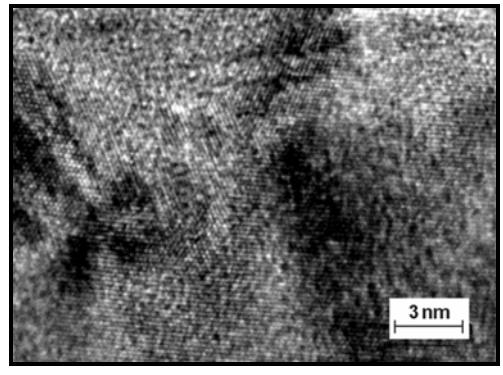

Fig. 4. High-resolution image of the granular structure formed within bands as seen in Fig. 2

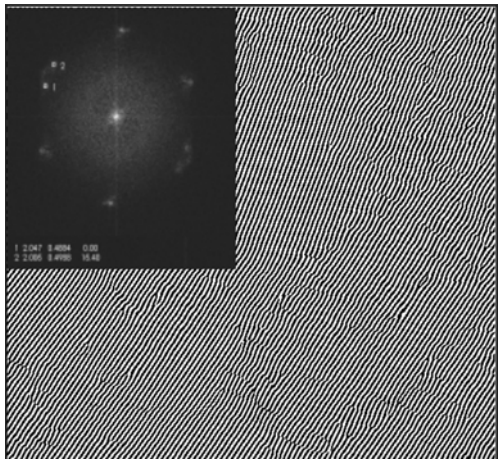

Fig. 5. The area of Fig. 4, with granular structures visible after applying Fourier filtration and diffraction

Based on HREM examinations, it was demonstrated that the structures formed (Figs. 3 and 4) are separated from one another by high angle boundaries (Fig. 4). The value of disorientation presented in Fig. 5, determined on the basis of diffraction examinations, amounts to about 15.5°. It can be expected that a larger deformation will result in a higher misorientation.

The quantitative analysis carried out on the basis of images recorded in the dark field mode has demonstrated that the average diameter of the granular structures

formed is 130 nm, with about 70% of the values being in the range 50–200 nm (Fig. 6). The rest of the population is in the range 300–400 nm.

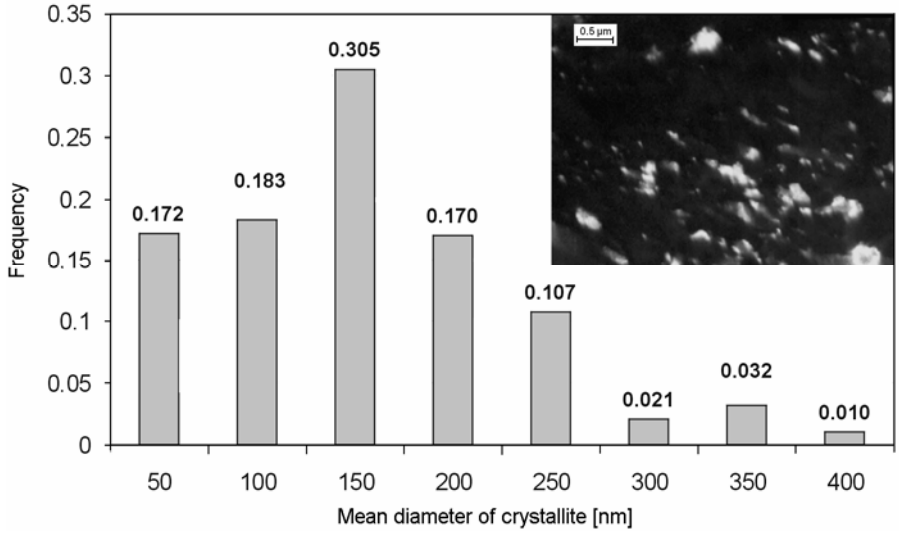

Fig. 6. Frequency distribution of the occurrence of austenitic steel crystallites in specified size classes (equivalent diameters d), and an example structure after compression by oscillatory torsion used for the quantitative examination of crystallite sizes, dark field

4. Conclusions

The examinations carried out enabled observation of an intensive influence of the deformation route on parameters related to power and energy and on the structure of the examined steel. Compression with simultaneous oscillatory torsion leads to a considerable decrease in the plastic flow resistance of the metal. The development of shear microbands in the areas of deformation bands is also observed. Within shear microbands, a granular structure is formed, with an average crystallite size of 130 nm. Large disorientation angles (above 15°) between the structures formed, have been found. The share of large disorientation angles between grain boundaries may increase the deformation growth. This can be obtained by a proper choice of process parameters, i.e. the compression rate and the number of oscillatory torsion cycles. The data obtained indicate the possibility of producing nanomaterials from austenitic steel using the method of compression by oscillatory torsion.

References

[1] VALIEV R.Z., ISLAMGALIEV R.K., Progress Mater. Sci., 45 (2000), 106.
[2] RICHERT J. AND RICHERT M., Aluminium, 62 (1986), 604.

[3] SEGAL V.M., Mat. Sci. Eng., A338 (2002), 331.
[4] ZHILYAEV A.P., Acta Mater., 51 (2003), 753.
[5] FERGUSON D., CHEN W., KUZIAK R., ZAJĄC S., Proc. Conf. Mat 5th Int. ESAFORM Conference on Materials Forming, M. Pietrzyk (Ed.), Cracow (2002), 599.
[6] GROSMAN F., PAWLICKI J., Acta Metal. Slov. R, 8 (2002), 178.

Received 21 November 2005
Revised 5 January 2006

Materials Science-Poland, Vol. 25, No. 1, 2007

Effect of lanthanum on the tensile properties of carbon-fibre reinforced thermoplastic polyimide composites

J. LI[1], X.H. CHENG[1, 2*]

[1]School of Mechanical & Power Engineering, Shanghai Jiao Tong University, Shanghai 200030, P.R. China

[2] The State Key Laboratory of Tribology, Tsinghua University, Pekin 100084, P.R. China

Rare earth (RE) La modification and air-oxidation methods were used to improve the interfacial adhesion of the carbon fibre reinforced polyimide (CF/PI) composite. The interfacial characteristics of composites reinforced by carbon fibres, treated with different surface modification methods, were investigated comparatively. Results showed that both RE modification and air-oxidation method improved the adhesion between the reinforcement and matrix, and that the RE modification method was superior to the air-oxidation method. For the CF/PI composite, optimum interfacial adhesion was obtained at 0.3 wt. % of La concentration. The fracture surfaces of samples were investigated by scanning electronic microscopy (SEM) to analyse the effects of various surface treatment methods.

Key words: *rare earth; carbon fibre; polyimide; composite*

1. Introduction

Polyimide and its composites attract extensive concern from tribological scientists world-wide because of their high mechanical strength, high wear resistance, good thermal stability, high stability under vacuum, good anti-radiation, and good solvent resistance [1, 2]. Carbon fibre reinforcement dominates in high-performance applications due to its outstanding mechanical properties combined with low weight. Strong interfacial adhesion strength must be achieved to improve the mechanical properties of composites, as it determines their mechanical properties [3]. Carbon fibre, however, often exhibits poor adhesion to polymers because its surface is chemically inert and smooth, and there are very few oxygen-containing functional groups. Much re-

*Corresponding author, e-mail: Xhcheng@mail.sjtu.edu.cn

search has been devoted to enhance the adhesion between carbon fibre and polymer, hence it is well known that the surfaces of carbon fibres can be modified by surface treatment. Many approaches, such as electrochemical oxidation, plasma treatment, and liquid phase oxidation of carbon fibre, have been pursued in order to improve interfacial adhesion strength of carbon fibre reinforced composites [4].

RE surface modification has extensive application prospects due to its extraordinary properties, such as no environmental pollution, low cost, high efficiency, simple process, and no damage to the fibre. RE surface treatment has been successfully applied to improve the adhesion of glass fibre and PTFE, and aramid fibre and epoxy, respectively [5–7].

2. Experimental

In the present research, two types of methods of surface modification were used: RE modification and air-oxidation. The composites and the methods of treatment of carbon fibres are listed in Table 1. The effects of different surface treatment methods were comparatively investigated by the Erichsen test. The tensile fracture surfaces were observed by SEM. In addition, the effects of RE La concentration on the tensile properties of CF/PI composites were investigated in detail to explore an optimum amount of La in solution for modifying carbon fibre.

Table 1. Materials and surface treatments of carbon fibre

Material	Carbon fibre	Modifier
A	untreated	no modification
B	treated with RE	$LaCl_3$
C	treated with air (oxidation method)	air

Table 2. Main properties of PI (GCTP^{TM})

Parameter	Value
Density (kg/m^3)	1350
Impact strength (kJ/m^2)	25
Tensile strength (MPa)	95
Thermal expansion (°C^{-1})	4.8×10^{-5}
Breaking elongation (%)	7
Glass transition temperature (°C)	260
Flexural strength (MPa)	150
Heat decomposition temperature (°C)	240

The reinforcements used in the present study were polyacrylonitrile (PAN)-based, unmodified, and unsized high strength (HS) carbon fibres (supplied by Shanghai Sxcarbon Technology Co. Ltd, China) with the following properties: tensile strength

2500 MPa, elastic modulus 200 GPa, density 1760 kg/m^3, diameter 7 μm, length 75 μm. $LaCl_3$, purchased from Shanghai Yuelong New Materials Co. Ltd. was used as the main component of the RE solution applied in surface modification. The matrix was a GCTP^{TM} TPI powder with a grit size of about 500 μm, provided by Nanjing University of Technology. Its main physical and mechanical properties are listed in Table 2.

Before the RE surface treatment of carbon fibres, RE solutions with the hot moulding technique was employed to prepare the composite specimens, which is the most common technique for the sintering of pure PI without sintering aids. In this process, the filler and resin were churned together in the mixer. Mixing was done for a few minutes after the addition of each component for about 20 minutes. The sintering powder was placed inside a stainless mould with its inner walls coated with a BN slurry to avoid any interaction between the powder and steel and also to facilitate the demoulding process. The compounds were put into the QLB–D170×170 vulcanising machine at 280 °C for 1 hour with a constant pressure of 12 MPa, then heated from 280 °C to 340 °C with the heating rate of 60 K/h in 1 hour. When the temperature reached 340 °C, it was kept constant for 1 hour. Afterwards, the compounds were cooled from 340 °C to 200 °C with the cooling rate of 120 K/h for 70 minutes. Pressure was kept constant during the whole process. The sintering cycle is shown in Fig. 1.

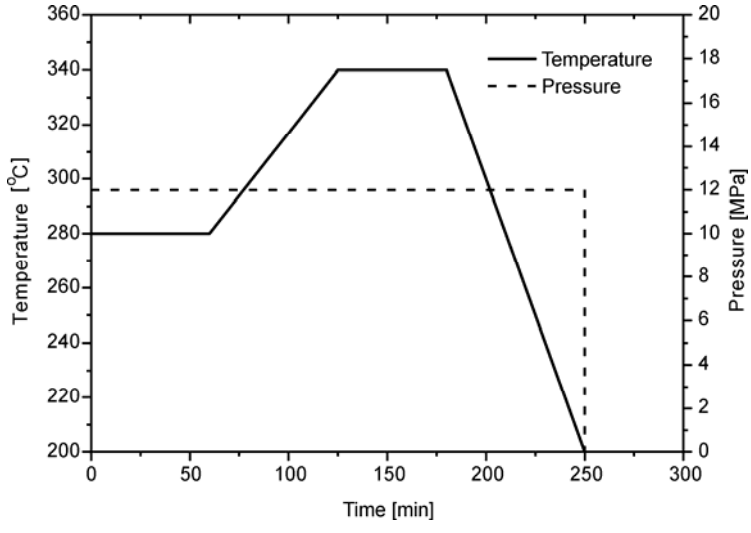

Fig. 1. Changes of temperature and pressure with time

The materials were then cooled to room temperature to get the composites. The CF/PI composite plates were cut into narrow-waisted dumbbell-shaped specimens in accordance with the Chinese standard GB/T1040–1992. The Erichsen tests were carried out on a computer-controlled Universal Testing Machine (made in China) at room temperature. The beam rate was 5 mm/min. For a more accurate determination

of the material parameters and consideration of the possible scatter in the experimental data, the measurements were made at five constant loads for five specimens in tension. The obtained quantities were then averaged. All fracture surfaces were gold coated for 40 seconds using a Desk II Sputter-Coater (Denton Vacuum, New Jersey, USA) to reduce the incidence of surface charging in the SEM.

3. Results and discussion

The tensile strength and tensile modulus of CF/PI composite treated with RE as a function of La concentration is shown in Fig. 2. The La concentration was varied from 0.1 to 0.5 wt. %. It is seen that the tensile strength and tensile modulus increase with increasing La concentration, reaching the maximum value of 123 MPa and 3.3 GPa, respectively, at 0.3 wt. % La concentration. Above this maximum value, the tensile properties decrease gradually with increasing La concentration.

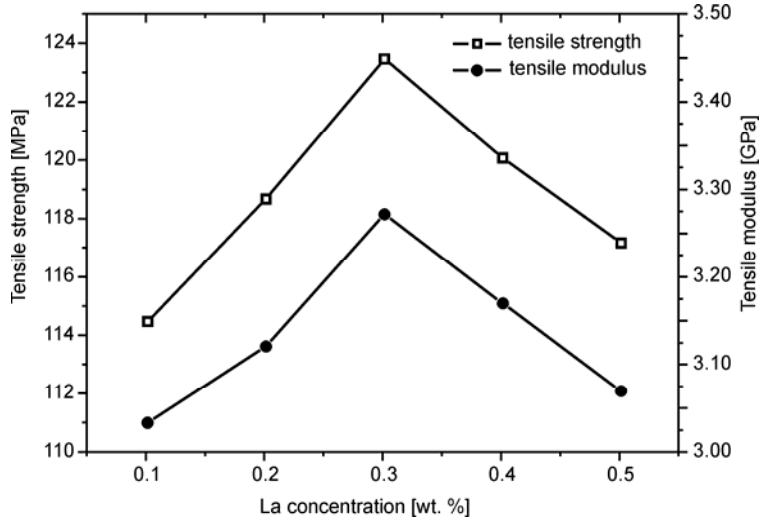

Fig. 2. The effect of La concentration on tensile properties

According to the chemical bonding theory, it is suggested that La atoms are adsorbed onto both the carbon fibre surface and PI matrix through chemical bonding, forming the effective bond between the reinforcement and matrix. The main component of the bond is the coordinate bond formed by functional groups (such as hydroxyl (C–OH), carbonyl (C=O), and carboxyl (COOH) groups) on the fibre surface and the PI matrix (such as the sulfuric group ($–SO_2–$) and carbonyl group (C=O)), with the concentration of reactive functional groups determined by the chemical activity of La [4]. These reactive functional groups can improve the interfacial adhesion between carbon fibres and the PI matrix. Excess La, however, may cause a decrease in the tensile properties of CF/PI through the formation of La salt crystals on the carbon

fibre surface, which affects the effective bond between the fibre and matrix. This can be explained by monomolecular layer theory: when the monomolecular layer is formed (Fig. 3 b), the organic long-chains tangle with the functional groups on the two corresponding surfaces. When free La atoms are present at the interface (Fig. 3a), the adhesion force between macromolecules is reduced due to the existence of weak van der Waals forces. On the other hand, when the La atoms are too scarce to form a full monomolecular layer (Fig. 3c), there is no effective adhesion effect in the void, affecting the entire tensile strength. This monomolecular layer theory model is illustrated below.

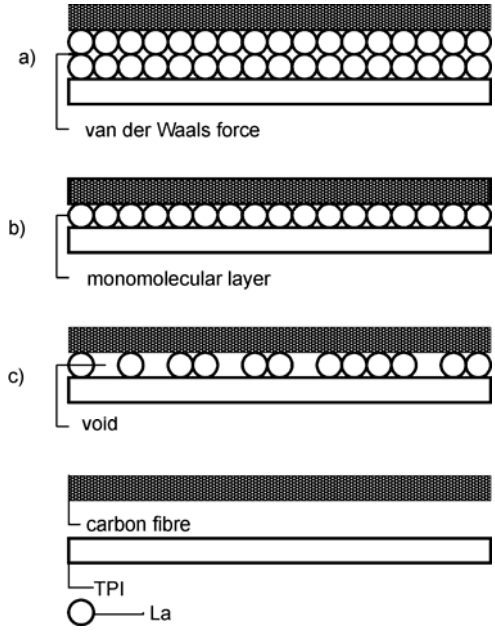

Fig. 3. The model according to monomolecular layer theory

SEM of the fracture surface is shown in Fig. 4 to illustrate the effect of La concentration on interfacial characteristics. Figures 4a, b show that the surfaces of carbon fibres are smooth and little resin is adhered to it. With an increase in La concentration, more resin becomes adhered to the carbon fibres and long carbon fibres are exposed on the fracture surface without forming effective adhesion with the resin. During the process of extraction, the fibres are easily separated from the matrix and the high strength of carbon fibres is not exerted. Thus, the composite showed poor tensile properties. Holes are found in Figs. 4d, e due to the extraction of carbon fibres, and the carbon fibres have the features of being extracted. The amount of resin adhered to the carbon is still small although La concentration increases, in accordance with the model shown in Fig. 3a. Only Fig. 4c shows effective adhesion between the carbon fibres and PI resin. The carbon fibres on the fracture surface are short and the surface is smooth. Nearly no gaps are found on the fracture surface in the case of strong adhesion between the reinforcement and matrix. The interfacial changes are still under investigation.

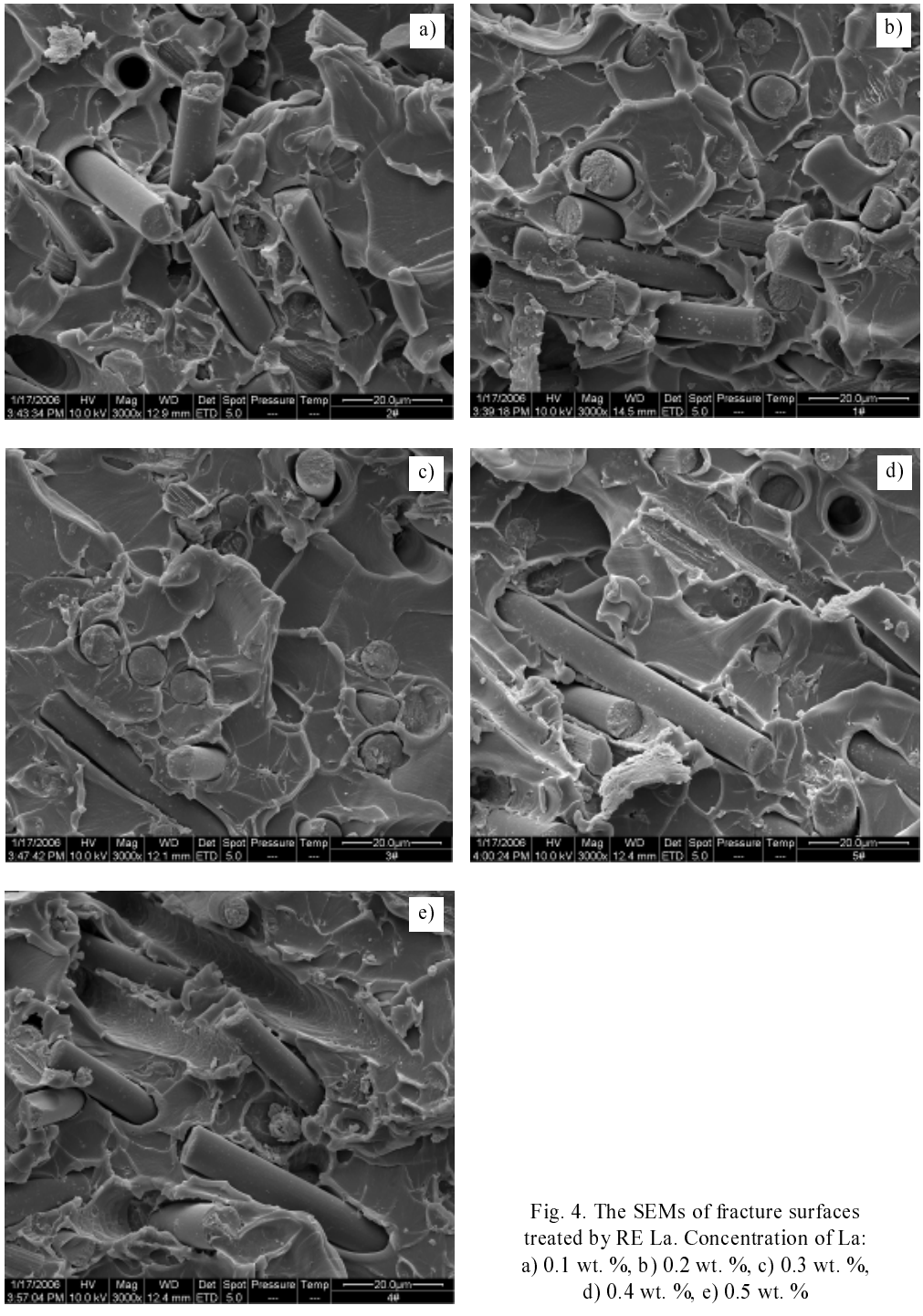

Fig. 4. The SEMs of fracture surfaces treated by RE La. Concentration of La: a) 0.1 wt. %, b) 0.2 wt. %, c) 0.3 wt. %, d) 0.4 wt. %, e) 0.5 wt. %

According to the tensile experimental results, the concentration of La was fixed at 0.3 wt. %, while a comparison between RE treatment and air-oxidation was made as shown in Fig. 5. It can be seen that although, both surface treatments improve the tensile properties of CF/PI composites, carbon fibres treated with RE yielded better results than the air-oxidized ones. The tensile strengths of CF/PI composites treated with RE and air-oxidation were improved by about 18.2% and 4.1%, respectively, compared to the untreated composite. The tensile modulus of the composite treated with the RE method had the highest value. Since the fibre types and fibre contents are identical in these specimens, the differences between the tensile properties shown in Fig. 5 must reflect the effects of the various treatment methods.

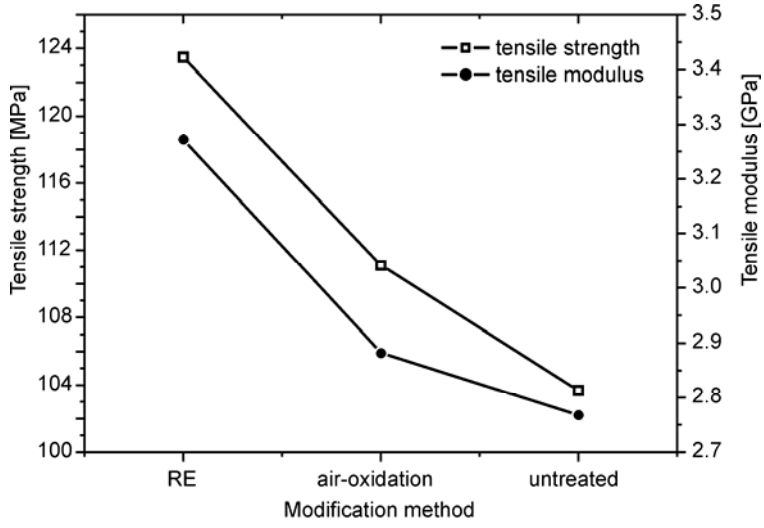

Fig. 5. The influence of the modification method on tensile properties

The details of the fracture surfaces are shown in Fig. 6. Figure 6a shows that the untreated carbon fibres are smooth and large gaps exist between the fibres and resin, which causes poor adhesion between the reinforcement and matrix, with obvious holes are scattered among the matrix. The fractures of the air-oxidized carbon fibres shown in Fig. 6b are rough due to the damage during the oxidation process. Small gaps can still be seen between the fibres and resin. The fractures of carbon fibres formed sharp slants, since the breaks on the carbon fibres introduced by air-oxidation caused non-uniform stress during tension. Air-oxidation mainly increases the surface functional groups of carbon fibres and roughness in order to improve the adhesion ability of the interface, which will do damage to the carbon fibre. The generation of voids and defects at interfaces affects the load transfer between the fibre and matrix, and finally affects the tensile properties of the composites. RE treatment, however, does no damage to the carbon fibres. The fracture shown in Fig. 6c is a flat surface compared to the one mentioned above. The carbon fibres on the fracture surface are

short and broken along with the matrix, without leaving holes, which shows that the matrix and reinforcement a strongly adhered together.

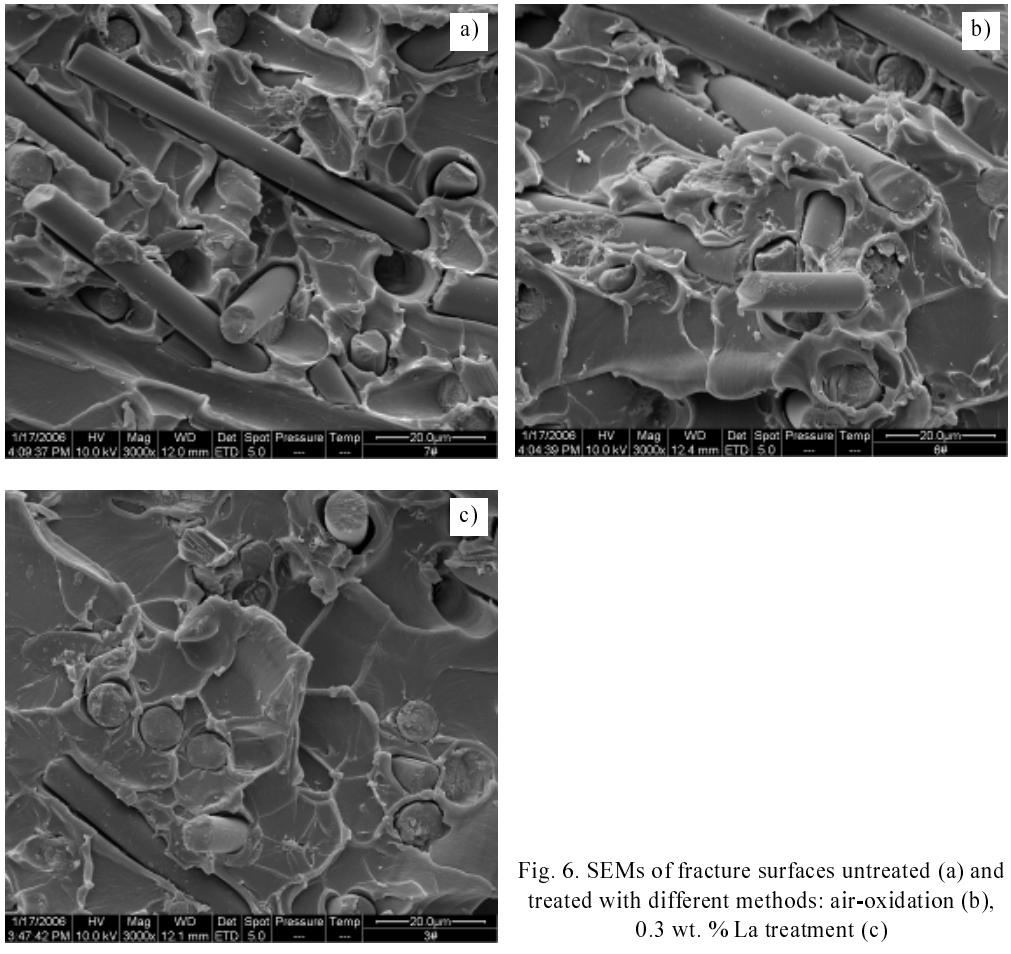

Fig. 6. SEMs of fracture surfaces untreated (a) and treated with different methods: air-oxidation (b), 0.3 wt. % La treatment (c)

4. Conclusions

La treatment is superior to air-oxidation in promoting interfacial adhesion between carbon fibre and the TPI matrix. The tensile properties of RE-treated CF/PI composites are affected by the La concentration in solution. The tensile properties of the CF/PI composite can be improved considerably when La concentration is in the range 0.2–0.4 wt. %. The optimum amount of La is 0.3 wt. %.

Acknowledgements

The authors would like to thank Professor Huang Pei, Nanjing University of Technology, for providing preparation of specimens in this study. The help of the Instrumental Analysis Center, Shanghai

Jiaotong University with optical microscopy is also appreciated. Financial support for this work was provided by the National Natural Science Foundation of China (No. 50275093).

References

[1] FUSARO R.L., Tribology Trans., 31 (1987), 174.
[2] TEWARI U. S., BIJWE J., Composites, 22 (1991), 204.
[3] JANG J., YANG H., J. Mater. Sci., 35 (2000), 2297.
[4] HUANG Y.D., QIU J. H., LIU L.X., ZHANG Z.Q., J. Mater. Sci., 38 (2003), 759
[5] XUE Y.J., CHENG X. H., J. Mater. Sci. Lett., 20 (2001), 1729.
[6] CHENG X. H., XUE Y.J., J. Rare Earths., 19 (2001), 238.
[7] WU J., CHENG X. H., XIE C. Y., J. Mater. Sci., 39 (2004), 289.
[8] YANG Y.G., HE F., WANG M.Z., LI Z. J., ZHANG B.J., Carbon Technol. (in Chinese), 6 (1997), 12.

Received 18 January 2006

Materials Science-Poland, Vol. 25, No. 1, 2007

PTFE encapsulation for pentacene based organic thin film transistors*

C. PANNEMANN[1**], T. DIEKMANN[1], U. HILLERINGMANN[1], U. SCHÜRMANN[2], M. SCHARNBERG[2], V. ZAPOROJTCHENKO[2], R. ADELUNG[2], F. FAUPEL[2]

[1]University of Paderborn, Department EIM-E/Sensorik, Warburger str. 100, D-33098 Paderborn

[2]University of Kiel, Chair for Multicomponent Materials, Technical Faculty, Kaiserstr. 2, D-24143 Kiel

Unprotected organic devices suffer from degradation due to water and oxygen incorporation. To validate the function of organic thin film transistor capsulation, interdigital transistor structures (W/L = 16 830 and W/L = 23 400) were prepared on p-type silicon wafers, and a high current was driven (initially up to –15 mA and –6.8 mA, respectively, at $-40V_{DS}$, $-40V_{GS}$) in order to detect their explicit reactions to degradation. Subsequently, the OTFT active layer was encapsulated with 1.5 μm of sputtered polytetrafluoroethylene (PTFE). The degradation experiment for 4 months in dark laboratory conditions revealed reduced degradation compared to earlier experiments using thinner protection films. During the experiment, the threshold voltage shifted in the positive direction, suggesting degradation only due to oxygen. Obviously, degradation due to humidity was blocked, as it would have caused a negative threshold voltage shift.

Key words: *pentacene; OTFT; interdigital structure; degradation; encapsulation*

1. Introduction

Organic semiconductor materials such as small-molecule pentacene provide many advantages when used in electronic devices. They are cheap, easily processed at relatively low temperatures [1, 2], and allow the use of flexible substrates [3, 4]. In contrast, the degradation of organic semiconductor materials is still an unsolved problem. The electrical properties of organic thin film transistors (OTFT) suffer from contact with oxygen, humidity, and UV light. Calculations have revealed a high probability of oxygen-forming a stable chemical bond with the middle ring of pentacene in a reaction leading to pentacenequinone [5]. Embedded in a crystalline pentacene film, this

---

*The paper presented at the 5th International IEEE Conference on Polymers and Adhesives in Microelectronics and Photonics, Wrocław, Poland, 23–26 October, 2005.

**Corresponding author, e-mail: pannemann@sensorik.uni-paderborn.de

molecule serves as a scattering (trapping) centre for charge carriers in the OTFT channel [6] and would affect the electrical performance of the device, i.e. reduce the on-current, decrease the on-off ratio, and shift the threshold voltage in positive direction [7]. Humidity is incorporated in the organic film from ambient air while the transistor is operating. Driven by the electrical field induced by the operating voltages at the drain and gate, water molecules dissociate and attach to the grain boundaries of the pentacene layer and to the dielectric interface [6]. At the grain boundaries, trapping states and disturbing potential walls are generated, resulting in a decrease of charge carrier mobility.

Accumulated at the dielectric interface of the OTFT, water molecules cause a threshold voltage shift in the negative direction. A degradation experiment with unprotected OTFTs kept in dark laboratory conditions for a period of 9 months (ambient air, room temperature) revealed a decrease in the on-current of one order of magnitude per quarter of a year [8]. Meanwhile, the threshold voltage shifted from the value of 4.8 V to –8 V. After the investigation period, the OTFT still showed typical output and transfer characteristics, however the electrical parameters had been strongly affected. Even if OTFTs are intended for use in short term applications, the operational lifetime should reside in a period of several months in order to guarantee the secure functioning of the organic circuits. To extend transistor shelf life, an encapsulation of the organic film against environmental effects seems to be essential. Lee et al. [9] have proposed a lamination process with an Al film, which, however, still needs an additional insulation layer to prevent shortcuts between the drain- and source-contacts. The deposition of additional layers on the pentacene in the channel area of an OTFT must be carried out very prudently, as the morphological structure of the organic film can be impaired. This letter presents a sputtering procedure with polytetrafluoroethylene (PTFE) at a low deposition rate and sputtering energy for encapsulating the pentacene film.

Organic field-effect transistors were prepared using two layouts. Small transistors with $W = 1000$ μm and $L = 1$ μm were fabricated to investigate the influence of oxygen plasma treatment on pentacene film formation during organic semiconductor evaporation. Interdigital structures with $W = 46.8$ cm and $L = 20$ μm, as well as $W = 16.83$ cm and $L = 10$ μm, were integrated for testing PTFE capsulation. These should drive a large current and a clear reaction should be detected due to external effects, and they should still provide a measurable current after months of degradation.

2. Experimental

Bottom contact OTFTs (Fig. 1) were fabricated on p-type silicon substrates instead of polymeric substrate materials for the degradation experiments, in order to exclude side effects from the unintended degradation of the substrate. The gate oxide layer was grown by thermal oxidation at 960 °C up to a thickness of 150 nm, determined by laser ellipsometry. Subsequently, the drain and source contacts were defined

using UV contact photolithography and lift-off in acetone. The drain and source contacts consisted of a thin (8 nm) nickel layer and nearly 80 nm of gold, while the sub

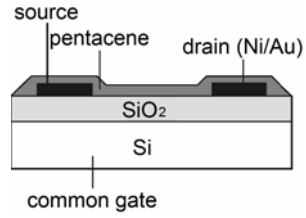

Fig. 1. Cross-section of an OTFT based on a silicon substrate using the organic semiconductor pentacene

strate served as the common gate contact. Previously to the thermal evaporation of up to 30 nm of pentacene at 6×10^{-7} mbar, the wafers were treated in oxygen plasma for 30 s at low power (100 W). This was done to prepare the dielectric surface for pentacene deposition and to remove residual resist at the contact edges. By this treatment, the diameter of the pentacene crystallites was increased from 250 nm (on untreated silicon oxide) to nearly 1 μm (on the treated wafer) as confirmed by AFM (Fig. 2).

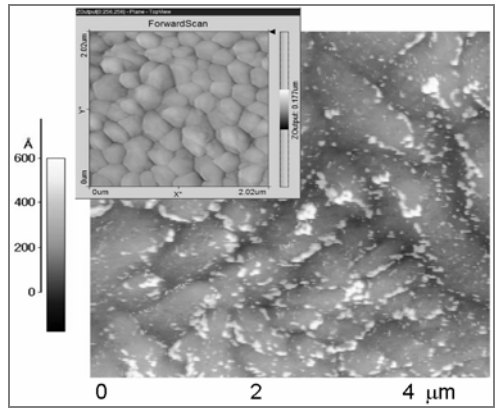

Fig. 2. Large grains of pentacene on SiO_2 treated with oxygen plasma (AFM image, contact mode). Inset: small grains of pentacene evaporated on an untreated dielectric. Both images have the same scale

Finally, after the first electrical characterization an interdigitally structured OTFT (W/L = 23 400) was encapsulated with a sputtered layer of 1.5 μm PTFE. The deposition rate was as low as 21 nm/min and the circular gradient was below 10%. A detailed description of the experimental conditions and deposition technique are given elsewhere [10]. All electrical characterizations were carried out in a shielded metal box in dark laboratory conditions with a HP 4156A semiconductor parameter analyzer.

3. Results and discussion

One of the main advantages of photolithographically defined OTFTs is the high geometrical reproducibility of fabricated structures. Compared to earlier experiments [7, 8], a uniform distribution of electrical parameters was now achieved, introducing a tight feed-

back of favourable preparation conditions to the fabrication process. The distribution of threshold voltages on a 100 mm wafer showed a strongly emphasized Gaussian peak at (1.3±1.44) V for a small OTFT geometry of W = 1000 μm and L = 1 μm (Fig. 3).

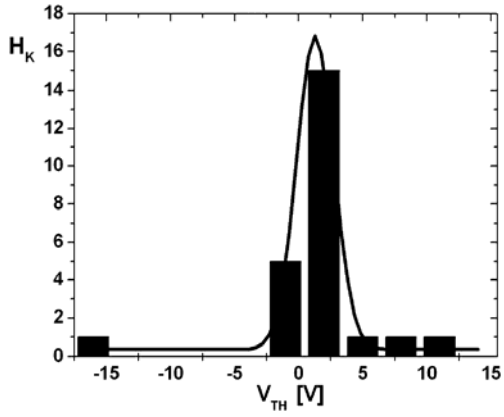

Fig. 3. Distribution of threshold voltages measured for photolithographically structured OTFTs (W = 1000 μm, L = 1 μm) on a 100 mm wafer. The pentacene was thermally evaporated on a SiO_2 dielectric without previous oxygen plasma treatment. The final thickness of pentacene was 30 nm

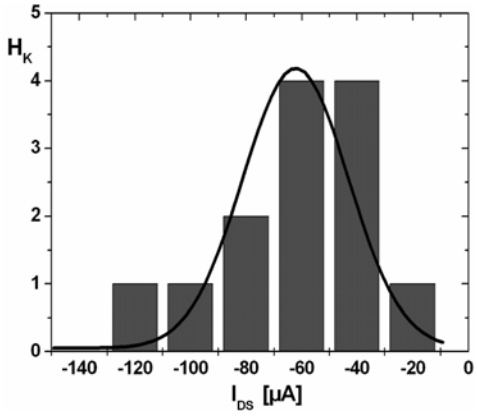

Fig. 4. Distribution of the on-currents measured at $-40V_{DS}$ and $-40V_{GS}$ for OTFTs with W = 1000 μm and L = 1 μm, providing a pentacene layer of 30 nm

The maximum on-current at $-40V_{DS}$ and $-40V_{GS}$ for these devices was measured to be as large as –(63.3±17) μA (Fig. 4). By introducing oxygen plasma treatment of the gate dielectric layer before pentacene deposition, the on-current of a comparable OTFT structure was enhanced up to –644 μA for $-80V_{DS}$ and $-25V_{GS}$. An inspection of the pentacene surface using an atomic force microscope confirmed large pentacene grains in the transistor channel, compared to smaller grains of the untreated pentacene film (Fig. 2). This results in a decreased number of grain boundaries and traps across the channel. Unfortunately, the increase in the on-current was accompanied by a large positive threshold voltage of 15.9 V. This is attributed to the plasma treatment, which leaves behind plenty of trapping states at the dielectric interface. In a preliminary encapsulation experiment, the above stated OTFT (I_{DS} = –644 μA) was coated with a thin PTFE layer 20 nm thick. As a result of the high power sputtering process, however, the transistor exhibited a strong decrease in electrical parameters, as the pentacene film was obviously affected by the PTFE deposition. OTFTs with a larger W/L ratio were then structured with the intention of supplying a measurable current in the following degradation experiment.

Interdigitally structured OTFT with the W/L ratio of 16 830 was prepared and characterized directly after pentacene deposition. The on-current was found to be as large as –15 mA for $-40V_{DS}$ and $-40V_{GS}$ (Fig. 5), due to the large W/L ratio. The threshold voltage was extracted from the square root current of the transfer character-

istic (Fig. 6). This remained at a rather high value of 7 V due to the above mentioned trapping states induced by the plasma treatment and to a large channel area, which provides numerous free charge carriers inhibiting the depletion of the channel. As a result of the large threshold voltage, the calculated charge carrier field effect mobility was 2.6×10^{-2} cm^2/(V·s).

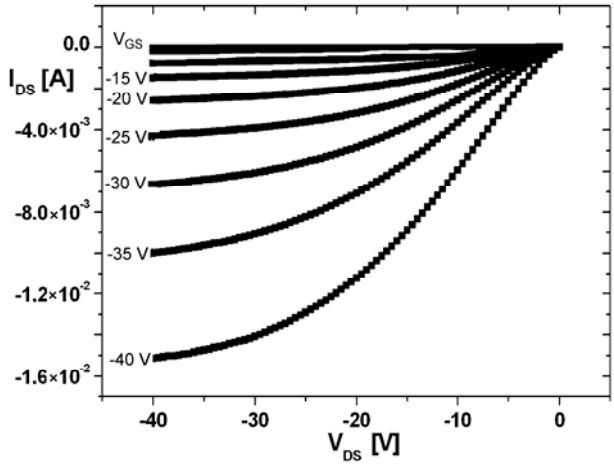

Fig. 5. I_{DS}–V_{DS} characteristics of an OTFT with W = 16.83 cm and L = 10 μm, providing a 30 nm pentacene layer, evaporated at 6×10^{-7} mbar on a substrate cleaned with oxygen plasma

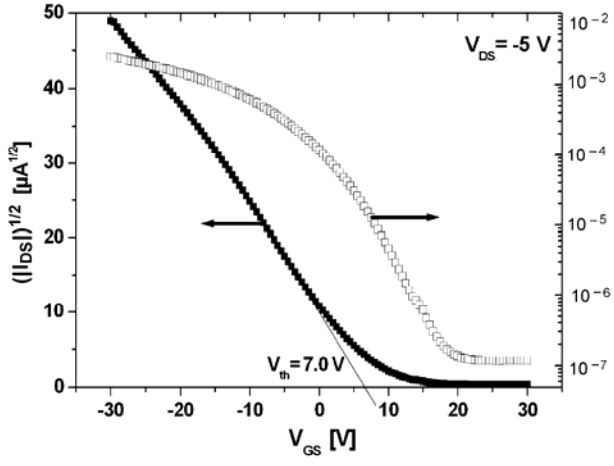

Fig. 6. I_{DS}–V_{GS} characteristics of the same OTFT as in Fig. 5. An on-off ratio of more than 10^4 and a threshold voltage of 7 V can be extracted from the transfer curve

Another interdigital OTFT structure (W/L = 23 400) was prepared for the degradation experiment. The transistor maximum on-current was determined to be as large as –6.8 mA and the threshold voltage was 12.3 V before the pentacene was covered with PTFE. After sputtering 1.5 μm of PTFE onto the surface of the interdigital OTFT

structure at low power, the initial values of the electrical parameters for the degradation experiments were measured (I_{DS} = –6.2 mA, V_{TH} = 13.2 V). This characterization was repeated periodically after 1 month of degradation.

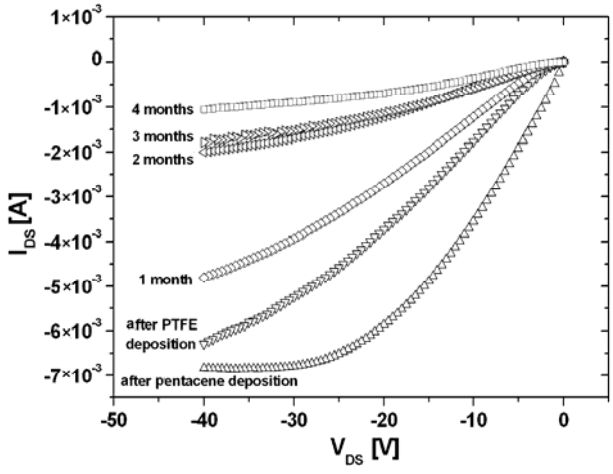

Fig. 7. I_{DS}–V_{DS} characteristics at $-40V_{GS}$ for an OTFT with W/L = 23 400 using a nearly 30 nm thick pentacene layer. The measurements were carried out directly after pentacene evaporation, PTFE deposition, and in intervals of 1 month for a period of 4 months, and represent the reduction of the on-current due to degradation. As a second reaction to the degradation experiment, the contact resistance was influenced, which can be deduced from the bending of the characteristics in the linear region

In Figure 7, one can see the time-dependent behaviour of the transistor on-current at $-40V_{GS}$. For the first 2 months of degradation the on-current was reduced significantly (–4.7 mA, –1.9 mA), but the rate of the degradation seemed to slow down at least after 3 months of investigation (–1.7 mA, –1.1 mA). Earlier experiments revealed a decrease in the OTFT on-current of one order of magnitude per quarter of a year for an unprotected pentacene layer stored in comparable conditions [8]. In the current experiment, a strong degradation of the transistor parameters was obviously inhibited by the PTFE layer. Nevertheless, the threshold voltage shifted from an initial value of 13.2 V directly after sputtering to 18.2 V (after 1 month) and 23.2 V (after 4 months). This threshold voltage shift cannot be neglected but one has to keep in mind that the initial value was rather high. As the PTFE layer is hydrophobic in character, it protects the pentacene from reacting with humidity. Oxygen can still diffuse through the encapsulation and cause threshold voltage shift. As reported elsewhere, oxygen induces a positive threshold voltage shift in organic field effect transistors [7]. The effect of humidity on the degradation of transistor parameters, however, is much larger and would evoke a negative shift in the threshold voltage as reported before [8].

Even if the required shelf life of organic circuits in single-use applications is rather limited, the secure functioning of OTFTs must be guaranteed. PTFE films may be recommended as capsulation layers on pentacene transistors to prevent degradation by humidity and to enhance the shelf life of transistors.

4. Conclusions

This paper reports a reproducible fabrication of organic field effect transistors, using photolithography to structure the devices and thermally evaporated pentacene films as the organic semiconductor. Oxygen plasma was applied to clean the dielectric surface before the deposition of pentacene and to ensure large organic crystallites in the transistor channel. With this treatment, the maximum on-current of the transistor was notably enhanced. Interdigital OTFT structures with a W/L ratio of 23 400 were prepared for the degradation experiments. The pentacene layer was encapsulated with 1.5 μm of PTFE and stored for 4 months in laboratory conditions. The on-current at $-40V_{DS}$ and $-40V_{GS}$ was reduced from an initial value of –6.2 mA to –1.1 mA after 4 months of degradation. Compared to unprotected samples, the rate of degradation was strongly reduced. A positive threshold voltage shift occurred, indicating that humidity can be excluded as a degradation factor. Oxygen may have diffused through the PTFE layer. Earlier experiments revealed a positive threshold voltage shift due to the presence of oxygen.

Acknowledgements

The authors acknowledge the Fraunhofer Insitute (IPMS), Dresden, for providing purified pentacene and the German founding institution DFG for financial support (AD-183/3-2 and Hi-551/7-3).

References

[1] KLAUK H., HALIK M., ZSCHIESCHANG U., EDER F., SCHMID G., DEHM C., Appl. Phys. Lett., 82 (2003), 4175.
[2] BAUDE P.F., ENDER D.A., HAASE M.A., KELLEY T.W., MUYRES D.V., THEISS S.D., Appl. Phys. Lett., 82 (2003), 3964.
[3] EDER F., KLAUK H., HALIK M., ZSCHIESCHANG U., SCHMID G., DEHM C., Appl. Phys. Lett., 84 (2004), 2673.
[4] SEKITANI T., KATO Y., IBA S., SHINAOKA H., SOMEYA T., SAKURAI T., TAKAGI S., Appl. Phys. Lett., 86 (2005), 073511.
[5] NORTHRUP J.E., CHABINYC M.L., Phys. Rev. B, 68 (2003), 041202(R).
[6] JURCHESCU O.D., BAAS J., PALSTRA T.T.M., Appl. Phys. Lett., 84 (2004), 3061.
[7] PANNEMANN C., DIEKMANN T., HILLERINGMANN U., Proc. of the 16th International IEEE Conf. on Microelectronics ICM 2004, ISBN: 0-7803-8656-6, IEEE Catalog Number: 04EX918 (2004), p. 79.
[8] PANNEMANN C., DIEKMANN T., HILLERINGMANN U., J. Mater. Res., 19 (2004), 1999.
[9] LEE J.H., KIM G.H., KIM S.H., LIM S.C., YANG Y.S., YOUK J.H., KANG J., ZYUNG T., Synth. Metals, 143 (2004), 21.
[10] SCHÜRMANN U., HARTUNG W.A., TAKELE H., ZAPOROJTCHENKO V., FAUPEL F., Nanotechnology, 16 (2005), 1078.

Received 23 January 2006
Revised 14 May 2006

Materials Science-Poland, Vol. 25, No. 1, 2007

Polishing of poly(methyl methacrylate), polycarbonate, and SU-8 polymers*

Z.W. ZHONG [1**], Z.F. WANG [2], B.M.P. ZIRAJUTHEEN [1], Y.S. TAN [1], Y.H. TAN [1]

[1]School of Mechanical and Aerospace Engineering, Nanyang Technological University, 50 Nanyang Avenue, Singapore 639798

[2]Singapore Institute of Manufacturing Technology, 71 Nanyang Drive, Singapore 638075

Polymers such as poly(methyl methacrylate), polycarbonate, and SU-8 epoxy resin replace silicon as the major substrate in microfluidic system (or BioMEMS) fabrication. Chemical-mechanical polishing is an important technology for many advanced microelectromechanical systems (MEMS) and micro-optoelectromechanical system applications. In this study, the chemical-mechanical polishing of polycarbonate, poly(methyl methacrylate), and SU-8 polymers was investigated. Four types of slurry were tested for chemical-mechanical polishing of polycarbonate and poly(methyl methacrylate). Experiments were then designed and performed to investigate the effects of two key process parameters. Experimental results show that an increase in head load or table speed causes an increase in material removal rates. Within the chosen experimental parameter ranges, the variation of table speed introduced a more significant change in material removal rates than that of head load. An analysis of variance was also carried out, and it was found that the interaction of head load and table speed had a significant effect (95% confidence) on the surface finish of polished poly(methyl methacrylate) samples, while table speed had a significant effect on the surface finish of polished polycarbonate samples. Chemical-mechanical polishing is also a process well suited for polishing SU-8 structures with high aspect ratios. Polished polycarbonate, poly(methyl methacrylate), and SU-8 surfaces had nanometer-order surface roughness, acceptable for most MEMS applications.

Key words: *polymer; MEMS; chemical-mechanical polishing; surface finish; material removal rate*

1. Introduction

Although there are issues affecting the use of the technology [1], chemical-mechanical polishing has become a leading planarisation technique in the manufacturing of advanced integrated circuit chips [2]. As semiconductor chips are highly inte-

---

*The paper presented at the 5th International IEEE Conference on Polymers and Adhesives in Microelectronics and Photonics, Wrocław, Poland, 23–26 October 2005.

**Corresponding author, e-mail: mzwzhong@ntu.edu.sg

grated and multi-layer electro-wired, more precise planarisation of each layer on chips is needed [3]. With decreasing device dimensions, inter-level dielectric planarisation by chemical-mechanical polishing is necessary for technologies beyond the 0.35 μm CMOS generation [4]. Chemical-mechanical polishing has emerged as the preferred manufacturing process for planarising sub-micron multi-level metal layers in integrated circuits [5, 6]. It is also adopted in microelectromechanical system (MEMS) applications [7].

Compared to silicon dioxide, polymers excel due to their relatively low dielectric constants, minimized interconnection delays, and improved conductor packaging densities [5]. A low dielectric constant, gap filling at high aspect ratios, and global planarisation are challenging demands for dielectrics in conventional multilevel metallisation schemes in modern integrated circuit technologies [8]. Novel integrated circuit devices based on low-*k* material/Cu structures have been proposed recently using the chemical-mechanical polishing technology [9]. Deep scratches at surfaces of low-*k* organic layers have been observed when the surfaces are polished mechanically, and thus reduction of scratches is required in advanced chemical-mechanical polishing processes [10].

Silicon [11] and glass have traditionally been the two major materials used in MEMS. Many biomedical devices, however, require polymers such as polycarbonate and polyimide, which provide a more suitable interface with biological tissue [12]. Imprinting techniques can be used to fabricate microfluidic devices on poly(methyl methacrylate) substrates [13]. In microfluidic applications, important material properties include machinability, surface charge, molecular adsorption, electroosmotic flow mobility, and optical properties [14].

One polishing condition of chemical-mechanical polishing can make a large difference in the material removal rates of different processes [15]. Chemical-mechanical polishing may also introduce surface defects and thus increase the demand for automatic defect-detection techniques [16]. It is extremely difficult to analyse its polishing mechanisms [17, 18]. Therefore, a large number of experiments are required for each set of process conditions [19].

Conventionally, poly(methyl methacrylate) resists are patterned by electron beam lithography, followed by appropriate pattern transfer techniques. The sensitivity of poly(methyl methacrylate) resists is low, however, limiting exposure speed and throughput. To extend high resolution writing ability, other types of resists with higher electron beam sensitivity have been explored [20]. SU-8 is used mostly for high aspect ratio MEMS applications on thick resist layers using ultraviolet or X-ray illumination [21].

SU-8 is a high contrast, epoxy-based photoresist for micromachining applications, where a thick, chemically, and thermally stable image is desired [22]. By using a faster drying and more polar solvent systems, improved coating properties and higher throughput are realized. The exposed and subsequently cross-linked portions of the film are rendered insoluble to liquid developers [23]. SU-8 is over two orders of magnitude more sensitive to X-ray radiation than poly(methyl methacrylate), and the

accuracy of the SU-8 microstructures fabricated by deep X-ray lithography is superior to ultraviolet lithography and comparable to poly(methyl methacrylate) structures [24]. The good pattern quality together with high sensitivity offers rapid prototyping and direct lithographic capability. High sensitivity, fairly good adhesion properties, and relatively simple processing of SU-8 make it a good substitution for novolac-based chemically amplified negative e-beam resists in optical mask manufacturing [25].

Chemical-mechanical polishing of polycarbonate, poly(methyl methacrylate), and SU-8 polymers was investigated in this study. Four types of slurry were tested. Chemical-mechanical polishing experiments were then designed and performed to investigate the effects of key process parameters on material removal rates and the surface finish of polycarbonate and poly(methyl methacrylate) substrates. Patterned and non-patterned SU-8 samples were prepared using the negative photolithography process, and the chemical-mechanical polishing of SU-8 was also investigated.

2. Chemical-mechanical polishing experiments

Poly(methyl methacrylate) and polycarbonate substrates were cut into 2 mm thick round plates with the diameter of 150 mm. Chemical-mechanical polishing experiments were carried out with an Okamoto SPP-600S polishing machine. A SUBA 800 polishing pad was used for the experiments. Four types of slurry, such as ILD1200, Simlox, Mazin SRS1, and SRS3, were evaluated for polishing poly(methyl methacrylate) and polycarbonate. ILD1200 is fumed silica polishing slurry containing ammonium hydroxide, designed for oxide chemical-mechanical polishing. Mazin SRS1 and SRS3 are colloidal silica polishing slurries for stock removal applications. Simlox is a type of slurry specially designed for removing polymers. Throughout the chemical-mechanical polishing experiments, the slurry flow rate was set to 100 cm^3/min, the spindle rotation speed was kept at 40 rpm, and the oscillation speed – 2 mm/sec. Two key process parameters, head load and table speed, were varied to examine their effects on the quality and efficiency of polishing poly(methyl methacrylate) and polycarbonate.

Before and after polishing, the thicknesses of the polymer workpieces were measured using a head thickness gauge to compute the material removal rate, which was defined as thickness reduction per minute in this study. After polishing, the surface roughness of workpieces was measured using a profilometer. The average roughness height R_a, one of the most commonly used roughness parameters, was used to represent the surface roughness.

The SU-8 material was spin-coated on silicon wafers under proper conditions to produce low defect coatings. The thickness of the resist was approximately 25 μm after the spin-coating process. Soft-baking was carried out on hot plates with two different temperatures to remove the solvents from the photoresist coating, which became photosensitive after soft-baking. The mask was aligned with the wafer so that the pattern could be transferred onto the wafer surface. The photoresist was exposed

through the pattern on the mask with high-intensity ultraviolet light. The wafer was then exposed for 30 sec. Post-expose baking was carried out on a hot plate to cross-link the exposed portions of the film. The parameters used to polish SU-8 were: table speed – 30 rpm, head load – 100 g/cm^2, slurry flow rate – 100 cm^3/min, spindle rotation speed – 50 rpm, and oscillation speed – 2 mm/sec. Mazin SRS3 was used as the slurry for polishing SU-8.

A scanning electron microscope and an atomic force microscope were used to analyse the polished surfaces. Hardness tests were performed on a Vickers hardness tester to measure and compare the hardness of examined materials.

3. Experimental results

Figure 1 shows the results of hardness tests of the polymers. The SU-8 resist is more than twice harder than the poly(methyl methacrylate) and polycarbonate materials. Hardness is the property of being rigid and resistant to pressure. With higher hardness, SU-8 is also more resistant to be scratched than poly(methyl methacrylate) or polycarbonate.

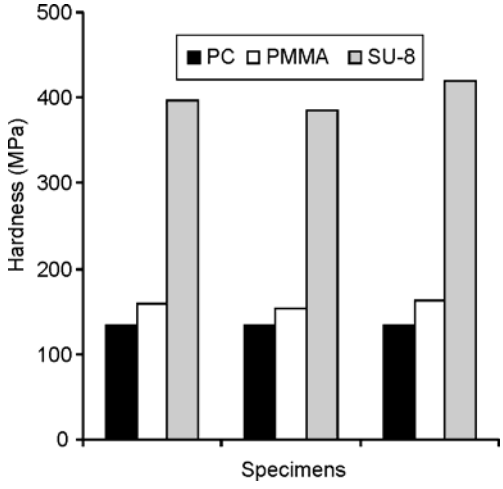

Fig. 1. Hardness of poly(methyl methacrylate) (PMMA), polycarbonate (PC), and SU-8

Since poly(methyl methacrylate) samples are harder than polycarbonate, after chemical-mechanical polishing they have shallower scratches and thus better surface finish than polished polycarbonate samples.

As shown in Fig. 2, the smoothest poly(methyl methacrylate) and polycarbonate surfaces were obtained by chemical-mechanical polishing using Simlox, which also produced relatively high material removal rates. Therefore, it was selected to be the slurry for polishing poly(methyl methacrylate) and polycarbonate, and was used to evaluate the effects of key process parameters.

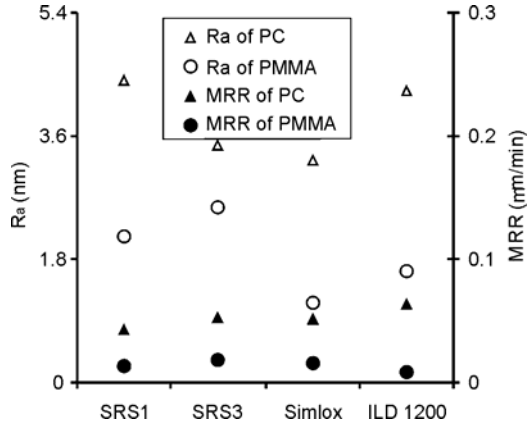

Fig. 2. Surface roughness R_a and material removal rate (MRR) of poly(methyl methacrylate) (PMMA) and polycarbonate (PC) polished using four types of slurry

Two process parameters, head load and table speed, were investigated for polishing poly(methyl methacrylate) and polycarbonate substrates, while the other conditions were fixed. Three levels (low, median, and high) for each parameter were assigned: 20, 30, and 40 rpm for table speed, and 75, 100, and 125 g/cm^2 for head load, in order to limit the number of experiments. 100 g/cm^2 head load and 30 rpm table speed are polishing conditions commonly used with the Okamoto SPP-600S chemical-mechanical polishing machine for typical applications. 20 and 40 rpm for table speed, and 75 and 125 g/cm^2 for head load were additionally chosen being low and high factor levels, respectively, in order to investigate the effects of the two key process parameters.

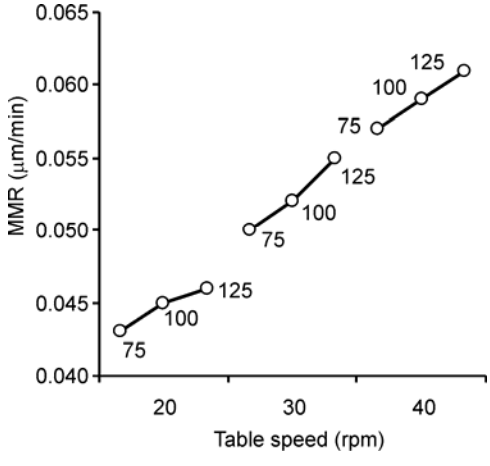

Fig. 3. Effects of head load and table speed (in g/cm^2) on the material removal rates (MRRs) of polycarbonate

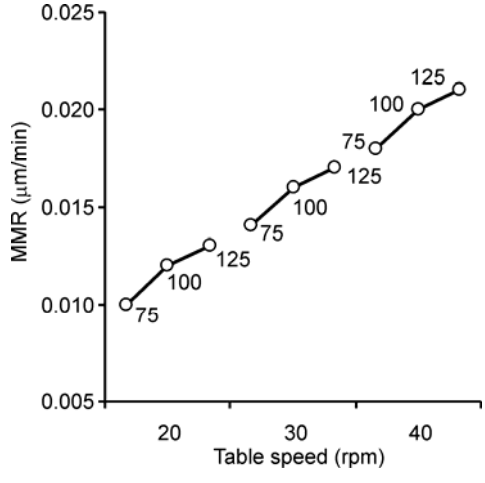

Fig. 4. Effects of head load and table speed (in g/cm^2) on the material removal rates (MRRs) of poly(methyl methacrylate)

Figures 3 and 4 show the effects of head load and table speed on the material removal rate in polishing polycarbonate and poly(methyl methacrylate), respectively.

Material removal rates increase for increased head load and table speed. These results approximately agree with the Preston equation [1], which theoretically expresses that the material removal rate is proportional to the pressure applied to the workpiece. Another trend revealed from Figs. 3 and 4 was that within the chosen experimental parameter ranges, the variation of table speed introduced a more significant change in material removal rate than that of head load. Since polycarbonate is softer than poly(methyl methacrylate), its material removal rate is higher than that of poly(methyl methacrylate).

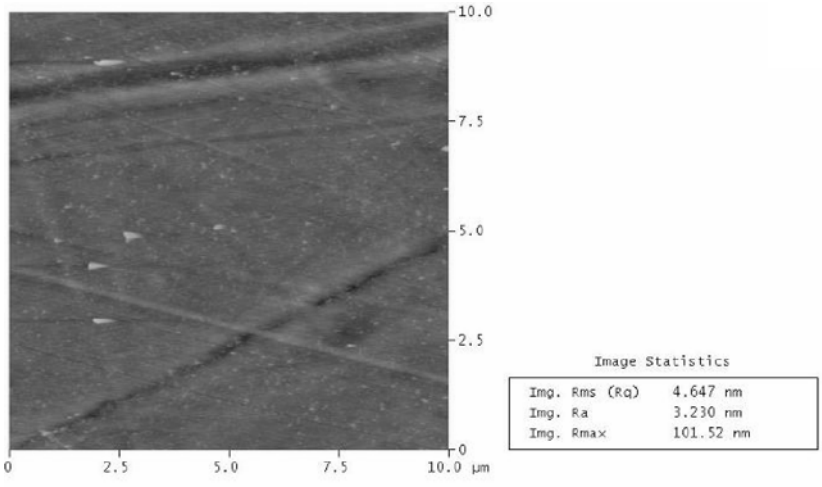

Fig. 5. Atomic force microscope image of polycarbonate polished with a table speed of 30 rpm and head load of 100 g/cm^2

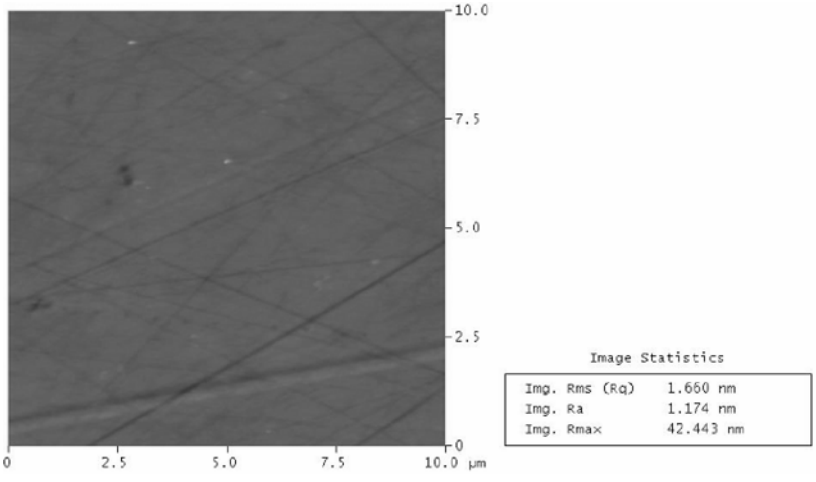

Fig. 6. Atomic force microscope image of poly(methyl methacrylate) polished with a table speed of 30 rpm and head load of 100 g/cm^2

Figures 5 and 6 show examples of atomic force microscope images of polished polycarbonate and poly(methyl methacrylate), respectively. In order to draw any conclusions whether there were any significant effects of head load and table speed on the surface roughness of polished poly(methyl methacrylate) and polycarbonate, an analysis of the variance (ANOVA) of two-factor factorial experiments was carried out using the measured surface roughness values. Tables 1 and 2 are the ANOVA tables for polished polycarbonate and poly(methyl methacrylate), respectively.

Table 1. ANOVA table for polished polycarbonate

Source of variation	Sum of squares (nm^2)	Degrees of freedom	Mean square (nm^2)	F value
Factor A: head load	2.35	2	1.18	0.87
Factor B: table speed	22.79	2	11.40	8.44
Interaction of A and B	10.23	4	2.56	1.90
Error	12.18	9	1.35	
Total	47.55	17		

Table 2. ANOVA table for polished poly(methyl methacrylate)

Source of variation	Sum of squares (nm^2)	Degrees of freedom	Mean square (nm^2)	F value
Factor A: head load	0.68	2	0.34	0.47
Factor B: table speed	0.50	2	0.25	0.35
Interaction of A and B	12.53	4	3.13	4.35
Error	6.47	9	0.72	
Total	20.18	17		

Table 3. Effects of the factors (critical F values: $F_{0.05,2,9} = 4.26$ and $F_{0.05,4,9} = 3.63$, for 95% confidence or risk $\alpha = 0.05$)

Factor	Polished material	
	Polycarbonate	Poly(methyl methacrylate)
Head load	No significant effect (F value $0.87 < F_{0.05,2,9}$)	No significant effect (F value $0.47 < F_{0.05,2,9}$)
Table speed	Significant effect (F value $8.44 > F_{0.05,2,9}$)	No significant effect (F value $0.35 < F_{0.05,2,9}$)
Interaction	No significant effect (F value $1.90 < F_{0.05,4,9}$)	Significant effect (F value $4.35 > F_{0.05,4,9}$)

The summary of the ANOVA results is shown in Table 3, in which $F_{0.05,2,9} = 4.26$ and $F_{0.05,4,9} = 3.63$ are the critical F values for 95% confidence (risk $\alpha = 0.05$). Only the interaction of head load and table speed had a significant effect, but individually

head load and table speed had no significant effects on the surface finish of polished poly(methyl methacrylate) samples. Further analysis of the roughness data obtained from atomic force microscope measurements revealed that to obtain smooth poly(methyl methacrylate) surfaces, the table speed of 40 rpm and head load of 75 g/cm^2 should be used. On the other hand, only table speed had a significant effect, but individually head load and the interaction of head load and table speed had no significant effects on surface finish of polished polycarbonate samples. Further analysis of the roughness data obtained from atomic force microscope measurements revealed that to obtain smooth polycarbonate surfaces, the table speed of 20 rpm should be used.

The patterns of the SU-8 resist before and after chemical-mechanical polishing were studied using a scanning electron microscope. To get a better and more accurate view of the profile of the patterned SU-8, the wafer was cross-sectioned and examined under a microscope.

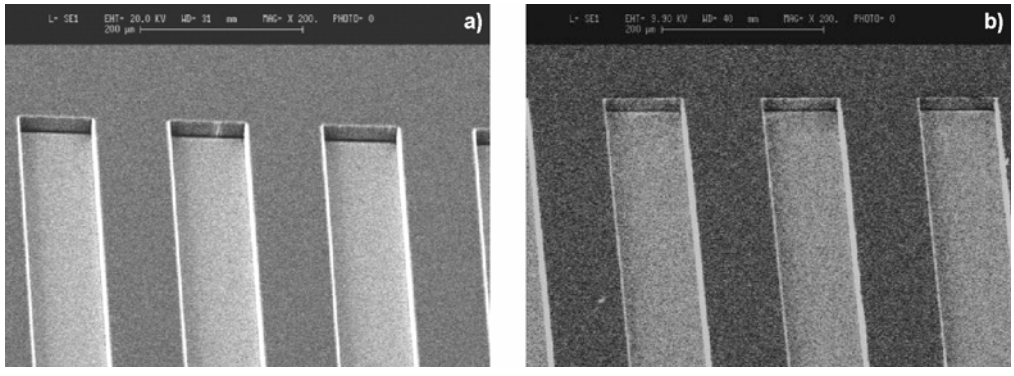

Fig. 7. 100–100 μm channel pattern before (a) and after (b) chemical-mechanical polishing

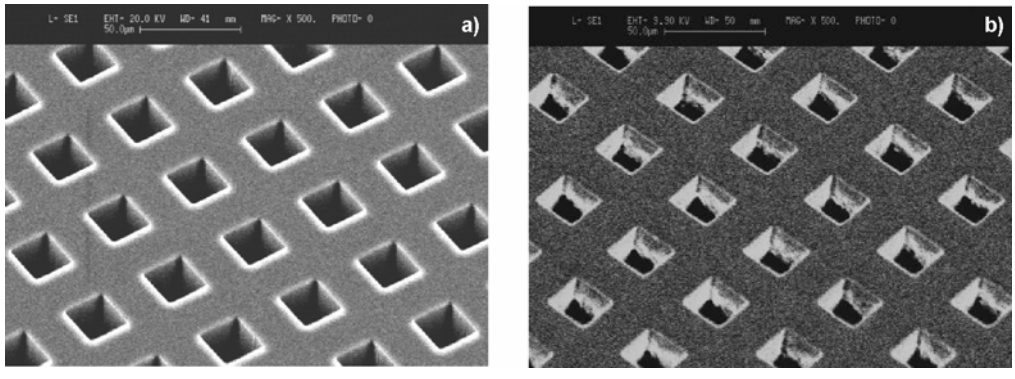

Fig. 8. 25–25 μm pattern before (a) and after (b) chemical-mechanical polishing

Figures 7 and 8 show examples of scanning electron microscope images of SU-8 patterns before and after chemical-mechanical polishing. The shapes of the patterns

were retained after the chemical-mechanical polishing process. Figure 9 shows the cross-section of the patterned SU-8 before and after chemical-mechanical polishing.

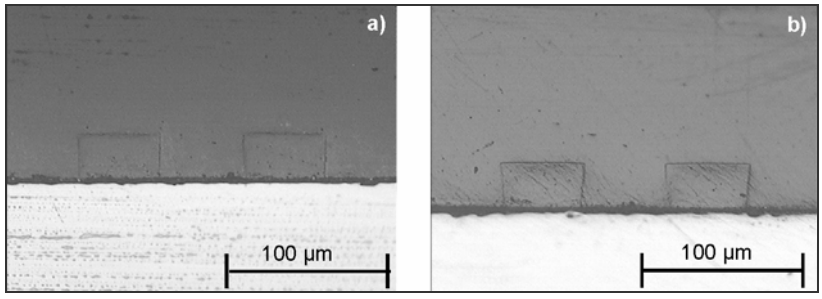

Fig. 9. Cross-section of 50-50-µm channel pattern
before (a) and after (b) chemical-mechanical polishing

The shapes and edges of the patterns were the same before and after the polishing. There was little or no sign of distortions or deformations in the patterns of the SU-8 resist. This shows that the chemical-mechanical polishing is well suited for planarising SU-8.

4. Conclusions

Four types of slurry were tested for chemical-mechanical polishing of polycarbonate and poly(methyl methacrylate) substrates. Experiments were designed and performed, and ANOVA was also carried out to investigate the effects of two key process parameters. The following conclusions could be drawn:

- The smoothest poly(methyl methacrylate) and polycarbonate surfaces were obtained by polishing using Simlox slurry, designed for the removal of polymers, which also produced relatively high material removal rates.
- An increase in head load or table speed causes an increase in material removal rates. Within the chosen experimental parameter ranges, the variation of table speed introduced a more significant change in material removal rates than head load.
- The interaction of head load and table speed had a significant effect on the surface finish of polished poly(methyl methacrylate) samples, while table speed had a significant effect on the surface finish of polished polycarbonate samples. To obtain smooth poly(methyl methacrylate) surfaces, the table speed of 40 rpm and head load of 75 g/cm^2 are recommended. To obtain smooth polycarbonate surfaces, a table speed of 20 rpm is recommended.
- Chemical-mechanical polishing is a process well suited for polishing SU-8 structures. The parameters used to polish SU-8 were: table speed – 30 rpm, head load – 100 g/cm^2, slurry flow rate – 100 cm^3/min, spindle rotation speed – 50 rpm, and oscillation speed – 2 mm/sec. Mazin SRS3 colloidal silica polishing slurry for stock

removal applications was used, because the hardness of SU-8 is more than twice that of poly(methyl methacrylate) or polycarbonate.

• All polished polycarbonate, poly(methyl methacrylate), and SU-8 surfaces had nanometer-order surface roughness heights, acceptable for most MEMS applications.

Acknowledgements

The authors would like to thank Ms. Liu Yuchan of SIMTech for her help and assistance.

References

[1] STEIGERWALD J.M., MURARKA S.P., GUTMANN R.J., *Chem.-Mechanical Planarization of Microelectronic Materials*, Wiley, New York, 1997.
[2] OLIVER M.R., *Chem.-Mechanical Planarization of Semiconductor Materials*, Springer, New York, 2004.
[3] CHO W., AHN Y., BAEK C.-W., KIM Y.-K., Microelectron. Eng., 65 (2003), 13.
[4] VAN DER VELDEN P., Microelectron. Eng., 50 (2000), 41.
[5] KOUROUKLIS C., KOHLMEIER T., GATZEN H.H., Sensors Actuat., A, 106 (2003), 263.
[6] LAI C.L., LIN S.H., Chem. Eng. J., 95 (2003), 205.
[7] DU T., VIJAYAKUMAR A., SUNDARAM K.B., DESAI V., Microelectron. Eng., 75 (2004), 234.
[8] HARTMANNSGRUBER E., ZWICKER G., BEEKMANN K., Microelectron. Eng., 50 (2000), 53.
[9] CHEN W.-C., LIN S.-C., DAI B.-T., TSAI M.-S., J. Electrochem. Soc., 146 (1999), 3004.
[10] HARA T., TOMISAWA T., KUROSU T., DOY T.K., J. Electrochem. Soc., 146 (1999), 2333.
[11] ZHONG Z.W., TOK W.H., Mater. Manufact. Proc., 18 (2003), 811.
[12] ZIAIE B., BALDI A., LEI M., GU Y., SIEGEL R.A., Adv. Drug Deliv. Rev., 56 (2004), 145.
[13] WEIGL B.H., BARDELL R.L., CABRERA C.R., Adv. Drug Deliv. Rev., 55 (2003), 349.
[14] BECKER H., LOCASCIO L.E., Talanta, 56 (2002), 267.
[15] NGUYEN V.H., DAAMEN R., HOOFMAN R., Microelectron. Eng., 76 (2004), 95.
[16] SHANKAR N.G., ZHONG Z.W., Microelectron. Eng., 77 (2005), 337.
[17] LIN Y.-Y., LO S.-P., Int.l J. of Adv. Manufact. Technol., 23 (2004), 644.
[18] LIN Y.-Y., LO S.-P., Int.l J. of Adv. Manufact. Technol., 22 (2003), 401.
[19] HO C.-Y., LIN Z.-C., Int.l J. of Adv. Manufact. Technol., 21 (2003), 10.
[20] BRAINARD R.L., BARCLAY G.G., ANDERSON E.H., OCOLA L.E., Microelectron. Eng., 61–62 (2002), 707.
[21] PEPIN A., STUDER V., DECANINI D., CHEN Y., Microelectron. Eng., 73–74 (2004), 233.
[22] BOGDANOV A.L., PEREDKOV S.S., Microelectron. Eng., 53 (2000), 493.
[23] LORENZ H., DESPONT M., FAHRNI N., BRUGGER J., VETTIGER P., RENAUD P., Sensors Actuat. A: Phys., 64 (1998), 33.
[24] JIAN L., DESTA Y.M., GOETTERT J., BEDNARZIK M., LOECHEL B., JIN Y., AIGELDINGER G., SINGH V., AHRENS G., GRUETZNER G., RUHMANN R., DEGEN R., Proc. SPIE, 4979 (2003), 394.
[25] BOGDANOV A.L., Proc. SPIE, 3999 (2000) 1215.

Received 24 January 2006
Revised 12 May 2006

Materials Science-Poland, Vol. 25, No. 1, 2007

Optimisation of carbon fibres made from commercial polyacrylonitrile fibres using the screening design method

R. ESLAMI FARSANI[1*], S. RAISSI[2], A. SHOKUHFAR[3], A. SEDGHI[4]

[1]Islamic Azad University, South Tehran Branch and Faculty of Mechanical Engineering, K. N. Toosi University of Technology, Tehran, Iran

[2]Industrial Engineering, Islamic Azad University, South Tehran Branch, Tehran, Iran

[3]Faculty of Mechanical Engineering, K. N. Toosi University of Technology, Iran

[4]Faculty of Engineering, IKI University, Qazvin, Tehran, Iran

Stabilization and carbonisation conditions are the main factors influencing the properties of carbon fibres manufactured from polyacrylonitrile (PAN) fibres. In this report, low-cost commercial PAN fibres (textile grade) were used as precursors and the effects of the two mentioned factors on the tensile strength of carbon fibres were evaluated. By using the well-known Plackett–Burman screening method in the design of experiments, the best conditions to produce an economical product were determined. The results showed that this method can improve carbon fibre tensile strength by more than 15.7%.

Key words: *carbon fibre; commercial polyacrylonitrile fibre; screening method; Plackett–Burman method*

1. Introduction

At present, three precursors, including polyacrylonitrile-based, rayon-based, and pitch-based fibres, are mainly used for the production of carbon fibres. Due to its high degree of molecular orientation, higher melting point, and greater yield of carbon fibres, polyacrylonitrile (PAN) fibre has been found to be the most suitable precursor for making carbon fibres [1]. PAN fibre is a form of acrylic fibre, composed of acrylonitrile (AN) units in at least 85% by weight. The remaining 15% consists of neutral and/or ionic co-monomers, used to improve the properties of the fibres [2, 3].

Carbon fibres are prepared by a controlled pyrolysis of special grade PAN fibres. The overall process for converting PAN to carbon fibres involves stabilization and

*Corresponding author, e-mail: reslamifarsani@yahoo.com

carbonisation. The stabilization should be carried out in air at relatively low temperatures (180–300 °C). This step converts the precursor to a thermally stable structure capable of withstanding high temperature processing. Stabilization is a necessary and important step in achieving the desired product. The carbonisation involves rapid thermal pyrolysis in an inert environment (usually high purity nitrogen) at 1200–2000 °C, with an increase in carbon content to 85–99%. During this step, most of the non-carbon elements within the stabilized PAN fibres are volatilised in the form of H_2O, CH_4, NH_3, CO, HCN, CO_2, and N_2 [4, 5].

Carbon fibres have found several applications in modern technology. They have been utilized for advanced composites of plastics, metals, or ceramics based on their superior mechanical properties, such as high strength, high modulus, and low density. The main problem in this respect, however, is the high cost of carbon fibres. The high price of carbon fibres is mainly due to the high price of the precursor (i.e., special grade acrylic fibres) and high cost of processing. In order for this valuable material to become more popular in civilian applications, prices should definitely be lowered. One way of achieving this is through the use of cheap commercial acrylic fibres (textile grade PAN fibres). In recent years, there have been many attempts to use commercial acrylic fibres as precursors for the fabrication of carbon fibres, with the intention of producing lower priced carbon fibres [3, 6, 7].

Textile grade PAN fibres (commonly used in producing blankets, carpets, and clothes) have higher cross section areas and linear densities, smaller tensile strength, and different types and amounts of co-monomers compared to special PAN fibres. The modification of various parameters in these fibres (such as the types and amounts of co-monomers and linear density) is not easily possible and, if applicable, it causes their price to increase. On the other hand, producing carbon fibres with desirable properties using commercial PAN fibres through common processing routines is not possible. In recent years, however, some studies have been done using textile low price PAN fibres that led to the reduction of the price of carbon fibres, and these studies almost succeeded in this regard. In previous studies, carbon fibres with suitable mechanical properties were produced by using chemical and mechanical treatments before and after stabilization [6–8].

In this work, low-cost commercial PAN fibres were used as precursors in producing carbon fibres. The stabilization conditions and carbonisation temperature are the mainly affected factors in the properties of carbon fibres. In order to study the effects of these factors, a special screening experimental design method called the Plackett –Burman method [9] was applied, and the optimum factors were attained.

2. Experimental

Commercial PAN fibres used in this study, were produced by dry spinning. Table 1 shows the composition of these PAN fibres.

Table 1. Chemical analysis of commercial PAN fibres

Constituent	Weight (%)
Acrylonitrile (AN)	93
Methyl acrylate (MA)	6
Sodium methallyl sulphonate (SMS)	1

The PAN fibres were converted into carbon fibres through the following stages:

- Stabilization in a chamber furnace with air circulation at temperatures ranging from 180 to 280 °C in discontinuous working conditions.
- Carbonisation of the stabilized PAN fibres in a horizontal tubular furnace with a ceramic tube under a high purity nitrogen atmosphere (99.999%) at temperatures ranging from 1350 to 1450 °C for 10 minutes.

Tensile strength testing was done on single fibre samples by the ISO 11566 standard procedure. The test apparatus consisted of an Instron 5565 tensile tester equipped with a 2.5 N load cell and a crosshead speed of 2 mm·min^{-1}. The gauge length was kept at 25 mm. At least 25 tensile tests were done on each sample and the average of the test results was reported.

3. Results and discussion

In this research, nine affecting variables and their influence on the properties of carbon fibres made from PAN fibres were examined and listed in Table 2. Accordingly, two main levels are considered for each variable, with 1 used for the low level of each factor and 2 for the high level.

Table 2. The most important factors (variables) influencing the properties of carbon fibres and their main levels

Variable		Main levels		Unit
No.	Name	Low	High	
1	1st step temperature of stabilization	180	200	°C
2	1st step maintaining time in stabilization	30	60	min
3	2nd step temperature of stabilization	210	220	°C
4	2nd step maintaining time in stabilization	30	60	min
5	3rd step of temperature stabilization	230	240	°C
6	3rd step maintaining time in stabilization	30	60	min
7	4th step temperature of stabilization	270	280	°C
8	4th step maintaining time in stabilization	30	60	min
9	Temperature of carbonisation	1350	1450	°C

In order to study 9 factors, the minimum necessary number of runs in the experiment would be $2^9 = 512$. Since each run is time-consuming, costly, and requires set-

ting and resetting the furnace, it is often not feasible to expect so many different production runs for the experiment. In these conditions, fractional factorials are used to "sacrifice" interaction effects so that the main effects may still be determined properly. A technical description of how fractional factorial designs are constructed is beyond the scope of this article. Detailed accounts of how to design $2^{(k-p)}$ experiments may be found, for example, in Refs. [10–12], to name just a few of many textbooks covering the subject.

The special screening design method called the Plackett–Burman method was used [9]. Screening designs are used to find the important factors of two-level factors. When the number of runs is 12, 20, 24, or 28, the Plackett–Burman design method is ordinarily used. By using STATISTICA Version6 software, a random design of the standard $\mathbf{L}_{12}$ orthogonal array [13] as tabulated by Taguchi [14] was constructed, which requires only 12 observation runs. The $\mathbf{L}_{12}$ vector allows the maximum number of main effects to be estimated in an unbiased (orthogonal) manner, with a minimum number of experiment runs. For 12 randomly designed experiments, average values of tensile strength for 25 filaments in the tow of carbon fibres measured are presented in the last column of Table 3.

Table 3. The arrangement of a $\mathbf{L}_{12}$ orthogonal random design and the experiment results (the low level of each variable denoted by 1 and its high level by 2)

Run No.	Variable No.									Average tensile strength
	1	2	3	4	5	6	7	8	9	
1	2	1	2	1	1	1	2	2	2	1684
2	2	2	1	2	1	1	1	2	2	1488
3	1	2	2	1	2	1	1	1	2	1420
4	2	1	2	2	1	2	1	1	1	1521
5	2	2	1	2	2	1	2	1	1	1619
6	2	2	2	1	2	2	1	2	1	1570
7	1	2	2	2	1	2	2	1	2	1477
8	1	1	2	2	2	1	2	2	1	1522
9	1	1	1	2	2	2	1	2	2	1418
10	2	1	1	1	2	2	2	1	2	1621
11	1	2	1	1	1	2	2	2	1	1426
12	1	1	1	1	1	1	1	1	1	1376

To determine significant variables, an analysis of variance is performed twice. The first step showed the first eight variables and the interactions between pairs of variables (1–2, 1–3, 1–4, and 1–7), all considered meaningful in 95%. Customarily, in order to obtain a more stable estimate of the error variance, small and non-significant effects are pooled into the error term. Table 4 shows the consequence of variance analysis after pooling factor No. 9 (temperature of carbonisation) into the error term.

Table 4. The analysis of the variance table after pooling the meaningful variable into the error term

Parameter	*SS*	*df*	*MS*	*F*	*P* value
(1) 1st step temperature	62208.0	1	62208.00	7776.000	0.007219
(2) 1st step time	1814.1	1	1814.07	226.759	0.042214
(3) 2nd step temperature	35392.2	1	35392.16	4424.020	0.009571
(4) 2nd step time	1236.2	1	1236.20	154.526	0.051103
(5) 3rd step temperature	2612.6	1	2612.56	326.570	0.035192
(6) 3rd step time	12222.9	1	12222.87	1527.858	0.016283
(7) 4th step temperature	38384.2	1	38384.20	4798.025	0.009190
(8) 4th step time	8557.0	1	8557.04	1069.630	0.019459
1 by 2	10069.4	1	10069.41	1258.677	0.017939
1 by 3	4182.5	1	4182.50	522.813	0.027825
1 by 4	9188.7	1	9188.70	1148.587	0.018779
1 by 7	23918.2	1	23918.22	2989.778	0.011642
Error	8.0	1	8.00		
Total *SS*	359756.9	13			

The effects of statistically meaningful variables being present in the regression model, with their coefficient estimates based on the original factor values, are shown in Table 5.

Table 5. The point estimation of coefficients in the coded value regression model

Parameter	Regression coefficient	Standard error	*t*	*P* value
Mean/Interc.	1861.333	17.39732	106.9897	0.005950
(1) 1st step temperature	–613.000	10.89342	–56.2725	0.011312
(2) 1st step time	–391.556	11.29405	–34.6692	0.018358
(3) 2nd step temperature	457.333	14.78738	30.9273	0.020577
(4) 2nd step time	–301.889	9.59166	–31.4741	0.020220
(5) 3rd step temperature	–57.778	3.19722	–18.0712	0.035192
(6) 3rd step time	137.889	3.52767	39.0878	0.016283
(7) 4th step temperature	–305.444	8.74325	–34.9349	0.018218
(8) 4th step time	84.444	2.58199	32.7052	0.019459
1 by 2	235.333	6.63325	35.4778	0.017939
1 by 3	–199.333	8.71780	–22.8651	0.027825
1 by 4	179.333	5.29150	33.8908	0.018779
1 by 7	289.333	5.29150	54.6789	0.011642

On this basis, the average tensile strength of the produced fibre $\overline{Y}$ can be introduced by following regression model:

$$\begin{aligned}\overline{Y} = {} & 1861.333 - 613X_1 - 391.556X_2 + 457.333X_3 - 301.889X_4 - 57.778X_5 \\ & +137.889X_6 - 305.444X_7 + 84.444X_8 + 235.333X_1X_2 - 199.333X_1X_3 \\ & +179.333X_1X_4 + 289.33X_1X_7\end{aligned} \quad (1)$$

Here, X_1 through X_8 stand for the 8 statistically meaningful factors in the analysis. The effects shown earlier also contain these parameter estimates. Regarding the given model coefficients, the error terms of the model are close to zero, which is an appropriate reason to verify the model. One of the most important results is to predict the tensile strength of carbon fibres for different procedure conditions. It is obvious that the more variables of procedural settings should be around its high and low values.

4. Model verification

In order to verify the models, error analysis followed based on the experimented results. The achieved regression model exhibits the smallest error possible. By substituting the experiment run results in the model, no errors were obtained. Figure 1 illustrates the observed value of carbon fibre tensile strength versus the strength predicted by the model, which presents a perfect fit.

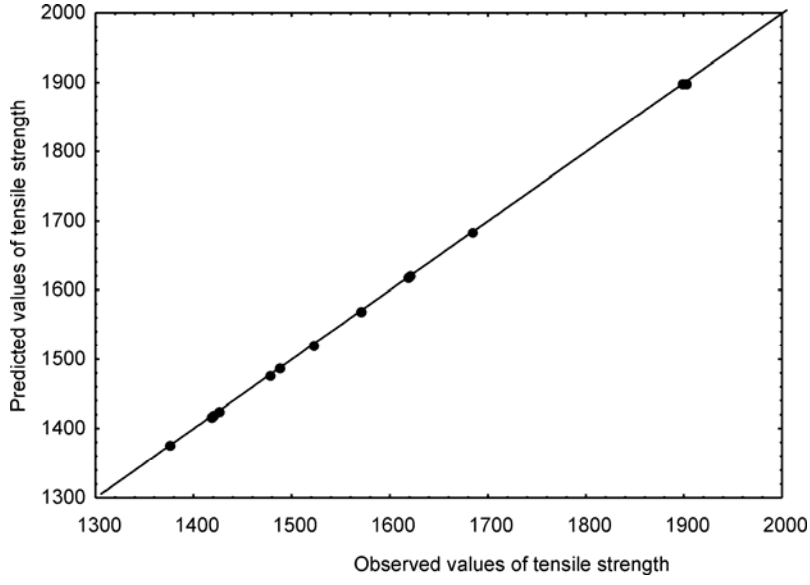

Fig. 1. Observed values of carbon fibre tensile strength versus the strength predicted by the regression model

In order to obtain an estimate of any run result, it is possible to substitute an arrangement of the model through coded units. For example, to estimate the tensile strength at the conditions 180 °C, 30 min, 220 °C, 60 min, 230 °C, 60 min, 280 °C, 60 min, and 1450 °C for X_1–X_9, respectively, the relevant coded value (1, 1, 2, 2, 1, 2, 2, 2, 2) can be applied to obtain the expected tensile strength. Table 6 shows the results of predicted (later abbreviated by Pre.) versus observed (Obs.) values for some experimental arrangements.

Table 6. The observed model values versus predicted ones
for the tensile strength of carbon fibres in a couple extra pilot experiments

Experimental arrangement								Pre. value	Obs. value
2	2	1	2	2	1	1	2	1430	1433
2	2	2	2	2	2	2	2	1900	1897
1	1	2	2	1	2	2	2	1953	1948

According to the model, the maximum value of carbon fibre tensile strength that could be deduced mathematically was 1953 MPa at the arrangement showed in detail in Table 7. This arrangement was experimentally investigated and the observed value of 1948 MPa deviates less than 0.3% from the expected value. This shows the way to optimise the desired quality characteristics from 1684 MPa (the best previously observed value) to 1948 MPa, improving it by more than 15.7%. Such a value contains reasonably appropriate quality characteristic when raw material cost is near the ground.

Table 7. Optimum levels of the main variables and maximum tensile strength of carbon fibres

Variable No.	1	2	3	4	5	6	7	8	Tensile strength (MPa) 1953
Optimum level code	1	1	2	2	1	2	2	2	
Optimum process arrangements and value	180 (°C)	30 (min)	220 (°C)	60 (min)	230 (°C)	60 (min)	280 (°C)	60 (min)	

5. Conclusions

In this article, using local textile grade PAN fibres, which seem to be a suitable alternative for producing low price carbon fibres, was surveyed. In order to achieve a mathematical model for evaluating the effect of the 9 variables of stabilization conditions and carbonisation temperature on tensile strength, a well-known experimental analysis method (Plackett–Burman) was used and a non-linear mathematical function attained. The optimisation procedure was conducted using the STATISTICA version 6 package. By analysing this model, an optimum set of process arrangements was obtained. According to the model, it is possible to predict the tensile strength of carbon fibres for different stabilization and carbonisation conditions. The optimum process arrangement showed the possibility of increasing the tensile strength of carbon by more than 15.7% with a maximum 0.3% error.

References

[1] WALSH P.J., *ASM Handbook-Composites*, ASM, Ohio, 2001.
[2] BANSAL R.C., DONNET J.B., *Comprehensive Polymer Science*, Pergamon Press, Oxford, 1990.
[3] MASSON J.C., *Acrylic Fiber Technology and Applications*, Marcel Dekker, New York, 1995.

[4] LEE S.M., *International Encyclopedia of Composites*, VCH, New York, 1990.
[5] KOSTIKOV V.I., *Fibre Science and Technology*, Chapman & Hall, London, 1995.
[6] BAHL O.P., MANOCHA L.M., Chem. Age India, 38 (1987), 181.
[7] EZEKIEL H.M., *Formation of Very High Modulus Graphite Fibers from a Commercial Polyacrylonitrile Yarn*, Composite & Fibrous Materials Branch, Non-metallic Materials Divisions, Air Force Materials Laboratory, Wright Patterson Air Force Base, Ohio, USA, 184.
[8] EDIE D.D., Carbon, 36 (1998), 345.
[9] PLACKETT R.L., BURMAN J.P., Biometrika, 34 (1964), 255.
[10] MONTGOMEY D.C., *Design and Analysis of Experiments*, Wiley, New York, 2004.
[11] DEMING S.N., MORGAN S.L., *Experimental Design – A Chemometric Approach*, Elsevier, Amsterdam, 1993.
[12] RYAN T.P., *Statistical Methods for Quality Improvement*, Wiley, New York, 1989.
[13] HEDAYAT A.S., SLOANE N.J.A., STUFKEN J., *Orthogonal Arrays – Theory and Applications*, Springer-Verlag, New York, 1999.
[14] TAGUCHI G., *Jikken Keikakuho*, Maruzen, Tokyo, 1987, English translation *System of Experimental Design*, D. Clausing (Ed.), Unipub/Kraus International, New York.

Received 9 February 2006
Revised 20 June 2006

Materials Science-Poland, Vol. 25, No. 1, 2007

Study of Nb–Zn co-doped $Ba(Ti,Zr)O_3$ ceramics

Y. WANG[1*], Z. ZHUANG[2], J. ZHOU[1]

[1] State Key Laboratory of New Ceramics and Fine Processing, Department of Materials Science and Engineering, Tsinghua University, Beijing 100084, China

[2]College of Materials Science and Engineering, South China University of Technology, China

The surface coating processing technique was used to modify hydrothermally synthesized-$Ba(Ti,Zr)O_3$ (BTZ) with an Nb-organic compound and Zn-organic compound in an organometallic precursor (Nb-EDTA and Zn-EDTA), which were coated on the powders uniformly. The sintering temperature was decreased and dense ceramics were obtained with well-developed grain growth at 1300 °C. Both increasing the amount of Nb–Zn and decreasing the Nb/Zn ratio greatly promoted grain growth. On increasing the Nb/Zn ratio, the Curie point temperature was markedly lowered, accompanied by a large decrease in the corresponding dielectric maximum and a simultaneous enhancement of the ferroelectric relaxor characteristic. At Nb/Zn = 2, the Curie temperature was monotonously lowered with increasing Nb–Zn content. The shift rate of the phase transition point of Nb–Zn co-doped BTZ was 6.5 °C/mol %. The corresponding dielectric maximum was enhanced rapidly from 9020 for a 0.35 mol % Nb–Zn doped sample to more than 12000 for a 0.90 mol % Nb–Zn doped sample.

Key words: *barium titanate zirconium; Nb–Zn co-doped; microstructure; dielectric property*

1. Introduction

Barium titanate zirconium $Ba(Ti_{1-x}Zr_x)O_3$ (BTZ) ceramics, based on a solid solution of $BaZrO_3$ and $BaTiO_3$, have been widely studied and adapted to meet the Y5V and Z5U specifications of multilayer ceramic capacitors, owing to their very high and broad relative permittivity maximum at the ferroelectric Curie point [1, 2]. Owing to the solid-state reaction during sintering, the sintering temperature of BTZ ceramics is always above 1350 °C [3]. Therefore, it is of great importance to select a proper technique and additives in order to acquire high-performance ceramics based on BTZ.

Aliovalent cations incorporated in the perovskite lattice serve as donors or acceptors, capable of greatly affecting electrical characteristics even though their solubilities remain on a trace level [4–7]. The distribution of these additives in the starting

*Corresponding author, e-mail: yuehuiwang@263.net

powder is usually realized by milling but achieving a uniform distribution of the additives by this method is difficult, particularly if the main component is a submicrometer powder. It has been anticipated that this problem can be solved by coating the surface of the powder with appropriate additives using a chemical method [8]. In general, chemically prepared powders have high purity submicrometer particle sizes, and much better compositional uniformity than those made with the traditional method of mixing solid constituents followed by calcination [9].

In this paper, a surface coating processing technique was used to modify hydrotherrmally synthesized $Ba(Ti,Zr)O_3$ with an Nb-organic compound and Zn-organic compound in an organometallic precursor (Nb-EDTA and Zn-EDTA), used as the donor and acceptor dopants, respectively. Nb^{5+}-donors were compensated by Zn^{2+}-acceptors on Ti sites and the complex $[Nb_{2/3}Zn_{1/3}]^{4+}$ was substituted for Ti^{4+}. The effect of co-doped Nb–Zn on the microstructure and dielectric properties of BTZ ceramic was then investigated and the possible mechanism discussed.

2. Experimental

The main starting material was commercial $Ba(Ti_{0.90}Zr_{0.10})O_3$ (GuoTeng Co., Ltd.), synthesized by the hydrothermal method. All reagents used were of reagent grade and used directly without any further purification. Homogeneous and stable Nb–Zn metal-organic compounds were prepared in aqueous solutions by a complex route, with their soluble inorganic compounds as metal ionic sources and EDTA as the complex chelate agent.

The typical experimental procedure can be described as follows. According to the required concentrations of Nb–Zn, precisely measured amounts of the metal-organic compounds were added and adjusted so that the concentration of BTZ in solution was 10 wt. % and the amount of Nb–Zn was 0–0.90 mol %. pH of the solution was then adjusted to about 10 using 1 mol/dm^3 NH_4OH. The BTZ powders were added into the aqueous solutions of the metal-organic compounds, and ultrasonically dispersed for 15–20 minutes. The gelation time was longer than 2 h. During the sol-gel process, electromagnetic stirring was used. The sol temperature was kept at 80 °C. After coating, the slurry was dried in a vacuum oven at 50 °C for 24 h. The modified powders were cold-pressed uniaxially into disks 10 mm in diameter and 1 mm thick under 3 MPa and sintered at 1260–1300 °C for 1 h in air and cooled in the furnace. Then, disk samples were electroded by applying silver paste on opposing surfaces and fired at 750 °C.

The density of the sintered compacts was measured by the Archimedes method with water as the liquid medium. Electric permittivity as a function of the temperature of the sintered disks was measured using an automatic measurement system with an LCR (HP4291A) at 1 kHz. The phase compositions were characterized by powder X-ray diffraction (XRD), using a Rigaku X-ray diffractometer equipped with CuK_α ra-

diation (λ = 1.5418 Å). Microstructures of fracture surfaces were observed by a scanning electron microscope (SEM), JSM-6301F.

3. Results and discussion

Sintering behaviour. The densities of BTZ ceramic samples doped with various amounts of Nb–Zn are shown in Fig. 1. As observed, the densities of sintered samples became high at temperatures above 1260 °C. This indicates that the additives decrease the sintering temperature of the studied powder. Maximum density was achieved at 1300 °C, and at sintering temperatures above 1320 °C the densities of all samples decreased. This decrease has been attributed to the increased intragranular porosity resulting from discontinuous grain growth [10]. It is obvious that the densification of BTZ ceramics is improved by increasing the amount of Nb–Zn and by decreasing the Nb/Zn ratio. Therefore, it can be concluded that the densification of BTZ ceramics is greatly affected by Nb–Zn co-doping.

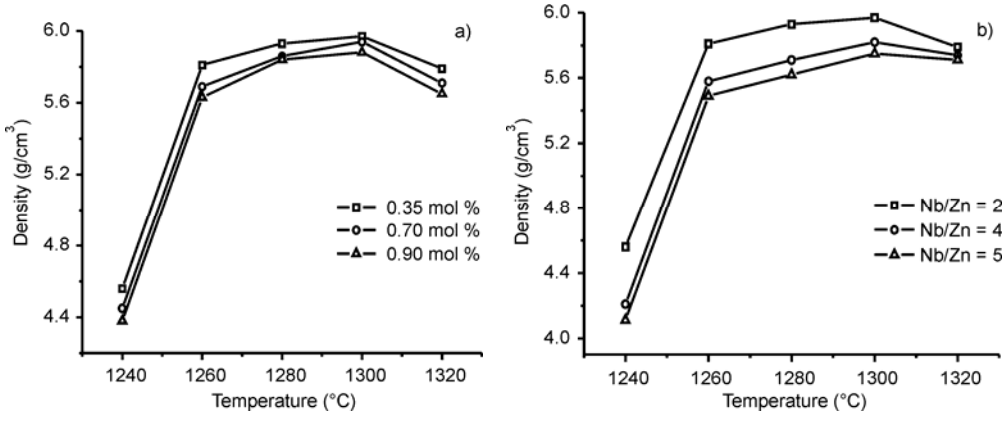

Fig. 1. The influence of sintering temperatures on the densities of BTZ ceramic samples doped with various: a) Nb–Zn amounts, b) Nb/Zn ratios

Phase identification. Figure 2 shows X-ray diffraction patterns of the disk surface fired at 1300 °C for 1 h. BTZ solid solutions were formed after sintering and there existed no secondary phase in the XRD of the solution. This indicates that Nb and Zn ions were dissolved in BTZ. The crystal structure of BTZ solid solutions was pseudocubic for all samples. Lower-angle (200) and (002) diffraction lines separated each other on the tetragonal system merged in this system (see the insert of Fig. 2a). We interpreted these results as the substitution reactions of $[Nb_{2/3}Zn_{1/3}]^{4+}$ for Ti-site cations, leading to the distortion of the perovskite lattice. The interstices between oxygen octahedra diminished with increasing barium vacancies, and the *c*/*a* ratio was lowered as well [5].

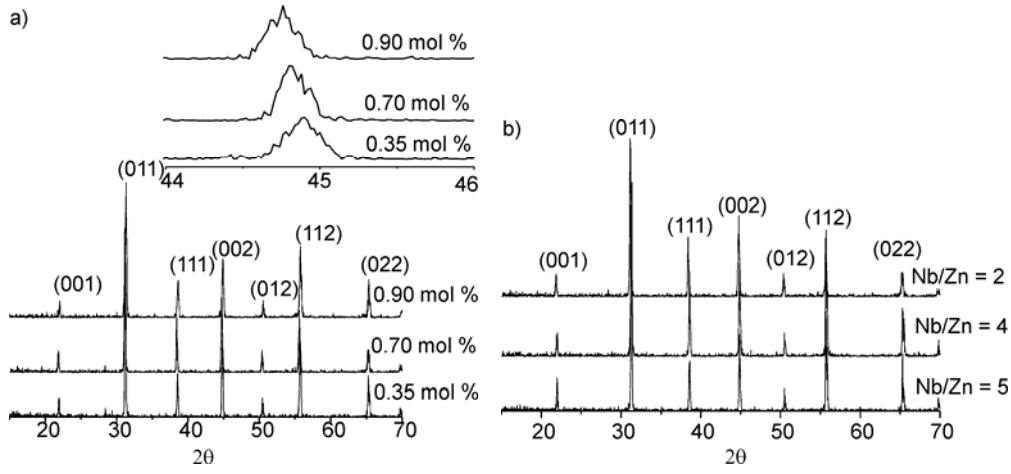

Fig. 2. XRD patterns of BTZ ceramics doped with various: a)Nb–Zn amounts, b) Nb/Zn ratios, sintered at 1300 °C for 1 h

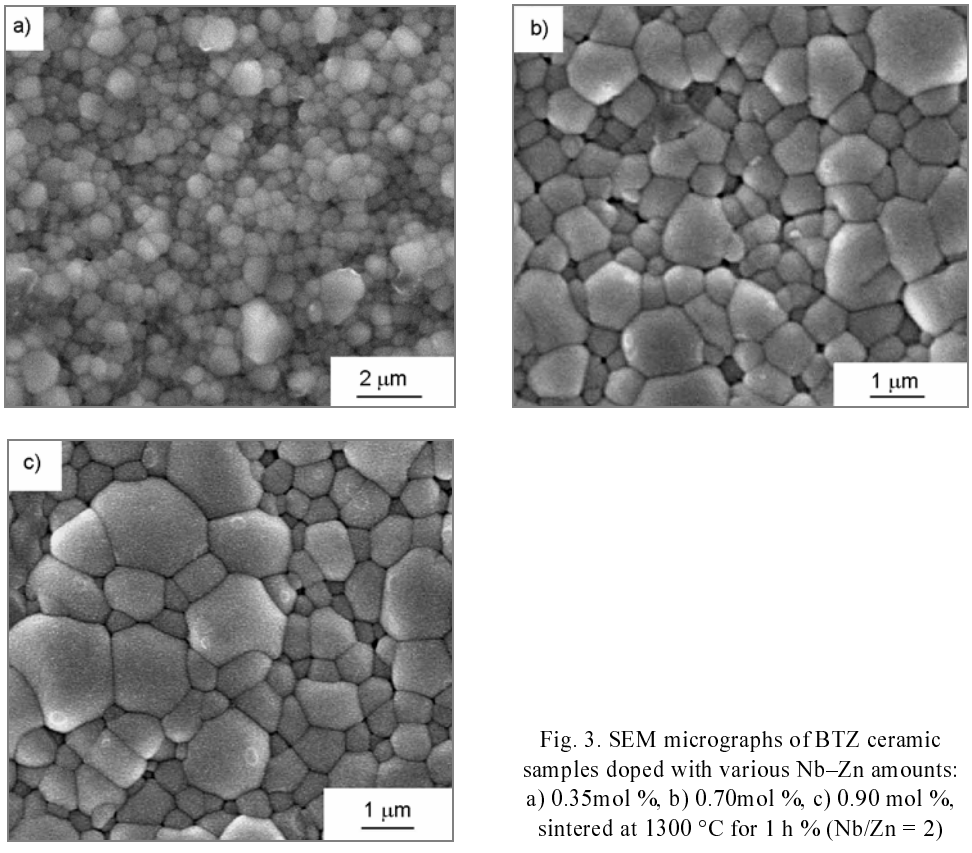

Fig. 3. SEM micrographs of BTZ ceramic samples doped with various Nb–Zn amounts: a) 0.35mol %, b) 0.70mol %, c) 0.90 mol %, sintered at 1300 °C for 1 h % (Nb/Zn = 2)

Microstructure. Figure 3 shows the microstructure of samples with various compositions sintered at the same conditions (1300 °C/h). It can be seen that the grain size was decisively affected by the dopant content. Both an increasing amount of Nb–Zn and decreasing Nb/Zn ratio greatly promoted grain growth. The grain size changed from 0.7 μm for the sample with Nb/Zn = 2 to about 0.5 μm for the sample with Nb/Zn = 5. When Nb/Zn is equal to 2, the grain size changed from 0.4 μm for the 0.35 mol % Nb–Zn doped sample to about 1.2 μm for the 0.90 mol % Nb–Zn-doped sample. These alterations demonstrate that appropriate amount of Nb–Zn additive and Nb–Zn ratio can improve the microstructure of BTZ ceramics.

The substitution of $[Nb_{2/3}Zn_{1/3}]^{4+}$ complexes for Ti sites in the perovskite lattice seems to account for the influence of the stoichiometry (Nb/Zn ratio). When Nb/Zn is above 2, the positively charged donor centre can be compensated by the cation vacancies of Ba ions [11]. At this point, mass transport was reduced and grain growth was also greatly restrained. In addition, excess Nb ions possibly segregate on the grain boundary and restrained grain growth. When Nb/Zn is equal to 2, however, both Nb^{5+} and Zn^{2+} not only serve as modifying aids, but also as sintering aids that contribute to mass transport and grain growth.

Dielectric properties. The temperature dependence of the relative electric permittivity for Nb–Zn co-doped BTZ ceramics sintered at 1300°C/h is illustrated in Fig. 4. It is clear that both the Nb/Zn ratio and amount of Nb–Zn have a large influence on dielectric properties. With increasing Nb/Zn ratio, the Curie point temperature is lowered from 68 °C for the sample with Nb/Zn, from 2 °C to 42°C for the sample with Nb/Zn = 5, accompanied by a large decrease in the corresponding dielectric maximum and an enhancement of the ferroelectric relaxor characteristic. At Nb/Zn = 2, the obvious phase transition point shifts towards lower temperatures with increasing Nb–Zn amount.

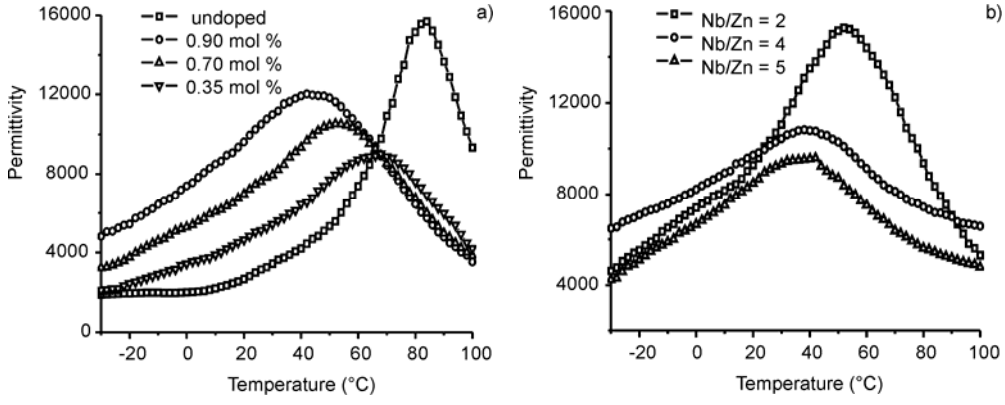

Fig. 4. Temperature dependence of electric permittivity for BTZ ceramic samples doped with various: a) Nb–Zn amounts, b) Nb/Zn ratios, sintered at 1300 °C for 1 h

It can be seen that increasing the amount of Nb–Zn from 0 to 0.9 mol % lowers the Curie temperature monotonously from 85 °C to 42 °C. The shift rate of the phase

transition point of Nb–Zn co-doped BTZ was –46.5 °C/mol % (Fig. 5). The corresponding dielectric maximum, however, was enhanced rapidly from 9020 for the 0.35 mol % Nb–Zn doped sample to more than 12 000 for the 0.90 mol % Nb–Zn doped sample.

The sintering temperature had little effect on the Curie temperature for certain amounts of Nb–Zn doped BTZ ceramics, while it can influence the dielectric constant maximum to a considerable extent. It appeared that the samples sintered at 1300 °C had the highest dielectric constant and the ones sintered at 1260 °C had the lowest dielectric constant in the mass. The dielectric losses of all samples were less than 1.0 %, and resistivities were about $10^{11}\Omega\cdot$cm.

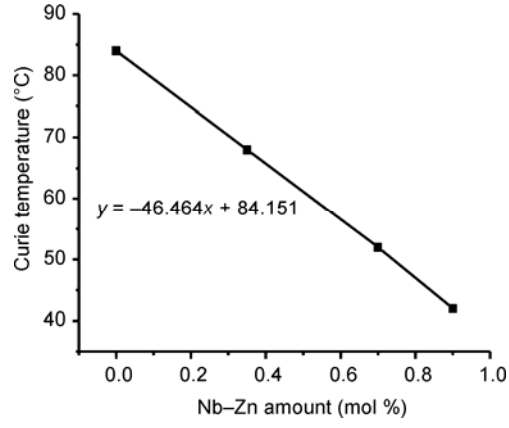

Fig. 5. The Nb–Zn amount dependence of the Curie temperature for BTZ ceramics

The influence of the Nb–Zn co-doping on the dielectric properties of BTZ ceramics was first attributed to the promotion effect of the dopants on the sintering of the ceramics. When doped with a proper Nb–Zn content, fully densified ceramics can be obtained with well-developed grain growth, which was helpful for the improvement of the dielectric properties of BTZ ceramics. Secondly, the substitution reactions of $[Nb_{2/3}Zn_{1/3}]^{4+}$ for Ti-site cations lead to the distortion of the perovskite lattice. The interstices between oxygen octahedra diminished with increasing barium vacancies, and the *c*/*a* ratio decreased as well. Therefore, the spontaneous polarization was depressed due to the restraint of B-site cations, and as a result the Curie point of the BTZ ceramics descends steeply. On the other hand, the distortion of the perovskite lattice can strengthen the structure fluctuations in the materials, which may account for the diffusion phase transition characteristics of doped BTZ ceramics.

4. Conclusions

The sintering behaviour, microstructure, and dielectric characteristics of Nb–Zn co-doped barium zirconium titanate ceramics were investigated. Sintering temperature was decreased by this technique and dense ceramics were obtained with well-

developed grain growth at 1300 °C. Ba(Ti,Zr)O_3 solid solutions were formed after sintering, and no secondary phase was found in the XRD of the solution. Both increasing of the amount of Nb–Zn and decreasing the Nb/Zn ratio seriously promoted grain growth. The influence of dopants on the sintering characteristics of BTZ ceramics was attributed to the substitution tendency of $[Nb_{2/3}Zn_{1/3}]^{4+}$ for Ti-site cations in the perovskite lattices. With increasing Nb/Zn ratio, the Curie temperature decreased significantly, accompanied by a large decrease in the corresponding dielectric maximum and an enhancement of the ferroelectric relaxor characteristic. At Nb/Zn = 2, the Curie temperature monotonously decreased with increasing Nb–Zn content. The shift rate of the phase transition point of Nb–Zn co-doped BTZ was 6.5 °C/mol %. The corresponding dielectric maximum was enhanced rapidly from 9020 for the 0.35 mol % Nb–Zn doped sample to more than 12 000 for the 0.90 mol % Nb–Zn doped sample.

References

[1] NEIMAN S.M., J. Mater. Sci., 23 (1988), 3973.
[2] FANG T.T., WU P.H., Mater. Chem. Phys., 72 (2002), 346.
[3] HENNINGS D., SCHNELL A., SIMON G., J. Am. Ceram. Soc., 65 (1982), 539.
[4] BUSCAGLIA M.T., BUSCAGLIA V., VIVIANI M., J. Eur. Ceram. Soc., 20 (2000), 1997.
[5] WANG Y.L., LI L.T., QI J.Q., GUI Z., Ceram. Int., 28 (2002), 657.
[6] HANSEN P., HENNINGS D., SCHREINEMACHER H., J. Electroceram., 2 (1998), 85.
[7] WATANABE K., OHSATO H., KISHI H., OKINO Y., Solid State Ionics, 108 (1998), 129.
[8] ABICHT H.P., ÖLTZKE D.V., SCHMIDT H., Mater. Chem. Phys., 51 (1997), 35.
[9] BRUNO S.A., SWANSON D.K., J. Am. Ceram. Soc., 76 (1993), 1233.
[10] ARMSTRONG T.R., MORGENS L.E., MAURICE A.K., BUCHANAN R.C., J. Am. Ceram. Soc., 72 (1989), 605.
[11] CHAN N.H., SMYTH D.M., J. Am. Ceram. Soc., 67 (1984), 285.

Received 16 February 2006
Revised 30 April 2006

Materials Science-Poland, Vol. 25, No. 1, 2007

Influence of milling time on the performance of ceramic ball grinding media prepared from refractory waste

L.Y. ZHONG[1, 2, 3], B. L. WU[2,3], L. M. ZHANG[1*], J. G. SONG [1, 2]

[1]State Key Lab of Advanced Technology for Materials Synthesis and Processing, Wuhan University of Technology, Wuhan 430070, China

[2]Key Lab of Nonferrous Materials and New Processing Technology of Guilin University of Technology of Ministry of Education, Guilin, Guangxi 541004, China

[3]Department of Materials and Chemical Engineering, Guilin University of Technology, Guilin 541004, China

Aluminosilicate refractory waste was used to prepare high performance ceramic ball grinding media with 75% Al_2O_3. The influence of milling time on the particle size of raw materials, the sintering temperature, and performance of ceramic balls were studied. Results show that with increasing milling time the particle size of the raw materials decreased, resulting in a decrease of ceramic ball sintering temperature and an increase in wear resistance and volume density. The wear rate and volume density of balls prepared by milling the materials for 72 h were 0.01886 %/h and 3.374 g/cm^3, respectively.

Key words: *aluminosilicate refractory waste; particle size; ceramic grinding media; wear resistance*

1. Introduction

Large amounts of refractory wastes are discarded during the production and application of refractories, and after refractories reach the end of their service life. In particular, more than 3 million tons of refractory waste is produced per year in China [1]. The majority of such refractory waste is accumulated inside or outside factories, causing severe problems with storage, disposal, and the environment, while only small amounts of the waste are now used as raw materials for refractories, cement, glass, ceramics, steels, etc., because of the potential undesirable influence of the waste on the quality of the product and its large crystal and high hardness, which make it difficult to mill and lead to increasing recycling costs. At present, reusing refractory waste

*Corresponding author, e-mail: lmzhang@mail.edu.cn

has been widely studied, because of the scantiness of natural mineral resources, high landfill costs and the aim to reduce environmental pollution [1–4]. Since there are few reports on reusing aluminosilicate refractory waste as raw materials for high performance ceramics [5], the present paper reports the influence of raw material milling time on the sintering temperature and performance of as-prepared ceramic balls.

2. Experimental procedure

Alumina ceramic balls with 75% Al_2O_3 were prepared by reusing aluminosilicate refractory waste as a raw material. The waste (84.4 wt. %) was mixed with CaO –MgO–Al_2O_3–SiO_2 quaternary system fluxing agents, then milled for 6 h, 12 h, 24 h, 48 h, and 72 h at a weight ratio of powder:media:water = 1:(3–6):(1–1.5) and dried at 100 °C for 24 h, respectively. The obtained powders were shaped by cold isostatic pressing at 65 MPa for 3 minutes. The ceramic blanks were sintered at 1270 °C, 1285 °C, 1300 °C, 1325 °C, or 1350 °C for 2.5 h. The chemical compositions of the waste and ceramic balls are given in Table 1. The particle size distributions of the original waste and obtained powders were measured by a LS-POP (III) OMEC particle size analyser. The water absorption ratio of the balls was measured according to Chinese National Standard GB/T3810.3-1999. The volume density of the balls was measured according to the Archimedes principle. The microstructure of ceramic balls was observed with a JSM-5610LV scanning electron microscope (SEM).

Table 1. Chemical composition of refractory waste and ceramic balls

Composition	Al_2O_3	SiO_2	TiO_2	CaO	MgO	Fe_2O_3	Other
Waste [%]	80.92	12.14	2.91	0.61	0.30	2.92	0.2
Ceramic ball [%]	75.01	17.26	2.18	1.39	0.99	2.48	0.69

A kind of alumina ceramic ball with 90% Al_2O_3 was selected as the reference ball, which was an imported alumina ceramic ball grinding media used in the architectural and sanitary ceramics industries. The prepared balls and reference ball were milled together with corundum media in a ball mill for 24 h, then dried at 300 °C for 30 minutes and weighed. The wear rate of the balls was calculated from the formula:

$$W = \frac{m_0 - m_1}{24 m_0} \times 100\% \tag{1}$$

where W is the wear rate of the ceramic balls (%/h), m_0 and m_1 are the ball masses before and after milling.

3. Results and discussion

3.1. Influence of milling time on the particle size of raw materials

Figures 1 and 2 show the particle differential distributions of the original waste and raw materials, respectively, milled for various times. Figure 1 indicates that the average particle size and maximum particle size of the original waste was 38 μm and 169 μm, respectively. Figure 2 shows that with increasing milling time the particle distribution of the raw materials became narrow and the particle size decreased.

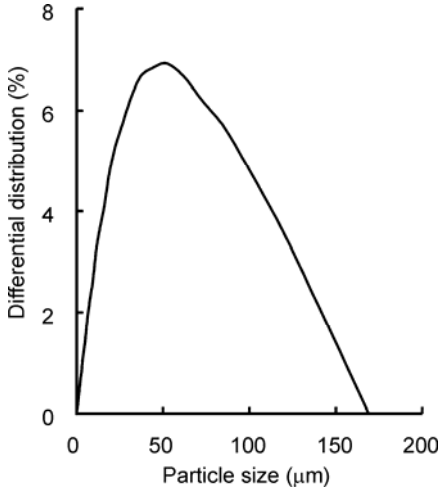

Fig. 1. Particle size differential distribution of the original waste

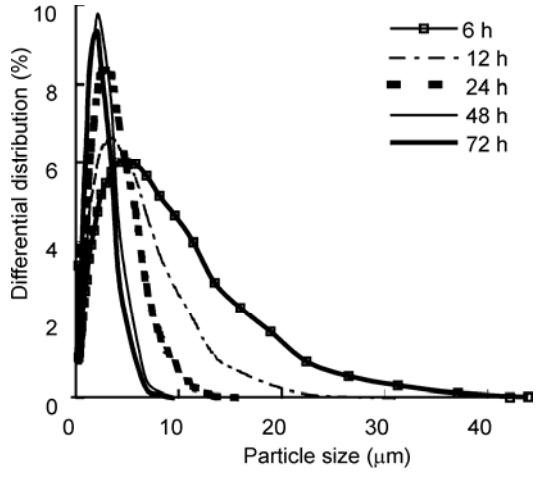

Fig. 2. Particle size differential distributions of the raw of materials, with milling time changed from 6 to 72 hours

The average particle sizes of raw materials milled for 6 h, 12 h, 24 h, 48 h, and 72 h were 3.15 μm, 2.50 μm, 2.30 μm, 1.64 μm, and 1.42 μm, and the maximum particle sizes were 52 μm, 31.3 μm, 15.98 μm, 9.64 μm, and 9.64 μm, respectively. The results suggest that the waste was easily milled at the experimental ratio of raw materials:media:water of 1:(3–6):(1–1.5). The water ratio increased with milling - the longer the milling time, the more water was needed.

3.2. Influence of raw material milling time on ceramic ball sintering temperature and performance

The influence of raw material milling time on ceramic ball sintering temperature, water absorption, wear rate, and density are shown in Table 2, Figs. 3 and 4. The results indicate that when the raw material milling time was the same, the ceramic balls water absorption and wear rate both initially decreased and then increased (Table 2,

Fig. 3a)), while the volume density initially increased and then decreased (Fig. 3b). The sintering temperature was optimum when water absorption and wear rate were the lowest and the volume density was the highest.

Table 2. Influence of milling time on ceramic ball sintering temperature .

Milling time [h]	Water absorption ratio [%]				
	1270 °C	1285 °C	1300 °C	1325 °C	1350 °C
6	1.7353	0.2758	0.0083	0.0002	0.0015
12	0.1684	0.0084	0.0004	0.0006	0.0469
24	0.1171	0.0031	0.0004	0.0006	0.0342
48	0.0219	0.0004	0.0004	0.0008	0.0015
72	0.0010	0.0004	0.0007	0.0011	0.0290

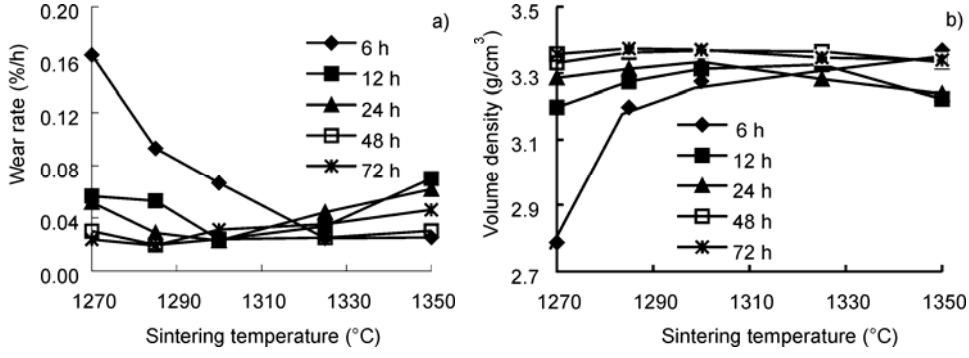

Fig. 3. Temperature dependence of wear rate (a), and density (b) of ceramic balls

During firing, small pores moved toward large pores or excluded through the crystal boundary. On the other hand, the granules grew quickly, leading to some enclosed pores in the ceramics. At an elevated firing temperature, the pores inside ceramics became smaller, resulting in a decrease in water absorption and an increase in density before the temperature reached the optimum sintering temperature. When the firing temperature was higher than the optimum sintering temperature, the air pressure in the enclosed pores increased quickly, leading to an increased pore size and porosity, and to an expansion of the ceramics resulting in an increase in water absorption and a decrease in volume density. With decreasing pore size and porosity and increasing volume density, the ceramic ball wear rate decreased before the sintering temperature reached the optimum. On the contrary, the ceramic ball wear rate increased and wear resistance decreased with increasing sintering temperature after the temperature rose above the optimum sintering temperature. Figure 4a shows that the optimum sintering temperature of balls prepared from materials milled for 6 h, 12 h, 24 h, 48 h, and 72 h was 1325 °C, 1300 °C, 1300 °C, 1285 °C, and 1285 °C, respectively, suggesting that the sintering temperature decreases with increasing milling time. When sintered at the optimum tempera-

ture, both ball density and wear resistance increases (wear rate decreases) with increasing milling time (Fig. 4b). The density and wear rate of the compared sample were 3.64 g/cm^3 and 0.0537 %/h, respectively. The volume density and wear rate of the balls prepared from raw materials milled for 24 h and sintered at 1300 °C were 3.334 g/cm^3 and 0.02272 %/h, respectively, and for the ceramic balls prepared from raw materials milled for 72 h and sintered at 1285 °C were 3.374 g/cm^3 and 0.01886 %/h, respectively. These results indicate that the wear resistance of the prepared ceramic balls was higher than that of the reference balls. The wear rate of the prepared balls was only (1/3)–(1/2) that of the reference ball.

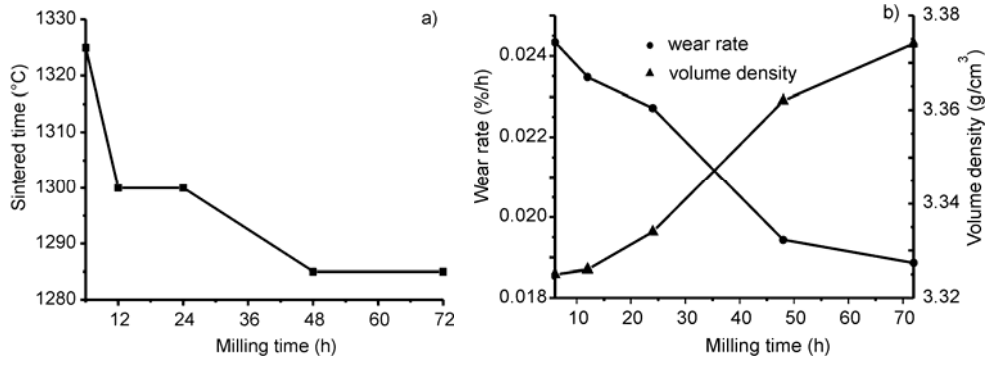

Fig. 4. Influence of milling time on ceramic ball sintering temperature, wear rate, and density

Experimental results indicate that the sintering temperature of the prepared ceramic balls decreases and performance increases with increasing raw material milling time, however increasing milling time increases ceramic ball production cost. Considering the ceramic ball economy performance, 24 hours is the optimum milling time.

3.3. Microstructure of ceramic balls

The cross-sections of ceramic balls without any treatment were analysed by SEM, and the results are shown in Fig. 5. Figure 5 shows that the average grain sizes of the balls prepared from raw materials milled for 6 h, 24 h, and 72 h were about 10 μm, 5–6 μm, and 3–4 μm, and the pore diameters were about 10 μm, 3 μm, and 2 μm, respectively. SEM microstructures indicate that with increasing raw material milling time, the as-prepared ball grain size, pore size, and porosity decrease, especially when the milling time is increased from 6 h to 24 h, which explains the decrease in balls wear rates and the increase in volume densities.

The prepared ceramic ball surfaces after milling with other balls and ultrasonic cleaning were observed under SEM, and the results are shown in Fig. 6. Comparing Fig. 6 with Fig. 5 indicates that the milled surface grain size was smaller than that inside the ceramics, suggesting that the balls were mainly worn by transcrystalline fracture.

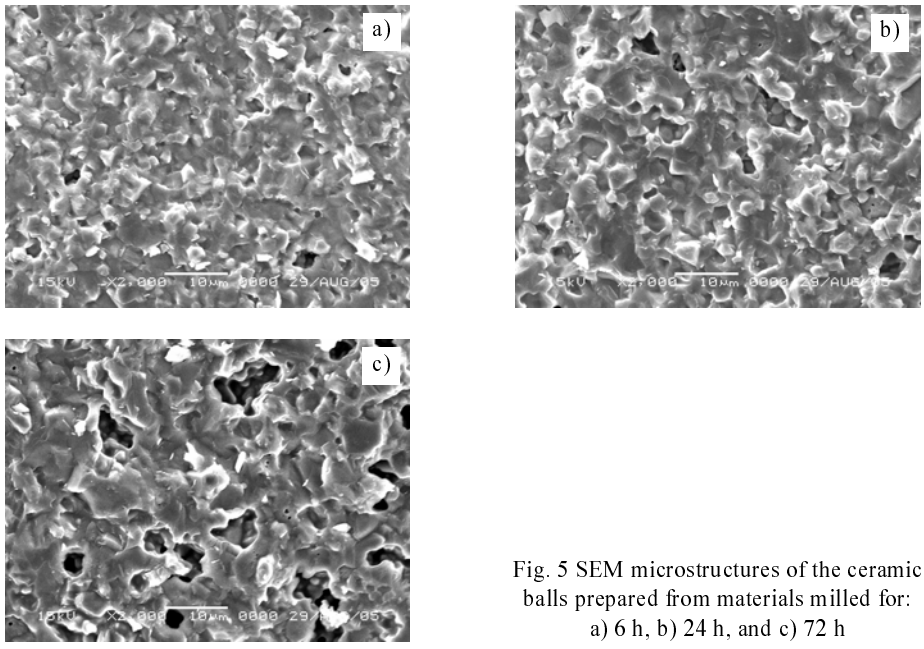

Fig. 5 SEM microstructures of the ceramic balls prepared from materials milled for: a) 6 h, b) 24 h, and c) 72 h

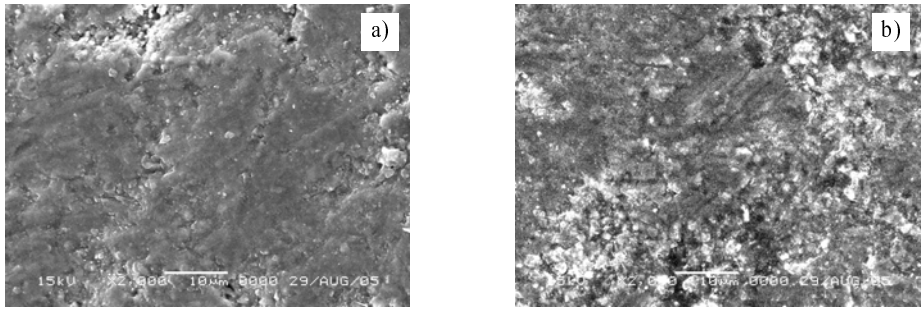

Fig. 6. SEM microstructures of the surfaces of ceramic balls prepared from materials milled for: a) 6 h, b) 72 h

During the milling process the large grains on the surface were first broken and worn off, and the remains were still combined as original adjacent crystals, then part of the remaining grain was further broken, and the remaining grains became smaller. The transcrystalline fracture explains the low wear rate of the prepared ceramic balls.

4. Conclusions

High performance alumina ceramic balls with 75% Al_2O_3 were prepared from aluminosilicate refractory waste. The particle size of aluminosilicate refractory waste decreased with increasing milling time, resulting in the decrease of sintering temperature and an increase in the density and wear resistance of the as-prepared ceramic

balls. The optimum milling time at the weight ratio of powder:media:water of 1:(3–6) :(1–1.5) was 24 hours. The wear rate of the reference ball, with 90% Al_2O_3, was 0.0537%/h, and the wear rate of the balls prepared from waste milled for 24 hours (and sintered at 1300 °C) and 72 h (sintered at 1285 °C) was 0.02272 %/h and 0.01886 %/h, respectively. The wear mechanism of the prepared balls was transcrystalline fracture.

Acknowledgements

This work was mainly supported by National Natural Science Fund of China, under Grant No. 50272016, 2003 Academic Degree Construction Fund of Guangxi Academic Degrees Committee, and partly by Natural Science Fund of Guangxi Education Department under the science research paper No. 20044.

References

[1] SHOUXIN T., Refract. Mater., 36 (2002), 339.
[2] NYSTROM H.E., KEHR W.R., POLLOCK J., Resour. Conserv. Recycl., 31(2001), 317.
[3] FANG H., SMITH J.D., PEASLEE K.D., Resour. Conserv. Recycl., 2599 (1999), 111.
[4] AY N., ÜNAL M., Cement Concrete Res., 30 (2000), 497.
[5] ZHONG L., WU B., ZHANG LI., Proc. World Engineers' Convention Shanghai, China, 2004, Vol. G (2004), p. 264.

Received 17 February 2006
Revised 28 March 2006

Materials Science-Poland, Vol. 25, No. 1, 2007

Photovoltaic performance of dye-sensitized ZnO solar cell based on Eosin-Y photosensitizer

P. SURI, M. PANWAR, R. M. MEHRA*

Department of Electronic Science, University of Delhi South Campus, New Delhi-110021, India

The paper reports on the fabrication and characterization of dye sensitized solar cells using ZnO due to its stability against photo-corrosion and photochemical properties similar to TiO_2. Thin films of nanocrystalline ZnO and Al-doped ZnO (AZO) were deposited on transparent conducting oxide glass using glass rod spreading method. Both doped and undoped ZnO films were found to be polycrystalline in nature. The ZnO electrode was dye sensitized by using an organic dye, Eosin-Y. The maximum quantum efficiency appears at the wavelength of 550 nm in both cases. However, the maximum quantum efficiency is higher (12%) in the case of ZnO cell electrode than AZO (7%) cell. The electric energy conversion efficiency was found to be 1.43% and 0.6% for undoped ZnO and Al-doped ZnO electrodes respectively. The lower conversion efficiency of the Al-doped ZnO solar cell could be attributed to lower injection efficiency due to less porosity in dye sensitized Al-doped ZnO electrode.

Key words: *ZnO electrode; dye sensitized solar cells; Eosin-Y*

1. Introduction

Since the pioneering work of Regan and Gratzel [1], a great attention has been paid to dye sensitized solar cells (DSSC) as cheap, effective and environmentally benign candidates for a new generation solar power devices [2]. DSSC is a photo-electrochemical device which effectively utilizes a property of nanocrystalline wide bandgap metal oxide semiconductor porous electrode. Generally, a DSSC consists of an indium-tin oxide (ITO), dye modified electrode, electrolyte and a counter electrode. When the DSSC is illuminated with sunlight, the dye absorbs the light and becomes excited. The absorption of light by the dye is followed by the injection of an electron from the excited state of the dye to the conduction band of the semiconductor. Simultaneously the oxidized dye is reduced by the electron donor in the electrolyte and returns to the ground state. The electrons in the conduction band of the semiconductor are collected at the counter electrode and flow through the external circuit.

*Corresponding author, e-mail: rammehra2003@yahoo.com

Through these processes, radiant energy is converted into electricity [3, 4]. It is understood [1] that cations influence the electron injection yield at the electrode. Optimization of DSSC is still a challenging task as it is a highly complex interacting molecular system. Surface-adsorbed cations exert a profound influence on the efficiency of DSSC. Further, the interfacial cations concentration also affects the stability of sensitizer surface attachment.

Nanoparticle TiO_2 is typically used as the photoanode material, made into a porous thick film (ca. 10 μm) by coating its colloidal paste onto a conductive glass substrate and sintering it at around 450 °C [5–11]. Alternative wide band gap metal oxide semiconductor such as ZnO [12] and Nb_2O_5 [13] have also exhibited decent performance when prepared into porous electrodes in the same manner. Although various dye molecules have been investigated as photo-sensitizers in the last decade, Ru complexes with carboxylated polypyridine ligand such as $Ru(dcbpy)_2(NCS)_2$ remains as one of the best sensitizers for TiO_2 [5]. Recently Keis et al. [14, 15] achieved the conversion efficiency of ~5% with a porous ZnO electrode prepared by the high-pressure compression method and sensitized with $Ru(dcbpy)_2(NCS)_2$. Nonomura et al. [16] have indicated that thinner films of ZnO and $Ru(dcbpy)_2(NCS)_2$ performed considerably better than thicker films synthesized by one step cathodic electrodeposition from oxygen-saturated aqueous solutions containing zinc chloride and the Ru complex. Particle size and shape, porosity, necking structure, film thickness, distance between electrodes, electrolyte composition and illumination direction are significant factors in DSSC. Thus it is also essential to compare various materials for fundamental understanding of nanostructured systems. Most of the research concerning nanostructured systems is based on particles around 10–40 nm in size. Rensmo et al. [17] reported that sensitized films consisting of 150 nm large Al-doped ZnO crystallites yield a solar energy conversion efficiency of 0.5%. Lee et al. [18] showed the variation of efficiency and fill factor with ZnO thin film thickness. The conversion efficiency of the solar cell was 2.4%. Law et al. [19] fabricated DSSCs with nanowires of ZnO and TiO_2 sensitized with $Ru(dcbpyH)_2(NCS)_2$. At a full sun intensity of 100mW/cm^2 the cell exhibited photoconversion efficiency $\eta \sim 1.5\%$.

In this paper, we report on the photo-conversion properties of undoped and Al-doped ZnO (AZO) films. The particle size of the ZnO particles was ~30 nm. The dye sensitized solar cell is fabricated using an organic dye, namely, Eosin-Y which is water soluble and approximately 1000 times cheaper than ruthenium bipyridyl complex dyes. The DSSCs are characterised for their quantum efficiency and other solar cell parameters. The efficiency of solar cells was found to depend on the porosity of the ZnO layer.

2. Experimental details

Electrode preparation. For the present work nanosize (~30 nm) ZnO powder (Finex 30, Sakai Chemical Industry, Japan) was used. The nanoporous semiconductor electrode was prepared by the glass rod spreading method. In order to break the ag-

gregates into separate particles, the ZnO powder was ground in a porcelain mortar with a small amount of deionised water containing poly(ethylene glycol) to prevent re-aggregation of the particles. The ITO glass substrates were covered on two parallel edges with adhesive tape to control the thickness of the ZnO film and to provide non-coated areas for electrical contact. Before deposition, the substrates were cleaned in acetone and methanol using an ultrasonic cleaner and etched with 10% aqueous HF solution for 10 sec. The colloid was applied to one of the edges of the conducting glass and distributed with a glass rod sliding over the tape-covered edges. After air drying, the electrode was sintered for 30 min. at 400 °C in air. Al_2O_3 (2 wt. %) was used as the dopant material to prepare aluminium doped ZnO. [20]

Dye sensitization. The dye (Eosin-Y) was used as received. The dye was dissolved in ethanol at the concentration of 3.2×10^{-4} M. Colouring of the ZnO surface with dye was carried out by soaking the film for 1 hr in a solution of the Eosin-Y in ethanol. The electrode was dipped into the dye solution while it was still hot at 80 °C. This process helps in the prevention of rehydration of the ZnO surface or capillary condensation of water vapours from ambient air inside the nanopores of the film. The presence of water in the pores decreases the injection efficiency of the dye. After dye adsorption, dye-coated films were rinsed in ethanol, dried by blowing N_2 stream and were kept in dark in an air tight case till the assembly of the cell.

Characterization of electrode. Thickness of ZnO layer was measured with a SF220 surface profiler. The thickness of the ZnO electrode was 6–9 μm. Absorption spectrum of Eosin-Y in ethanol adsorbed on ZnO and AZO thin films were recorded using a UV-spectrophotometer 1601. Surface morphology of the films was observed by a high resolution scanning electron microscope (SEM) JEOL JSM-6300. Incident photon conversion efficiency (IPCE) was also recorded using monochromatic light for various wavelengths. X-ray diffraction (XRD) patterns of the deposited films were taken by X'pert PRO Philips using CuK_α radiation.

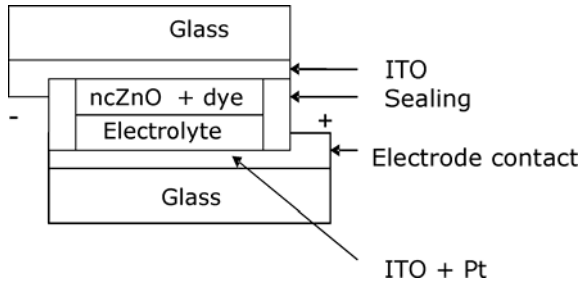

Fig. 1. Schematic diagram of DSSC

Fabrication of DSSC. The dye sensitized ZnO electrode was incorporated into a thin-layer sandwich-type solar cell with a spacer. The counter electrode was thin platinum sheet. The electrolyte solution was a mixture of 0.5 mol/dm^3 tetrapropyl-ammonium iodide and 0.05 mol/dm^3 iodine in ethylene carbonate and acetonitrile

mixed solvent (60:40 by volume). *I–V* characteristics were recorded with a computerized Keithley source meter (Model 2400). The active electrode area was typically 1 cm^2. The schematic diagram of DSSC is shown in Fig. 1.

3. Results and discussion

The X-ray diffraction pattern (Fig. 2) shows the polycrystalline nature of undoped and AZO films. Planes corresponding to (100), (002) and (101) are observed in the pattern. The SEM micrographs of undoped ZnO and AZO films are shown in Fig 3. Both undoped ZnO and AZO films exhibited porous structure. It is also revealed from the SEM micrographs that particle size in AZO films decreased and the microstructure of the film became denser. The increase in packing density resulted in the reduction of porosity [21].

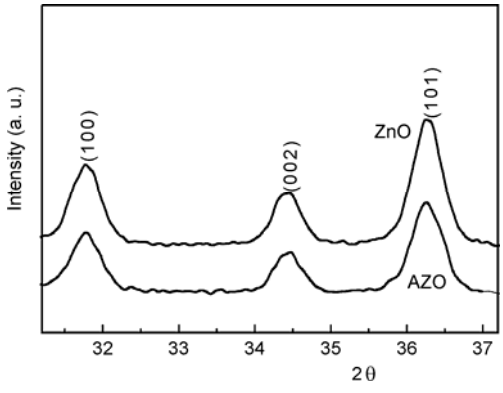

Fig. 2. X-ray diffraction pattern of undoped ZnO and doped ZnO films

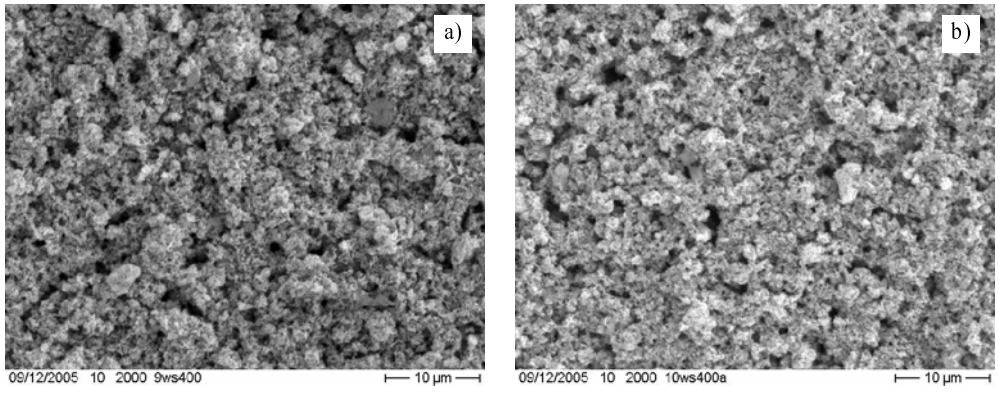

Fig. 3. SEM photographs of ZnO: a) undoped, b) doped

The absorption spectrum of Eosin-Y adsorbed on ZnO electrode and AZO electrode is shown in Fig. 4. The absorption spectra of 10^{-4} M solution of Eosin-Y in ethanol shows that this compound can absorb visible light in the range of 500–550 nm wavelength with

the characteristic absorption peak at 525 nm. Thus this compound absorbs light of appropriate wavelength and can be used as photo sensitizer for wide-band gap semiconductors such as ZnO (E_g = 3.2 eV) which alone cannot absorb visible light. It is seen from the figure that absorption of is lower in the AZO film as compared to the undoped ZnO.

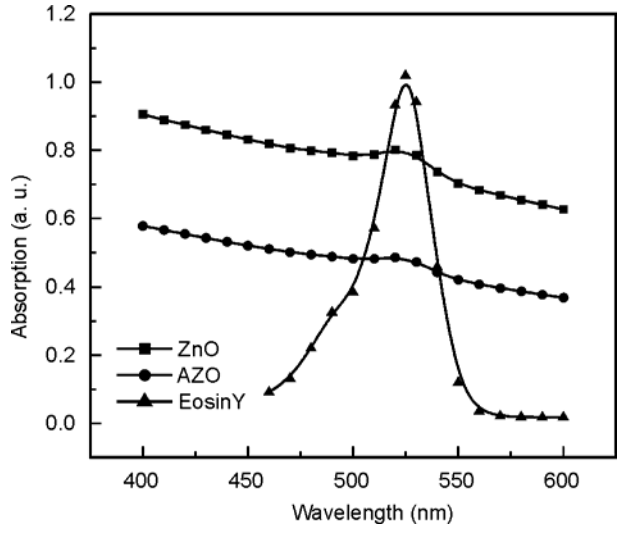

Fig. 4. Absorption spectra of aqueous solution of Eosin Y, ZnO/EosinY, AZO/Eosin Y films

The incident photon-to-current conversion efficiency (IPCE) value is the ratio of the observed photocurrent divided by the incident photon flux, uncorrected for reflective losses for optical excitation through the conducting glass electrode. The IPCE was calculated using the following relation [5]

$$\text{IPCE (\%)} = \frac{1250 \times \text{photocurrent density (A/cm}^2\text{)}}{\text{Wavelength (nm)} \times \text{photon flux (W/cm}^2\text{)}} \times 100$$

and is shown in Fig. 5. The maximum value of 53% at 520 nm for an undoped ZnO film was found to be higher than that for Al-doped film (50%). A low value of IPCE in AZO case may be attributed to high degree of charge carrier recombination. The observed value of maximum IPCE was comparable with the results obtained for TiO_2, [5] showing that ZnO-based electrodes can be considered as candidates for photoelectrochemical devices.

Figure 6 shows the quantum efficiency of the ZnO and AZO solar cell. The maximum quantum efficiency appears at the wavelength of 550 nm in both cases. However, the maximum quantum efficiency is higher (12%) in the case of ZnO cell electrode than AZO (7%) cell. Figure 7 shows the photocurrent–voltage characteristics of the solar cells based on the nano-structured ZnO/Eosin-Y electrode and AZO/Eosin-Y electrodes under white light illumination (100 mW/cm^2).

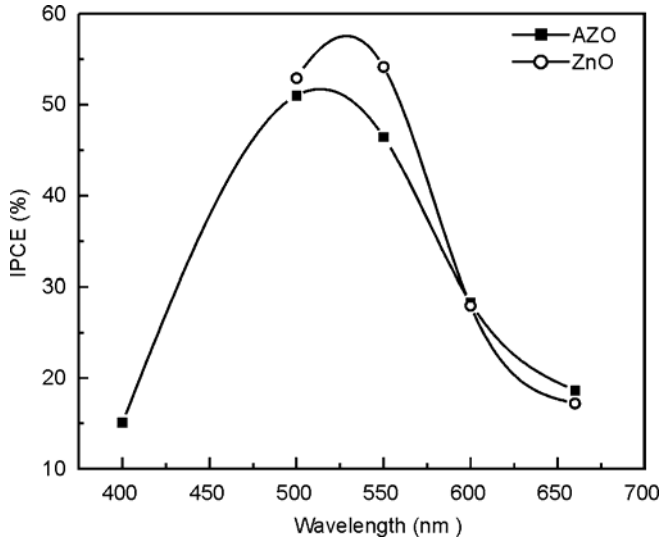

Fig. 5. Photocurrent action spectrum of ZnO/Eosin Y thin film electrode in comparison with Al-doped ZnO/Eosin Y electrode

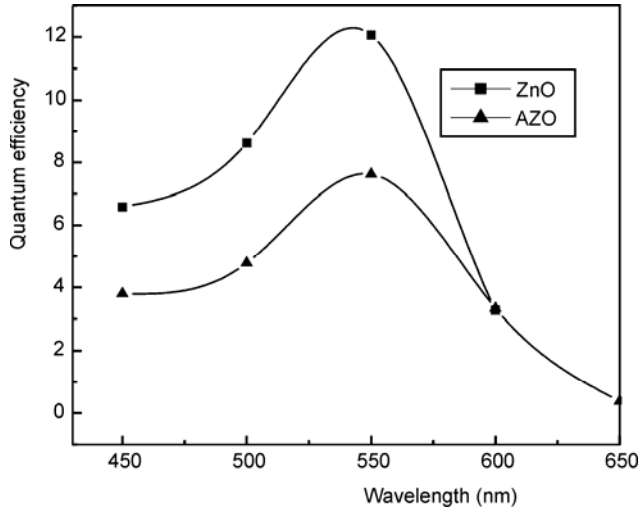

Fig. 6. Quantum efficiency of the ZnO/EosinY and AZO/EosinY solar cell

The energy conversion efficiency (η) and fill factor (FF) were evaluated using the following relations

$$\eta = \frac{I_m V_m}{P_{inc}}; \qquad FF = \frac{I_m V_m}{I_{sc} V_{oc}}$$

The short circuit photocurrent (I_{sc}), the open circuit voltage (V_{oc}), FF and η for the undoped ZnO electrode were found to be 4.0 mA/cm^2, 0.588 V, 61% and 1.43%, re-

spectively. I_{sc}, V_{oc}, FF and η for the AZO electrode were found to be 2.86 mA/cm^2, 0.425V, 50% and 0.6% respectively.

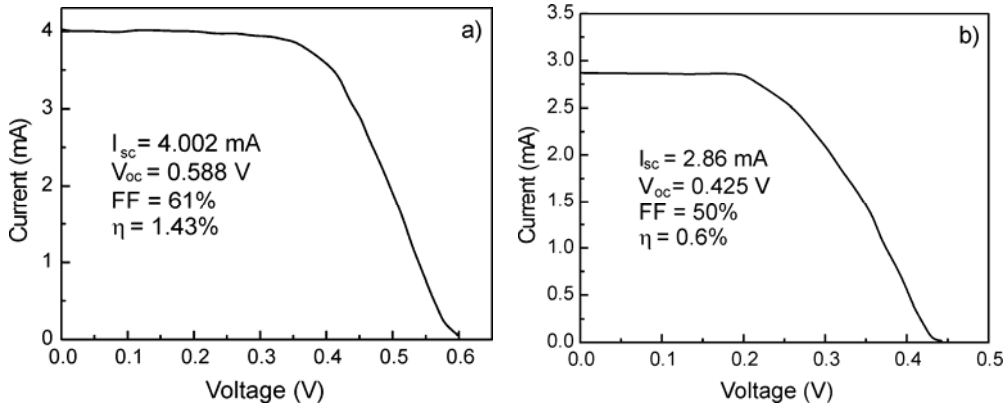

Fig. 7. Output power characteristics of the cell based on Eosin Y sensitized ZnO electrode (a) undoped and (b) doped

The lower energy conversion efficiency in AZO cell could be attributed to the lower porosity of the AZO film. Due to the lower porosity, a lower amount of dye is adsorbed in the film resulting in lower absorption of light as is also clear from Fig.4. The lower adsorption of dye and absorption of light reduces the injection efficiency of carriers and the energy conversion efficiency.

4. Conclusions

Dye sensitized solar cells using ZnO/Eosin-Y and AZO/Eosin-Y electrodes have been successfully fabricated. The maximum value of IPCE = 53% at 520 nm obtained in the present work is higher than the values reported earlier. The quantum efficiency of 12% is achieved in ZnO DSSC at 550 nm. The incident solar light to electric energy conversion efficiency was found to be 1.43% and 0.6% for undoped ZnO and Al-doped ZnO electrode respectively. The efficiency of the cell depends on the porosity of ZnO layer. The reason for lower efficiency of AZO solar cell could be attributed to the injection efficiency due to lower porosity.

Acknowledgement

This work was partly supported by DST, India and JSPS, Japan under India-Japan Co-operative Science Programme. Thanks are also due to Prof. K. L. Chopra for fruitful discussions.

References

[1] REGAN B.O., GRATZEL M., Nature, 353 (1991), 737.
[2] HAGFELDT A., GRATZEL M., Acc. Chem. Res. 33 (2000), 269.

[3] SMESTAD G., BIGNOZZI C., ARGAZZI R., Sol. Energy Mater. Sol. Cells, 32 (1994), 259.
[4] KIM S.S., YUM J.-H., SUNG Y.-E., Sol. Energy Mater. Sol. Cells, 79 (2003), 495.
[5] NAZEERUDDIN M.K., KAY A., RODICIO I., HUMPHRY-BAKER R., MULLER E., LISKA P., VLACHOPOULOS N., GRATZEL M., J. Am. Chem. Soc., 115 (1993), 6382.
[6] CERVINI R., CHENG Y., SIMON G., J. Phys. D: Appl. Phys., 37 (2004), 13.
[7] HARA K., NISHIKAWA T., KURASHIGE M., KAWAUCHI H., KASHIMA T., SAYAMA K., AIKA K., ARAKAWA H., Sol. Energy Mater. Sol. Cells, 39 (2005), 21.
[8] SEBASTIAN P.J., OLEA A., CAMPOS J., TOLEDO J.A., GAMBOA S.A., Sol. Energy Mater. Sol. Cells, 81 (2004), 349.
[9] WANG Z.S., SAYAMA K., SUGIHARA H., J. Phys. Chem. B, 109 (2005), 22449.
[10] FUKUI A., KOMIYA R., YAMANAKA R., ISLAM A., HAN L., Sol. Energy Mater. Sol. Cells, 90 (2006), 649.
[11] PERERA V.P.S., PITIGALA P.K.D.D.P., SENEVIRATHNE M.K.I., TENNAKONE K., Sol. Energy Mater. Sol. Cells, 85 (2005), 91.
[12] TENNAKONE K., BANADARA J., BANDARANAYAKE P.K.M., KUMARA G.R.A., KONNO A., Jpn. J. Appl. Phys., 40 (2001), 732.
[13] SAYAMA K., SUGIHARA H., ARAKAWA H., Chem. Mater., 10 (1998), 3825.
[14] KEIS K., MAGNUSSON E., LINSTROM H., LINDQUIST S.E., HAGFELDT A., Sol. Energy Mater. Sol. Cells, 73 (2002), 51.
[15] KEIS K., BAUER C., BOSCHLOO G., HAGFELDT A., WESTERMARK K., RENSMO H., SIEGBAHN H., J. Photochem. Photobiol. A, 148 (2002), 57.
[16] NONOMURA K., YOSHIDA T., SCHLETTWEIN D., MINOURA H., Electrochim. Acta, 48 (2003), 3071.
[17] RENSMO H., KEIS K., LINSTROM H., SODERGREN S., SOLBRAND A., HAGFELDT A., LINDQUIST E., WANG L.N., MUHAMMED M., J. Phys. Chem. B 101 (1997), 2598.
[18] LEE W.J., SUZUKI A., IMAEDA K., OKADA H., WAKAHARA A., YOSHIDA A., Jpn. J. App. Phys., 43 (2004), 152.
[19] LAW M., GREENE L.E., JOHNSON J.C., SAYKALLY R., YANG P., Nature Mater., 4 (2005), 455.
[20] SINGH A.V., MEHRA R.M., BUTHRATH N., WAHAHARA A., YOSHIDA A., J. Appl. Phys., 90 (2001), 11.
[21] LEE J.-H., PARK B.-O., Thin Solid Films, 426 (2003), 94.

Received 14 February 2006
Revised 1 May 2006

Materials Science-Poland, Vol. 25, No. 1, 2007

Energetics, electronic structure, and structure stability of the calcium alloying $Mg_{17}Al_{12}$ phase from first principles calculations

D. W. ZHOU*, P. PENG, J. S. LIU

School of Materials Science and Engineering, Hunan University, Changsha 410082, China

The energetics and electronic structure of the Ca alloying $Mg_{17}Al_{12}$ phase have been calculated using a first principles pseudopotential plane-wave method based on the density functional theory. According to the calculation results, the negative heat of formation and the cohesive energy of $(Mg_{17-x}Ca_x)Al_{12}$ (x = 0, 1, 4, 12) gradually increase when the Mg atoms at the I, II, III positions of the $Mg_{17}Al_{12}$ phase are substituted with Ca, which indicates that the alloying ability of $(Mg_{17-x}Ca_x)Al_{12}$ with the replacement of Ca for Mg(III) atoms is the strongest among the three substitutions and $(Mg_5Ca_{12})Al_{12}$ formed in this manner has the highest structural stability. After comparing the densities of states (DOS) for $(Mg_{17-x}Ca_x)Al_{12}$ (x = 0, 1, 4, 12), it is found that the increase in the structural stability of $Mg_{17}Al_{12}$ alloyed by Ca attributes to an increase in the bonding electron numbers at energy levels below the Fermi level, which mainly originates from the contribution of the valence electron numbers of Al (p) and Ca (s) orbitals.

Key words: *$Mg_{17}Al_{12}$ phase; pseudopotential plane-wave method; cohesive energy; electronic structure*

1. Introduction

Magnesium alloys have emerged as prospective candidates for numerous applications, especially in the automotive, aerospace, and electronic industries. Their good properties, such as low density, high specific strength, and damping capacity, make them promising replacements for many other structural materials, for instance steel, cast iron, and even aluminium. Widely used magnesium alloys belong to the Mg–Al-based series, exhibiting excellent castability, good room-temperature mechanical properties, and low cost. The use of these alloys, however, has been limited due to their poor heat resistance, especially poor creep property. It has been reported that the as-cast microstructure of Mg–Al-based alloys is composed of two phases:

*Corresponding author, e-mail: ZDWe_mail@yahoo.com.cn

α-Mg and β-$Mg_{17}Al_{12}$ [1]; β-$Mg_{17}Al_{12}$ is an essential phase playing an important role in strengthening the crystal boundary and controlling high-tempeature crystal running, whereas the softening of the phase at elevated temperatures is detrimental to the creep property of the alloys. Due to low cost, calcium has been used since the 1980s to improve the poor heat resistance properties of Mg–Al-based alloys. Ca alloying magnesium alloys are a relatively new development [2, 3].

Recent investigations [4, 5] have shown that the addition of calcium to Mg–Al -based alloys has the effect of increasing the melting point and enhancing the thermal stability of the $Mg_{17}Al_{12}$ phase at elevated temperatures, by forming the structure of $(Mg,Ca)_{17}Al_{12}$ solid solution and the valence electron structure (VES) of the $Mg_{17}Al_{12}$ phase with Ca replacing Mg atoms at III positions. According to calculations by Min et al. [6] based on the empirical electron theory (EET), when the dissolved calcium atoms are substituted for Mg(III) atoms in $Mg_{17}Al_{12}$, the distribution of the valence electrons on the main bonds becomes more uniform, leading to an increase in the melting point and thermal stability of $Mg_{17}Al_{12}$. The alloying ability and structural stability of the Ca alloying $Mg_{17}Al_{12}$ phase, however, have not been well studied yet from the alloy energy point of view. Based on previous work, a first principles plane-wave pseudo-potential method based on density functional theory is used in this paper to investigate the energetics and electronic structure of the Ca alloying $Mg_{17}Al_{12}$ phase. Moreover, the structural stability and electronic mechanism of these phases are also analysed and discussed, and some new results will be presented.

2. Crystalline structures

The $Mg_{17}Al_{12}$ phase has an A_{12}-type structure as shown in Fig. 1a. Its unit cell has the highest symmetry T_d^3, space group $I\bar{4}3m$, and 58 atoms with lattice parameters of a =10.5797Å. The atomic coordinates in the unit cell are:

- 2Mg(I): (0,0,0), (1/2,1/2,1/2);
- 8Mg(II): (x, x, x), ($-x$, $-x$, x) x = 0.32;
- 24 Mg(III): (x, x, z), (–x, –x, z), (–x, x, z), (x, –x, z), x = 0.36, z = 0.04;
- 24Al (x, x, z), ($-x$, $-x$, z), ($-x$, x, $-z$), (x, $-x$, $-z$) x = 0.09 z = 0.28.

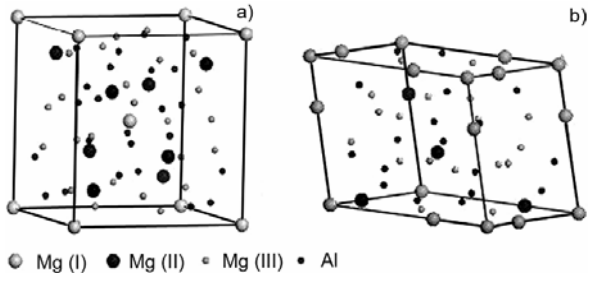

Fig. 1. The modes of the cell (a) and primitive cell (b) of the $Mg_{17}Al_{12}$ phase

The primitive cell of $Mg_{17}Al_{12}$ is used in the calculations is shown in Fig. 1b. The cell consists of 29 atoms, including 12 Al atoms, and 17 Mg atoms (1 Mg(I) atom, 4 Mg(II) atoms, and 12 Mg(III) atoms). In order to reduce computational cost, we have considered in this work structures with all Mg atoms at the I or II or III positions of the $Mg_{17}Al_{12}$ phase substituted with Ca. Hence, the corresponding structures of $Mg_{17}Al_{12}$ with calcium additions are $(Mg_{16}Ca)Al_{12}$, $(Mg_{13}Ca_4)Al_{12}$, and $(Mg_5Ca_{12})Al_{12}$.

3. Method of computation

The Cambridge Serial Total Energy Package (CASTEP) [7,8], a first principles plane-wave pseudopotential method based on the density functional theory [9] was used in this work. CASTEP uses a plane-wave basis set for the expansion of the single-particle Kohn–Sham wave functions, and psudopotentials to describe the computationally expensive electron–iron interaction, in which the exchange-correlation energy by the generalized gradient approximation (GGA) of Perdew is adopted for all elements in our models by adopting the Perdew–Burke–Ernzerhof parameters [10, 11]. Ultrasoft psudopotentials [12] represented in reciprocal space are used.

The atomic orbitals used in the present calculations are: Mg $2p^6 3s^2$, Al $3s^2 3p^1$, Ca $3s^2 3p^6 4s^2$. The cut-off energy of atomic wave functions (PWs), E_{cut}, was set at 330 eV. Sampling the irreducible wedge of the Brillouin zone was performed with a regular Monkhorst–Pack grid of special 6×6×6 *k*-points [13].

A finite basis set correction and the Pulay scheme of density mixing [14] were applied for the evaluation of energy and stress. All atomic positions in our model have been relaxed according to the total energy and force by using the Broyden–Flecher–Goldfarb–Shanno (BFGS) scheme [15], based on cell optimisation criterion: a RMS force of 5.0×10^{-6} eV/Å, stress of 0.01 GPa, and displacement of 5.0×10^{-4} Å. The calculation of the total energy and electronic structure was followed by the cell optimisation with a self-consistent-field (SCF) tolerance of 5.0×10^{-7} eV.

4. Results and discussion

4.1. Crystal structure

The atomic coordinates and lattice constants of the primitive cells of $Mg_{17}Al_{12}$, $(Mg_{16}Ca)Al_{12}$, $(Mg_{13}Ca_4)Al_{12}$, and $(Mg_5Ca_{12})Al_{12}$ are estimated from the minimized total energy, and the results are given in Tables 1 and 2. It is found that there are almost no changes in the space group structure of the $Mg_{17}Al_{12}$ phase, and in the atomic coordinates of the unit cell with and without the addition of Ca. Moreover, the present lattice constant *a* of $Mg_{17}Al_{12}$ is 9.057 Å, which is close to the experimental value of a = 9.145 Å (the value is obtained by converting the experimental lattice constant 10.56 Å [6] of the unit cell of $A_{12}Mg_{17}Al_{12}$), and the error of the lattice constant calcu-

lated here relative to the experimental result is about 0.962%. When the Mg atoms at the I, II, III positions of the $Mg_{17}Al_{12}$ phase are substituted with Ca, the lattice constants of the corresponding phases gradually increase, whereas the cell volume of the Ca alloying $Mg_{17}Al_{12}$ phase is in good agreement with the experimental result [6], for example the lattice constant 10.608Å of the $Mg_{16.5}Ca_{0.5}Al_{12}$ unit cell is larger than that of $Mg_{17}Al_{12}$. Hence, the computational parameters selected in this paper are suitable.

Table 1. The atomic coordinates of the $Mg_{17}Al_{12}$ phase, with and without the addition of Ca

Model		Mg(I)			Mg(II)			Mg(III)			Al		
		x	*y*	*z*	*x*	*y*	*z*	*x*	*y*	*z*	*x*	*y*	*z*
Calc.	$Mg_{17}Al_{12}$	0.5	0.5	0.5	0.328	0.328	0.328	0.356	0.356	0.040	0.090	0.090	0.274
	$(Mg_{16}Ca)Al_{12}$	0.5	0.5	0.5	0.322	0.322	0.322	0.357	0.357	0.038	0.091	0.091	0.277
	$(Mg_{13}Ca_4)Al_{12}$	0.5	0.5	0.5	0.317	0.317	0.317	0.355	0.355	0.029	0.090	0.090	0.274
	$(Mg_5Ca_{12})Al_{12}$	0.5	0.5	0.5	0.357	0.357	0.357	0.356	0.356	0.076	0.086	0.086	0.243
Exp. [6]	$Mg_{17}Al_{12}$	0.5	0.5	0.5	0.320	0.320	0.320	0.360	0.360	0.040	0.090	0.090	0.280

Table 2. Equilibrium lattice constant (*a*), formation heat (ΔH), and cohesive energy (E_{coh}) of the $Mg_{17}Al_{12}$ phase with and without the addition of Ca

Phase	*a* (Å)	E_{tot} (eV)	ΔH (eV·atom^{-1})	E_{coh} (eV·atom^{-1})
$Mg_{17}Al_{12}$	9.057	–17311.6439	–0.034	–2.465
$(Mg_{16}Ca)Al_{12}$	9.094	–17338.3387	–0.059	–2.508
$(Mg_{13}Ca_4)Al_{12}$	9.260	–17417.4775	–0.1023	–2.604
$(Mg_5Ca_{12})Al_{12}$	9.887	–17625.3379	–0.1085	–2.751

4.2. Heat of formation

The heat of formation (ΔH) of the $(Mg_{17-x}Ca_x)Al_{12}$ (x = 0, 1, 4, 12) primitive cell per atom was calculated using the following expression [16, 17]:

$$\Delta H = \frac{1}{29}\left[E_{tot} - (17-x)E_{solid}^{Mg} - xE_{solid}^{Ca} - 12E_{solid}^{Al}\right] \quad (1)$$

where E_{tot} refers to the total energy of the primitive cell at the equilibrium lattice constant, E_{solid}^{Mg}, E_{solid}^{Ca} and E_{solid}^{Al} are the single atomic energies of *hcp*-Mg, *fcc*-Ca and *fcc*-Al in the solid states, respectively, x refers to the numbers of the alloying Ca atoms. In this paper, we calculate the single atomic energy by the following method: at first, the energy of a pure metal crystal in the solid state was calculated, then the energy was divided by the number of atoms involved in the crystal, and this result is the energy of a single atom in the pure metal. The calculated energies of Mg, Al, and Ca atoms for our

considered systems were –977.87 eV, –57.24 eV and –1003.83 eV, respectively. The calculated heats of formation for $Mg_{17}Al_{12}$, $(Mg_{16}Ca)Al_{12}$, $(Mg_{13}Ca_4)Al_{12}$ and $(Mg_5Ca_{12})Al_{12}$ are also listed in Table 2. It was found that the heat of formation of the Ca alloying $Mg_{17}Al_{12}$ phases is always negative, which means that the structure of these phases can exist and be stable [18]. Since the negative heat of formation of Ca alloying $Mg_{17}Al_{12}$ phases gradually increases when the Mg atoms at the I, II, III positions of the $Mg_{17}Al_{12}$ phase are substituted with Ca, it can be concluded that the alloying ability of the $(Mg_{17-x}Ca_x)Al_{12}$ phase is the strongest when substituting Mg(III) atoms with Ca.

4.3. Cohesive energy

The cohesive energy (E_{coh}) of the $(Mg_{17-x}Ca_x)Al_{12}$ (x = 0, 1, 4, 12) primitive cell per atom was calculated using the following expression [17]:

$$E_{coh} = \frac{1}{29}\left[E_{tot} - (17 - x) E_{atom}^{Mg} - xE_{atom}^{Ca} - 12E_{atom}^{Al} \right] \quad (2)$$

where E_{atom}^{Mg}, E_{atom}^{Ca} and E_{atom}^{Al} are the total energies of isolated Mg, Ca, and Al atoms. The energy of a free atom is defined as the energy of the supercell with a free atom in the centre, while the lattice parameter of the supercell with the $P1$ space group is set to $a = 10$ Å. The calculated energies of Mg, Al, and Ca free atoms are –976.39 eV, –53.46 eV, –1001.84 eV, respectively. The cohesive energy of a single atom of the primitive cell is calculated from Eq. (2) and the results are listed in Table 2 and shown in Fig. 2.

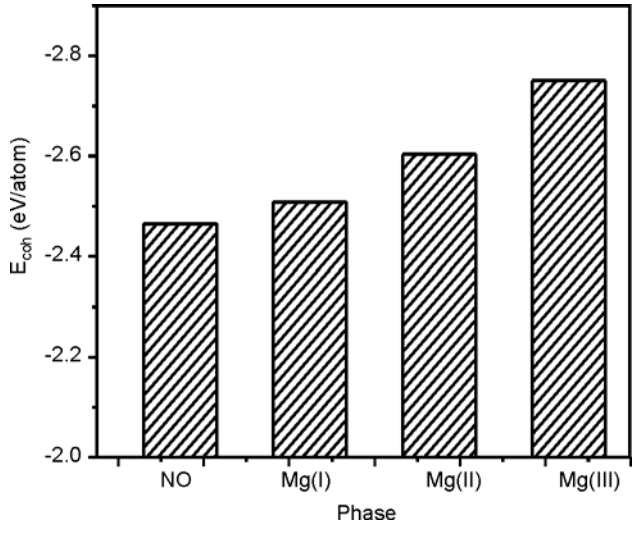

Fig. 2. Cohesive energy (E_{coh}) of the $Mg_{17}Al_{12}$ phase with and without addition of Ca. NO, Mg (I), Mg(II), and Mg(III) denote $Mg_{17}Al_{12}$, $(Mg_{16}Ca)Al_{12}$, $(Mg_{13}Ca_4)Al_{12}$, and $(Mg_5Ca_{12})Al_{12}$, respectively

It is found that the cohesive energy of the Ca alloying $Mg_{17}Al_{12}$ phase gradually increases when the Mg atoms at the I, II, III positions of the $Mg_{17}Al_{12}$ phase are substituted with Ca. This is due to the fact that the cohesive intensity and structural stability of the crystal are correlated with its cohesive energy [19] being defined as either the energy needed to form the crystal from free atoms or the work needed to decompose the crystal into isolated atoms. Moreover, Li et al. [20] have studied the correlation between the melting temperature and cohesive energy based on the Laves phases with the same space group structure. They found that the melting temperature of the Laves phases is roughly proportional to their cohesive energy, which means that the larger the cohesive energy, the more stable is the corresponding crystal structure. In the present work, since there are almost no changes in the structure of the $Mg_{17}Al_{12}$ phase and the atomic coordinates in the unit cell with and without the addition of Ca, it can be concluded that the structural stability of the $(Mg_{17-x}Cax)Al_{12}$ phase is the highest when Mg(III) atoms are replaced with Ca. Hence, the experimental result [6] on increasing the melting point and thermal stability of $Mg_{17}Al_{12}$ with the addition of Ca are well explained from the alloy energy point of view.

4.4. Density of states

An analysis of the total and partial density of states (DOS) of the Ca alloying $Mg_{17}Al_{12}$ phase is performed to understand the electronic structure mechanism of improving structural stability, and the total and partial DOSs of $Mg_{17}Al_{12}$, $(Mg_{16}Ca)Al_{12}$, $(Mg_{13}Ca_4)Al_{12}$, and $(Mg_5Ca_{12})Al_{12}$ primitive cells are plotted in Figs. 3 and 4. Before Ca alloying, it is found that the main bonding peaks between 0 eV and –10.0 eV originate from the contribution of the valence electron numbers of Mg (s), Al (s), and Al (p) orbitals (see Fig. 3a). When Mg atoms at the I positions of the $Mg_{17}Al_{12}$ phase are substituted with Ca, the contribution of valence electrons of $(Mg_{16}Ca)Al_{12}$ (Fig. 3b) in the energy range between 0 eV and –10.0 eV is the same as that of $Mg_{17}Al_{12}$ but there is a new bonding peak between –20 eV and –25 eV, dominated by the valence electron numbers of Al (p) orbitals. When the Mg atoms at the II and III positions of the $Mg_{17}Al_{12}$ phase are substituted with Ca atoms, the contribution of valence electrons of $(Mg_{13}Ca_4)Al_{12}$ (Fig. 3c) and $(Mg_5Ca_{12})Al_{12}$ (Fig. 3d) in the energy range between 0 eV and –10.0 eV is almost the same as that of $Mg_{17}Al_{12}$ but there is a contribution from Ca atoms to the peaks. The peak between –20 eV and –25 eV also originates from the valence electron numbers of Al (p) orbitals, but the altitude of the peak is significantly increased compared to that of $(Mg_{16}Ca)Al_{12}$.

A further analysis of the total DOS (Fig. 4) of $Mg_{17}Al_{12}$, $(Mg_{16}Ca)Al_{12}$, $(Mg_{13}Ca_4)Al_{12}$, and $(Mg_5Ca_{12})Al_{12}$ was done. It was found that the main bonding peaks of $Mg_{17}Al_{12}$ are located from 0 eV to –10.0 eV, the peaks of $(Mg_{16}Ca)Al_{12}$ are similar to those of $Mg_{17}Al_{12}$, and the heights of the peaks are not significantly changed, but there is a new bonding peak between –20 eV and –25 eV. The height of the new peak is 10.97 electronic states/eV, which indicates that the bonding electron numbers of $Mg_{17}Al_{12}$ with the addition of Ca increase in the low energy range far below the Fermi level.

Hence, the structure of $Mg_{17}Al_{12}$ with Mg(I) atoms replaced with Ca is more stable than that of $Mg_{17}Al_{12}$ [21, 22].

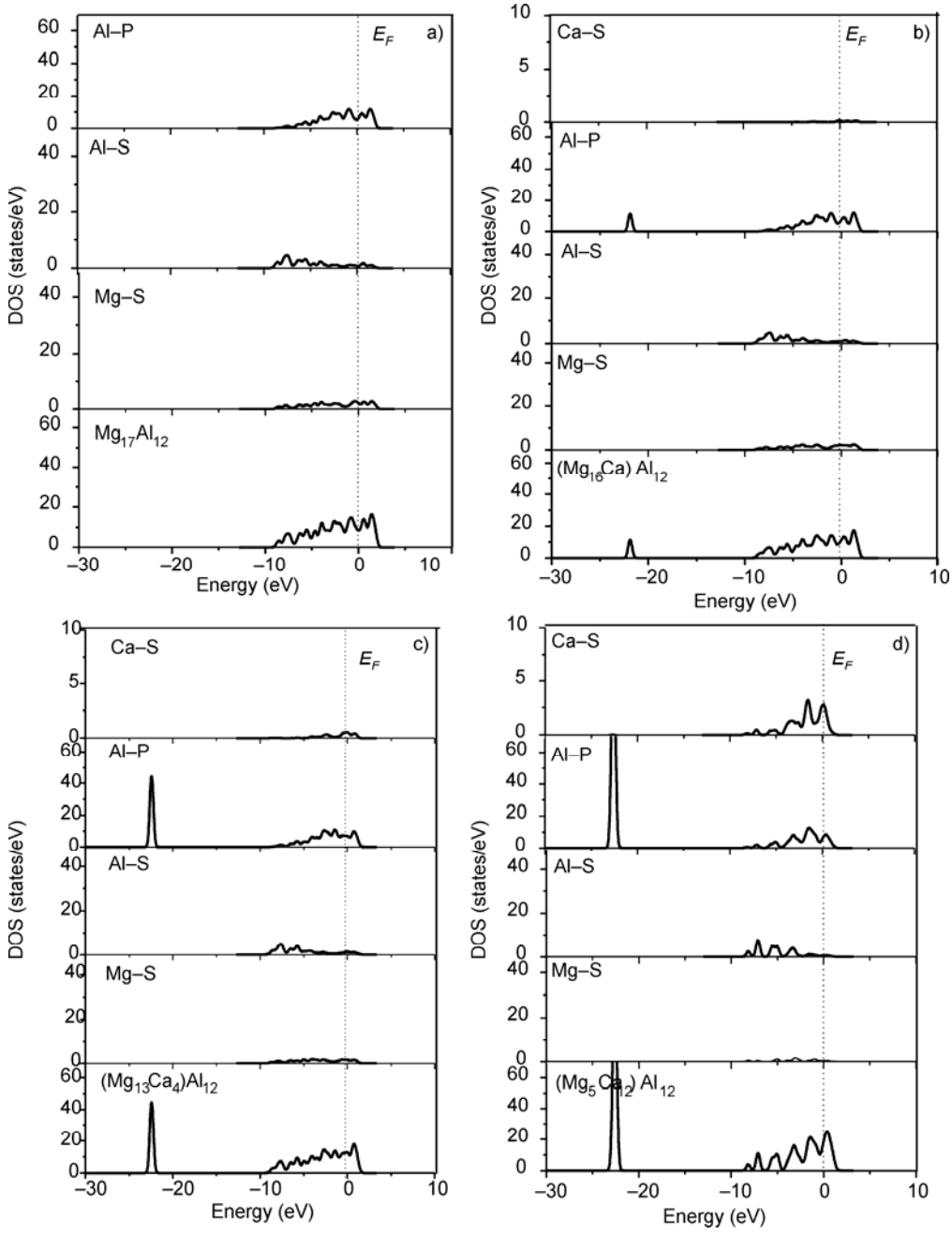

Fig. 3. Partial DOS of Ca alloying $Mg_{17}Al_{12}$ phases:
a) $Mg_{17}Al_{12}$, b) $(Mg_{16}Ca)Al_{12}$, c) $(Mg_{13}Ca_4)Al_{12}$, d) $(Mg_5Ca_{12})Al_{12}$

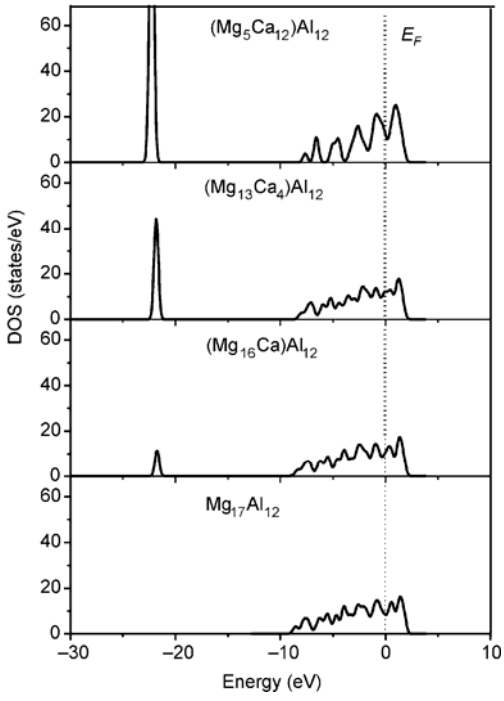

Fig. 4. Total DOS of Ca alloying $Mg_{17}Al_{12}$ phase

When the Mg atoms at the II and III positions of the $Mg_{17}Al_{12}$ phase are substituted with Ca, the main bonding peaks of $(Mg_{13}Ca_4)Al_{12}$ and $(Mg_5Ca_{12})Al_{12}$ are also located from 0 eV to –10.0 eV, but the heights of these peaks are significantly larger. Especially between –20 eV and –25 eV, there is a new, higher bonding peak, and the height of the new peak is 43.45 electronic states/ eV and 125.45 electronic states/eV for $(Mg_{13}Ca_4)Al_{12}$ and $(Mg_5Ca_{12})Al_{12}$, respectively. Based on the above analysis, as far as $(Mg_5Ca_{12})Al_{12}$ is concerned, it is found that the number of bonding electrons from 0 eV to –10.0 eV and from –20 eV to –25 eV exceeds that in $Mg_{17}Al_{12}$, $(Mg_{16}Ca)Al_{12}$ or $(Mg_{13}Ca_4)Al_{12}$. The higher the number of bonding electrons, the stronger are electrostatic interactions. Furthermore, the presence of electrons in the energy range far below the Fermi level will lead to a more stable structure. Hence, the $Mg_{17}Al_{12}$ phase with Mg (III) atoms replaced by Ca has the highest structural stability among the three studied substitutions.

5. Conclusions

The energetics and electronic structures of Ca alloying $Mg_{17}Al_{12}$ phase were investigated using a first principles plane-wave pseudopotential method based on the density functional theory. The results show that the negative formation heat and cohesive energy of $(Mg_{17-x}Ca_x)Al_{12}$ (x = 0, 1, 4, 12) phases gradually increase when the Mg atoms at the I, II, III positions of the $Mg_{17}Al_{12}$ phase are substituted with Ca, indicat-

ing that the alloying ability of the $(Mg_{17-x}Ca_x)Al_{12}$ phase for replacing Mg(III) atoms with Ca is the strongest, and the $(Mg_5Ca_{12})Al_{12}$ phase formed in this manner has the highest structural stability. Upon comparing the densities of states of $(Mg_{17-x}Ca_x)Al_{12}$ (x = 0, 1, 4, 12) phases, it is found that the increase in the structural stability of the $Mg_{17}Al_{12}$ phase alloyed by Ca contributes to the increase in the bonding electron numbers in the lower energy level below the Fermi level, which originates mainly from the contribution of the valence electron numbers of Al (p) and Ca (s) orbitals.

Acknowledgements

This work was supported by the Ph.D. Programs Foundation of the Ministry of the Education of China (20020530012).

References

[1] LUO A., PEKGULERYUZ M.O., J. Mater. Sci., 29 (1994), 5259.
[2] MIN X.G., SUN Y.S., XUE F., DU W.W., WU D.Y., Mater. Chem. Phys., 78 (2003), 88.
[3] SHAW C., JONES H., Mater. Sci. Tech, 15 (1999), 78.
[4] REGEV M., AGHION E., ROSEN A., Mater. Sci. Eng. A, 234–236 (1997), 123.
[5] MIN X.G., SUN Y.S., YUAN G.Y., DU W.W., XUE F., Chin. J. Nonferr. Met., 12 (2002), 166.
[6] MIN X.G., DU W.W., XUE F., SUN Y.S., Chin. Sci. Bull., 47 (2002), 109.
[7] PAYNE M.C., TETER M.P., ALLEN D.C., ARIAS T.A., JOANNOPOULOS J.D., Rev. Mod. Phys., 64 (1992), 1045.
[8] SEGALL M.D., LINDAN P.J.D., PROBERT M.J., PICKARD C.J., HASNIP P.J., CLARK S.J., PAYNE M.C., J. Phys. Cond. Matter, 14 (2002), 2717.
[9] HOHENBERG P., KOHN K., Phys. Rev. B, 136 (1964), 864.
[10] HAMMER B., HANSEN L.B., NORKOV J.K., Phys. Rev. B, 59 (1999), 7413.
[11] WHITE J.A., BIRD D.M., Phys. Rev. B, 50 (1994), 4954.
[12] VANDERBILT D., Phys. Rev. B, 41 (1990), 7892.
[13] MONKHORST H.J., PACK J.D., Phys. Rev. B, 13 (1976), 5188.
[14] FRANCIS G.P., PAYNE M.C., J. Phys. Cond. Matter, 19 (1990), 4395.
[15] MARLO M., MILMAN V., Phys. Rev. B, 62 (2000), 2899.
[16] MEDVEDEVA N.I., GORNOSTYREV Y.N., NOVIKOV D.L., MRYASOV O.N., FREEMAN A.J., Acta Mater., 46 (1998), 3433.
[17] SAHU B.R., Mater. Sci. Eng. B, 49 (1997), 74.
[18] SONG Y., GUO Z.X., YANG R., LI D., Acta Mater., 49 (2001), 1647.
[19] ZUBOV V.I., TRETIAKOV N.P., TEIXEIRA RABELO J.N., SANCHEZORTIZ J.F., Phys. Lett. A, 198 (1995), 470.
[20] LI C., HOE J.L., WU P., J. Phys. Chem. Solids, 64 (2003), 201.
[21] FU C.L., WANG X. D., YE Y.Y., HO K.M., Intermetallics, 7 (1999), 179.
[22] NYLEN J., GARCIA F.J., MOSEL B.D., PÖTTGEN R., HÄUSSERMANN U., Solid State Sci., 6 (2004), 147.

Received 23 February 2006
Revised 14 June 2006

Materials Science-Poland, Vol. 25, No. 1, 2007

Evaluation study of cast Al–SiC_p composites

J. T. AL-HAIDARY[1*], A. S. JABUR AL-KAABY

Department of Materials and Metallurgical Engineering,
Al-Balqa Applied University, Al-Salt 19117 Jordan

Department of Production Engineering and Metallurgy,
University of Technology Baghdad, 12906 Baghdad, Iraq

The present work is concerned with the wear properties of aluminium matrix–SiC particles cast composites. It was found that introduction of SiC particles into Al alloys causes a drastic reduction in the wear rate. With SiC content above 13.5 wt. %, however, the wear rate starts to increase again. The particle size of 25 μm is optimum for the improvement of wear resistance compared to other sizes (1 and 125 μm). The friction coefficient and sliding surface temperature decrease with increasing particles content.

Key words: *Al–SiC_p composite; wear rate; friction coefficient; temperature*

1. Introduction

In tribological applications, aluminium alloys are desirable because of their low densities and cost, but their relatively poor wear resistance has impeded progress in this direction. Therefore, the development of aluminium–ceramic particulate composites could significantly increase wear resistance, assuring these composites considerable applications in industry [1, 2].

Mechanical properties of particle-filled metal-matrix composites are not considerably enhanced, but the tribological properties are clearly improved. Soft solid lubricant particles like graphite and mica improve the antiseizing properties of aluminium alloys. The most promising application of cast graphitic–aluminium composites is for bearings that would be cheaper and lighter in addition to being self-lubricating when compared to the bearings currently made of alloys containing Cu, Pb, Sn, and Cd. The use of graphite in automobile engine pistons considerably reduces the wear of cylinder liners as well as improves fuel efficiency and reduces frictional horse power losses.

[*]Corresponding author, e-mail: Jalhaidary@yahoo.com

Hard particles like SiC, Al_2O_3, WC, TiC, ZrO, and BC greatly improve the abrasive resistance of aluminium alloys, especially at elevated temperatures. Such composites find applications in a number of components, including impellers, pistons, piston rings, cylinder liners, connecting rods, machine shrouds, brake systems, and other tribological systems that run at relatively high temperatures. They have also been tried as turbocharger impellers that run at high temperatures [3]. Finally, SiC is considered to be an optimal reinforcement phase for aluminium and its alloys, because it has low density, only one slightly higher than aluminium, a high modulus and strength, and it is readily available at low cost.

The effects of high energy ultrasonic vibrations and other parameters on some properties of Al–SiC_p composites have been studied by Al-Haidary and Al-Kaaby [4]. The present work focuses on the tribological properties (wear rate, friction coefficient, and sliding surface temperature), since the Al–SiC particulate composite has been classified mainly as a tribological material.

2. Experimental

In our previous work [4], several ingots with different combinations of SiC particle contents and sizes have been prepared. These samples were used in this work as well. A pin-on-disc machine (Fig. 1) was used to investigate the manufactured composites.

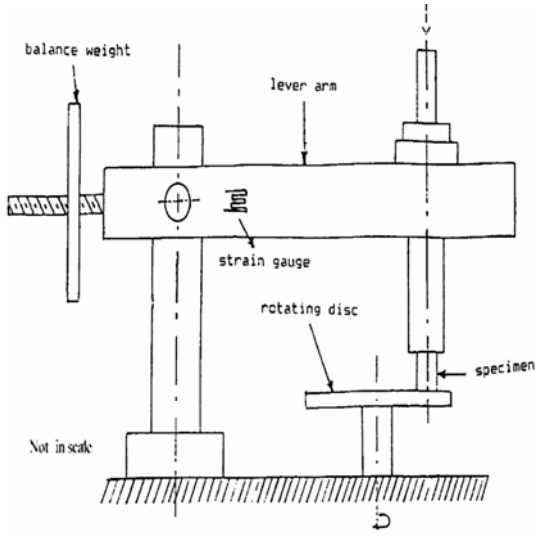

Fig. 1. A scheme of the pin-on-disc apparatus

For this purpose, seven ingots with different SiC contents, three ingots with different SiC particle sizes, and three with various amounts of magnesium in addition to the

base one were prepared, as shown in Tables 1–3. The tests were conducted to study the effect of SiC particle content, size, and Mg wt. % on the wear rate, friction coefficient and sub-surface temperature of the composites under two loads, namely 10 and 20 N.

The as-cast composites were machined on lathe to prepare 10×25 mm^2 rod samples. One base of each sample was ground with 1000 grit silicon carbide paper, then polished with 0.25 μm alumina, cleaned with water, degreased with ethanol, and dried. A hardened, 45HRC, carbon steel counterface disc was used.

Table 1. The compositions of Al–SiC composites[1]

Code	Mg content [wt. %]	Retention [wt. %]
A1	0.001	13.5
A2	0.45	14.6
A3	0.8	19.1
A4	3.8	21.4
A5	5	21.9
A6	6.6	22.5

[1]Average particle size – 25 μm.

Table 2. The composition of Al composites containing SiC particles with three different sizes

Code	Average particle size [μm]	Mg content [wt. %]	Retention [wt. %]
C1	1	0.85	8.1
C2	25	0.9	19.1
C3	125	0.9	14.0

Table 3. The composition of Al-matrix alloys

Code	Mg content [wt. %]
B	0.001
B1	1.2
B2	2.7
B3	4.9

Wear rates were calculated by measuring the weight loss of the sample using a sensitive balance with an accuracy of 0.1 mg. The formula used to convert the weight loss into wear rate is:

$$\text{Wear rate} = \frac{\Delta W}{S} \qquad [\text{mg}\cdot\text{cm}^{-1}]$$

where ΔW is the weight difference of the sample before and after the test in mg, S is total sliding distance in cm.

To estimate the friction coefficient, the friction force was measured between the pin and the disc surfaces. For this purpose, two strain gauges were cemented on the vertical faces of the lever arm (Fig. 1) and the elastic bending strain of the lever arm was measured. An estimate of the heat generated at the sliding interface due to friction was obtained by impeding a thermocouple head in a deep hole near the rubbing surface of the pin by about 1 mm. The readings of the thermometer can be used for comparing between different composites and metal cases as particle content and size are changed, and thereby their role in generating heat at the rubbing surface.

3. Results and discussion

The effect of magnesium additions alone (base aluminium, that with 1.2, 2.7 and 4.9 wt. % Mg) on the wear rate were also taken into account. Figure 2 shows the positive role of adding Mg on the wear rate of Al. This is due to the solution hardening of Mg in Al. As a consequence, the wear resistance of the alloys increased somewhat.

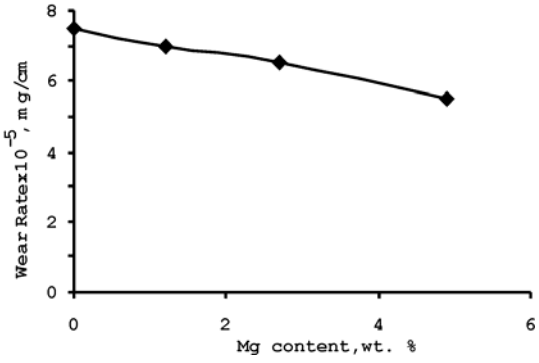

Fig. 2. Wear rate vs. Mg content (wt. %) in Al at a 10 N load.
The wear rate values were taken at a steady state, i.e. after 180 min

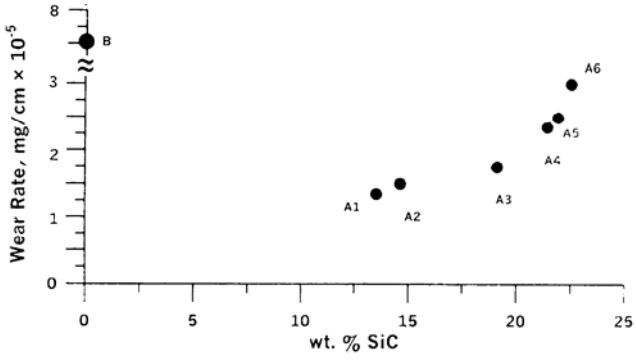

Fig. 3. Wear rate vs. SiC content for various Al-alloy matrices (load – 10 N,
SiC average particle size – 25 μm, wear rate values taken after 180 min of sliding time)

The main indication which can be noticed from Fig. 3 is that the introduction of SiC particles (25 μm) to the matrix alloy (B) reduced the wear rate drastically. Increasing SiC content from 13.5 wt. % to 22.5 wt. % by adding Mg, however, increased the wear rate to some extent.

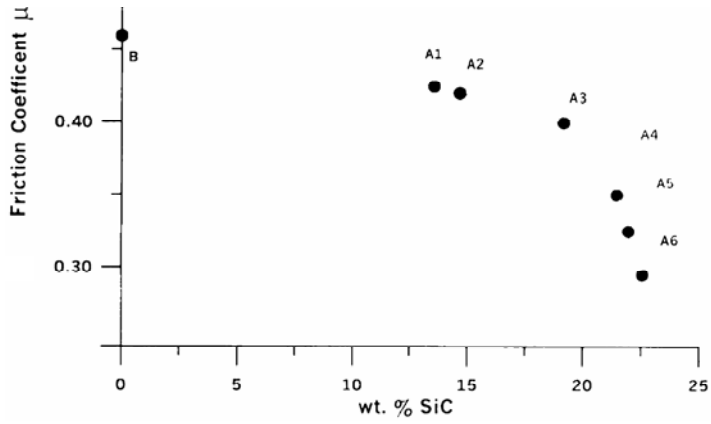

Fig. 4. Friction coefficient vs. SiC content for various Al-alloy matrices (load – 10 N, SiC average particle size – 25 μm, the values of the friction coefficient were taken after 180 min of sliding time)

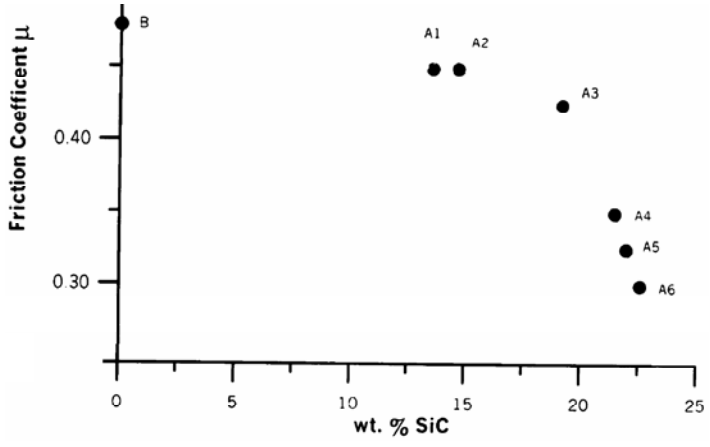

Fig. 5. Friction coefficient vs. SiC content for various Al-alloys matrices (load – 20 N , SiC average particle size – 25 μm, the values of the friction coefficient were taken after 180 min of sliding time)

The improvement in wear resistance accompanying the presence of ceramic particles in the aluminium matrix is due to an increase in average hardness [5, 6] and to reduction of the friction coefficient (Figs. 4, 5). This has been confirmed by Sato and Mehrabian [5] and Hosking et al. [6] for the aluminium matrix–Al_2O_3 system, by Rohatgi and Surappa [7] for the aluminium matrix–SiC system, by Rohatgi et al. [8] for the aluminium matrix–SiO_2 system, and by Rohatgi et al. [9, 10] for the aluminium matrix–zirconia system. The change in behaviour of the curve in Fig. 3 accompanying

the increase in SiC content from 13.5 wt. % to 22.5 wt. % can be explained by the fact that delamination is the dominating mechanism in the wear of matrix alloys (Fig. 6a) and composites (Figs. 6b–6d) where worn surfaces of samples B, A1, A4 and A6 are shown.

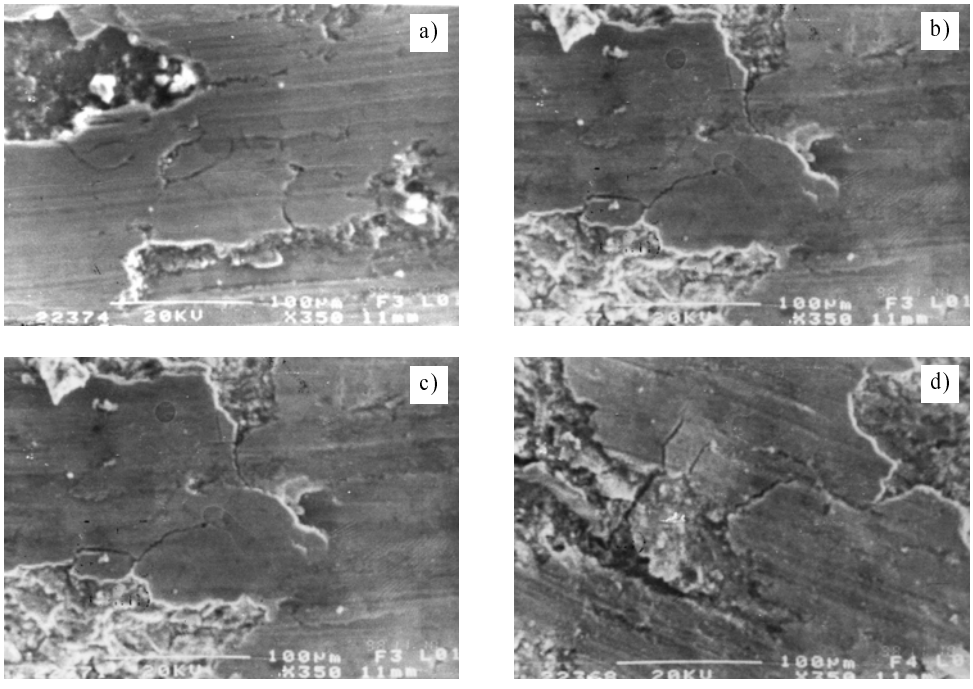

Fig. 6. Worn surfaces of the samples: a) 3, b) A1, c) A4 and d) A6;
load – 10 N, sliding time – 180 min, magnification 250×

It is clear that the addition of Mg to the composite improves wettability [4], but generally the adhesion between SiC surfaces and the aluminium matrix is poor due to the formation of a weak Al_4C_3 layer around SiC particles [11]. As a result, the interface will be more or less equivalent to pre-existing cracks. Therefore, although the hardness increases with an increasing volume fraction of reinforcements in the matrix, the wear rate also increases owing to the increasing number of pre-existing cracks and to the decreasing distance that a crack must propagate to link with other cracks. Figure 6 shows the wear tracks of unreinforced alloy (B), the tendency to form delaminated wear flakes, and the final surface cracking. Suh et al. [12–14] have overviewed the mechanism of wear and proposed that the crackings result from the repeated surface tracting exerted by the hard asperities of the steel counterface. They state that plastic shear deformation accumulates with repeated loading, causing the cracks to nucleate below the surface, because nucleation on the surface is not favoured due to compression stress existing just below the contact region. Once the cracks are present (owing either to crack nucleation or to pre-existing voids), further loading and defor-

mation cause cracks to extend and propagate, and join neighbouring ones. Finally, the cracks extend to the surface at certain weak positions. Proof of delamination theory (cracks and holes) are clearly seen in Figs. 6b–6d which show the worn surfaces of composites A1, A4, and A6. This is due to the fact that there are many cracks propagating at the aluminium matrix–SiC interface. These cracks increase with increasing SiC particle content, which causes a reduction in the distance that a crack must propagate to link with others.

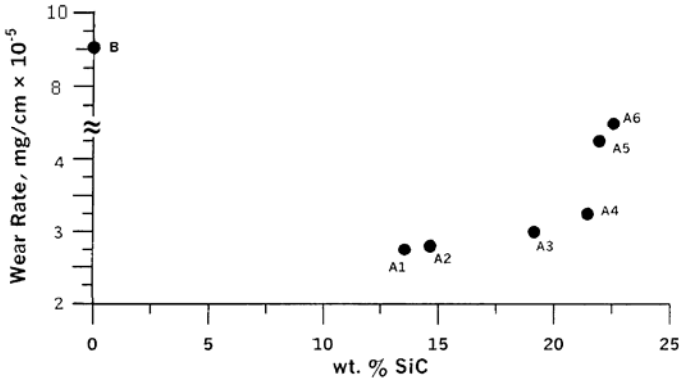

Fig. 7. Wear rate vs. SiC content for various Al-alloys matrices (load – 20 N, SiC average particle size – 25 μm, wear rate values taken after 180 min of sliding time)

Many investigators [7, 6, 15, 17], studied the wear behaviour of various aluminium-matrix composites. They confirmed our results on the reduction of wear rate with the addition of ceramic particles (Figs. 3 and 7), but none of them have stated that wear rate starts to increase again when particle content further increases above a specified limit. This phenomenon may depend on the nature of the particle–matrix interface, which also depends on many other factors, such as the ceramic phase type and shape, manufacturing method, the testing load, and manufacturing conditions.

Returning to Fig. 3, it can be noticed that the aluminium matrix–SiC particulate composites resist adhesive wear better than the matrix alloys (B in Fig. 2) for all volume fractions of SiC particles. Bhansali and Mehrebian [18], on the other hand, stated that composites containing SiC particles offered virtually no or moderate improvement in wear resistance at different loads. They attributed this poor improvement to the brittle interface between SiC particles and aluminium matrix alloy which facilitates shearing unable to resist the action of the adhesive wear under loads.

Figure 8 illustrates the variation of wear rate with particle size under the 10 N load. To prevent confusion resulting from mixing the variations of particle content and particle size, one can return to Fig. 3 and use the effect of particle content on wear rate as a reference when investigating the effect of particle size on wear resistance alone. From Figure 8 it is obvious that a particle size of 25 μm was optimum for improving wear resistance compared to other sizes (1 and 125 μm). The wear resistance improvement of aluminium-matrix composites that accompanied increasing

reinforcement particle size agrees with some previous works [6, 18], since the agglomeration tendency of fine particles (1 μm, Fig. 9) leads to a decrease in the wear resistance due to the reduction of bulk mechanical properties [4], whereas other variables are kept constant.

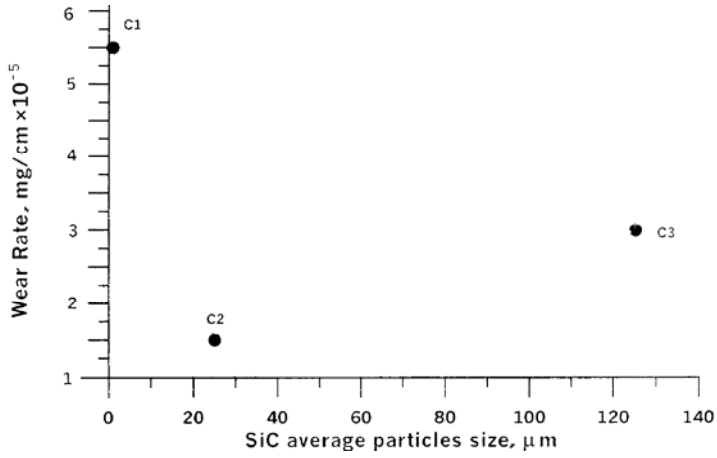

Fig. 8. Wear rate vs. SiC average particle size (load – 10 N, C2 = A3, wear rate values taken after 180 min of sliding time)

The deterioration of wear resistance that accompanied increasing particle size from 25 to 125 μm has not been reported before this study. This can be explained referring again to the delamination mechanism of wear. The crack propagation rate controls the wear rate rather than the crack nucleation rate in materials containing a weakly bonded second phase [14]. Therefore, the coarsening of SiC particles means that the pre-existing crack sizes increase, resulting in the ease of crack propagation and linking with other cracks. The relative wear rate increasing in the 125 μm particle sample can be due to fragmentation fracturing and there may be some dissolution of these particles in the matrix (Fig. 10).

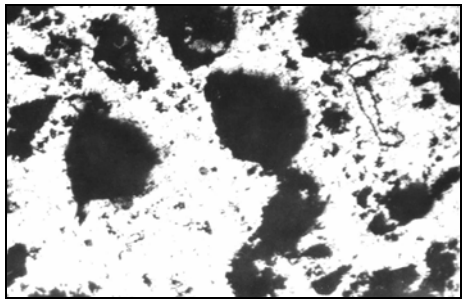

Fig. 9. Agglomeration of fine particles in sample C1, magnification 70×

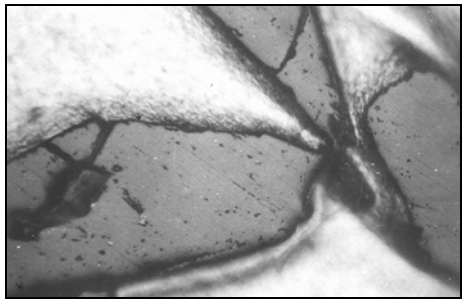

Fig. 10. Fragmentation and possibly some dissolution of large particles, magnification 300×

The steady state value of the coefficient of friction μ is plotted against particle content in Fig. 4. The figure shows that, in general, the addition of ceramic particles to the aluminium alloy matrix reduces the coefficient of friction continuously with increasing particle content. This can be attributed to an overall hardening effect that resulted from increasing the ceramic particle volume fraction. An identical result has been reported by Hosking et al. [6].

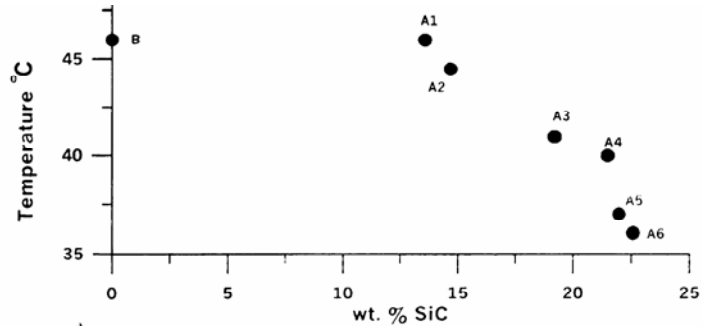

Fig. 11. Rubbing subsurface temperature vs. SiC content for various Al-alloy matrices (load – 10 N, SiC average particle size – 25 μm, temperatures were taken after 27 min of sliding time, i.e. at a temperature steady state)

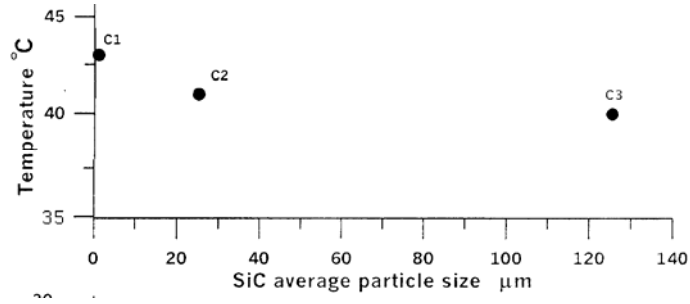

Fig. 12. Rubbing surface temperature vs. SiC average particle size (load – 10 N, C2 = A3, temperatures were taken after 27 min of sliding time)

Figures. 114 and 12 develop the effect of particle content and size, respectively, on the sample near (1 mm) surface temperature during sliding. From Figure 11 it can be seen that the temperature decreases with increasing SiC particle content. This is due to the reduction in the friction coefficient (Figs. 4, 5). Figure 12 shows a narrow range of temperature change. It is not reasonable to attribute this temperature change to the variation in particle size alone, and the particle content should be taken under consideration as well. Figures 5, 7, 13 and 14 describe previous experiments with the 20 N load. They show that the general trend is equivalent, although the applied load is higher.

The influence of particle size on the coefficient of friction under the 20 N load is illustrated in Fig. 15. From this figure it can obviously be recognized that the compos-

ite containing the finer size (1 μm) has a lower friction coefficient compared to other samples, taking the effect of the difference in particle content under consideration (Fig. 5). This is in agreement with the results of Hosking et al. [6]. As a result of the agglomeration tendency of the fine particles, they are easily pulled out of the matrix and produce three-body abrasive wear conditions or a ceramic particle separating layer between the two sliding metals, which obviously results in a reduction of the friction coefficient.

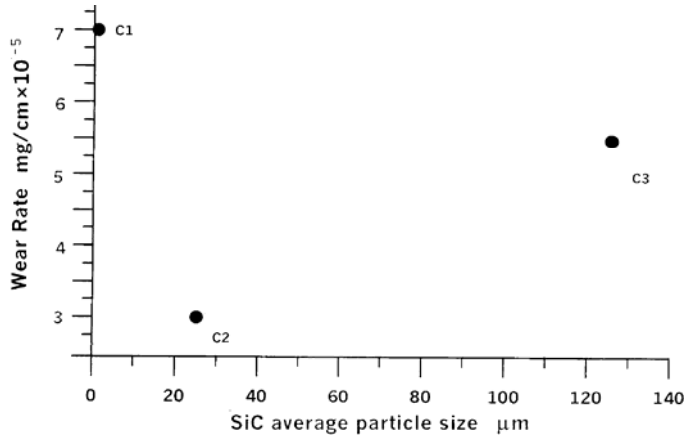

Fig. 13. Wear rate vs. SiC average particle size (load – 20 N, C2 = A3, wear rate values were taken after 180 min of sliding time)

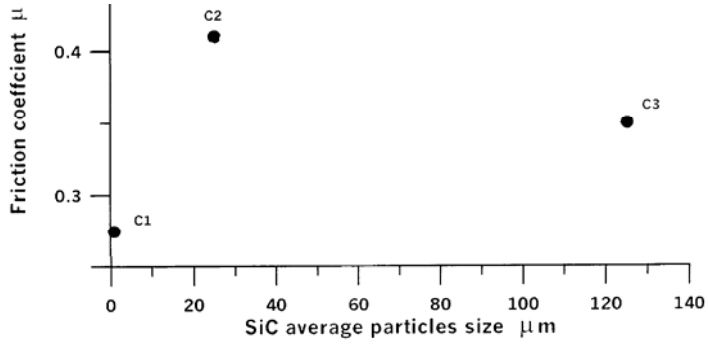

Fig. 14. Friction coefficient vs. SiC average particle size (load – 20 N, C2 = A3, the values of the friction coefficient were taken after 180 min of sliding time)

Finally, when concentrating on the micrographs of the worn surfaces (Figs. 6b–6d), it can be noticed that SiC particles disappear. This can be attributed either to the coating of these particles with a viscous aluminium film, resulting from localized fusion at the sample surface during rubbing, or to the particles being embedded in a soft matrix, since the heating effect of rubbing and normal load promote such phenomena.

4. Conclusions

• Addition of SiC particles to the Al-alloy matrix clearly improves wear resistance. Above the content of 13.5 wt. % of SiC, however, the wear resistance begins to decrease under both 10 N and 20 N loads.

• The friction coefficient decreases with increasing SiC particle content under both 10 N and 20 N loads.

• The particle size of 25 μm is optimum for improving the wear resistance when compared to other sizes (1 and 125 μm) under both 10 N and 20 N loads.

• The surface temperature decreases with increasing SiC particle content.

• The finer particle size (1 μm) gives a lower friction coefficient compared to the other sizes (25 and 125 μm).

References

[1] NARAYAN M., SURAPPA M., BAI B., Wear, 183 (1995), 563.
[2] SONG W.Q., KRAUKLIS P., MOURTIZ A., BYOPADHYAY S., Wear, 185 (1995), 125.
[3] ROHATGI P., SAMUEL C., J. Advances in Mat. Tech. Monitor, U. N. Industrial Dev. Org. 17 (1990), 1.
[4] AL-HAIDARY J., AL-KAABY A., 1st Jordanian Int. Conf. Materials Science and Engineering, 3–5 May, 2005, 72, Al-Salt, 19117 Jordan.
[5] SATO A., MEHRABIAN R., J. Metall. Trans., 7 B (1976), 443.
[6] HOSKING F., FOLGAR F., WUNDERLIN R., J. Mater. Sci., 17 (1982), 477.
[7] ROHATGI P., SURAPPA M., J. Mater. Sci., 16 (1981), 983.
[8] ROHATGI P., PAI B., PA S., J. Mater. Sci., 14 (1979), 2277.
[9] ROHATGI P., BANERJI A., SURAPPA M., J. Metall. Trans., 14B (1983), 273.
[10] ROHATGI P., BANERJI A., PRASAD S., SURAPPA M., Wear, 82 (1982), 141.
[11] JEONG J., KIM Y., LEE J., Met. Mater. Trans., 34A (2003), 1361.
[12] SUH N., SAKA N., PAMIES J., Wear, 44 (1977), 77.
[13] SUH N., SAKA N., PAMIES J., Wear, 44 (1977), 65.
[14] SUH N., Wear, 44 (1977), 1.
[15] AN K., KISHORE M., Wear, 85 (1983), 163.
[16] MCQUEEN H., MYSHLYAEV M., KONOPLEVA E., SAKARIS P., J. Can. Metall. Quart., 37 (1998), 125.
[17] ROHATGI P., SURAPPA M., PRASAD S., Wear, 77 (1982), 295.
[18] BHANSALI K., MEHRABIAN R., J. Metals Sep., (1982), 30.

Received 17 May 2006

Materials Science-Poland, Vol. 25, No. 1, 2007

Submicron-sized hybrid SiO_2–Ni powders produced with the sol-gel method

B. BORAK[1], S. LASKOWSKI[2], O. HECZKO[3], A. AALTONEN[3], A. BASZCZUK[4], M. JASIORSKI[5], O. SÖDERBERG[3], B. MAZUREK[2], M. OJA[6], S-P. HANNULA[3], K. MARUSZEWSKI[1,2*]

[1]Institute of Material Sciences and Applied Mechanics, Wrocław University of Technology, Smoluchowskiego 25, 50-370 Wrocław, Poland

[2]Electrotechnical Institute, Skłodowskiej-Curie 55/61, 50-369 Wrocław, Poland

[3]Laboratory of Materials Science
Helsinki University of Technology, P.O. Box 6200, FI-02015 TKK, Finland

[4]Institute for Low Temperature and Structure Research, Polish Academy of Sciences
Okólna 2, P.O. Box 1410, 50-950 Wrocław 2, Poland

[5]Institute of Inorganic Chemistry and Metallurgy of Rare Elements, Technical University of Wrocław
Smoluchowskiego 23, 50-372 Wrocław, Poland

[6]Laboratory of Mechanical Process Technology and Recycling,
Helsinki University of Technology, P.O. Box 6200 FI-02015 TKK, Finland

Magnetic powders based on metallic nickel nanoparticles encapsulated in submicron-sized spherical silica shells have been obtained and investigated. The nickel clusters were produced by the exploding wire method. The silica shells were prepared via the modified sol-gel Stöber method, and the metallic particles were entrapped by their occlusion during silica powder formation. The obtained hybrid materials were investigated by electron microscopy, X-ray diffraction, magnetic, and ζ potential techniques. The obtained materials can potentially be employed in such applications as magnetically controlled drug vectors or electromagnetic field shielding.

Key words: *nickel particles; magnetic SiO_2–Ni particles; sol-gel method*

1. Introduction

Nanometer-sized metal and semiconductor particles have received much attention due to their novel properties, significantly different from those of the corresponding

*Corresponding author, e-mail: krzysztof.maruszewski@pwr.wroc.pl

bulk materials, such as quantum-size effects, nonlinear optical properties and unusual magnetic properties [1–5]. Such particles are attractive dopants for a broad spectrum of matrices. One of the most promising host materials is submicron-sized powder obtained via the sol-gel technology. These have drawn considerable attention owing to their relative ease of preparation and various potential applications [6–10].

The sol-gel technique is based on the hydrolysis of liquid precursors and formation of colloidal sols [11–13]. The precursors are usually organosilicates (e.g., tetraethoxysilane, TEOS) which yield silicate sol-gel materials via the chemical reaction of hydrolysis

$$\equiv Si{-}OR + H_2O \longrightarrow \equiv Si{-}OH + ROH \tag{1}$$

and the subsequent formation of the silicate network:

$$\equiv Si{-}OH + HO{-}Si\equiv \longrightarrow \equiv Si{-}O{-}Si\equiv + HOH \tag{2}$$

$$\equiv Si{-}OR + HO{-}Si\equiv \longrightarrow \equiv Si{-}O{-}Si\equiv + ROH \tag{3}$$

As sol-gel materials are prepared from liquid solutions, the preparation process allows them to be doped by dissolving or suspending dopants in hydrolizates. An alternative way is to introduce various substances into sol-gel matrices via impregnation in solutions (suspensions) of the target molecules. A very attractive feature of the sol-gel technology is its application in manufacturing free and doped uniform silica spheres of submicron sizes [14–16].

The interesting and promising applications of sol-gel powders are based on SiO_2 submicron particles with dopants inducing a magnetic response. These materials could be used for vectorial drug administration and the control of their distribution, in magnetothermia or in magnetic resonance imaging [17–24]. These doped powders could also be applied as additives for textile coatings, various bulk plastics, or paints in order to induce their magnetic response (e.g., for electromagnetic radiation shielding). Since the size of the hybrid particles is less than 1 μm, however, the metallic magnetic particles need to be even smaller in order to achieve their encapsulation within the sol-gel silica shells.

The literature on sol-gel silica powders with magnetic inclusions is not very extensive and is usually limited to iron. Such materials have been usually made by the procedure developed for preparing conventional ferrofluids where mixtures of ferric and ferrous salts were appropriately reduced [20, 22, 25–30]. Attempts to entrap metallic particles are even less frequent. An example is the laser pyrolysis of ferrocene *in situ* during TEOS polymerization in a nebulized vapour cloud [17]. The entrapment of metallic nickel nanoparticles has been reported mainly for bulk silica materials obtained by the sol-gel method [31, 32].

The present work reports the sol-gel preparation of magnetic spherical submicron powders, in which the metallic nickel particles are entrapped within silica shells. The Ni particles were obtained by the exploding wire method [33–35]. The synthesized

materials were investigated by various methods: electron microscopy, X-ray diffraction, magnetic, and ζ potential measurements. The obtained results indicate that the hybrid powders possess magnetic properties. These materials could be employed as additives introducing magnetic properties in various products, e.g. paints, plastics, and magnetically controlled drug vectors.

2. Experimental

The nickel nanopowders were obtained by exploding a 99.99% Ni wire (length 9 cm, ∅ 0.5 mm) in a 6 dm^3 vessel filled with 4 dm^3 of deionised water. The explosion was triggered by a current impulse of 50 kA for 23 μs at a condenser discharge voltage of 8.5 kV. During each synthesis, the procedure was repeated six times in order to accumulate more product. The powders were removed from water with magnetic field. A typical size of the obtained Ni particles was 20–40 nm.

The hybrid nickel-silica particles were prepared by the sol-gel method. 0.02 g of Ni nanopowder was ultrasonically dispersed in a mixture of 42×10^{-3} dm^3 of alcohol (methanol or ethanol), 7×10^{-3} dm^3 of distilled water, and 4×10^{-3} dm^3 of ammonia solution (25%, POCh). 3×10^{-3} dm^3 of tetraethoxysilane (Alfa Aesar) was added drop-wise to the dispersed mixture. Then, the suspension was agitated ultrasonically for 1 hour and the solvent was evaporated, yielding a grey powder.

One batch of the hybrid particles was dissolved in hydrofluoric acid (HF) in order to estimate their metal content. The metal clusters were held by a magnet and the supernatant was removed. The Ni particles separated in this way were washed with diluted NaOH solution and deionised water and dried.

The size and morphology of the hybrid powders were determined by scanning electron microscopy (XL 30 Philips CP) and transmission electron microscopy (TESLA BS 500). To investigate the crystal structure of the magnetic powders, a DRON-3 diffractometer (CoK_α radiation; λ = 0.178892 nm) was employed. The diffraction intensities were recorded within the 2θ range 20°–80° in steps of 0.05°. Magnetic properties of the materials were analysed by an in-house made Vibrating Sample Magnetometer (VSM). A Coulter Delsa 440 Doppler Electrophoretic Light Scattering Analyser was used for the ζ potential measurements in ultra-pure water.

3. Results and discussion

The sol-gel entrapment of nickel nanoparticles by SiO_2 shells was carried out in two different solvents (methyl and ethyl alcohols). As it can be seen from SEM (Fig. 1) and TEM (Fig. 2) micrographs, the methanol (MeOH) route yields smaller hybrid particles (MeNi) than the ethanol (EtOH) route (EtNi particles). It is important to note that in both cases the particles are almost perfectly spherical. Thus, the en-

trapment of the nickel particles in silica shells does not prevent the typical Stöber-like sol-gel process from yielding regular hybrid structures. Furthermore, a proper choice of the synthetic conditions (e.g. solvents) allows the product parameters (e.g., the grains size) to be controlled to a certain extent.

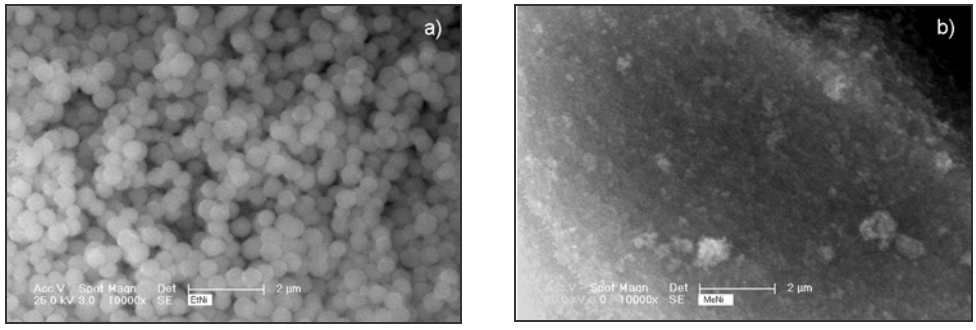

Fig. 1. SEM micrographs of EtNi hybrid particles (a) and MeNi particles (b)

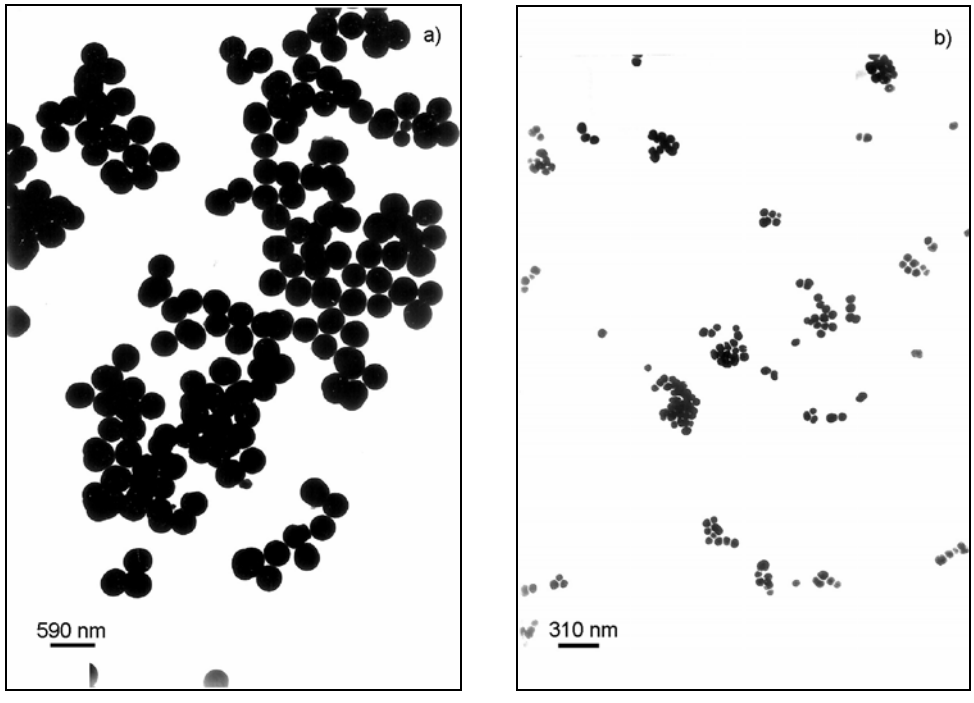

Fig. 2. TEM micrographs of EtNi hybrid particles (a) and MeNi particles (b)

Free metallic nickel particles and silica–metal hybrids were investigated by the XRD. The results are presented in Fig. 3. In addition to the metallic nickel (Ni) phase, a small amount of nickel oxide (NiO) is present. This presumably surface oxide can be the result of the fact that the nickel powders are obtained by wire explosion in wa-

ter. In addition, the conditions during the sol-gel synthesis of the silica shells might also induce some surface oxidation of the metal particles.

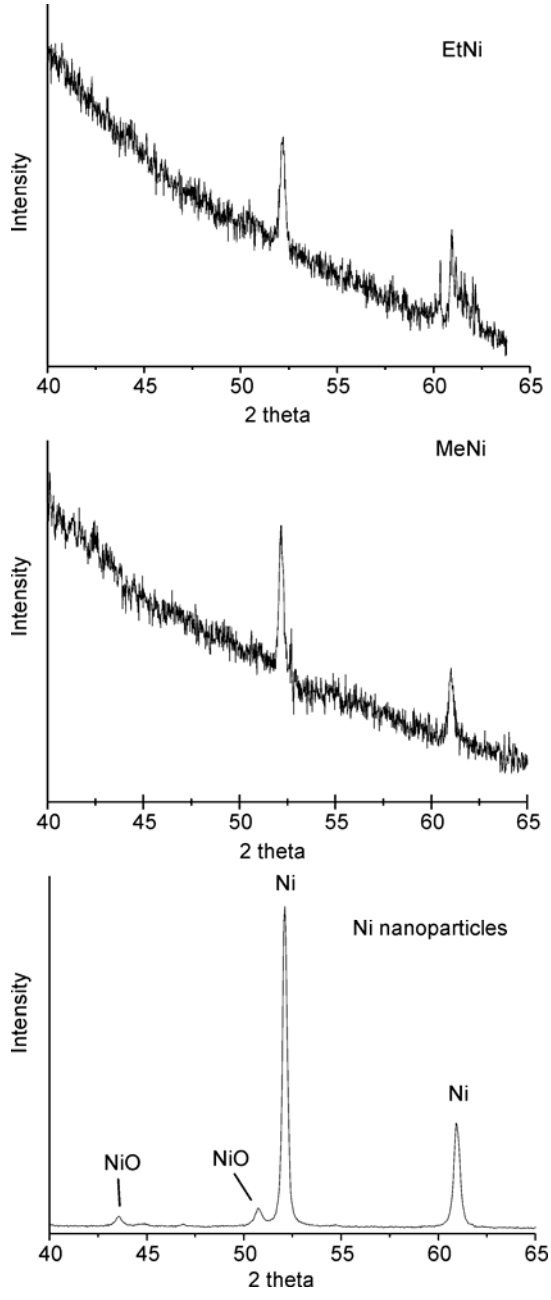

Fig. 3. The XRD patterns obtained for EtNi and MeNi hybrid SiO_2–nickel powders and for pure nickel nanoparticles

Figure 4 presents the distribution of the hybrid particle sizes obtained from the analysis of TEM results. The smaller particles (MeNi) have an average size of approximately 65 nm ($\varnothing \subset$ (50–80) nm), while the larger EtNi particles have an average diameter of ca. 350 nm ($\varnothing \subset$ (310– 390) nm). It is noteworthy that in both cases the fluctuations of grain size are relatively small, which is important from the point of view of potential applications.

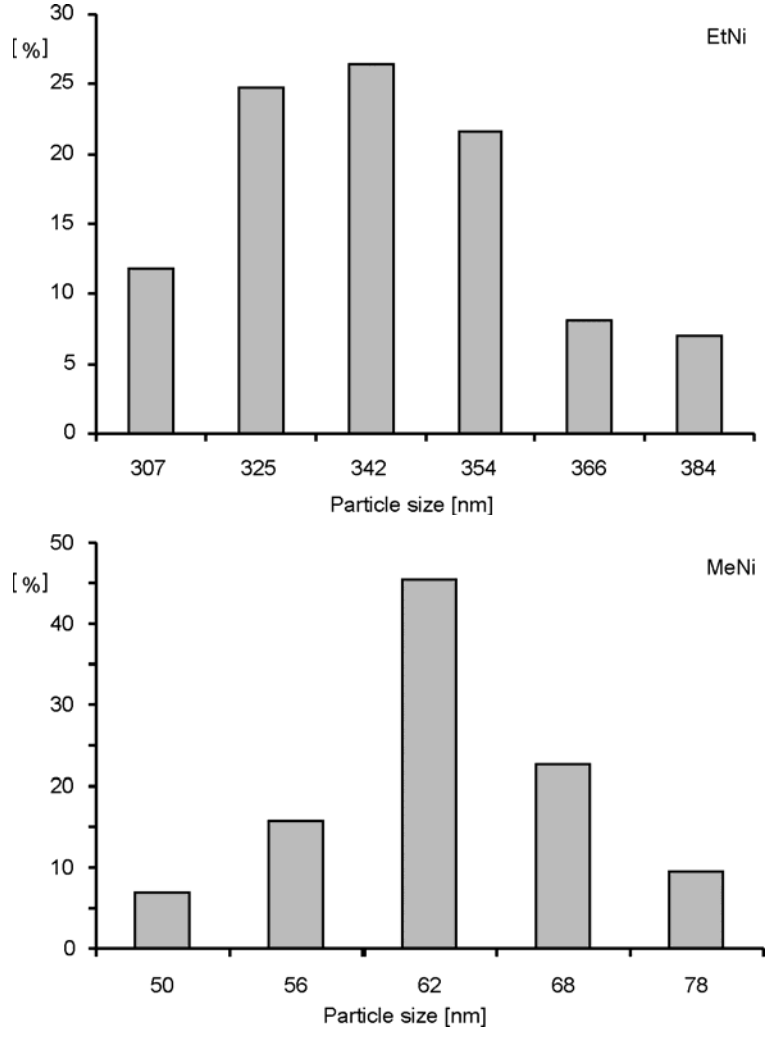

Fig. 4. Distributions of hybrid particles sizes

The ζ potential of pure (i.e. without any dopants) silica spherical particles produced via the ethanol route with the diameter of ca. 500 nm has been established to be –46.8 mV in pure water. This value is similar to results reported for other pure silica powders (–40.5 mV) [18] and for silica microspheres in water (–48 mV) [22]. The

ζ potential measured for the nickel-doped hybrid powders are –41.5 mV for the MeNi particles and –66.2 mV for EtNi. The EtNi hybrid particles may possess more terminal hydroxyl groups (which can be ionised in water) than the MeNi particles. This would mean larger negative surface charge and, consequently, higher absolute ζ potential.

The ζ potential observed for the pure silica particles, however, is lower than the one observed for the EtNi particles and comparable to the potential measured for the MeNi particles. This seems to indicate that the nickel–nickel oxide inclusions either increase the silica acidity (enhance surface hydroxyl group dissociation) or (and) increase the number of accessible surface –OH groups (e.g., due to the introduction of surface defects during silica spherical shell formation). Similar behaviour has been observed for iron nanoparticles entrapped in silica shells [36].

Figure 5 presents the magnetization curves obtained for silica-coated nickel particles at room temperature. From the shape of the curves, i.e. they approach magnetic saturation and exhibit hysteresis (not discernible in the figure), it appears that both powders are ferromagnetic. The hysteresis of the curves is relatively small: H_c = 8.5 mT for MeNi and H_c = 6.1 mT for EtNi. The hysteresis is slightly larger for particles with smaller size (MeNi). This increase in hysteresis could be related to the hysteretic behaviour of small particles approaching the single domain regime.

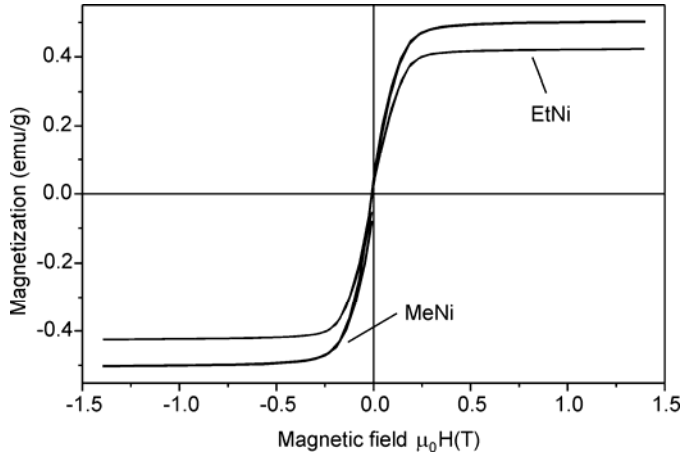

Fig. 5. Magnetization curves obtained
for silica-coated nickel particles at room temperature

The saturation magnetization is slightly larger in the case of the smaller hybrid particles (MeNi; 0.51 emu/g) than for the larger particles (EtNi; 0.43 emu/g). This observation suggests that the efficiency of metallic particle entrapment was somewhat larger in the case of the smaller silica particles. Assuming that the dopant particles are pure nickel (the saturation magnetization of 54 emu/g at 20 °C), it is possible to estimate the weight percentage of nickel in the hybrid particles from the magnetic data.

This approach gives a nickel content of approximately 1.0% for the larger EtNi particles and 1.9% for the MeNi particles. These results are virtually identical to those for the magnetically separated nickel particles extracted from the silica shells with hydrofluoric acid. The magnetic measurement indicates that the amount of the residual nickel oxide is rather small, which corresponds well to the XRD data (Figure 3).

4. Conclusions

Ni nanopowders were successfully entrapped in spherical silica shells via the sol-gel method. The size of the hybrid particles depends on the alcohol solvent used during synthesis. Methanol yields smaller (ca. 65 nm; MeNi) and ethanol larger (ca. 350 nm; EtNi) Ni–SiO_2 particles. The X-ray diffraction data suggest that the free nickel particles contain very small amounts of the metal oxide (NiO), while clearly only the peaks corresponding to metallic nickel occur in the hybrid powder diffractograms. The pure silica spherical particles exhibit a ζ potential comparable to MeNi hybrid particles, while for EtNi it is higher. This suggests that Ni-dopant particles influence the surface chemistry of the hybrids. The Ni–SiO_2 particles display ferromagnetic behaviour at room temperature. The hybrid powder materials obtained could be used in magnetothermia, magnetic resonance imaging, as magnetically controlled drug vectors, or as additives for electromagnetic radiation shielding coatings.

Acknowledgements

The authors express thanks to Dr. M. Zawadzki and Z. Mazurkiewicz for the TEM measurements and to V. Tyrpekl for the SEM measurements. Also, support from Finnish institutions is gratefully acknowledged (K. Maruszewski, Helsinki University of Technology, B. Borak and M. Jasiorski, the Academy of Finland).

References

[1] GLEITER H., Acta Mater., 48 (2000), 1.
[2] BARD A.J., Science, 207 (1980), 139.
[3] BARD A.J., J. Phys. Chem., 86 (1982), 172.
[4] JOSELEVICH E., WILLNER I., J. Phys. Chem., 98 (1994), 7628.
[5] LESLIE-PELECKY D.L., RIEKE R.D., Chem. Mater., 8 (1996), 1770.
[6] PARK S.K., KIM K.D., KIM H.T., Colloids Surf. A: Physicochem. Eng. Asp., 197 (2002), 7.
[7] SADASIVAN S., RASMUSSEN D.H., CHEN F.P., KANNABIRAN R.K., Colloids Surf. A: Physicochem. Eng. Asp., 132 (1998), 45.
[8] RECULUSA S., MASSE P., RAVAINE S., J. Colloid Int. Sci., 279 (2004), 471.
[9] MONER-GIRONA M., ROIG A., MOLINS E., LLIBRE J., J. Sol-Gel Sci. Tech., 26 (2003), 645.
[10] ZUKOSKI C.F., Chem. Eng. Sci., 50 (1995), 4073.
[11] BRINKER C.J, SCHERER G.W., *Sol-Gel Science*, Academic Press, San Diego, 1990.
[12] KLEIN L.C., *Sol-Gel Optics*, Kluwer, Boston, 1994.
[13] REISFELD R., JORGENSEN C.K., *Chemistry, Spectroscopy and Applications of Sol-Gel Glasses*, Springer-Verlag, Berlin, 1992.

[14] WONG S., KITAEV V., OZIN G.A., J. Am. Chem. Soc., 125 (2003), 15589.
[15] BLANCO A., CHOMSKI E., GRABTCHAK S., IBISATE M., JOHN S., LEONARD S.W., LOPEZ C., MESEGUER F., MIGUEZ H., MONDIA J.P., OZIN G.A., TOADER O., VAN DRIEL H.M., Nature, 405 (2000), 437.
[16] JASIORSKI M., HRENIAK D., MARUSZEWSKI K., STRĘK W., Mater. Sci., 20 (2002), 51.
[17] BOMATÍ-MIGUEL O., LECONTE Y., MORALES M.P., HERLIN-BOIME N., VEINTEMILAS-VERDAGUER, J. Magn. Magn. Mater., 290–291 (2005), 272.
[18] CHAE K.P., LEE J.G., KWEON H.S., LEE Y.B., J. Magn. Magn. Mater., 283 (2004), 103.
[19] KORNAK R., MARUSZEWSKI K., STRĘK W., HAIMANN K., DUDZIŃSKI W., VOGT A.A., KOŁODZIEJ H.A., J. Alloys Comp., 380 (2004), 268.
[20] DORMER K., SEENEY C., LEWELLING K., LIAN G., GIBSON D., JOHNSON M., Biomaterials, 26 (2005), 2061.
[21] SUN Y., DUAN L., GUO Z., DUAN Y., MA M., XU L., ZHANG Y., GU N., J. Magn. Magn. Mater., 285 (2005), 65.
[22] ZHOU W., GAO P., SHAO L., CARUNTU D., YU M., CHEN J., O'CONNOR C., Nanomedicine: Nanotechnol., Biol., Medicine, 1 (2005), 233.
[23] MA Z.-Y., LIU X.-Q., GUAN Y.-P., LIU H.-Z., Colloids Surf. A: Physicochem. Eng. Asp., 275 (2006), 87.
[24] LEE J., ISOBE T., SENNA M., J. Colloid Int. Sci., 177 (1996), 490.
[25] ZHANG L., PAPAEFTHYMIOU G.C., ZIOLO R.F., YING J.Y., Nanostructured Mater., 9 (1997), 185.
[26] YASUMORI A., MATSUMOTO H., HAYASHI S., OKADA K., J. Sol-Gel Sci. Tech., 18 (2000), 249.
[27] ZHU Y., DA H., YANG X., HU Y., Colloids Surf. A: Physicochem. Eng. Asp., 231 (2003), 123.
[28] LIU X., MA Z., XING J., LIU H., J. Magn. Magn. Mater., 270 (2004), 1.
[29] ATARASHI T., KIM Y.S., FUJITA T., NAKATSUKA K., J. Magn. Magn. Mater., 201 (1999), 7.
[30] TARTAJ P., GONZALEZ-CARRENO T., BOMATÍ-MIGUEL O., SERNA C.J., BONVILLE P., Phys. Rev. B, 69 (2004), 94401.
[31] ISOBE T., WEEKS R.A., ZUHR R.A., Solid State Commun., 105 (1998), 469.
[32] ESTOURNES C., LUTZ T., HAPPICH J., QUARANTA T., WISSLER P., GUILLE J.L., J. Magn. Magn. Mater., 173 (1997), 83.
[33] KIM J.-S., Scripta Mater., 44 (2001), 2247.
[34] SABARI-GIRIA V., SARATHIA R., CHAKRAVARTHYB S.R., VENKATASESHAIAH C., Mater. Lett., 58 (2004), 1047.
[35] WANG Q., YANG H., SHI J., ZOU G., Mater. Sci. Eng. A, 307 (2001), 190.
[36] BORAK B., LASKOWSKI S., HECZKO O., AALTONEN A., BASZCZUK A., JASIORSKI M., SODENBERG O., MAZUREK B., OJA M., HANNULA S.-P., MARUSZEWSKI K., J. Sol.-Gel. Tech., 41 (2007), 185.

Received 2 June 2006
Revised 3 August 2006

Materials Science-Poland, Vol. 25, No. 1, 2007

Transport properties of as-deposited cadmium phthalocyanine Schottky-barrier devices

MAMMEN SAMUEL*, C. S. MENON, N. V. UNNIKRISHNAN

School of Pure and Applied Physics, Mahatma Gandhi University, Kottayam-686 560, Kerala, India

Sandwich samples of the type (Au–CdPc–Al) have been fabricated by successive vacuum deposition of gold (Au), cadmium phthalocyanine (CdPc), and aluminium (Al) thin films on glass substrates. Good rectification properties have been observed in the device. Ohmic conduction in the lower voltage range has been identified from the forward bias current density-voltage characteristics at room temperature. At higher voltages, a space charge limited conductivity (SCLC) controlled by an exponential trapping distribution above the valence band edge has been observed. The transport properties of the material at ambient temperature have been obtained from an analysis of the samples in the SCLC region. Schottky emission has been identified at lower voltages from the analysis of the reverse bias characteristics.

Key words: transport properties; Schottky barrier; organic semiconductor

1. Introduction

Metal phthalocyanines (MPcs) are generally p-type semiconductors and have the advantage of being sufficiently stable towards chemical and thermal treatment. They can easily be vacuum deposited, resulting in high purity thin films without decomposition. Electronic devices with MPcs as the active materials can be fabricated on a wide variety of substrates, including flexible materials. Many of them have been extensively studied in recent years due to their potential applications in thin-film electronic devices such as light emitting devices [1], transistors [2–4], photovoltaic cells [5, 6], and in photoreceptor devices such as laser beam printers and photocopiers [7]. Basic electrical conduction processes observed in these materials depend on many factors, including the phthalocyanine species, film thickness, film deposition temperature, and the electrode materials. DC electrical studies of thin-film heterostructures of the metal–organic semiconductor–metal type have provided lots of information regarding the electrical conduction mechanism, transport properties, characteristics of

*Corresponding author, e-mail: masabe@rediffmail.com

metal-organic semiconductor interfaces, etc. [8–10]. Such information is vital in the development of high performance thin film electronic devices. Among various phthalocyanines, cadmium phthalocyanine (CdPc) has received considerably less attention. The object of this paper is to investigate the transport properties of cadmium phthalocyanine (CdPc) thin films using Ohmic gold [11, 12] and blocking aluminium [13, 14] electrodes.

2. Experimental

Cadmium phthalocyanine (CdPc) powder (Aldrich Chemicals, USA) purified by train-sublimation using nitrogen gas as a carrier [14, 15] was used as the source material. Three-layer sandwich samples were prepared on glass substrates by sequential vacuum thermal evaporation in a single vacuum cycle, using a Hind Hivac 12A4 evaporation plant under the base pressure of 10^{-3} Pa. A thin layer of gold (~100 nm) was first deposited onto a pre-cleaned glass substrate from an electrically heated tungsten spiral. Over this, a CdPc layer was deposited using an electrically heated molybdenum boat. Finally, an aluminium layer with thea thickness of ~100 nm was deposited using another tungsten spiral. The thickness of the film was measured using Tolansky's multiple beam interference technique [16]. Sandwich structures with an effective area of 2.0×10^{-5} m^2 and CdPc layer thicknesses of 240 nm, 315 nm, 410 nm, and 485 nm were used in the analysis. A Keithley electrometer (model No. 617) was used for the current–voltage measurements. Temperature measurements were performed with a Chromel-Alumel thermocouple placed in close proximity of the samples. To avoid contamination and any photoelectric effects, all measurements were performed under a subsidiary vacuum of 10^{-1} Pa in a lightproof conductivity cell. Capacitance measurements were done using a Hioki 3532 LCR Hi-tester.

3. Results and discussion

The current–voltage (I–V) characteristics of the Au–CdPc–Al device (240 nm) are shown in Fig. 1. The forward bias direction corresponds to the positive Au (bottom) electrode and negative Al (top) electrode of the device. The characteristics as shown in Fig. 1 are attributed to the low work function of Al and high work function of Au electrodes and to the p-type conduction of CdPc. Detailed information about the transport mechanism through the organic thin film can be obtained from an analysis of the forward current density–voltage (J–V) characteristics of the device. The forward J–V characteristics are shown in Fig. 2. At low voltages, the slope of log J vs. log V is around unity (1.06), and at higher voltages, above a well-defined voltage V_x, this slope is 3.26. These slopes indicate an Ohmic region due to thermally generated carriers at lower voltages and a power-law region at higher voltages typical of a space-charge-limited conduction (SCLC) mechanism controlled by the presence of traps distributed exponentially with energy within the band gap of the CdPc.

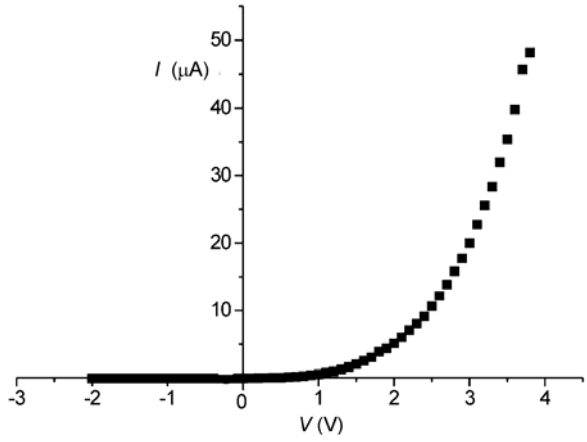

Fig. 1. Current–voltage characteristics
of the Au–CdPc–Al device at room temperature

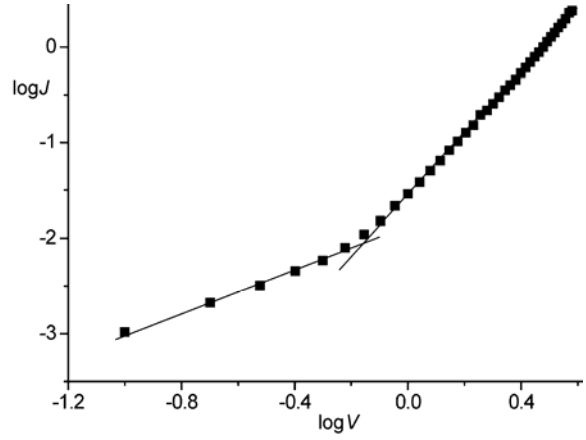

Fig. 2. Plot of log J [A·m^{-2}] vs. log V [V] at 300 K.
The lower voltage region corresponds to Ohmic conductivity
and the higher one corresponds to SCLC

Shown in Fig. 3 is the thickness dependence of forward current density J at room temperature for various applied voltages in the Ohmic region. Slopes of ~ –1 provide evidence of Ohmic conductivity at low voltages, satisfying the current density–voltage relation [17]:

$$J = ep\mu\left(\frac{V}{d}\right) \tag{1}$$

where p is the concentration of thermally generated holes in the valence band, e is the electronic charge, μ is hole mobility, V is the applied DC voltage, and d is the thickness of CdPc thin film.

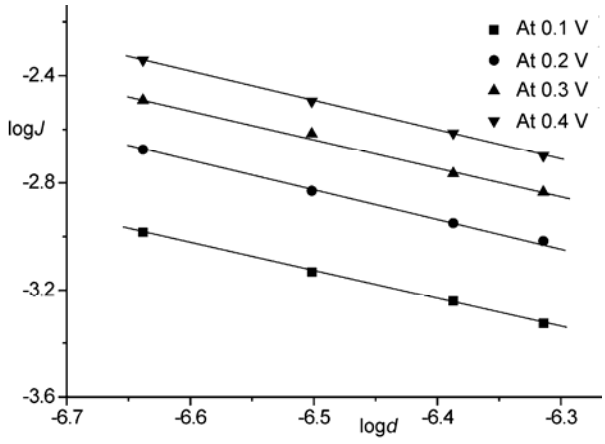

Fig. 3. Dependence of log J on thickness (log$d$) for the various applied voltages in the Ohmic region at room temperature; d is expressed in meters

Within the SCLC region, the current density J is given by [18, 19]

$$J = e\mu N_V \left(\frac{\varepsilon_r \varepsilon_0}{e P_0 k_B T_t} \right)^L \frac{V^{L+1}}{d^{2L+1}} \tag{2}$$

where P_0 is the trap density per unit energy range at the valence band edge, ε_0 is the permittivity of free space (8.85×10^{-12} F·m^{-1}), ε_r is the relative permittivity of the sample ($\varepsilon_r = 3.08$ is obtained from capacitance measurements), and L is the ratio T_t /T where T is the ambient temperature, T_t is a temperature parameter describing the exponential trapping distribution, and k_B is the Boltzmann constant. The exponential trap distribution may be described in terms of T_t as [14,19]

$$P(E) = P_0 \exp\left(\frac{-E}{k_B T_t} \right) \tag{3}$$

where $P(E)$ is trap concentration per unit energy range at an energy E above the valence band edge. In Eq. (2), the slope of 3.26 implies that L = 2.26 and thus the temperature parameter T_t = 678 K for T = 300 K. Figure 4 shows the thickness dependence of current density for the SCLC region at room temperature for various applied voltages. The slopes of ~ –5.6 provide evidence of SCLC conductivity satisfying Eq. (2) at higher voltages. Figure 5 shows the log J vs. 1/T in the SCLC region at V = 2.0 V for the sample with a CdPc thickness of 240 nm. For the temperature range within which samples were investigated, the characteristics show a linear fit whose slope derived from Eq. (2) is given by

$$S = T_t \log\left(\frac{\varepsilon_o \varepsilon_r V}{e d^2 P_0 k_B T_t} \right) \tag{4}$$

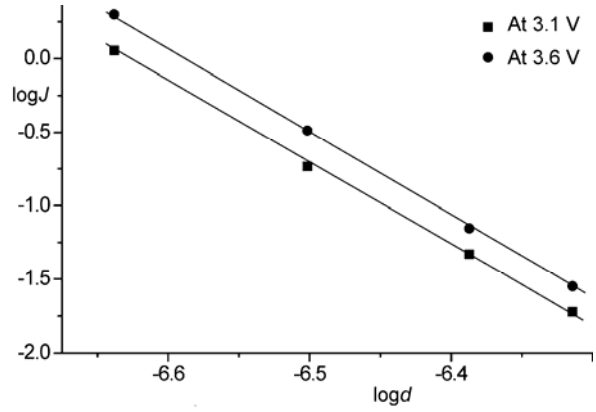

Fig. 4. Dependence of log J on thickness (log$d$) for the various applied voltages in the SCLC region at room temperature

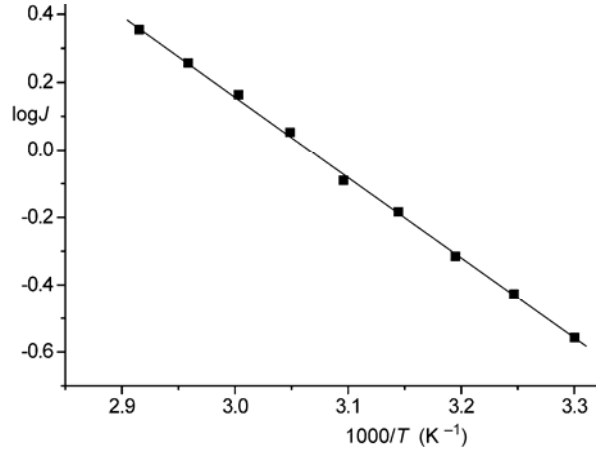

Fig. 5. Plot of log J versus $1000/T$ in the SCLC region

From the slope of Fig. 5, P_0 is determined equal to 2.12×10^{45} $J^{-1}\cdot m^{-3}$. The total concentration of the traps is given by [14,19]

$$N_t = P_0 k_B T_t \tag{5}$$

and is equal to 1.98×10^{25} m^{-3}. The trap concentration ranging from 10^{22} to 10^{25} m^{-3} is usually found in phthalocyanine thin films [15, 20, 21]. The intercept on the log J axis in Fig. 5 as obtained from Eq. (2) is given by

$$\log J_0 = \log\left(\frac{e\mu N_V V}{d}\right) \tag{6}$$

where J_0 represents the current density at infinite temperature ($1/T = 0$) and gives the value of μN_V. Taking $N_V = 10^{27}$ m^{-3}, which corresponds to one state per molecule

[13, 14, 17], the as-measured mobility $\mu = 1.61\times10^{-8}$ $m^2\cdot V^{-1}\cdot s^{-1}$. Here, it is to be noted that temperature- and field-dependent mobilities are observed in several organic materials. The present work does not include an investigation on the temperature and field dependence of the mobility of the material.

The changeover from Ohmic to SCLC conduction takes place at a particular voltage V_x, known as the transition voltage. V_x is obtained from Eqs. (1) and (2) as

$$V_x = \left(\frac{p}{N_V}\right)^{1/L} \frac{ed^2 P_0 k_B T_t}{\varepsilon_0 \varepsilon_r} \tag{7}$$

At ambient temperature, $V_x \sim 0.71$ V. Using Eq. (7), the thermally generated hole concentration (p) at room temperature is 1.04×10^{18} m^{-3}.

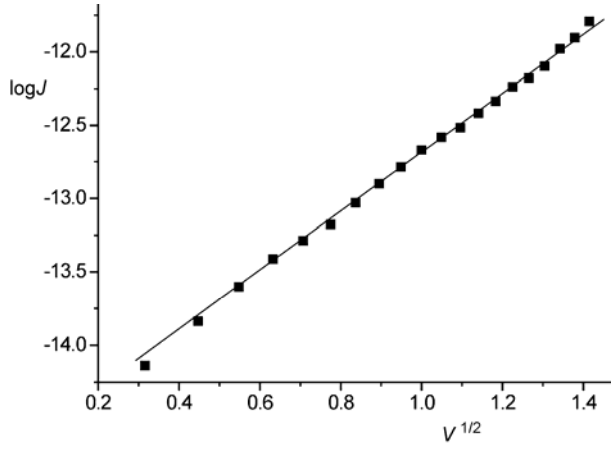

Fig. 6. Dependence of log J on $V^{1/2}$ for the reverse-biased device

The reverse bias I–V characteristics give information about the properties of the metal-semiconductor contact. Figure 6 shows the reverse bias characteristics plotted with ln$J$ against $V^{1/2}$. This linear plot can be analysed in terms of the two field-lowering mechanisms, namely, the Schottky effect and Poole–Frenkel effect. The J–V expression for the Schottky effect is given by [22, 23]:

$$J = A^* T^2 \exp\left(\frac{-\phi}{k_B T}\right) \exp\left(\frac{e\beta_S V^{1/2}}{k_B T d^{1/2}}\right) \tag{8}$$

and for the Poole–Frenkel effect it is given by

$$J = J_{PF} \exp\left(\frac{e\beta_{PF} V^{1/2}}{k_B T d^{1/2}}\right) \tag{9}$$

In these expressions, $A^* = 1.2\times10^{-6}$ A·m^{-2} is the Richardson constant, ϕ is the Schottky barrier at the injecting electrode interface, and J_{PF} is the low-field current density. β_S and β_{PF} are the Schottky and Poole-Frenkel field-lowering coefficients, respectively, related by [22]

$$2\beta_S = \beta_{PF} = \left(\frac{e}{\pi\varepsilon_0\varepsilon_r}\right)^{1/2} \tag{10}$$

This gives $\beta_S = 2.16\times10^{-5}$ eV m$^{1/2}$·V$^{-1/2}$ and $\beta_{PF} = 4.32\times10^{-5}$ eV m$^{1/2}$·V$^{-1/2}$. The value of β resulting from the slope in Fig. 6 is 2.55×10^{-5} eV m$^{1/2}$·V$^{-1/2}$. It is in reasonable agreement with the computed value of β_S, rather than the computed value of β_{PF} obtained from Eq. (10). Thus, in the case of field-lowering behaviour, the Schottky emission may be confirmed for the voltage range within which the samples were studied. The observed variance of the experimental value of β_S with respect to the theoretical value of β_S obtained from Eq. (10) is attributed to the fact that the entire thickness d of the film is not depleted. From the intercept on the ln$J$ axis in Fig. 6 and from Eq. (8), the Schottky barrier height of $\phi = 1.03$ eV was obtained. Using the theoretical value of β_S together with the slope in Fig. 6, the Schottky barrier width of ω = 172 nm was obtained. J–V characteristics typical of the Schottky barrier have also been observed in some other phthalocyanine–aluminium interface structures [18, 19, 22, 24].

4. Conclusions

I–V characteristics typical of a rectifier have been observed in the device. Under forward bias, the electrical characteristics of as-deposited devices show Ohmic conduction at low voltages. At higher voltages, space-charge limited conduction controlled by an exponential distribution of traps above the valence band edge is observed. The high concentration of traps is thought to be effective in establishing the space-charge layer. The transport parameters, derived at room temperature, are consistent with the values reported for some other MPcs. Under reverse bias, the low field conductivity is limited by the Schottky barrier 172 nm wide and 1.03 eV high.

Acknowledgement

One of the authors, M.S., is grateful to the University Grants commission of India for providing a teacher fellowship under the FIP scheme.

References

[1] FUJII A., OHMORI Y., YOSHINO K., IEEE Trans. Electron Devices, 44 (1997), 1204.
[2] JOSEPH C. M., MENON C. S., Mater. Lett., 52 (2002), 220.

[3] JOSEPH C. M., NARAYANANUNNI K. N., MENON C. S., Mater. Lett., 50 (2001), 18.
[4] JIAN Z., JUN W., HAIBO W., DONGHANG Y., Appl. Phys. Lett., 84 (2004), 142.
[5] LAW K.Y., Chem. Rev., 93 (1993), 449.
[6] RUDIONO., SHUICHI O., MANABU T., Thin Solid Films, 334 (1998), 187.
[7] BORSENBERGER P. M., WEISS D. S., *Organic Photoreceptors for Imaging Systems*, Marcel Dekker, New York, 1993.
[8] REDDY N.V., RAO B.S., RAO V.V.R.N., Mater. Lett., 13 (1992), 147.
[9] RUSU M., RUSU G.I., Appl. Surf. Sci., 126 (1998), 246.
[10] CHOPRA K.L., *Thin Film Phenomena*, McGraw-Hill, New York, 1969.
[11] GRAVANO S., HASSAN A.K., GOULD R.D., Int. J. Electron., 70 (1991), 477.
[12] GOULD R.D., Coord. Chem. Rev., 156 (1996), 237.
[13] GOLD R.D., HASSAN A.K., Thin Solid Films, 193/194 (1990), 895.
[14] RIAD A. S., Physica B, 270 (1999), 148.
[15] ABDEL-MALIK T.G., AHMED A. A., RIAD A. S., Phys. Stat. Sol. A, 121 (1990), 507.
[16] MAISSEL L.I., GLANG R., *Handbook of Thin Film Technology*, McGraw-Hill, New York, 1985.
[17] ABDEL-MALIK T.G., ABDEL-LATIF R.M., Thin Solid Films, 305 (1997), 336.
[18] MAMMEN SAMUEL, MENON C.S., UNNIKRISHNAN N.V., Semicond. Sci. Technol., 21 (2006), 677.
[19] MAMMEN SAMUEL, MENON C.S., UNNIKRISHNAN N.V., J. Phys.: Condens. Matter., 18 (2006), 135.
[20] ABDEL-MALIK T.G., Int. J. Electron., 72 (1992), 409.
[21] SHAFAI T. S., GOULD R.D., Int. J. Electron., 69 (1990), 3.
[22] SHARMA G.D., Synth. Metals, 74 (1995), 227.
[23] SZE S.M., *Physics of Semiconductor Devices*, Wiley, New York, 1969, p. 496.
[24] FAN F.R., FAULKNER L.R., J. Chem. Phys., 69 (1978), 3334.

Received 5 June 2006
Revised 14 August 2006

Materials Science-Poland, Vol. 25, No. 1, 2007

The influence of γ-Al_2O_3 and Na_2O on the formation of calcium silicate hydrates in the CaO–quartz–H_2O system

K. BALTAKYS*, R. SIAUCIUNAS

Department of Silicate Technology, Kaunas University of Technology,
Radvilenu 19, LT – 50270 Kaunas, Lithuania

The influence of γ-Al_2O_3 and Na_2O additives on the formation and sequence of calcium silicate hydrates in the CaO–quartz–H_2O system with CaO/SiO_2 (C/S) molar ratio equal to 0.66 was determined. The synthesis was carried out in unstirred suspensions. The molar ratios of the primary mixtures were $CaO/(SiO_2 + Al_2O_3) = 0.66$ and $Al_2O_3/(SiO_2 + Al_2O_3) = 0$ or 0.025. The amount of NaOH, corresponding to 5% of Na_2O in the mass of dry material, was added in the form of solution. Due to the low solubility rate of quartz in the CaO–quartz–H_2O system with C/S = 0.66 in the temperature range 150–200 °C, low-base calcium silicate hydrates (Z-phase, gyrolite, pectolite, and others) do not form even after 72 hours of hydrothermal curing. It has been proved that γ-Al_2O_3 and Na_2O additives change the reaction mechanisms and composition of intermediate (final) products. In mixtures with Na_2O, gyrolite starts to form already at 175 °C. It should be noted that in the temperature range 175–200 °C the final products are gyrolite and pectolite, and the intermediate compounds are C–S–H(I) and Z-phase. The formation of low-base calcium silicate hydrates in the CaO–quartz–Na_2O–H_2O system is slowed down when Al_2O_3 is added because Al^{3+} ions stimulate the formation of tobermorite and prevent the formation of pectolite and Z-phase.

Key words: *gyrolite; Z-phase; pectolite; tobermorite; calcium silicate hydrate*

1. Introduction

Conditions for the formation and stability of various calcium silicate hydrates in the CaO–SiO_2–H_2O (C–S–H) system have been extensively studied. C–S–Hs are a class of poorly defined calcium silicate hydrates with CaO/SiO_2 (C/S) ratios ranging from 0.44 to 3 and crystallographic structures from amorphous to highly crystalline [1–10]. As a rule, the amorphous compounds are formed during hydration of portland cement [11–13] and the crystalline ones in hydrothermal conditions [1, 4, 6]. The synthesis, properties, and structure of compounds with the molar ratio C/S from 0.8 to 1.0 (1.13 nm tobermorite, xonotlite) have been analysed in detail [1, 4–10].

*Corresponding author, e-mail: kestutis.baltakys@ktu.lt

Recently, interest in low-base calcium silicate hydrates (gyrolite, Z-phase, truscottite, reyerite) has increased because the application possibilities have been found [14–16]. Meanwhile, the data presented in references about the properties of low-base compounds (C/S = 0.5–0.8) and their formation in hydrothermal conditions are not extensive and often controversial [17–21].

At the molar ratios of C/S = 0.50 and 0.66 in the system $CaO–SiO_2–H_2O$, the most stable phases under hydrothermal conditions in the temperature range 200–300 °C are truscottite and gyrolite. The phase composition of the hydrates in the given system depends on the C/S ratio chosen, the character and properties of the silicon oxide employed, as well as on the temperature and duration of the hydrothermal process. Gyrolite can be synthesized from CaO and various forms of SiO_2 with the molar ratio of C/S = 0.66 in aqueous suspension at temperatures near 200 °C. Kalousek and Nelson [22], and also Ševula and Petrovič [23] have found that gyrolite could likewise be prepared by reacting dicalcium silicate ($2CaO·SiO_2$) with SiO_2 in an aqueous suspension under hydrothermal conditions. Ševula et al. reported that natural and synthetic gyrolite behaved analogously in the temperature range 200–300 °C under hydrothermal conditions. At 200 °C and under the pressure of saturated water vapour, gyrolite and laumonite can coexist in natural specimens owing to similar C/S ratios. Above this temperature, both natural and synthetic gyrolite decompose, forming stable phases such as truscottite and xonotlite. The stable phase association of truscottite + xonotlite + laumonite exists in the temperature range 250–300 °C [18].

Okada et al. [25], using lime and amorphous silica as the starting materials, hydrothermally prepared gyrolite with the C/S molar ratio of 0.66 and 0.50 at 200 °C for 0.5–128 h. The initially formed C–S–H consisted mainly of long chains of silicate anions. For C/S = 0.66, the chain that formed was broken, and C–S–H changed into gyrolite and xonotlite. For C/S = 0.50, only gyrolite was formed from a long chain of silicate anions. It is thought that the differences in the C–S–H structures, which were formed in the initial stage, greatly influenced the final products. In addition, for C/S = 0.50, the Z-phase was also formed as a precursor of gyrolite and its silicate anion structure was similar to that of the gyrolite [24]. Some specimens of gyrolite probably also contained small amounts of the Z-phase as impurity intergrowths [2]. The Z-phase was obtained by Funk and Thilo [25] by autoclaving calcium silicate hydrated gel at 180 °C; as well as by Assarsson [2] by autoclaving a mixture of lime and silicic acid at 195 °C. Gard et al. [21] showed that the Z-phase can be produced by decomposing Al-substituted tobermorite and they presented results of thermal electron diffraction, and infrared studies that confirm the relationship to gyrolite.

Jauberthie et al. [19] reported that tobermorite gel formed by the hydrothermal reaction of silica and lime is transformed either into the Z-phase if the quantity of lime is less than 37% or into 1.0 nm tobermorite if the quantity of lime is between 37% and 42%. The 1.0 nm tobermorite is stable in the presence of gyrolite, whereas the Z-phase is metastable [19].

Luke [26] established that at 180 °C the initially formed amorphous calcium silicate gel transforms into well-defined crystalline phases, the stabilities of which depend primarily on the C/S ratio and hydrothermal conditions. Gyrolite ($C_2S_3H_{\sim 2}$), tobermorite ($C_5S_6H_5$), truscottite ($C_7S_{12}H_{\sim 3}$), and xonotlite (C_6S_6H) were all reported to coexist stably in aqueous solutions with silica in the silica-rich part of the CaO–SiO_2 –H_2O system [26].

Shaw et al. [20], using a synchrotron X-ray radiation source of high energy, have explored the mechanical, kinetic and energetic processes proceeding during formation of gyrolite. In the temperature range 190–240 °C in a pure calcic system it involves three stages: amorphous gel, C–S–H gel and Z-phase gyrolite [20].

Crystal lattice of natural gyrolite always contains both sodium and aluminium ions [27, 28]. There are some data in the references about the influence of Al_2O_3 and Na_2O additives on the synthesis of low base calcium silicate hydrates (in contrast to 1.13 nm tobermorite) [14, 29–32]. It should be noticed that Miyake, Iwaya, and Suzuki [14] successfully synthesized (Al + Na)-substituted gyrolite ($Ca_8Si_{11.32}Al_{0.68}Na_{0.44}O_{30}(OH)_4 \cdot 6.6H_2O$) and used it for ion exchange reactions (K^+ and Cs^+) in aqueous solutions.

However, the conditions of low-base calcium silicate hydrates formation, the dependence of compounds stability on the mixture C/S ratio, as well as on the temperature and duration of the hydrothermal process were usually studied using active forms of SiO_2: finely dispersed aerosil, silicic acid, amorphous SiO_2. On the contrary, formation of the compounds is more difficult when quartz is used, and the sequence of their formation has not been determined. Therefore, it is necessary to look for additives promoting and/or accelerating the formation of the final products in the CaO–quartz –H_2O system.

The aim of this study was to determine the formation sequence of calcium silicate hydrates and their stabilities in the CaO–quartz–H_2O system with C/S = 0.66 and to examine the influence of γ-Al_2O_3 and/or Na_2O additives.

2. Experimental

The following reagents were used as starting materials: fine-grained quartz after grinding, with iron impurities washed away by hydrochloric acid (specific surface area S_a = 1100 m²/kg by Blaine); NaOH solution (c = 1.04%); CaO produced by burning $CaCO_3$ at 1000 ºC for 6 hours (S_a = 548 m²/kg); γ-Al_2O_3, obtained after heating $Al(OH)_3$ for 5 hours at 550 °C (S_a = 712 m^2/kg).

The synthesis of calcium silicate hydrates was carried out in unstirred suspensions in vessels of stainless steel. The molar ratios of the primary mixtures were C/(S + A) = 0.66 and A/(S + A) = 0.025 (C – CaO, S – SiO_2, A – Al_2O_3). The amount of NaOH corresponding to 5% of Na_2O in the mass of dry materials was added in the form of solution, together with the additional necessary quantity of water; the water/solid ratio of the suspension thus produced was equal to 10.0. Hydrothermal synthesis was car-

ried out under saturated steam pressure at temperatures of 150, 175, 200 ºC; the duration of isothermal curing was 4, 8, 16, 24, 32, 48, 72, or 168 hours. The products of the synthesis were filtrated, rinsed with ethyl alcohol to prevent carbonisation, dried at 100 ± 5 ºC, and sieved through an N 005 sieve.

X-ray powder diffraction data were collected with a DRON–6 X-ray diffractometer with Bragg–Brentano geometry using Ni-filtered CuK_α radiation and a graphite monochromator, operating with the voltage of 30 kV and emission current of 20 mA. The step-scan covered the angular range 2–60° (2θ) in steps of $2\theta = 0.02°$.

Simultaneous thermal analysis (STA) – comprising differential scanning calorimetry (DSC) and thermogravimetry (TG) – was also employed for measuring the thermal stability and phase transformation of the synthesized products at a heating rate of 10 °C/min; the temperature ranged from 30 to 1000 °C in ambient atmosphere. The test was carried out with a Netzsch instrument STA 409 PC Luxx. The ceramic sample handlers and crucibles used were made of Pt–Rh.

Scanning electron microscopy (SEM) (Oxford ISIS Leo 440 i, UK), coupled with energy dispersive X-ray spectrometry (EDS) of the samples, was performed using the accelerating voltage of 20 kV and a working distance of 10 mm for SEM observation and a 200 s accumulation time for EDS analysis.

IR spectra were carried out with Perkin Elmer FT-IR system spectrum X spectrometer. Specimens were prepared by mixing 1 mg of the sample with 200 mg of KBr. Spectral analysis was performed in the range 4000–400 cm^{-1} with a spectral resolution of 1 cm^{-1}.

The specific surface area of the raw materials was determined by Blaine's method.

3. Results and discussion

In a pure CaO–quartz–H_2O mixture after 24 hours of isothermal curing at 150 °C, the compounds with higher basicity – dicalcium silicate hydrates – α-C_2S hydrate and calcium silicate hydrates of unspecified composition with C/S > 1.5 (C–S–H(II)) were formed due to the fact that quartz dissolved slower than $Ca(OH)_2$ and the solution contained a significant excess of Ca^{2+} ions (Fig. 1, curve 1; Table 1). When hydrothermal synthesis was extended up to 48 hours, almost all of the $Ca(OH)_2$ reacted and the intensity of the basic reflections of quartz in the XRD pattern slightly decreased. This variation can be assigned to the dissolution of a significant amount of quartz, which stimulates the decomposition of C–S–H(II) and α-C_2S hydrate, the latter only remaining in traces. Consequently, calcium silicate hydrate of unspecified composition of C/S between 0.8 and 1.5 (C–S–H(I)) and a small quantity of 1.13 nm tobermorite form in the products. As was expected, when synthesis is continued (168 h) all of the α-C_2S hydrate decomposes and 1.13 nm tobermorite starts to prevail in the product (Table 1).

At the beginning of the reaction (24 h), the Al_2O_3 additive did not change the sequence of calcium silicate hydrate formation – α-C_2S hydrate, C–S–H(II), quartz, and

$Ca(OH)_2$ dominate the products (Fig. 1, curve 2; Table 1). It should be noticed that the compounds of the calcium aluminium silicate hydrate groups began to form when synthesis was prolonged to 48 h.

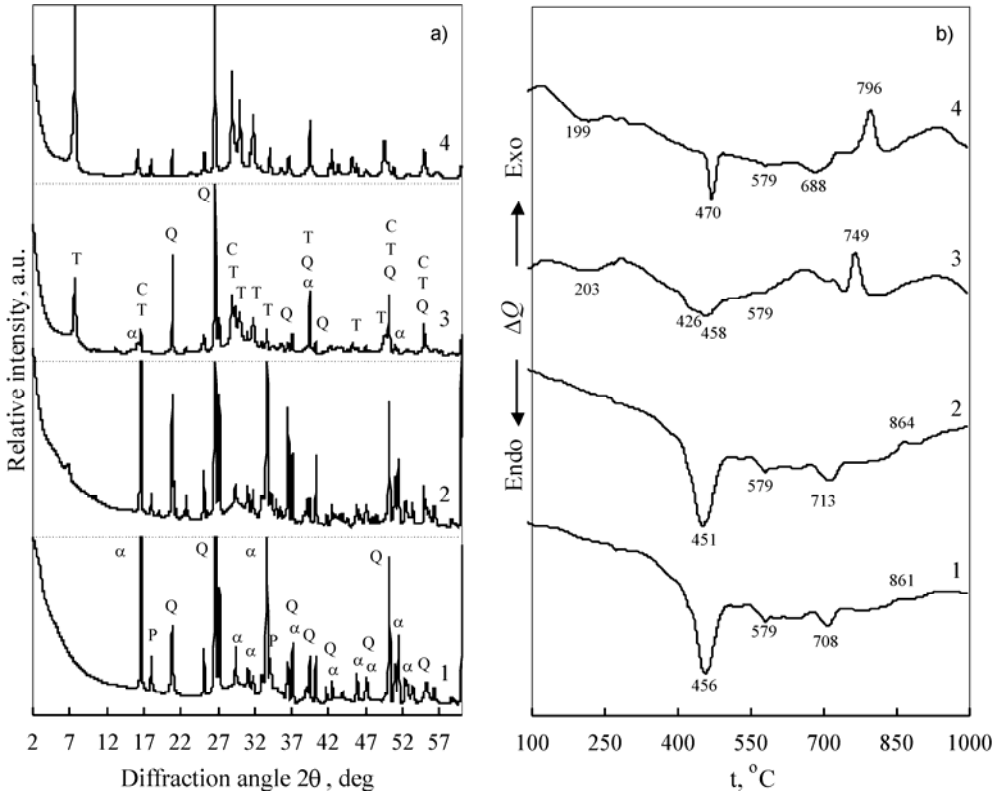

Fig. 1. X-ray diffraction patterns (a) and DSC curves (b)
of the products of synthesis: 1 – pure CaO–quartz–H_2O mixture; 2 – with Al_2O_3 additive;
3 – with Na_2O additive; 4 – with (Al_2O_3 + Na_2O) additive; indices: α – α-C_2S hydrate,
P – portlandite, Q – quartz, C – C–S–H(I), T – 1.13 nm tobermorite;
the duration of hydrothermal synthesis at 150 °C was 24 h

Many compounds form the group of calcium aluminium silicate hydrates or hydrogarnets, with almost the same interplanar distances *d*, and as a result their peaks overlap. The basic reflection intensities of the mentioned compounds in the X-ray diffraction patterns are rather small, as only 2.6% of Al_2O_3 was added to the initial mixture, and that is why it is very difficult to assign products to particular compounds. For this reason, these compounds will be named as calcium aluminium silicate hydrates (CASH), where the number of SiO_2 moles varies from 0 to 3.

It should be underlined that Al_2O_3 prolongs the existence of dibasic calcium silicate hydrates, and Al-substituted tobermorite forms only after 168 h of hydrothermal treatment. Furthermore, during this period CASH fully decompose.

Table 1. Stability of calcium silicate hydrates at 150 °C when the initial mixture molar ratio C/S = 0.66*

Initial mixture	Duration of curing (h)	P	Q	α	C(II)	C(I)	C	T
CaO–quartz–H_2O	24	●	●	●	●			
	48	●	●	●		●		●
	168		●			●		●
CaO–quartz–Al_2O_3–H_2O	24	●	●	●	●			
	48	●	●	●	●		●	
	168		●	●		●		●
CaO–quartz–Na_2O–H_2O	4	●	●	●				
	16	●	●	●		●		
	24	●	●	●		●		●
	72					●		●
CaO–quartz–Al_2O_3–Na_2O–H_2O	4	●	●				●	●
	16	●	●			●	●	●
	24	●	●			●		●
	72		●			●		●

*P – portlandite, Q – quartz, α – α-CS_2 hydrate, C(I) – C–S–H(I), C(II) – C–S–H(II), C – Calcium aluminum silicate hydrates, T – 1.13 nm tobermorite.

Na_2O intensified the hydrothermal reactions in the CaO–quartz–H_2O system. The main reason for this phenomenon was the presence of Na^+ ions in the solution accelerating the solubility rate of quartz by eroding the surface of particles and increasing the concentration of SiO_4^{4-} ions in the solution. The traces of α-C_2S hydrate are formed after the first 4 hours of synthesis, although large quantities of $Ca(OH)_2$ and unreacted quartz remain. Therefore, already after 16 h of isothermal curing C–S–H(I) begins to form, because the amount of unreacted quartz decreases. It should be stressed that dibasic calcium silicate hydrates are less stable than in the pure mixtures: after 16 h of synthesis they start to decompose, and after 24 h they almost fully transform into C–S–H(I) and 1.13 nm tobermorite (Fig. 1, curve 3). Quartz did not react completely even in 72 hours of synthesis, however, neither in pure mixtures nor in mixtures with the Na_2O additive (Table 1). Due to a low quartz solubility rate, the stoichiometric C/S ratio (0.66) of the primary mixture was not reached and both C–S–H(I) and 1.13 nm tobermorite dominated in the products.

In the CaO–Al_2O_3–SiO_2–H_2O mixture, Na^+ ions increase the solubility rate of quartz, too. On the other hand, Al^{3+} ions stimulated the formation of tobermorite and CASH: in the products they were identified already after 4 hours of isothermal curing. CASH began to decompose after 16 h of synthesis and tobermorite, together with C–S–H(I) and quartz, remained during the entire hydrothermal treatment (Table 1).

Thus, at 150 °C both Na_2O and complex (Al_2O_3 + Na_2O) additives accelerated the reactions by affecting the decomposition of dibasic calcium silicate hydrates and the formation of compounds of lower basicity. This temperature was still too low for the

synthesis of low-base calcium silicate hydrates (Z-phase, gyrolite, pectolite), however, as even after 168 h of isothermal curing a large quantity of quartz remained in the products.

In order to increase the reaction rate and avoid the formation of dicalcium silicate hydrates, hydrothermal synthesis was carried out at higher temperatures. In pure mixtures at 175 °C, after 16 hours of synthesis α-C_2S hydrate, C–S–H(II), $Ca(OH)_2$, and traces of 1.13 nm tobermorite form (Fig. 2, curve 1; Table 2).

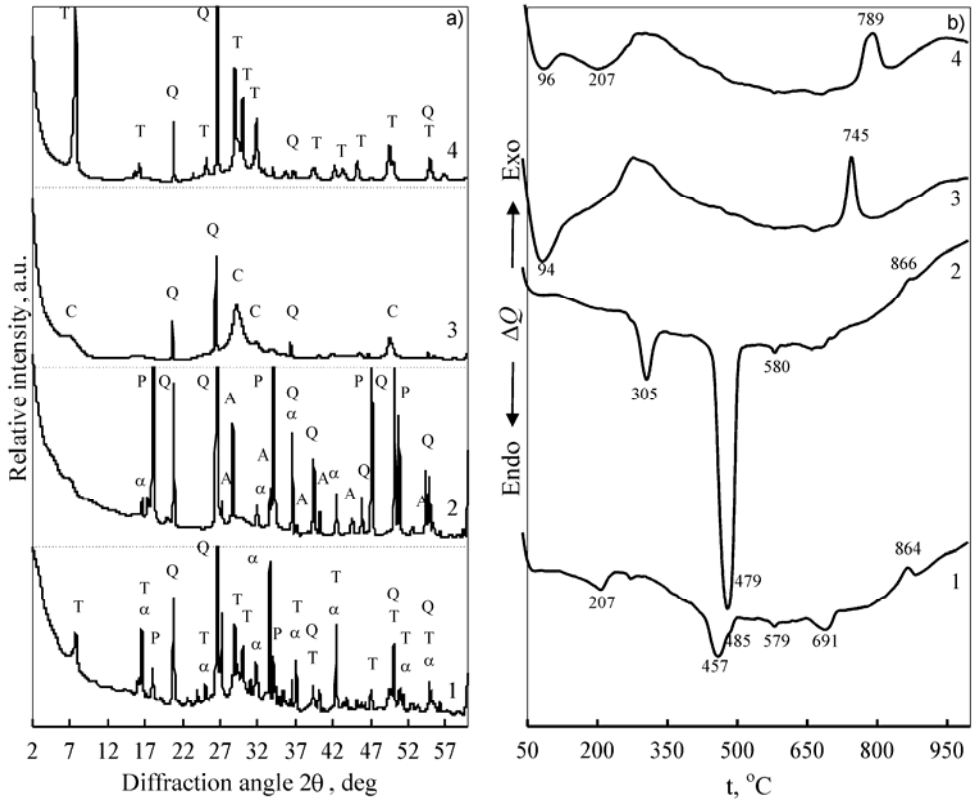

Fig. 2. X-ray diffraction patterns (a) and DSC curves (b) of the products of synthesis: 1 – pure CaO–quartz–H_2O mixture; 2 – with Al_2O_3 additive; 3 – with Na_2O additive; 4 – with (Al_2O_3 + Na_2O) additive; indices: α – α-C_2S hydrate, P – portlandite, Q – quartz, C – C–S–H(I), T – 1.13 nm tobermorite; the duration of hydrothermal synthesis at 175 °C was 16 h

Already in 1974, Taylor [33] noticed that at temperatures above 150 °C tobermorite is thermodynamically unstable in mixtures with C/S > 0.8, and that this compound tends to turn into xonotlite. This finding is confirmed by our experimental results: at sufficiently long hydrothermal curing (48 hours), when dibasic calcium silicate hydrates fully decompose, tobermorite partly transforms into xonotlite and not gyrolite, because even in the mixture reacting at 175 °C the C/S ratio is higher than 0.66 due to

the low quartz solubility rate. It should be noticed that both 1.13 nm tobermorite and xonotlite dominate in the products even after 72 hours of isothermal curing (Table 2).

Table 2. Stability of calcium silicate hydrates at 175 °C when the initial mixture molar ratio C/S = 0.66*

Initial mixture	Duration of curing (h)	P	Q	α	C(II)	C(I)	C	T	X	P	G	Z
CaO–quartz–H_2O	16, 24, 32	●	●	●		●		●				
	48, 72		●			●		●	●			
CaO–quartz–Al_2O_3–H_2O	16	●	●	●	●		●					
	24	●	●	●	●	●	●	●				
	32		●	●	●	●	●	●				
	48		●			●		●				
	72		●					●	●			
CaO–quartz–Na_2O–H_2O	4, 8, 16, 24, 32		●			●						
	72		●			●		●				
	168		●					●		●	●	●
CaO–quartz–Al_2O_3–Na_2O–H_2O	4	●	●			●	●	●				
	8, 16, 24, 32		●			●		●				
	72					●		●				
	168					●		●			●	

*P – portlandite, Q – quartz, α – α-CS_2 hydrate, C(I) – C–S–H(I), C(II) – C–S–H(II), C – calcium aluminum silicate hydrates, T – 1.13 nm tobermorite, X – xonotlite, P – pectolite, G – gyrolite, Z – Z-phase.

At 175 °C Al_2O_3 additive did not influence the formation and stability of α-C_2S hydrate, but retarded the formation of 1.13 nm tobermorite, which was identified in the products only after 24 h of synthesis; when in the pure mixture, after 16 h (Fig. 2, curves 1, 2). CASH fully decomposed after 48 h of isothermal curing and released Al^{3+} ions enter into the crystal structure of tobermorite or C–S–H(I). C–S–H(II) finished transforming into C–S–H(I), since the exothermic peak of that compound disappeared from the DSC curve.

It is well known that in mixtures with the molar ratio of C/S = 1.0, Al_2O_3 additives impede the formation of xonotlite. Our results show that the same sequence of calcium silicate hydrates form in the low basicity mixtures (C/S = 0.66), too. The most characteristic *d*-spacing of xonotlite in the XRD pattern (0.70 nm) was observed only after 72 h of synthesis at 175 °C (in the mixtures without aluminium additives after 48 h). Meanwhile, unreacted quartz remained in the products dominated by highly crystalline Al-substituted tobermorite (Table 2).

In the mixture with Na_2O, there was a substantial change in the sequence of calcium silicate hydrate formation at 175 °C: $Ca(OH)_2$ reacts completely and only a semi-crystalline C–S–H(I) is formed during the first 4 hours of synthesis. It should be emphasized that dibasic calcium silicate hydrates are not formed at this tempera-

ture or at 200 °C. This can be explained by the presence of Na^+ ions in the solution, which accelerate the solubility rate of quartz. It should be noted that the final amount of unreacted quartz (10–15%) dissolved very slowly and C–S–H(I) formed only after 8 hours of hydrothermal treatment (Fig. 2, curve 3; Table 2). At 175 °C, due to a rapid decrease of the C/S ratio to 0.7, 1.13 nm tobermorite was only the intermediary compound, because after 72 h of isothermal curing rudiments of calcium sodium silicate hydrate (pectolite) coexist. When synthesis was prolonged to 168 h, the amount of tobermorite decreased and low-base calcium silicate hydrates (pectolite, gyrolite, and Z-phase) prevail in the products (Fig. 3, curve 1).

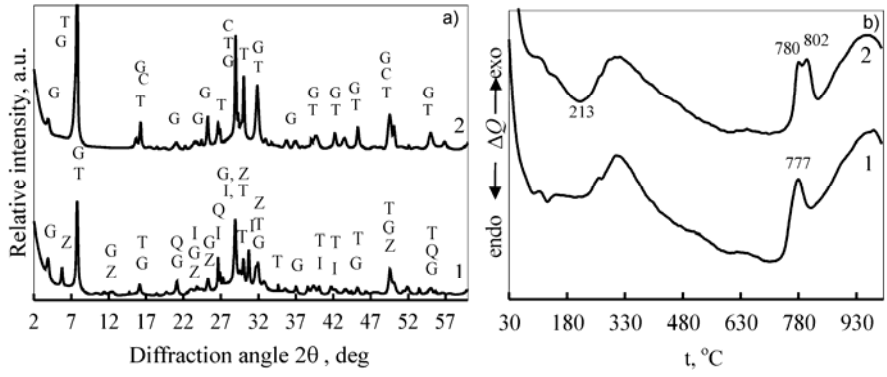

Fig. 3. X-ray diffraction patterns (a) and DSC curves (b) of the products of synthesis: 1 – with Na_2O additive; 2 – with (Al_2O_3 + Na_2O) additive; indices: Q – quartz, C – C–S–H(I), T – 1.13 nm tobermorite, I – pectolite, Z – Z-phase, G – gyrolite; the duration of hydrothermal synthesis at 175 °C was 168 h

Thus, low-base calcium silicate hydrates can be synthesized when a less active SiO_2 modification (quartz) and sodium oxide are used. Larger quantities of these compounds, however, form only after 168 hours of isothermal curing at 175 °C.

It was determined that in CaO–quartz mixtures the complex (Al_2O_3 + Na_2O) additive greatly accelerated the formation of 1.13 nm tobermorite and C–S–H(I) at 175 °C: those compounds were identified already after 4 h of synthesis (Table 2). The exothermic peak of C–S–H(I) at 813 °C became wider than in the mixtures without additives. It is presumable that they were affected by Al^{3+} and Na^+ ions, which entered the crystal structures of both tobermorite and C–S–H(I). Also, it was observed that Al^{3+} ions interfered in the crystal structures of calcium silicate hydrates significantly rather than at 150 °C, because traces of CASH were identified only at the beginning of synthesis (Table 2).

Thus, Al^{3+} and Na^+ions interfered in the crystal structures of calcium silicate hydrates and stabilized them. Almost the same quantities of 1.13 nm tobermorite and C–S–H(I) remain unchanged after 24, 48, and 72 hours of hydrothermal treatment.

After 168 h of isothermal curing, it started to transform into gyrolite (Fig. 3a, curve 2). The formation of Z-phase and pectolite was not observed, as in the mixtures with Na_2O (Fig. 3a, curve 1). The XRD data were confirmed by DSC measurements,

and in the DSC curve the two exothermic peaks at 780 °C, characteristic of C–S–H(I), and at 802 °C, associated to gyrolite, are observed (Fig. 3b, curve 2). (Al + Na) -substituted tobermorite formed together with gyrolite and C–S–H(I) is stable (the intensities of the basic reflections do not change after prolonging hydrothermal treatment from 24 to 168 h). Thus, at 175 °C gyrolite was successfully synthesized when an SiO_2 modification (quartz) was used, although other calcium silicate hydrates were formed together with it, namely 1.13 nm tobermorite and C–S–H(I).

Table 3. Stability of calcium silicate hydrates at 200 °C when the initial mixture molar ratio C/S = 0.66*

Initial mixture	Duration of curing (h)	P	Q	α	C(I)	C	T	X	P	G	Z
CaO–quartz–H_2O	4, 16, 24, 32		●		●		●	●			
	48, 72, 168		●				●	●			
CaO–quartz–Al_2O_3–H_2O	4, 16	●	●	●	●	●	●				
	24		●	●	●	●	●	●			
	32		●		●		●	●			
	48, 72		●		●		●	●			
	168		●		●		●				
CaO–quartz–Na_2O–H_2O	4, 8		●		●						
	16		●		●					●	●
	24		●						●	●	●
	32, 48, 72, 168								●	●	
CaO–quartz–Al_2O_3–Na_2O–H_2O	4, 8		●		●		●				
	16, 24		●		●		●			●	
	32				●		●			●	
	48, 72, 168						●			●	

*P – portlandite, Q – quartz, α – α-CS_2 hydrate, C(I) – C–S–H(I), C – calcium aluminum silicate hydrate, T – 1.13 nm tobermorite, X – xonotlite, P – pectolite, G – gyrolite, Z – Z-phase.

It should be pointed out that in the CaO–quartz–H_2O system neither α-C_2S hydrate nor C–S–H(II) formed at 200 °C. After 4 hours of isothermal curing, xonotlite formed, together with 1.13 nm tobermorite. These compounds were stable after prolonging the duration of isothermal curing to one week (Table 3). Quartz does not dissolve even after 168 h (Fig. 4, curve 1), however, and the quantity of 1.13 nm tobermorite changes unevenly, increases and decreases. We suppose that this is related to the changing C/S ratio during synthesis.

The Al_2O_3 additive slightly changed the sequence of calcium silicate hydrate formation. Primarily, like for lower temperatures, α-C_2S hydrate and CASH form, together with traces of C–S–H(I) and 1.13 nm tobermorite. Afterwards, when dibasic calcium silicate hydrates start to decompose, the amount of tobermorite increases, and xonolite begins to form. It should be underlined that the latter is not stable in mixtures of low basicity – after 168 hours of isothermal curing almost all quartz dissolved, and

the C/S ratio was approximately 0.66 and almost all of the xonolite turned into 1.13 nm tobermorite (Fig. 4, curve 2).

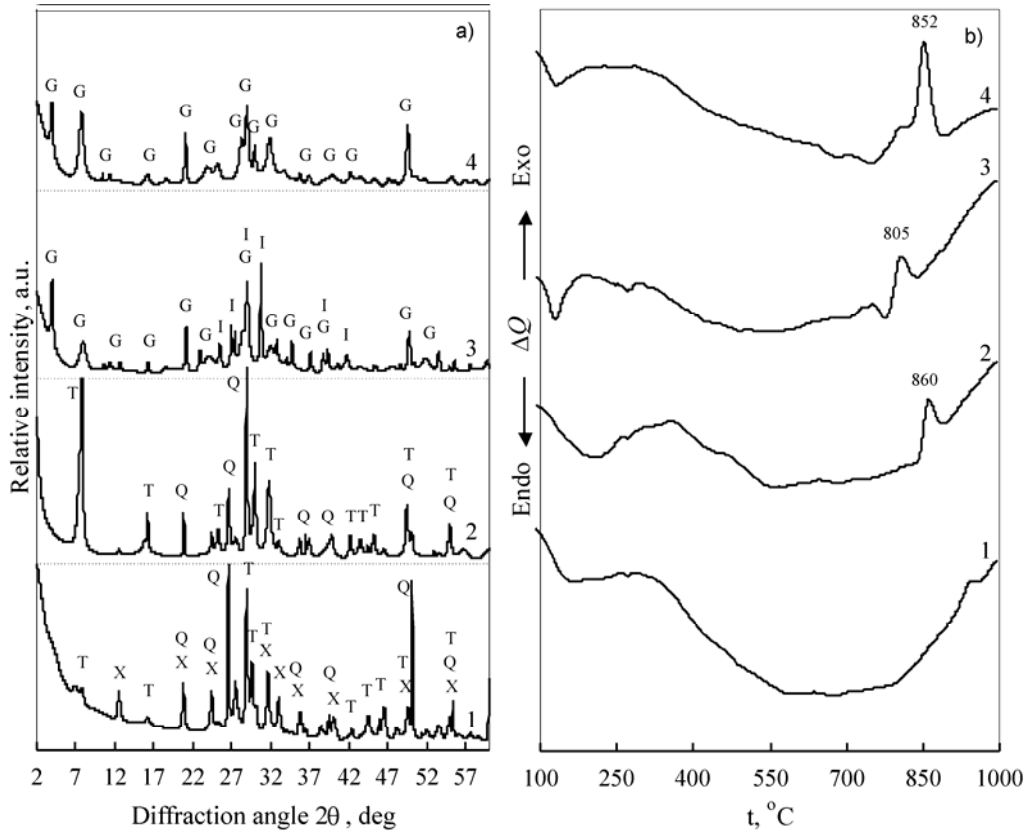

Fig. 4. X-ray diffraction patterns (a) and DSC curves (b) of the products of synthesis: 1 – pure CaO–quartz–H_2O mixture; 2 – with Al_2O_3 additive; 3 – with Na_2O additive; 4 – with (Al_2O_3 + Na_2O) additive; indices: Q – quartz, T – 1.13 nm tobermorite, X – xonotlite, I – pectolite, G – gyrolite. The duration of hydrothermal synthesis at 200 °C was 168 h

At 200 °C, Na_2O greatly affects the solubility rate of quartz, significantly accelerates the hydrothermal process, and totally changes the sequence of calcium silicate hydrate formation (Table 3). After 4 hours of synthesis, a large quantity of C–S–H(I) was formed and the larger part of the quartz reacted. After prolonged synthesis (16 hours), almost all of the quartz reacted. Therefore, it is not a coincidence that the basic peaks, characteristic of gyrolite (*d* spacing – 2.2 nm) and Z-phase (*d* spacing – 1.5 nm), start to dominate in the X-ray diffraction pattern of the reaction products. This is confirmed by DSC data: the exothermic peak at ~782 °C moves towards lower temperatures (~66 °C) and becomes wider.

It should be noted that the Z-phase was not stable in the mixtures with Na_2O, after 24 hours of hydrothermal synthesis only traces of this compound remained and al-

ready after 32 hours it finished transforming into gyrolite and pectolite. These compounds remain stable even after 168 h of isothermal curing (Fig. 4, curve 5). The accumulation of two morphologies crystals can be seen in the SEM micrographs: plate-shaped crystals characteristic of gyrolite and long, needle-shaped crystals characteristic of pectolite (Fig. 5, a).

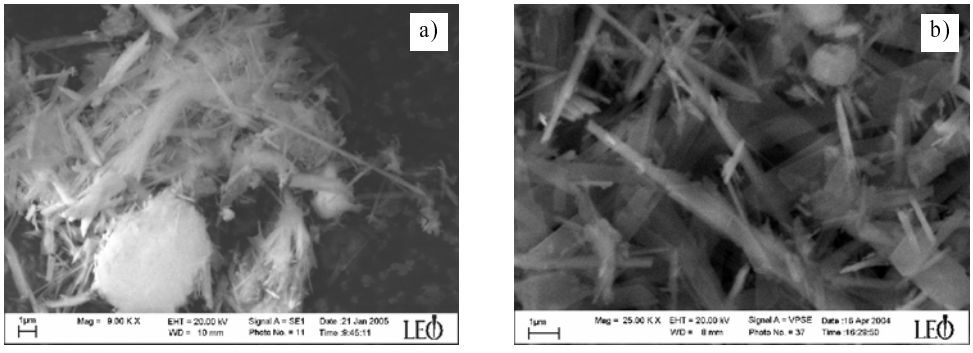

Fig. 5. SEM micrographs with Na_2O (a) and (Al_2O_3 + Na_2O) (b) additives; duration of isothermal curing at 200 °C was 168 h and 48 h, respectively

The formation of low-base calcium silicate hydrates in the CaO–SiO_2–Na_2O–H_2O system is rather slowed down when Al_2O_3 is added, because Al^{3+} ions stimulate the formation of tobermorite and after 16 hours of isothermal synthesis only traces of gyrolite were identified. When hydrothermal synthesis is continued, gyrolite further forms but even after 168 hours of synthesis 1.13 nm tobermorite remained in the products. At 175 °C, the presence of Al_2O_3 additive prevents the formation of pectolite and Z-phase (Fig. 4, curve 4). SEM observations confirmed that 1.13 nm tobermorite and gyrolite dominate in the products (Fig. 5b).

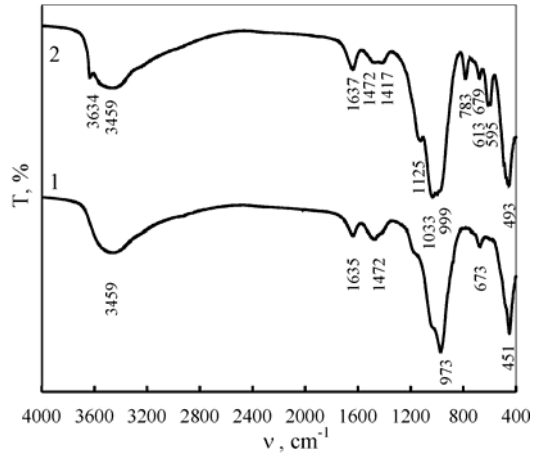

Fig. 6. IR spectra of the products of synthesis of the CaO–quartz–Na_2O–Al_2O_3–H_2O system; the duration of hydrothermal synthesis at 200 °C was 16 h (1) and 72 h (2)

All the data presented above have been confirmed by IR spectroscopy, which can be used to distinguish gyrolite from the Z-phase as well as from other calcium silicate hydrates [34, 35]. IR spectroscopy data show that after 16 h of synthesis the adsorption bands characteristic of tobermorite dominate (Fig. 6, curve 1). After extending the duration of isothermal curing (24, 32, 72 h), a doublet near ~595 and ~613 cm^{-1} due to Si–O–Si bending vibrations becomes more intensive, and gyrolite has two bands in the range 679–786 cm^{-1} (Fig. 6, curve 2). A sharp peak near 3634 cm^{-1}, which is visible only in the gyrolite spectrum, is missing in the IR spectra of all other calcium silicate hydrates. This clear band (3634 cm^{-1}) proves that clearly distinguished OH positions exist in the structure of gyrolite, being connected only to Ca atoms and the groups not being influenced by hydrogen bridge links.

4. Conclusions

- In the CaO–quartz–H_2O system with C/S = 0.66 the reactions proceed very slowly and low-base calcium silicate hydrates do not form in the temperature range 150–200 °C. α-C_2S hydrate and C–S–H(II) prevail during the beginning of synthesis, gradually recrystallising into 1.13 nm tobermorite and xonotlite, which remain stable even after 168 hours of isothermal curing.
- γ-Al_2O_3 has little influence on the hydrothermal process. At the beginning of the reaction this additive prolongs the lifetime of dibasic calcium silicate hydrates, and retards the formation of 1.13 nm tobermorite and its transformation into xonotlite.
- Na_2O increases the solubility rate of quartz and greatly affects the sequence of calcium silicate hydrate formation. In the temperature range 175–200 °C, the intermediate compounds are C–S–H(I) and the Z-phase, and the final products are gyrolite and pectolite.
- The complex (Al_2O_3 + Na_2O) additive stimulates the decomposition of α-C_2S hydrate, but prevents the formation of the Z-phase and pectolite. Gyrolite forms analogously as in the mixture with Na_2O, although it always coexists with 1.13 nm tobermorite.

References

[1] TAYLOR H.F.W., BESSEY G.E., Mag. Concr. Res., 2 (1950), 15.
[2] ASSARSSON G.O., J. Phys. Chem., 61 (1957), 473.
[3] SASAKI K., MASUDA T., ISHIDA H., MITSUDA T., J. Am. Ceram. Soc., 80 (1996), 472.
[4] KALOUSEK G.L., J. Am. Concr. Inst., 26 (1955), 989.
[5] MIYAKE M., KOMARNENI S., ROY R., Mater. Res. Bull., 24 (1989), 311.
[6] HARA N., CHAN C., MITSUDA T., Cem. Concr. Res., 8 (1978), 113.
[7] GABROVSEK R., KURBUS B., MUELLER D., WEIKER W., Cem. Concr. Res., 2 (1993), 321.
[8] HONG S.-Y., GLASSER F.P., Cem. Concr. Res., 34 (2004), 1529.
[9] BELL N.S., VENIGALLA S., GILL P.M., ADAIR J.H., J. Am. Ceram. Soc., 79 (1996), 2175.

[10] EL-HEMALY S.A.S., MITSUDA T., TAYLOR H.F.W., Cem. Concr. Res., 7 (1977), 429.
[11] ZHANG X., CHANG W., ZHANG T., KONG, C., J. Am. Ceram. Soc., 83 (2000), 2600.
[12] BLACK L., GARBEV K., STEMMERMANN P., HALLAM K.R., ALLEN G.C., Cem. Concr. Res., 33 (2003), 899.
[13] TAYLOR H.F.W., J. Am. Ceram. Soc., 69 (1986), 464.
[14] MIYAKE M., IWAYA M., SUZUKI T., J. Am. Ceram. Soc., 73 (1990), 3524.
[15] WINTERS M.A., RICHTER J.D., SAGAR S.L., LEE A.L., LANDER R.J., Biotechnol. Prog., 19 (2003), 440.
[16] STUMM A., GARBEV K., BEUCHLE G., BLACK L., STEMMERMANN P., NQESCH R., Cem. Concr. Res., 35 (2005), 1665.
[17] FLINT E.P., MCMURDIE H.F., WELLS L.S., J. Res. Natl. Bur. Stand., 21 (1938), 617.
[18] ŠTEVULA L., HARMAN M., HORVATH I., PUTYERA K., Ceram-Silik., 34 (1990), 315.
[19] JAUBERTHIE R., TEMIMI M., LAQUERBE M., Cem. Concr. Res., 26 (1996), 1335.
[20] SHAW S., HENDERSON C.M.B., CLARK S.M., Am. Mineral., 87 (2002), 533.
[21] GARD J.A., MITSUDA T., TAYLOR H.F.W., Mineral. Mag., 43 (1975), 325.
[22] KALOUSEK G.L., NELSON E.B., Cem. Concr. Res., 8 (1978), 283.
[23] ŠTEVULA L., PETROVIČ J., Cem. Concr. Res., 13 (1983), 684.
[24] OKADA Y., MASUDA T., ISHIDA H., J. Ceram. Soc. Japan., 103 (1995), 124.
[25] FUNK H., THILO E., Z. anorg. allg. Chem., 278 (1955), 237.
[26] LUKE K., Cem. Concr. Res., 34 (2004), 1725.
[27] MERLINO S., Mineral. Mag., 52 (1988), 377.
[28] ELTON N.J., HOOPER J.J., HOLYER V.A.D., Mineral. Mag., 62 (1998), 271.
[29] NOCUN-WCZELIK W., Cem. Concr. Res., 27 (1997), 83.
[30] NOCUN-WCZELIK W., Cem. Concr. Res., 29 (1999), 1759.
[31] SUZUKI K., NISHIKAWA T., IKENAGA H., ITO S., Cem. Concr. Res., 16 (1986), 333.
[32] EL-KORASHY S.A., J. Ion Exchange., 15 (2004), 2.
[33] TAYLOR H.F.W., *Crystal Chemistry of Portland cement hydration*, 6-th International Congress on the Chemistry of Cement, Research Institute VNIIESM of the USSR Ministry of Building Materials Industry, Moscow, 1974.
[34] YU P., KIRKPATRICK R.J., POE B., MCMILLAN P.F., CONG X., J. Am. Ceram. Soc., 82 (1999), 724.
[35] GARBEV K., PhD Dissertation, Faculty of Geology and Geography, University St. Kliment Ohridski, Sofia, 2004.

Received 19 June 2006
Revised 5 July 2006

Materials Science-Poland, Vol. 25, No. 1, 2007

The solidification of CuCr alloys under various cooling rates

Y. WANG[1, 2*], X. SONG[1], Z. SUN[1], X. ZHOU[1], J. GUO[1]

[1]School of Science, Xi'an Jiaotong University, Xi'an 710049, P. R. China

[2]Institute of Materials Science and Engineering, Taiyuan Science and Technology University, Taiyuan 030024. P. R. China

The paper focuses on the solidification especially on the liquid phase separation of Cu–35 at. % Cr alloys under various cooling rates. When the solidification temperature is below the liquidus and above the spinodal temperature, solidification runs normally, with the growth of primary Cr-rich dendrites. When the solidification temperature is below the spinodal temperature, liquid phase separation should occur through the solidification process and the primary Cr-rich phase has a special nodular structure under an appropriate cooling rate. Large Cr-rich particles obtained from liquid phase separation can grow by absorbing smaller ones via the transfer of matter. Furthermore, some particles collide with each other, mutually losing surface energy by joining to form a single particle. The size of the Cr-rich particles obtained from liquid phase separation decreases with increasing cooling rate. Using thermodynamic calculations and referring to literature data, the viewpoints on liquid phase separation are systematized and applied to the CuCr system. Liquid phase separation in an undercooled liquid is not advantageous in refining the microstructure of alloys and should be restricted.

Key words: *solidification; liquid phase separation; CuCr alloy; melt spinning; microstructure*

1. Introduction

Liquid phase separation in the solidification process will occur in some systems with a stable or metastable miscibility gap, denoted in their diagrams under a large undercooling. The liquid phase separation of Cu–Co, Cu–Fe, and Cu–Co–Fe alloys has been described in previous papers [1–10]. The CuCr alloy is also a binary system having a flat liquidus (20~75 at. % Cr), with a dashed line for the miscibility gap and a dashed line for the spinodal in its diagram. Its liquid phase separation has been elucidated only in theory on the CuCr diagram [11–13].

*Corresponding author, e-mail: Wyheyj@163.com

The electromagnetic levitation and fluxing techniques are generally used in research work on liquid phase separation. Since the difference in the melting points of Cu and Cr is very large and Cr is still in solid state when the Cu liquid starts to drop, the electromagnetic levitation technique cannot be used to study CuCr alloys. There are some consuming reactions between CuCr alloys and slag glass, therefore the fluxing technique also cannot be used. Melt spinning is a common method for rapid solidification nowadays. By controlling the rotary speed of the cooling roller, various cooling rates can be produced. Finally, we succeeded in using the melt spinning technique for studying the liquid phase separation of CuCr alloys. This paper focuses on the solidification of Cu–35 at. % Cr alloys under various cooling rates.

2. Experimental

Pure (>99.95%) Cu and Cr were used to prepare the CuCr alloys by arc-melting. Some of the CuCr alloys were used as specimens with a lower cooling rate ($<10^3$ K/s)[14]. Subsequently, about 10g of the CuCr alloys were inserted into quartz tubes. When they were heated by high frequency induction to the required temperature, a ribbon was prepared by liquid quenching on a single roller melt spinning under the pressure of 0.5 atm Ar gas. The velocities of the cooling roller were 0.8 m/s and 33 m/s, and the corresponding calculated ribbon cooling rates were about 10^4 K/s and 10^6 K/s, respectively [15]. The dimensions (width×thickness) of the prepared ribbons were about 5 mm×800 μm and 3 mm×40 μm. The maximum undercooling of the 3 mm×40 μm ribbons was about 400–450 K [16, 17].

The microstructures of the samples were analyzed with an optical JSM 6460 scanning electron microscope (SEM) equipped with an energy dispersive spectrometer (EDS), and with a Hitachi H-800 transmission electron microscope (TEM). The foil specimen for the TEM was prepared by a twin-jet thinning device.

3. Results

3.1. Solidification of Cu–35 at. % Cr ingots at a cooling rate below 10^3 K/s

The microstructure of arc-melted Cu–35 at. % Cr ingots observed by SEM is shown in Fig. 1. The solidification of the ingots runs normally with the growth of primary Cr-rich dendrites (dark phase). Since the direction of dendritic growth is different, the dendrite arrowed in Fig. 1 is in the typical dendritic morphology, while some sections of dendrite look like snatchy structures. The entire sample was filled with this dendritic morphology. The Cu-rich phase (bright) was formed through an eutectic reaction.

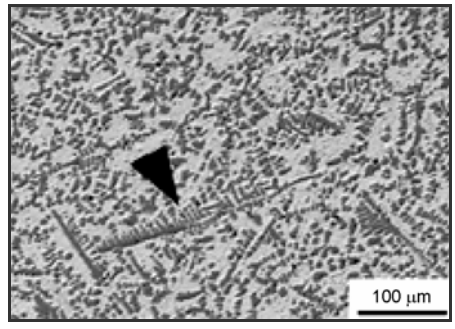

Fig. 1. The microstructure of arc-melted Cu –35 at. % Cr alloys observed by SEM. The arrow in the figure notes the primary Cr-rich dendrite. Etched with 5% HNO_3 + 95% C_2H_5OH

3.2. Solidification of CuCr ribbons at a cooling rate of about 10^4 K/s

In this part, ribbons about 5 mm wide and 800 μm thick were used as samples. There are many nodular particles in zone I oriented vertically, denoted by the arrow in Fig. 2a. The microstructure of zone I is shown in Fig. 2b and consists of large and nodular Cr-rich particles. Some particles are connected. The microstructure of zone II near the cooling surface in Fig. 2c consists of very small nodular Cr-rich particles. The microstructure of zone III near the free surface in Fig. 2d consists of Cr-rich dendrites.

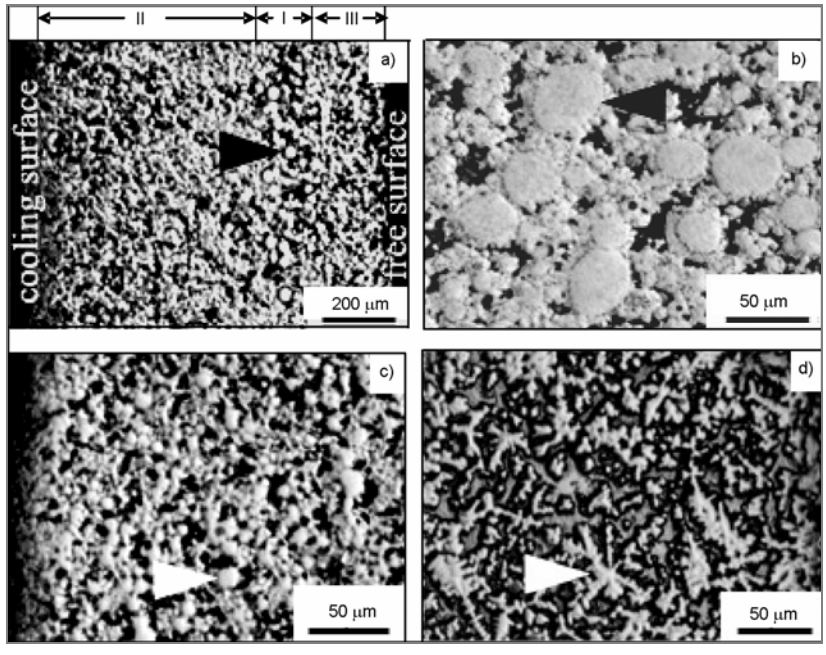

Fig. 2. The microstructures of melt spun Cu–35 at. % Cr ribbon at a cooling rate of about 10^4 K/s, observed by optical microscope: a) the cross section of the ribbon; b) zone I depicted by the arrow in Fig. 2a; c) zone II near the cooling surface; d) zone III near the free surface. The arrows in the Figure denote the Cr-rich particles obtained from liquid phase separation, except the arrow in Fig. 3d, which points to a Cr-rich dendrite. Etched with 80% $NH_3{\cdot}H_2O$ + 10% HCl + 10% Fe_2O_3

The change in the microstructures in melt spun Cu–35 at. % Cr ribbon is due to the change in the cooling rate or undercooling along the thickness of the ribbon. The higher the cooling rate, the smaller is the size of the primary Cr-rich phase. In contrast to Fig. 1, the microstructure of Cu–35 at. % Cr alloys was refined with increasing cooling rate. The larger nodular particle exists in zone I with a lower cooling rate.

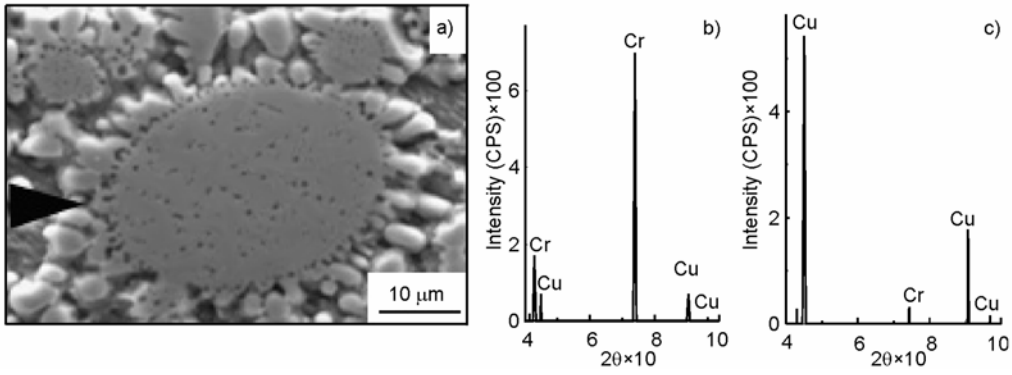

Fig. 3. The microstructure formed by liquid phase separation in a melt spun Cu–35 at. % Cr ribbon at a cooling rate of about 10^4 K/s, observed by SEM (a); X-ray diffraction diagrams of the gray phase in the Cr-rich particle (b); X-ray diffraction diagrams of the dark phase in Cr-rich particle (c); etched with 80% $NH_3{\cdot}H_2O$ + 10% HCl + 10% Fe_2O_3

Using SEM, the Cr-rich particle pointed out by the arrow in Fig. 2b was further studied and presented in Fig. 3a. Around its surface, there are many smaller Cr-rich particles that have an amalgamating tendency towards it. The large Cr-rich particle can grow by absorbing smaller ones via the transfer of matter. Furthermore, some particles collide with each other, mutually losing surface energy by joining to form a single particle [3]. Inside the particle, there is another phase (dark) besides the gray phase. According to EDS analysis (Figs. 3b, c), the gray phase is Cr-rich phase and the dark phase is Cu-rich. Robinson et al. [3] also observed a Cu-rich phase inside the Co particle obtained from liquid phase separation probably originating from liquid phase separation process. The behaviour of liquid phase separation in the CuCr system at a high cooling rate was confirmed experimentally.

3.3. Solidification of Cu–35 at. % Cr ribbons at a cooling rate of about 10^6 K/s

The microstructure of melt spun $CuCr_{35}$ ribbon 3 mm wide and 40 μm thick observed by TEM is shown in Fig. 4a. From their morphologies, one cannot tell whether these primary Cr-rich particles originate from liquid phase separation or from the general solidification process. This will be analyzed later in the discussion. The diameters of the primary Cr-rich particles were decreased to below 300 nm by increasing the cooling rate.

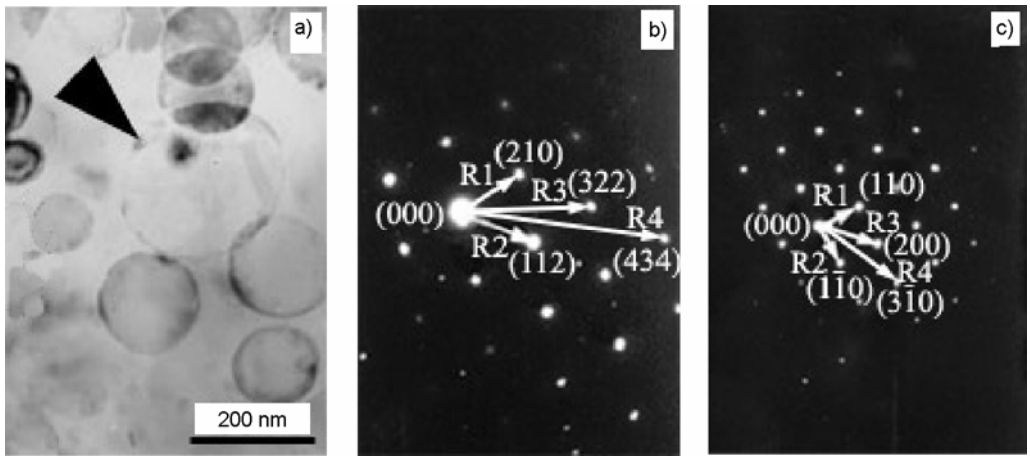

Fig. 4. Microstructure of melt spun Cu–35 at. % Cr ribbon at the cooling rate of about 10^6 K/s, observed by TEM (a); the arrow in the Figure points to a Cr-rich particle from liquid phase separation: electron diffraction pattern of the matrix (b); electron diffraction pattern of Cr-rich particle (c)

Figure 4b shows the electron diffraction pattern of the matrix, and the results of the analysis are given in Table; R_i is the distance between two points, N is the integer of $3R_i^2/R_1^2$, (hkl) is the index of the crystal face, $[uvw]$ is the zone axis, $d = K/R$ is the calculated interplanar spacing, K is the camera constant, $d_{\mathrm{Cu,standard}}$ is the interplanar spacing of Cu in a standard, $\angle R_1R_2$ is the angle between $(h_1k_1l_1)$ and $(h_2k_2l_2)$. As a result, we know that the matrix is *FCC* Cu. Figure 4c shows the electron diffraction pattern of the primary Cr-rich particle. The results of the analysis are shown in Table 2. Therefore, we know that the primary Cr-rich particle is *BCC* Cr.

Table 1. The results of the analysis for the electron diffraction pattern of the matrix in Fig. 4b*

R_i (mm)	$3R_i^2/R_1^2$	N	hkl	uvw	d = (Å)	$d_{\mathrm{Cu,standard}}$ (Å)
R_1 = 14.3	3.00	3	210	1$\bar{4}$1	1.6071	1.6168
R_2 = 16.3	3.90	4	112		1.4103	1.4759
R_3 = 27.5	11.05	11	322		0.8375	0.8768
R_4 = 37.0	27.01	27	434		0.5356	0.5646

*K = 23.03 mm·Å, $\angle R_1R_2$ = 57° (standard: 56.79°).

Table 2. The results of the analysis for the electron diffraction pattern of the Cr-rich particle in Fig. 4c*

R_i (mm)	$3R_i^2/R_1^2$	N	hkl	uvw	$d = K/R$ (Å)	$d_{\mathrm{Cu,standard}}$ (Å)
R_1 = 9	2.00	2	110	$\bar{2}0\bar{2}$	2.0106	2.0269
R_2 = 9	2.00	2	1$\bar{1}$0		2.0106	2.0269
R_3 = 13	4.17	4	200		1.3919	1.4332
R_4 = 20	9.88	10	3$\bar{1}$0		0.9048	0.9064

*K = 18.11 mm·Å, $\angle R_1R_2$ = 90° (standard: 90°).

4. Discussion

Figure 5 shows the Cu–Cr phase diagram [11–13] and mixing Gibbs energy (G_m) in undercooled CuCr liquid at 1500 K as calculated by us. According to the microstructure in Fig. 1 and considering the cooling rate in the solidification process, the solidification temperature of Cu–35 at. % Cr ingots should be below its liquidus and above its spinodal in Fig. 5a. The solidification in Fig. 5a can be expressed as: B (undercooled liquid) → A (liquid) + C (Cr solid), which runs normally. In this case, liquid phase separation does not occur during solidification.

Before discussing how the microstructures in Figs. 2, 3 were formed, the theory of liquid phase separation should be analysed. The mixing Gibbs energy of binary alloy systems can be expressed as:

$$G_m = RT(X_i \ln X_i + X_j \ln X_j) + \Omega_{ij} X_i X_j \tag{1}$$

where X_i is the mol fraction of a component i, Ω_{ij} is the interaction parameter between components i and j, R is the gas constant, and T is temperature in Kelvins.

Using the published data in [11], G_m of the undercooled liquid of the CuCr system at 1500 K was calculated from Eq. (1) as an example. The result is shown in Fig. 5b. Comparing Fig. 5a and Fig. 5b, the dashed line of the miscibility gap was calculated from the equality

$$\frac{\partial G_m}{\partial X_{\mathrm{Cr}}} = 0$$

The miscibility gap dashed line [18] corresponds to the minimum of the G_m value of the undercooled liquid. Undercooled liquids with compositions between points K and P in Fig. 5b tend to demix into a Cu-rich liquid (point K) and a Cr-rich liquid (point P), thus G_m of system will go down. The dashed line of the spinodal was calculated from the equality:

$$\frac{\partial^2 G_m}{\partial X_{\mathrm{Cr}}^2} = 0$$

Undercooled liquids with compositions between points M and O in Fig. 5b (inside the spinodal in Fig. 5a will start to demix spontaneously without nucleation. Undercooled liquids with compositions between points K, M, O, and P in Fig. 5b (outside the spinodal and inside the miscibility gap in Fig. 5a cannot demix at 1500 K, and will demix at a lower temperature.

After demixing, the solidification of the Cu-rich and Cr-rich liquids is inexplicit in theory. According to [3], there is a viewpoint that *once separated, the two liquids have different undercoolings with regard to their respective liquidus temperature.* [...] *As a result, L1 could solidify first according to the nucleation thermodynamics …* This implies that we can treat the two separated liquids within the general solidification theory after demixing.

Therefore, the solidification of the Cu-rich and Cr-rich liquids can be expressed as:

$$\text{I (Cr-rich liquid)} \rightarrow \text{D(liquid)} + \text{J(Cr solid)}$$

$$\text{E (Cu-rich liquid)} \rightarrow \text{D(liquid)} + \text{J(Cr solid)}$$

as seen in Fig. 5a. Robinson et al. [3], however, pointed out that the former transition is easier than the latter.

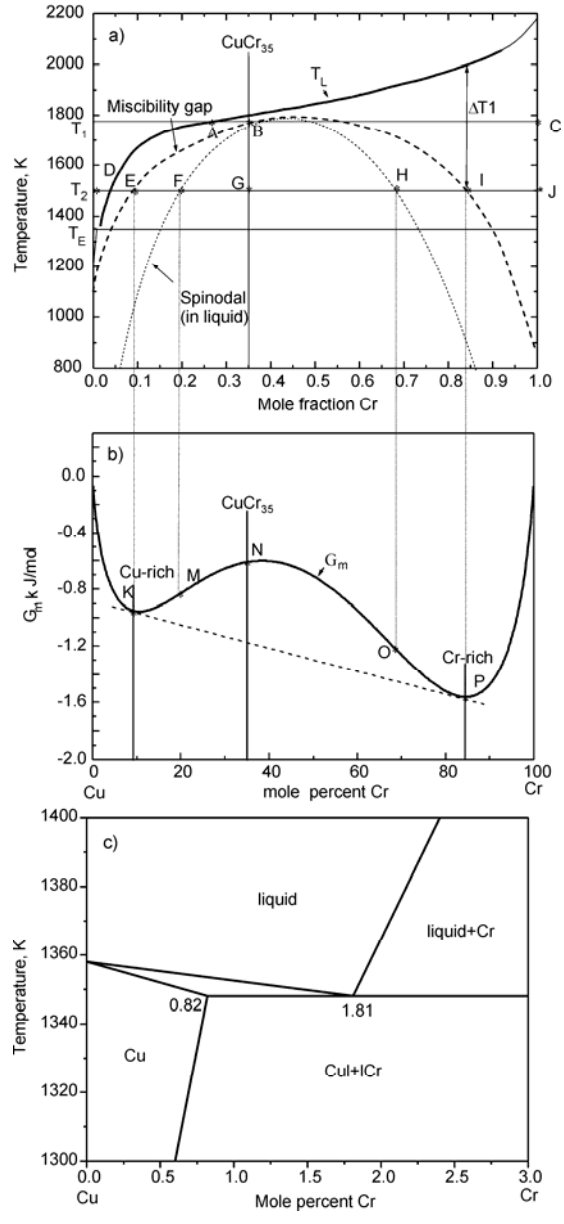

Fig. 5. Cu–Cr phase diagram [11] (a), mixing Gibbs energy of CuCr liquid at 1500 K (b), Cu–Cr phase diagram at the Cu-rich side (c)

Although the undercooling of the separated Cr-rich liquid is larger than that of the homogeneous $CuCr_{35}$ liquid at temperature T_2 in Fig. 5a, the size of the Cr solid phase in the Cr-rich liquid zone cannot be decreased by this factor because the growth of the Cr solid phase occurs in an undercooled liquid of about Cu–84% Cr, in which there are many Cr atoms. Therefore, the liquid phase separation in the undercooled liquid is not advantageous in refining the microstructure of alloys and should be restricted.

Considering the microstructures in Figs. 2, 3 and the cooling rate of the solidification process, the solidification temperature of zone II near the cooling surface and zone I pointed to by the arrow in Fig. 2a should be below its spinodal temperature. In the solidification processes of these two zones, liquid phase separation should occur. The solidification temperature of zone III near the free surface, however, should be above its spinodal temperature, as its solidification still runs normally.

Because undercooling increases as the cooling rate is increased, the solidification temperature at a cooling rate of about 10^6 K/s should be between the spinodal and the eutectic temperatures. According to the liquid phase separation theory presented above, the primary Cr-rich particles in Fig. 4a should originate from liquid phase separation.

5. Conclusions

When the solidification temperature is below its liquidus and above its spinodal, the solidification of Cu–35 at. % Cr alloys runs normally, with a growth of primary Cr-rich dendrites and the primary Cr-rich dendrites larger than 200 μm. After increasing the cooling rate to about 10^4 K/s, the solidification temperature of most of the cross section of melt spun Cu–35 at. % Cr ribbon, except zone III, should be below its spinodal temperature, and liquid phase separation should occur during the solidification process. The diameter of the larger Cr-rich particles is about 20 μm. The large Cr-rich particles can grow by absorbing smaller ones via the transfer of matter. Furthermore, some particles collide with each other, mutually losing surface energy by joining to form a single particle. After further increasing the cooling rate to about 10^6 K/s, the diameter of larger Cr-rich particles obtained from liquid phase separation is decreased to about 250 nm. The size of the Cr-rich particles obtained from liquid phase separation will decrease as the cooling rate is increased.

Using thermodynamic calculations and referring to other papers, the viewpoints on liquid phase separation are systematized and applied to the CuCr system. Liquid phase separation in undercooled liquid is not advantageous in refining the microstructure of alloys and should be restricted.

Acknowledgements

The authors would like to thank the National Science Foundation of China (grant No. 50371066) for their financial support.

References

[1] ELDER S.P., MUNITZ A., ABBASCHIAN G.J., Mater. Sci. Forum, 50 (1989), 137.
[2] MUNITZ A., J. Mater. Sci., 33 (1998), 3639.
[3] ROBINSON M.B., LI D., RATHZ T.J., WILLIAMS G., J. Mater. Sci., 34 (1999), 3747.
[4] SONG X., MAHON S.W., COCHRANE HOWSON R.F., Mater. Lett., 31 (1997), 261.
[5] PEREPECZKO J.H., SHIAHARA Y., PAIK J.S., FLEMINGS M.C., [in:] *Rapid Solidification Processing, Principles and Technologies III*, NBS, Gaithersburg, MD, (1982), 28.
[6] CHONGDE C., XIAOYU L., BINGBO W., Acta Metall. Sin., 5 (1998), 490.
[7] MUNITZ A., ELDER-RANDALL S.P., ABBASCHIAN R., Metall. Trans. A, 23 (1992), 1817.
[8] ABBASCHIAN G.J., FLEMINGS M.C., Metall. Trans. A, 14 (1983), 1147.
[9] XIAOYU L., CHONGDE C., BINGBO W., Acta Photon. Sin., Z3 (1998), 121.
[10] LI D., ROBINSON M.B., RATHZ T.J., J. Phase Equil., 21 (2000), 136.
[11] JACOB K.T., PRIYA S., WASEDA Y., Metall. Z., 91 (2000), 594.
[12] ZENG K., HÄMÄLÄINEN M., Calphad, 19 (1995), 93.
[13] MICHAELSEN C., GENTE C., BORMANN R., J. Mater. Res. 12 (1997), 1463.
[14] GRANT N.J., J. Metals, 1 (1983), 20.
[15] YOUHONG W., ZHANBO S., XIAOPING S., Chinese J. Nonferrous Met., 15 (2005), 1045.
[16] MASLOV V.V., NOSENKO V.K., J. Mater. Sci., 37 (2002), 4663.
[17] LIU F., YANG G., GUO X., J. Mater. Sci., 36 (2001), 3607.
[18] DEHOFF R.T., *Thermodynamics in Materials Science*, McGraw-Hill, Columbus, 1993, p. 255–260.

Received 19 June 2006
Revised 5 July 2006

Materials Science-Poland, Vol. 25, No. 1, 2007

Analysis of some properties of model system from low-melting illite clay and fibrous mineral wool waste

V. BALKEVIČIUS[1*], J. CHRISTAUSKAS[2], A. GAILIUS[2], A. ŠPOKAUSKAS[1], V. SIAURYS[1]

[1]Institute of Thermal Insulation, Vilnius Gediminas Technical University, Linkmenų str. 28, LT-08217, Vilnius, Lithuania

[2] Vilnius Gediminas Technical University, Saulėtekio al. 11, LT-10223 Vilnius, Lithuania

In recent years, recycling of fibrous mineral wool waste has become an acute problem. The present paper addresses this problem by suggesting a promising technique based on using fibrous mineral wool waste and low-melting illite clay with appropriate additives. The results obtained have shown that by applying an adequate calculation method it is possible to predict the fusibility characteristics of a selected chemical composition. The SiO_2–CaO–Na_2O system with the oxides Al_2O_3, MgO and Fe_2O_3 influencing its fusibility is considered. Fusibility characteristics of the investigated systems have been calculated and their structural changes were analysed.

Key words: *low-melting illite clay; fibrous mineral wool waste; fusibility characteristics*

1. Introduction

In recent years, recycling of waste materials has become an acute problem [1–4]. In manufacturing mineral wool, large amounts of waste materials are obtained. The waste consists of mineral wool fibres, pieces of unopened fibres (beads) and a small amount of organic binder (1–2%). Recycling of mineral wool waste is an important problem. When a melt used in mineral wool manufacture is obtained in bath furnaces, mineral wool waste may be remelted. However, when a cupola furnace is used, this is hardly possible because these furnaces are intended for melting lump raw materials. Therefore, small fibres of the waste clog up the feeding equipment of air and oxygen.

Jensen offered a briquetting technique to be used to charge cupola furnaces with briquettes and coke [5]. Miankovski described briquetting technology of basalt waste [6]. Some efforts were made to use briquetting for recycling mineral wool waste. Holdbek took out a patent for technology based on binding waste materials with Port-

* Corresponding author, e-mail: valdas.balkevicius@termo.vgtu.lt

land cement which is a hydraulic binder [7]. However, in melting the briquettes bound with Portland cement under high temperature, they split into small pieces before starting to melt, thereby making remelting in the cupola furnace impossible because of the broken feeding of air and gases [8].

In addition to Portland cement, some other binding materials may be used for waste material binding. Nefedova offered a technique based on binding waste materials with liquid glass [9]. However, this method has a drawback because in this case only beads may be used. The tests performed show that a promising mineral wool recycling technique is the use of low-melting illite clays [8, 10].

The main parameters considered in evaluating the silicate melt obtained in various furnaces are fusibility characteristics of the charge. It is well known that these characteristics can be determined by a theoretical approach which is extensively used in selecting the composition of various silicate glass charges [11]. To calculate technological parameters of various kinds of glass viscosity constant and additiveness, the formulas describing the viscosity characteristics of the Na_2O–CaO–SiO_2 glass with the additives MgO and Al_2O_3 are used. Having in mind that the compositions of low-melting illite clay and fibrous mineral wool system are close to that of silicate glass, the above theoretical method of determining fusibility characteristics can be applied to choose the composition of the investigated system consisting of low-melting illite clay and fibrous mineral wool waste. This is of particular importance for selecting the composition of the system under investigation as well as some additives and determining the effect of additives on the system fusibility.

The present paper aims to study the composition of fibrous mineral wool waste and low-melting illite clay and to determine theoretically the fusibility characteristics and the effect of some additives on relevant characteristics.

2. Experimental

Chemical compositions of the tested raw materials, i.e. low-melting illite clay, fibrous mineral wool waste, cement dust, dolomite and basalt, are given in Table 1.

Table 1. Chemical compositions of raw materials used in testing

Substance	Chemical composition, %						
	SiO_2	Al_2O_3	Fe_2O_3	CaO	MgO	$Na_2O + K_2O$	Loss on ignition
Low-melting illite clay	46.00	15.80	5.20	8.20	3.70	5.00	1.00
Cement dust	13.50	3.50	2.50	45.00	2.50	4.20	28.00
Mineral wool waste	46.00	14.50	10.00	18.60	9.10	1.50	0.00
Dolomite	3.80	1.20	0.00	28.40	19.80	0.00	46.80
Basalt	48.30	17.60	11.20	11.00	7.80	3.40	0.70

A model system of low-melting illite clay – fibrous mineral wool waste was used. The additives of dolomite or cement dust were also introduced. Four series of specimens were prepared for testing. The compositions of specimens were as follows: series S1 – 35% clay, 15% dolomite, 50% fibrous mineral wool waste; series S2 – 35% clay, 10% dolomite, 5% cement dust, 50% fibrous mineral wool waste; series S3 – 30% clay, 15% dolomite, 5% cement dust 50% fibrous mineral wool waste; series S4 – 66% clay, 17% cement dust, 17% fibrous mineral wool waste.

In testing, cement dust obtained from a joint-stock company 'Akmenės cementas' was used. Cement dust is a finely divided mineral material made up of the components of various compositions and origin. Non-calcined cement dust consists of calcite, mica, quartz and dolomite. Chemical compositions of test specimens are presented in Table 2.

Table 2. Chemical compositions of test specimens (without loss on ignition)

Specimen series	Chemical composition, %					
	SiO_2	Al_2O_3	Fe_2O_3	CaO	MgO	$Na_2O + K_2O$
Series one (S1)	44.97	12.23	7.58	19.81	11.00	2.13
Series two (S2)	45.13	12.26	7.66	20.57	9.94	2.34
Series three (S3)	43.32	11.94	7.48	21.81	10.84	2.19
Series four (S4)	47.23	10.99	6.21	21.23	7.15	3.59

Fusibility characteristics of test specimens have been calculated based on the relationship between their chemical compositions and additivities [11]. Temperatures (t_η) have been calculated at which the viscosity of the melt is 10^2 Pa·s, indicating a limiting fusibility value of the charge; 10^3 Pa·s is the value of fusibility characteristic of the beginning of fibre formation; 10^8 Pa·s is a limiting value, showing the lower bound of fibre formation.

The temperatures have been calculated from the following equations [10, 11]:

$$t_{\eta=10^2} = A_2 x + B_2 y + C_2 z + D_2 \quad (1)$$

$t_{\eta=10^2}$ is the melting temperature (°C) at which the viscosity is 10^2 Pa·s; the constants in the equation are as follows: $A_2 = -22.87$, $B_2 = -16.10$, $C_2 = 6.50$, $D_2 = 1700.40$;

$$t_{\eta=10^3} = A_3 x + B_3 y + C_3 z + D_3 \quad (2)$$

$t_{\eta=10^3}$ is the softening temperature of a specimen (°C), at which the viscosity is 10^3 Pa·s; a sample is deformed under its proper weight; $A_3 = -17.49$, $B_3 = -9.95$, $C_3 = 5.90$, $D_3 = 1381.40$;

$$t_{\eta=10^8} = A_8 x + B_8 y + C_8 z + D_8 \quad (3)$$

$t_{\eta=10^8}$ is a softening temperature of a specimen (°C), at which viscosity is 10^8 Pa·s; a sample is deformed under the action of an external force; $A_8 = -9.19$, $B_8 = 1.57$, $C_8 = 5.34$, $D_8 = 762.50$. In all equations x is the amount of $Na_2O + K_2O$, %, y is the quantity of CaO + MgO, %, and z is the amount of Al_2O_3, %.

Structural changes are determined by X-ray difractometer Dron-2 with the following operational characteristics: copper cathode, nickel filter, anode (plate) voltage – 30 kV, anode (plate) current – 8 mA, goniometer slots – 0.5, 1.0 and 0.5 mm, the rotation of the goniometer meter – 2°/min. Phase composition was identified by using ASTM card index of reference data.

Differential thermal analysis (DTA) was made with a derivatograph Q-1500, in ambient atmosphere, at the rate of temperature variation amounting to 10 °C/min. The melting point of the samples and characteristic changes in their shape in calcining were determined with a high-temperature microscope MHO-2.

3. Results and discussion

One of the major fusibility characteristics of a silicate system determining physical and mechanical properties of the charge of mineral wool is the viscosity of a silicate melt. Fusibility of a charge is determined experimentally by melting the charge of a known chemical composition in a laboratory furnace, as well as forming mineral wool in a special centrifuge and assessing the fibre yield. The experimental methods are reliable, but very expensive (requiring long-term testing and special equipment). However, fusibility of the considered charge can be determined by using the appropriate technique. It is claimed in the literature surveying theoretical methods of determining the viscosity of a silicate system that the choice of a particular method depends on its constituent oxides [11]. By using a mathematical method for determining the viscosity of the investigated silicate system, it is possible to determine the effect of particular oxides on the viscosity of the whole system and, consequently, to modify its composition. In the present investigation, the SiO_2–CaO–R_2O system with the oxides Al_2O_3, MgO and Fe_2O_3 influencing the system fusibility is considered. Fusibility characteristics of the investigated system are calculated and its structural changes are analysed.

Sample composition was proportioned for mineral wool manufacture and was calculated, taking into account mineral wool acidity modulus R_m which could not be lower than 1.9, and viscosity modulus K_m, the value of which should be lower than 1.6. The composition with 50% of mineral wool waste was used to make specimens of S1, S2 and S3 series. However, specimens of S4 contained only 17% of mineral wool waste.

The variation of the melting point and softening temperature of specimens, depending on their composition, is presented in Table 3. The temperatures at which the viscosity of test specimens was 10^2 Pa·s, 10^3 Pa·s and 10^8 Pa·s were calculated.

Table 3. The results obtained in calculating fusibility characteristics of specimens

Specimen series	$t_{\eta=10^2}$, °C	$t_{\eta=10^3}$, °C	$t_{\eta=10^8}$, °C	$t_{\eta=10^3} - t_{\eta=10^8}$, °C
Series S1	1235	1112	857	255
Series S2	1235	1112	854	258
Series S3	1202	1091	857	234
Series S4	1233	1104	833	271
Charge: basalt 80%, dolomite 20%	1294	1153	811	324

As shown in Table 3, fusibility characteristics of the specimens of series S1 and S2 are similar. A comparative analysis of the data obtained for S1, S2 and S3 specimens has shown that softening temperature of specimen S3 decreased from 1112 °C to 1091 °C when the viscosity was 10^3 Pa·s, while its melting point decreased from 1235 °C to 1202 °C, when the viscosity was 10^2 Pa·s. It should be noted that the addition of 15% dolomite to specimen S3 considerably changes its fusibility. Thus, the calculated temperature at which the viscosity of the specimen was 10^2 Pa·s decreased to 1202 °C, however, the smallest temperature interval of 234 °C was observed for fibre formation (Table 3).

The analysis of theoretical data has shown that the largest temperature interval of fibre formation was obtained for S4 specimens. The study of the calculation results has revealed that the addition of dolomite negatively affects melting characteristics. This may be accounted for the highest value of the relationship between CaO and MgO in the investigation system of the fourth series compared to the respective values obtained for three other compositions, also characterized by a smaller amount of Fe_2O_3.

A comparative evaluation of the calculated characteristics of all four series of specimens and the calculated fusibility characteristics of the specimen consisting of 80% basalt and 20% dolomite was made (Table 3). The comparative analysis has shown that the values of fusibility characteristics of all four specimen series (S1, S2, S3 and S4) are lower than those of the basalt and dolomite specimen.

The experimental results in determining fusibility of specimens were obtained by using the high-temperature microscope MHO-2 (Fig. 1). Test specimens were heated in the temperature interval of 20–1250 °C and typical changes in their shape were determined. Testing a specimen of S1 series at the temperature amounting to 1160 °C no characteristic changes in its shape were observed. When the temperature was increased up to 1210 °C, a considerable contraction of the specimen could be seen, while melting of the specimen was observed at 1230 °C.

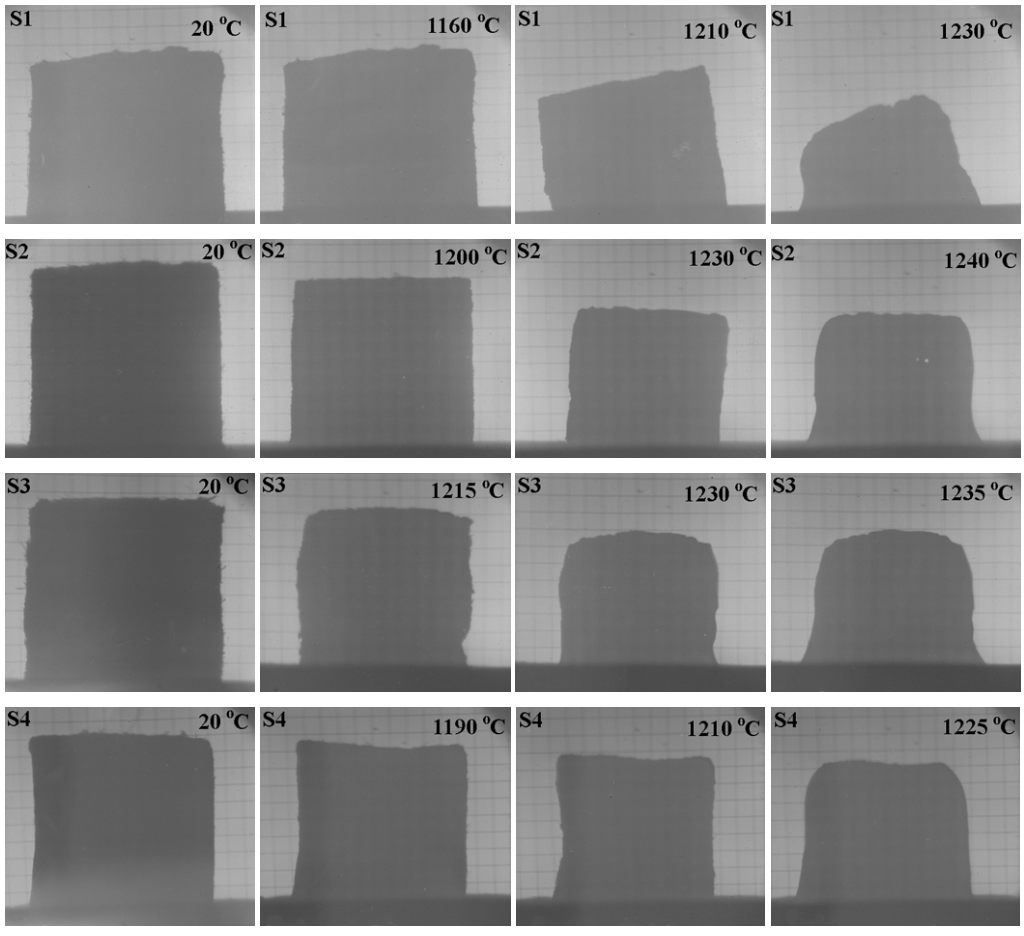

Fig. 1. The experimental results of determining fusibility of specimens S1–S4

When a portion of dolomite in the specimen S2 was substituted by cement dust, the character of the specimen contraction changed. A typical contraction could be observed at higher temperatures. In the temperature interval from 20 °C to 1200 °C the specimen did not change, while its contraction could be observed at a higher temperature (1230 °C). The melting point of the specimen also changed, increasing to 1240 °C. The analysis of the test results obtained for specimen S3 has shown that the increase of dolomite content in the specimen by 15% changes its fusibility. Characteristic changes in the specimen shape in heating, indicating the formation of a liquid phase, could be already seen at 1215 °C, while the observed contraction of the specimen was developing simultaneously with its melting. The melting point (1235 °C) of specimen S3 matches the test results of specimens S1 and S2.

The data obtained in differential thermal analysis (DTA) are presented in Fig 2. DTA curves are similar for all test specimens. They are characterized by exothermic

effect in the temperature interval of 400–500 °C, demonstrating the burning of phenol–formaldehyde binder found in the mineral wool waste. In tested specimens S1, S2 and S3, endothermic effects were observed at 800 °C and at 850–860 °C. DTA curves show that the above effects indicate a decomposition of carbonates introduced into the specimens together with illite clay minerals, dolomite and cement dust. Endothermic effect observed at 800 °C demonstrated the decomposition of $MgCO_3$ found in dolomite, while endothermic effect observed at 850 °C and 860 °C showed the decomposition of $CaCO_3$ found in dolomite and cement dust. It should be noted that the most intense $CaCO_3$ bonds breakage was observed in the test specimen containing the largest amount of dolomite and cement dust, reaching 15% and 5%, respectively.

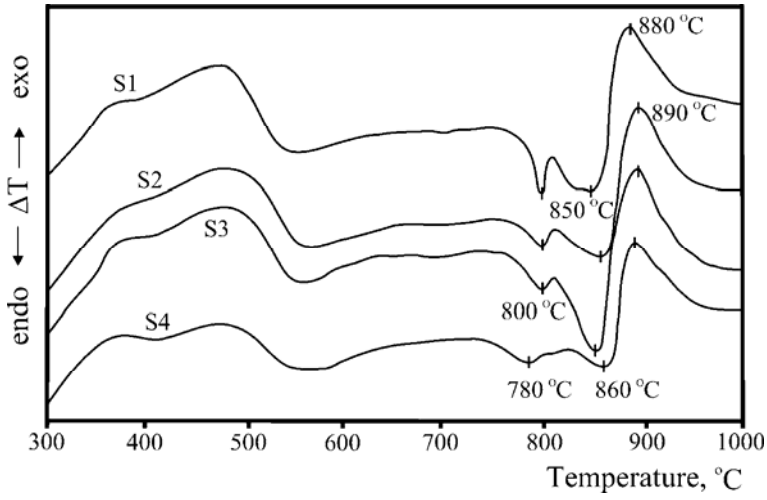

Fig. 2. DTA curves of specimens S1–S4

A comparative differential thermal analysis has revealed that decarbonization of low-melting clay takes place at a lower temperature in the case of specimen S4. This is shown by an endothermic effect observed at 780 °C. At the same time, decarbonization temperature of $CaCO_3$ did not change.

The crystallization of newly formed substances in heating test specimens was studied by the X-ray method (Fig. 3). The test specimens were heated up to 1000 °C. The results obtained show that fibrous mineral wool waste exothermal crystallization, taking place in the temperature interval of 820–850 °C, is accompanied by diopside formation (Figs. 2, 3). It was found that crystallization of mineral wool waste depends on the content of waste materials in the test specimens. The crystallization of the specimens S1, S2 and S3 containing 50% of mineral wool waste is accompanied by a clearly observed exothermic effect, while this effect is much weaker in the specimen S4 containing only 17% of mineral wool waste. A comparative X-ray analysis of the test data shows that after heating the specimens diopside spikes are less intense for specimens S4 than for specimens S1, S2 and S3. It should be noted that all test speci-

mens have the composition not allowing the formation of the ion concentration gradient of Ca^{2+} and Mg^{2+}. Thus, ion diffusion of Ca^{2+} and Mg^{2+} in the mineral wool waste is inhibited. At the same time, the concentration of Na^{+} ions is low enough to allow them to distribute in the crystalline structure of the test specimens without forming any compounds.

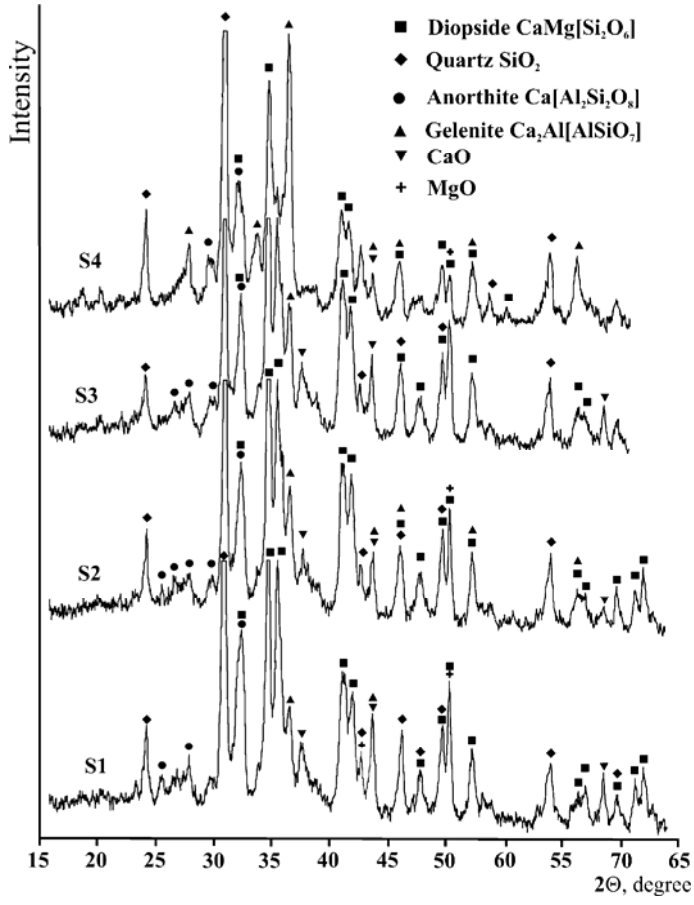

Fig. 3. X-ray diffraction patterns of specimens S1–S4

X-ray analysis of the data showed that the carbonates contained in the test specimens decarbonize without forming any compounds. The decarbonization of the carbonates contained in the test specimens which takes place between 800 °C and 860 °C causes the interaction between Ca^{2+}, Mg^{2+} ions and minerals of the illite clay. In the temperature interval of 880–900 °C crystallization of the exothermic reaction products was observed when the mineral anorthite and gelenite (of the plagioclase group) were crystallizing (Figs.2, 3). It should be noted that in the specimens S1, S2 and S3 containing 50% of fibrous mineral wool waste, a certain portion of carbonates formed in the decarbonization does not react with the illite clay minerals. Therefore, spikes of

free CaO and MgO can be clearly seen. This may be attributed to low illite clay content (30–35%) in these specimens.

The tests have shown that to avoid the formation of free CaO and MgO, the smaller amount of dolomite should be used in specimens. The analysis of roentgenograms of gelenite spikes in specimen S4 has revealed that calcite $CaCO_3$ found in cement dust reacts violently with illite clay minerals. Therefore, relatively small amounts of free CaO and MgO can be found in specimens S4.

4. Conclusions

The analysis of the data presented in the paper shows that a model system based on low-melting illite clay, cement dust, dolomite and mineral wool waste is an effective way to solve the problem of fibrous mineral wool waste recycling. The experimental data proved the effectiveness of the suggested methods of calculating fusibility characteristics for determining of model system from low-melting illite clay and fibrous mineral wool waste. The above methods were successfully used in calculating fusibility of investigation model system. The results obtained also show that the calculated temperature values for specimens of all four series, when the viscosity is 10^2 Pa·s and 10^3 Pa·s, are lower than those practically used for the charge consisting of 80% basalt and 20% dolomite. It was found that the formation of free CaO and MgO in calcining could be avoided by reducing the content of dolomite.

References

[1] BALKYAVICHUS V., VALYUKYAVICHUS CH., SHPOKAUSKAS A., LAUKAITIS A., PYATRIKAITIS F., Glass Ceram., 60 (2003), 179.

[2] EIDUKYAVICHUS K., MATSEIKIENE V., BALKYAVICHUS V., SHPOKAUSKAS A., LAUKAITIS A., KUNSKAITE L.YU., Glass Ceram., 61 (2004), 77.

[3] LEŠKEVIČIENĖ V., NIZEVIČIENĖ D., VALANČIUS Z., J. Civil Eng. Management, 9 (2003), 76.

[4] GAILIUS A., LAURIKIETYTĖ Ž., J. Civil Eng. Management, 9 (2003), 198.

[5] JENSEN L., U.S. Patent 4 345 035 (1982).

[6] MIANKOVSKI A., WASILEWSKI P., POLAŃSKI J., Powder Technol., 68 (1991), 101.

[7] HOLDBEK K., U.S. Patent 4 287 142 (1981).

[8] EIDUKEVIČIUS K., LAUKAITIS A., SIAURYS V., LINDBERG P. [in]: *Silicate technology*, Int. Conf. Chemistry and Chemical Technology, Kaunas, Lithuania, April 24–25, 2003 pp. 138–143.

[9] NEFEDOVA I.N., KRASHENINKOVA A.S., KOSINTSEV V.I, LOTOVA L.G., EHRDMAN S.V., RU Patent 2 234 473 (2003).

[10] EIDUKEVIČIUS K., BALKEVIČIUS V., SIAURYS V., LINDBERG P. [in]: *Silicate technology*, Int. Conf. Chemistry and Chemical Technology, Kaunas, Lithuania April 21–22, 2004, pp.113–118.

[11] KITAIGORODSKIJ I.I., SILVESTROVICH S.I, *Handbook of glass production*, State Publishing House Literature of Building, Architecture and Building Materials, Moscow, 1963 (in Russian).

Received 5 July 2006
Revised 29 November 2006

Materials Science-Poland, Vol. 25, No. 1, 2007

Some aspects of mechanochemical reactions

K. WIECZOREK-CIUROWA*, K. GAMRAT

Cracow University of Technology, Institute of Inorganic Chemistry and Technology,
Warszawska 24, 31-155 Cracow, Poland

A classification of mechanochemical syntheses occurring in various states of aggregation is presented. Peculiarities of phenomena that take place under the action of mechanical impulses operating in high-energy ball mills are discussed.

Key words: *mechanochemical reaction; mechanical activation; mechanical alloying; nano-sized material; reactive milling*

1. Introduction

Mechanochemistry, a branch of chemistry concerned with the chemical and physicochemical transformations of substances in all states of aggregation induced by mechanical energy, was formulated by Heinicke [1] more than twenty years ago and is currently fully accepted. Recently, mechanochemistry has become the subject of ever-increasing interest in relation to the theory and preparation of advanced metastable solids – novel, high-performance, and low-cost composite materials with new properties such as better dissolution and leaching (especially important in the case of metals extracted from minerals), and faster decomposition and synthesis. Moreover, these materials also show an improvement in the sintering processes [2].

From the chemical point of view, the mechanical treatment of solids using high-energy impulses can cause mechanical activation, mechanical alloying, and reactive milling of solids. Communition, always the first step of these processes, is the multiple particle rupture which results in their size reduction and a simultaneous increase in the specific surface area and surface energy within the systems. Mechanical activation results in changes partly in the tension state and partly in the dispersion state. Milling can be viewed as a mechanochemical activation if these changes also involve alterations in the structure of the material, its chemical composition, and chemical

*Corresponding author, e-mail: kwc@usk.pk.edu.pl

reactivity. Mechanical alloying, invented by Benjamin in 1970 [3, 4], is the process in which mixtures of powders are milled to achieve alloying at the atomic level. Reactive milling is related to the process in which chemical reactions occur.

2. Theoretical considerations on mechanochemical treatment

2.1. How can mechanochemical treatment be realized?

The concept of mechanical treatment is very simple. Generally, it is the milling of the already powdered materials which involves a reduction of particle size. Intimate contact between the milled materials is utilized to greatly enhance diffusion and the chemical reactivity of solids. The most popular devices, in which mechanochemical processes can be conducted are vibratory, planetary, and attritor ball mills. They differ in their capacities, efficiencies of milling and additional arrangements such as cooling, special systems for measuring the temperature and/or pressure; they all also have certain features in common. In all these devices, the ground material is periodically thrown into zones of ball collisions. Energy transfer to the powdered particles takes place by shearing and/or impact action of the balls.

Grinding in these special mills is several times more effective than in conventional devices. For example, diminishing tungsten carbide particles from 2–3 mm pieces to particles of 3 μm conventionally takes 70 hours, while the process realized in a planetary mill takes only 3 minutes [5].

The estimation of the amount of energy to be supplied to the system in order to achieve the desired final products is not a simple task. There have been many attempts at solving this problem [6, 7]. The mechanochemical results depend on many parameters, such as the milling speed (rpm), milling time, milling atmosphere, the process control agent (PCA) and the ball-to-powder weight ratio (BPR), as well as the type of the mill, and the size and material of the grinding balls. All these variables are not completely independent. Therefore, it is necessary to optimise the milling conditions experimentally, because the results generally are not predictable á priori. Some examples illustrating the milling process under different conditions are presented below.

It is observed that the rate of chemical reaction increases along with increasing BPR value. For example, the reduction of $TiCl_4$ with Mg is complete after 48 hours using a BPR of 2:1, whereas with a 6-fold higher BPR value the process lasts few hours [3]. This indicates that in the latter case the frequency of collisions is higher.

A very important factor influencing the reactions induced by milling is the inert or oxidizing atmosphere. Milling in an inert atmosphere can result in gradual product formation and if milling is performed in air the oxidation of any component (e.g., reactive metal) can produce sufficient heat to initiate an appropriate chemical reaction, thus accelerating the overall process [3, 6, 7].

The reaction rate also depends on the presence of a process control agent (PCA). The application of the PCA slows down the reaction rate, which is useful in explosive processes. Most PCAs are organic compounds with low melting and boiling points. When high-energy ball milling takes place in mixtures with a reactive metal in the absence of a PCA, self-propagating reactions may occur spontaneously after the induction period. When the PCA is used, however, the reaction proceeds in a controlled manner and completes after a longer time. PCA may also inhibit inter-particle welding during each collision and may favour decrease in particle size [3].

2.2. What kind of materials can be activated and obtained by milling for practical applications?

Generally, it is possible to indicate the usefulness of mechanical treatment for the production of intermetallic compounds and alloys in metallurgy, composites and complex oxides for materials applied in engineering, nanocrystalline substances for catalysis, and nanomaterials as fuel cells and other active materials for the production of fertilizers, building materials, pigments, etc.

For example, mechanical alloying in order to obtain a homogenous alloy at room temperature involves material transfer. The alloying process is independent of the melting points of the elements used, hence high temperature melting and thermally unstable alloys can be prepared. This technique was developed for producing oxide dispersion strengthened (ODS) Ni-base superalloys for gas turbine applications [6]. Another application of the mechanical activation process is the preparation of materials that have large surface areas and/or exhibit structural defects which may lead to the strong enhancement of their catalytic properties [8–10].

2.3. The principles of two types of mechanochemical reactions

Most reactions in the solid state are slow and complex. Their characteristic feature is that they involve product formation at the interfaces of reactants. Furthermore, product growth requires the diffusion of reactant phase atoms through the product which constitutes a barrier preventing further reaction. Thus, in order for this kind of reaction to proceed for a reasonable time, it should be realized at high temperatures. Moreover, in most cases a solid phase reaction requires charge transfer to be initiated. This can be carried out either thermally or via non-thermal routes including a mechanochemical procedure. It has been established that high energy ball milling of powder or powder mixtures may significantly accelerate chemical reactions between two solids, a solid and a liquid, or a solid and gas, making it possible for the reaction to occur at temperatures lower than those of conventional synthesis [11–13].

Mechanochemical processes do not proceed in the bulk. This means that chemical transformations occur in a different definite region of the particle each time. The size of these sites is usually estimated to be 10^{-5}–10^{-6} m [13].

It is evident that ball milling induces changes in the specific surface area of solid particles and/or the emission of exoelectrons. This is due to the repeated formation of fresh interfaces at any time between the reacting phases. This formation is brought about by means of dynamic deformation, fracturing, and cold welding of the solid particles [13, 14].

The impact energy usually reaches fractions of a Joule, the inelastic collisions last for 10^{-4}–10^{-5} s, and the amount of the matter in the collision zone is close to 10^{-9} m^3. The temperature and pressure increase, especially at the collision points between the solids. Two kinds of temperature effects during mechanical treatment are usually taken into account: local temperatures due to ball collisions, and the overall temperature in the milling vial. The local temperature impulse is approximately equal to the collision time (10^{-5} s). This temperature is defined as a flash temperature. It is the maximum local temperature generated at some points of colliding particles and balls or other grinding bodies. The flash temperature occurs at areas of real contact due to the frictional heat dissipated over these areas. The flash temperature occurs even when the overall temperature rise is lower, and its pressure can reach 10^6 Pa [14].

In the processes of plastic deformation, fracture and friction during ball collisions, the impact energy is converted into other forms of energy which induce structural defects, broken bonds, and other excess energy effects. These instances accumulate and a new, active state of the substances is produced. Such excited states are formed, because the rate of the energy release exceeds the rate of the energy dissipation. Consequently, the chemical reactivity of solids increases considerably. The ignition of the chemical reaction occurs after a period of milling, when the powder reaches a critical level of activation.

The kinetics of the mechanochemical reaction depends on the conditions of the milling process. The application of appropriate milling conditions allows the mechanical reaction to be conducted in two different kinetic ways – as a self-propagating reaction that is initiated when the reaction enthalpy is sufficiently high and develops slowly with each collision or as the one that results in a gradual transformation of the substrates [3, 7, 15–19]. The first type requires a critical time for the ignition of the reaction. It has been observed that the temperature of the vial initially increases slowly with time. After a certain period of milling, the temperature increases abruptly, confirming that ignition has occurred. The time at which a sudden increase in temperature occurs is referred to as the ignition time. After that time the reaction occurs within seconds. The ignition temperature is a function of the enthalpy change and microstructure parameters, e.g. interfacial area between the reactants [18].

It was assumed that after a period of comminution mixing and activation agglomerates begin to form and increase in size. The reaction starts in a single agglomerate or in the powder layer coating a milling ball or on the wall of the vial. One reaction front propagates into other parts of the powder. The powder can be attached to the surface of a milling ball or the inner wall of the container. When a ball hits this layer, a part of the kinetic energy is transferred to the powder as heat, increasing its temperature [3]. The stress inside the powder is not uniform but concentrated in few points. The

result is the formation of thermodynamically unstable zones, where the reaction can start even if the average temperature of the powder is not sufficient to initiate the reaction front.

Intimate contact between the reactant phases is an essential requirement for self -propagating synthesis. This condition is easy to achieve when mechanical activation is conducted in a system of ductile-brittle substances. The ductile component is flattened by a micro-forging process whilst the brittle is fragmented. One can assume that the brittle particles of the materials are dispersed in the ductile matrix. If both milled materials are brittle, however, this phenomenon is not observed.

The second type of mechanical synthesis concerns reactions proceeding more slowly up to the point at when processes become a function of the milling time [3, 7, 15]. If ignition does not occur, collisions between the milled material and grinding medium contributes to the comminution, mixing, and defect formation. The formation of the final product occurs step by step.

3. Practical examples of mechanochemical synthesis in various aggregation systems

3.1. Solid-solid systems

Synthesized $Pb(Zr,Ti)O_3$, lead zirconate titanate (PZT), of a perovskite structure is widely used in various sensing and actuating devices. The traditional method of obtaining this material is a solid-state reaction between stoichiometric mixtures of the constituent oxides – PbO, TiO_2 and ZrO_2 followed by calcination at high temperature. This procedure often leads to an incomplete reaction. Obtaining the PZT phase from $Pb(NO_3)_2$, $TiCl_4$, and $ZrO(NO_3)_2$, however, is possible by mechanical activation using a high-energy shaker mill operated at 900 rpm for 20 h [20].

It is known that modified thermal, optical and electrical properties of the material can be obtained when the powder particle size falls into the micro- or nanoscale. Thus, fine metal silver powders with particle sizes ranging from 50 to 100 nm, which allow the concentration of silver in the conducting composite materials to be reduced, were synthesised in a mechanochemical process by inducing a solid-state displacement reaction between AgCl and sodium in a planetary mill in an argon atmosphere [21]. The reaction is completed after 20 minutes of milling, whereas 2 hours of milling was required to obtain silver in a nanocrystalline form.

For building materials, silicate hydrates (CSHs) such as afwillite ($Ca_3(SiO_3(OH)_2 \cdot 2H_2O$) and tobermorite ($Ca_5(OH)_2Si_6O_{16} \cdot 4H_2O$) were used. These compounds are usually synthesized by hydrothermal reactions between lime and silica in the presence of water at high temperatures in an autoclave. The new method of CSH synthesis is based on grinding the initial components with water at room temperature. Grinding was carried out in a planetary mill at 700 rpm. It was shown that afwillite is almost

completely formed within 120 minutes of milling, while tobermorite forms within 180 minutes [22].

Binary oxides such as Ag–V and Cr–V have been extensively studied due to scientific and practical interest. For example, compounds of the Ag–V–O system doped with lithium can be applied as positive electrode materials [23], while the Cr–V–O system tested by us [24] has a number of applications in the field of heterogeneous catalysis, sensors, magnetic and ceramic technologies. In both cases, it was found that pure oxides, i.e. Ag_2O, V_2O_5, and Cr_2O_3, reveal strong stability during mechanochemical treatment. Their milling in mixtures composed of Ag_2O with V_2O_5 and Cr_2O_3 with V_2O_5 involved the formation of different spinel phases. In the former case, the presence of $Ag_4V_2O_7$ and Ag_3VO_4 in the milling products was detected, and the presence of $CrVO_4$ and $Cr_2V_4O_{13}$ in the latter one. X-ray diffractometry indicates that spinel phases appear in the milling products after several hours.

Zirconium phosphates (NZP) can be used as catalysts for skeletal isomerization and dehydroaromatisation. The prospective method of its synthesis is based on the mechanical activation of crystallohydrates of ammonium phosphate and zirconium oxochloride or oxonitrate. Materials prepared via the mechanochemical route possess a lower density of acid sites as compared to samples obtained using the sol-gel method, while mechanically synthesized NZP reveals the presence of the strongest Lewis centres [25].

Cr_2O_3 powders have a wide range of applications, including green pigments. Particles smaller than 50 nm can be used as transparent colorants. The reduction of Cr_2O_3 particles is also needed for improving sintering. Various methods of synthesizing nano-sized chromium oxide can be applied, including gas condensation, sol-gel, or laser induced pyrolysis. In a previous study [26], mechanochemical nanomaterial treatment was used. The mechanochemically realized process occurs according to the reaction:

$$Na_2Cr_2O_7 + S \rightarrow Cr_2O_3 + Na_2SO_4$$

Ten minutes of milling of the reactant mixture involved an abrupt increase in the vial temperature, confirming that Cr_2O_3 particles are formed in a combustion process during milling (with a large negative enthalpy change of $\Delta H = -562$ kJ/mol).

Reactive ball milling is almost an ideal method for preparing nano-sized metal matrix composites (MMCs) because of its simplicity and the possibility of composite formation characterized by uniform distribution of grain sizes. Moreover, such an *in situ* route of synthesis results in the production of materials that have more homogenous microstructures and are more thermodynamically stable than those synthesized using conventional *ex situ* techniques. For example, this kind of material consisting of ceramic and intermetallic phases, namely Cu–Al/Al_2O_3 and Ni–Al/Al_2O_3, can be obtained by milling mixtures of Cu(Ni) hydroxycarbonates with aluminium [27, 28]. The formation of these multiphase materials is a consequence of many complex, si-

multaneous and subsequent chemical reactions occurring during milling in air. These mechanochemical processes are described below:

- mechanical decomposition:

$$M_2(OH)_2CO_3 \rightarrow 2MO + H_2O\uparrow + CO_2\uparrow$$

- aluminothermic reduction:

$$3MO + 2Al \rightarrow 3M + Al_2O_3$$

- mechanical alloying:

$$xM + yAl \rightarrow M_xAl_y$$

where M is Cu or Ni.

The factor facilitating these reactions is heat emission in the process of rapid aluminium oxidation during its activation in air. It may be assumed that this heat (ΔH_{298} = –1675 kJ/mol) accelerates the decomposition of hydroxycarbonates, induces the alluminothermic reaction, and enhances the alloying of the two metallic phases. The initiation temperature of the aluminothermic reaction can be monitored by differential thermal analysis (exo-effects).

3.2. Solid-gas

There are some examples of mechanochemical reactions that proceed in solid–gas and solid–liquid systems. One of them is the production of rutile (TiO_2) from the mineral ilmenite $FeTiO_3$. For this purpose, ilmenite powder is milled in vacuum and air. In vacuum, no structural changes are observed. Activation carried out in air, however, involves ilmenite transformation to $Fe_2Ti_3O_9$ according to the reaction:

$$6FeTiO_3 + 1.5O_2 = 2Fe_2Ti_3O_9 + Fe_2O_3$$

where Fe_2O_3 is hematite and $Fe_2Ti_3O_9$ ($Fe_2O_3{\cdot}3TiO_2$) is a new iron titanate phase. This phase is thermally metastable and forms Fe_2TiO_5 and TiO_2 after a further annealing [29].

Another example of a solid–gas system is the synthesis of TiN which takes place during the ball milling of Ti in a pure nitrogen atmosphere [30]. It was proposed that nitrogen absorption in the milled metal powders occurs at the moment of ball collision, and the quantity of nitrogen absorbed during one collision event is proportional to the energy supplied to the powder from the colliding balls.

The phase evolution in this kind of systems under mechanochemical treatment is influenced by the initial pressure of the gas component.

3.3. Solid–liquid

The mechanochemical destruction of polyhalogenated pollutants or pure polyhalogenated compounds by pure metals (e.g., sodium, magnesium, aluminium, zinc, iron, alloys) and some suitable hydrogen donors (e.g. alcohols) is shown below:

$$\text{R–Cl (toxic)} + \text{Na} + \text{hydrogen donor} \rightarrow \text{R–H (biphenyl)} + \text{NaCl (harmless)}$$

Such pollutants can be eliminated at room temperature at times ranging from minutes up to one hour in a single step. The whole process can be characterized as a reductive dehalogenation facilitated by mechanochemical treatment [31].

Other researchers [32] have tested high energy milling as a method for lowering the amount of chlorinated compounds in contaminated soil. They used two substances, namely $NaBH_4$ and $LiAlH_4$ as reducing agents. $LiAlH_4$ proved more efficient, reducing poly(chlorobiphenyls) (PCBs) by over 9% in three hours.

Different kinds of processes occurring in solid–liquid systems can be represented by the mechanical treatment of a mixture of Al and Ti with pyrazine ($C_4H_4N_2$) [33]. Milling of this system in benzene solution (PCA) brings about the formation of the metal matrix composite Al–TiN. This was formed in two steps, i.e. at the beginning Ti was milled with pyrazine. After 48 hours of milling two kinds of nitrides, Ti_2N and TiN, were identified, and then Al was added to the nitrides. A homogenous Al–TiN composite was obtained after an additional 96 hours of milling.

4. Selected experimental methods of identifying and characterizing materials synthesized mechanochemically

A comprehensive study of the physical and chemical processes that occur during mechanical treatment by means of high-energy ball milling appears to be possible only if a reliable identification of solids and quantitative phase analysis of the activated products are performed. Due to the complexity of mechanochemical reactions, the nature of the obtained solids is closely related to the milling conditions, they should therefore be well-defined. Moreover, it is very important to determine the factors influencing the activation effects. Another difficulty arises from the fact that these reactions are composed of many successive stages, which are very different in many cases. The experimental methods required for identifying and characterizing materials synthesized mechanochemically involve not only techniques applicable to solids, but also those particularly adapted to the nanostructured character of the milling products. Thus various types of analytical methods must be applied [34–40].

The first type are thermal analysis methods. Such techniques as thermogravimetry and differential thermal analysis are very useful for describing mechanically activated substances, because they make it possible to identify highly defected, finely crystalline or even amorphous phases formed during milling, which might be difficult to achieve using other methods. Moreover, thermal analysis allows the quantitative phase composition of the activated mixture to be estimated, which enables, for example, estimating the consumption of initial components of the tested mixtures. Moreover, in some cases thermoanalytical experiments may be used for simulating the reactions that occur during reactive ball milling. Such simulations, done for mixtures of

Cu–hydroxycarbonate with aluminium (Fig. 1), simplified the estimation of the reaction mechanism that yields the composite Cu–Al/Al_2O_3 during milling. DTA curves reveal that $Cu_2(OH)_2CO_3$ thermally decomposesd into CuO, and that then copper oxide is reduced by Al. The consequence of such a process is the formation of Cu and a large amount of heat. This heat may accelerate the alloying of Cu with Al into intermetallic phases.

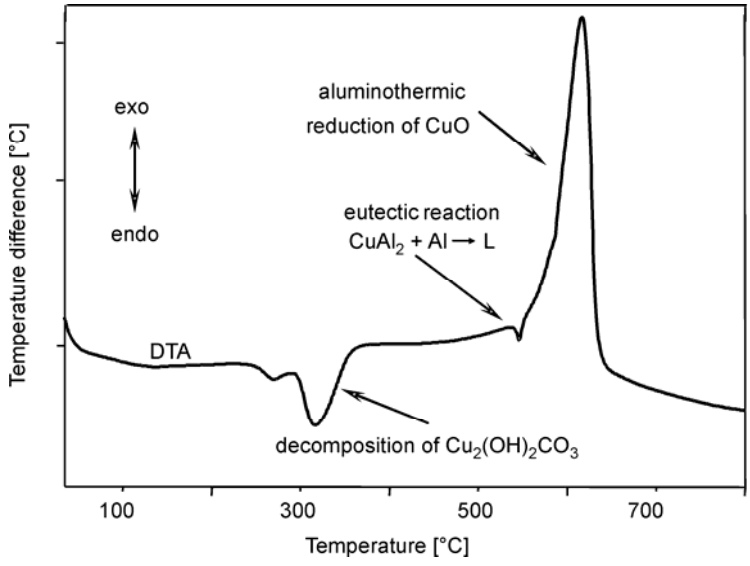

Fig. 1. DTA curve (non-oxidizing atmosphere) of the $Cu_2(OH)_2CO_3$–Al system simulating the reactions that may occur under mechanical action

Information about the qualitative phase composition of mechanically activated materials can be obtained from X-ray diffractometry. The technique is ideal for monitoring the progress of the process occurring during milling, if the materials are in their crystalline forms.

When the materials are in their fine or even amorphous forms, mechanosynthesis can be followed by using IR spectroscopy. An example of the special usefulness of IR spectroscopy for estimating the time in which the mechanosynthesized products start to form is the spinel synthesis of mechanically treated mixtures of Cr_2O_3 and V_2O_5. We observed $CrVO_4$ in the milled products after 1.5 hours of milling, which is confirmed by the stretching vibration of the VO_4^{3-} observable in the IR spectra shown in Fig. 2. The amount of spinel phases, however, is very small and can be detected without doubt by using X-ray diffractometry. Another useful spectroscopic technique is Mössbauer spectroscopy, used for substances with magnetic properties. It provides information on the magnetic states and local coordination of magnetic ions [37, 38].

Results obtained using thermoanalytical methods – X-ray diffractometry and IR spectroscopy – are useful especially for bulk analysis, however they must be supple-

mented with results from other analytical methods that provide more accurate data about the composition and structure of mechanically treated materials.

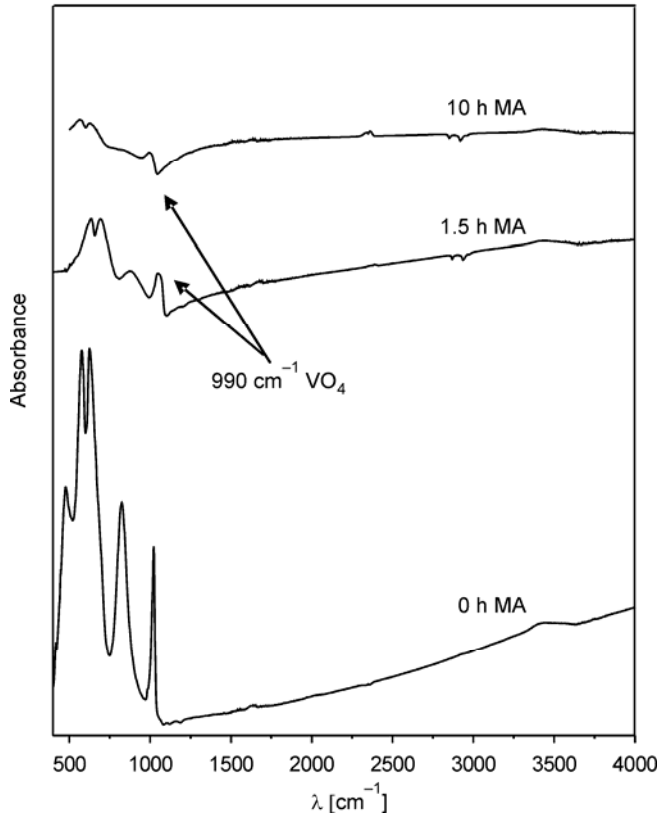

Fig. 2. IR spectra for the V_2O_5–Cr_2O_3 system after mechanochemical treatment

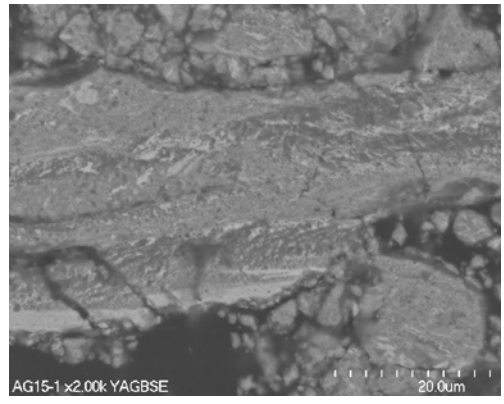

Fig. 3. SEM microphotographs of the $Cu_2(OH)_2CO_3$–Al mixture after mechanochemical syntheses of the Cu–Al/Al_2O_3 composite, characterized by a lamellar structure

One of the techniques used for this purpose is scanning electron microscopy with backscattered electron imaging and quantitative energy dispersive X-ray elemental

microanalysis (EDS). By combining the grey tone levels with the results of EDS, a single compound can be quickly identified and localized. For example, this technique reveals that mechanosynthesis in the $Cu_2(OH)_2CO_3$–Al systems involves the formation of a composite characterized by a lamellar morphology (Fig. 3). Moreover, on the basis of EDS analysis it was possible to estimate that such a material is composed of aluminium oxide and intermetallic phases. The disadvantages of scanning electron microscopy include low spatial resolution and the inability to image individual grains, dislocations, and defects in the tested material.

Another microscope method useful for analysing mechanically activated substances is transmission electron microscopy (TEM). TEM measurements can be applied for estimating the composition and microstructure of mechanically alloyed products. A high resolution obtained in this type of microscopy allows single grains of the products to be observed. Such single grains of mechanosynthesized copper can be seen in Fig. 4. Electron diffraction patterns unquestionably confirmed that the detected phase is nanocrystalline Cu (Fig. 4c).

Larger prospects in the analysis of nanometric substances can be achieved using high-resolution transmission electron microscopy (HRTEM). HRTEM allows the atomic structure of grain boundaries to be probed and atomic coordinate positions to be estimated. The final point to consider in preparing HRTEM and TEM specimens, however, is how closely representative the thin films are of the bulk material [39].

X-ray photoelectron spectroscopy (XPS) can provide characteristics of surface mechanochemically obtained materials. This technique gives information about the elements present on the surface and on their amounts. The exact description of surface composition is important for materials used as catalysts because their action depends on active sites localized strictly on the surface [40]. Therefore, the analytical method must give information about layers only several nanometers deep. This special usefulness of XPS spectroscopy can be demonstrated in the case of Cr_2O_3–V_2O_5 mixtures mechanochemically treated in argon (dry conditions) and ethanol (wet conditions). The tested mixtures were mixed at a ratio of V/Cr equal to 0.1. Only XPS shows that on the surface of the sample activated in the dry medium (V–Cr–O/Ar) the ratio V/Cr is fourfold higher than the theoretical one or that detected for the sample activated in wet conditions (V–Cr–O/Et) (Table 1). This suggests that the surface of the sample was enriched in vanadium when treated in argon. Due to this, one can conclude that mechanical activation in dry conditions involves the segregation of phases by covering Cr_2O_3 grains with a V_2O_5 layer.

It was necessary to find suitable analytical procedures to characterize phases in mechanochemically activated systems. The task appeared to be rather complex, however, because of the multiphase and nanocrystalline character of the reactive ball milling products. Therefore, a coupled analytical system should be applied in many cases. Such systems are especially useful for catalytic materials because they can test catalysts in action, such as UHV surface analyses systems equipped with catalytic reactors, X-ray photoelectron and Auger electron spectroscopy.

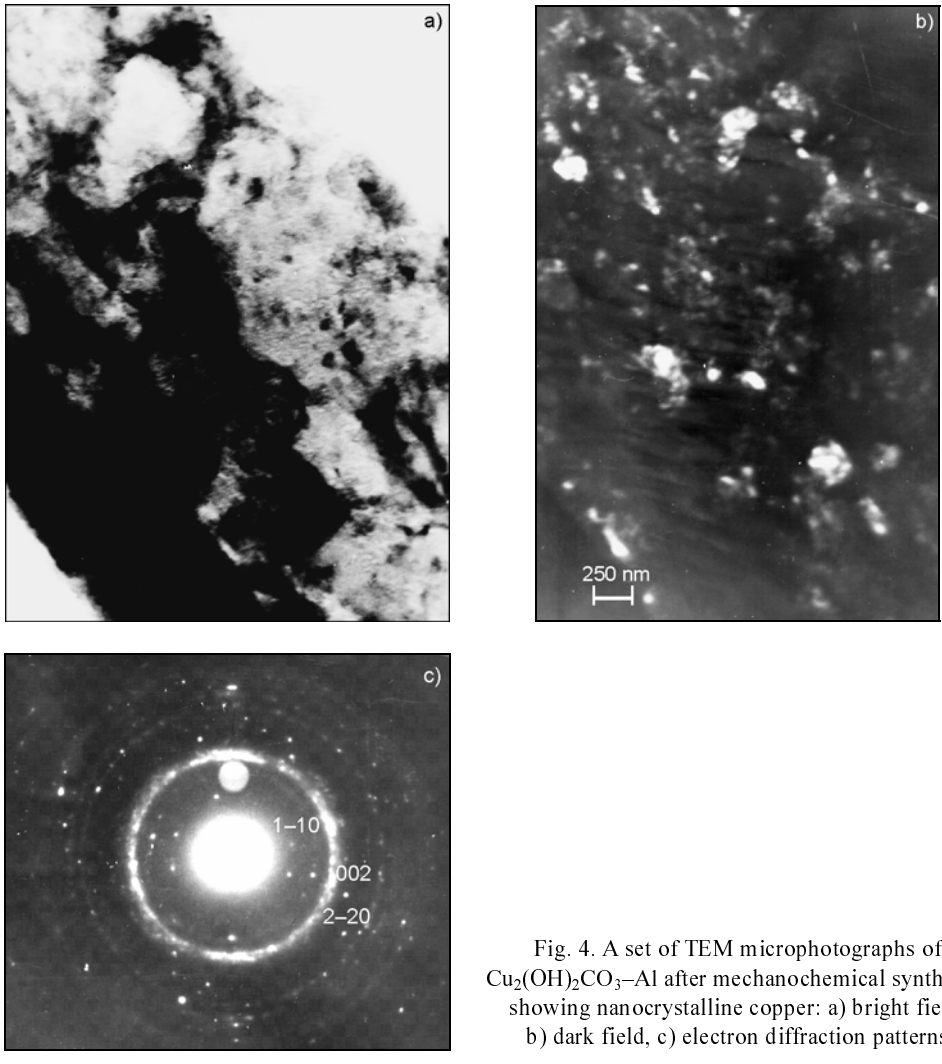

Fig. 4. A set of TEM microphotographs of $Cu_2(OH)_2CO_3$–Al after mechanochemical syntheses, showing nanocrystalline copper: a) bright field, b) dark field, c) electron diffraction patterns

Table 1. XPS data for mixtures of the oxides V_2O_5 and Cr_2O_3, not milled (V–Cr–O) and milled in dry and wet conditions (V–Cr–O/Ar and V–Cr–O/Et)*

Sample	BE, eV				V/Cr
	Cr 2p	(*N*)	V 2p	(*N*)	
V–Cr–O	576.1 578.3	(14582) (1570)	–	(*)	0
V–Cr–O/Ar	576.2 578.7 581.7	(13132) (2647) (617)	517.5	(6765)	0.41
V–Cr–O/Et	575.9 577.8	(13228) (3810)	517.1	(1636)	0.10

*(N) – relative amount of atomic form of elements, (*) - below the limit of detection.

All the above-mentioned methods are useful tools for obtaining information regarding the composition and localization of phases. Moreover, the complete phase analysis of mechanically activated products leads to a better understanding of the mechanism of chemical reactions under high-energy ball milling that provide materials with desired properties.

Acknowledgements

This work was supported by the Ministry of Science and Higher Education, Project No. PB 1234/H03/2006/30.

References

[1] HEINIKE G., *Tribochemistry,* Academie-Verlag, Berlin, 1984.
[2] BOLDYREV V.V., TKAČOVA K., J. Mater. Synth. Proces., 8 (2000), 121.
[3] TAKACS L., MANDAL S.K., Mater. Sci. Eng. A, 304–306 (2001), 429.
[4] BENJAMIN J.S., Metall. Trans., 1 (1970), 2943.
[5] BOBKOV S.P., FROLOV A.N., Izv. Vuzov, Khim. i Khim. Tekhnol., 34 (1991), 93.
[6] MURTY B.S., RANGANATHAN S., Intern. Mater. Rev., 43 (1998), 101.
[7] SURYANARAYANA C., Progress Mater. Sci., 46 (2001), 1.
[8] AVVAKUMOV E., SENNA M., KOSOVA N., *Some Theoretical Aspects of Mechanochemical Reactions. Soft Mechanochemical Synthesis: A Basis for New Chemical Technologies*, Kluwer, New York, 2002.
[9] TKAČOVA K., *Mechanical Activation of Minerals*, Elsevier, Amsterdam, 1989.
[10] ROUGIER A., SOIRON S., HAIHAL I., AYMARD L., TAOUK B., TARASCON J.-M., Powder Technol., 128 (2002) 139.
[11] URAKAEV F. KH., BOLDYREV V.V., Powder Technol., 107 (2000), 93.
[12] COURTNEY T.H., MAURICE D., Scripta Mater., 34 (1996), 5.
[13] BUTYAGIN P., Coll. Surf. A, 160 (1999), 107.
[14] KAJDAS C. K., Tribology Intern., 38 (2005), 337.
[15] WELHAM N.J., Mater. Sci. Eng. A, 255 (1998), 81.
[16] TOKUMITSU K., Solid State Ionics, 101–103 (1997), 25.
[17] SHAFFER G.B., MCCORMICK P.G., J. Mater. Sci. Lett., 9 (1990), 1014.
[18] KORCHAGIN M.A., GRIGOR'EVA T.F., BOKHONOV B.B., SHARAFUTDINOV M.R., BARINOVA A.P., LYAKHOV N.Z., Comb., Expl. Shock Waves, 39 (2003), 51.
[19] ZHANG D.L., ZHANG Y.J., J. Mater. Sci. Lett., 17 (1998), 1113.
[20] JUNMIN X., WANG J., WEISENG T., J. Alloys Comp., 308 (2000), 139.
[21] KESKINEN J., RUUSKANEN P., KARTTUNEN M., HANNULA S.P., Appl. Organometal. Chem., 15 (2001), 393.
[22] SAITO F., MI G., HANADA M., Solid State Ionics, 101–103 (1997), 37.
[23] KITTAKA S., NISHIDA S., OHTANI T., J. Solid State Chem., 169 (2002), 139.
[24] WIECZOREK-CIUROWA K., GOMUŁCZAK A., RAKOCZY. J., STOCH J., GAMRAT K., SAWŁOWICZ Z., Polish J. Appl. Chem., 49 (2005), 253.
[25] PAVLOVA S.N., SADYKOV V.A., ZABOLOTNAYA G.V., MAXIMOVSKAYA R.I., ZAIKOVSKII V.I., TSYBULYA S.V., BURGINA E.B., CHAIKINA M.V., AGRAWAL D., ROY R., Solid State Ionics, 141–142 (2001), 683.
[26] TSUZUKI T., MCCORMICK P.G., Acta. Mater., 48 (2000), 2795.
[27] WIECZOREK-CIUROWA K., GAMRAT K., SAWŁOWICZ Z., J. Therm. Anal. Cal., 80 (2005), 359.
[28] WIECZOREK-CIUROWA K., GAMRAT K., FELA K., Solid State Ionics, 164 (2003), 193.

[29] CHEN Y., J. Alloys Comp., 257 (1997), 156.
[30] PUCLIN T., KACZMAREK W.A., J. Alloys Comp., 266 (1998), 283.
[31] ARESTA M., DIBENEDETTO A., PASTORE T., Abstracts P-I-03. p. 69. IV Intern. Conf. of Mechano-Chemistry and Mechanical Alloying. 7–11 Sept. 2003. Braunschweig (Germany).
[32] BALEMA V.P., PECHARSKY V.K., DENNIS K.W., J. Alloys Comp., 13 (2003), 69.
[33] ZHANG F., KACZMAREK W.A., LU L., LAI M.O., Scripta Materialia, 43 (2000), 1097.
[34] WIECZOREK-CIUROWA K., GAMRAT K., SHIROKOV JU.G., Thermochim. Acta, 400 (2003), 221.
[35] WIECZOREK-CIUROWA K., GAMRAT K., PARYŁO M., SHIROKOV JU.G., J. Therm. Anal. Cal., 70 (2002), 165.
[36] WIECZOREK-CIUROWA K., GAMRAT K., PARYŁO M., SHIROKOV JU.G., J. Therm. Anal. Cal., 69 (2002), 237.
[37] ŠEPELAK V., WISMANN S., BECKER K.D., J. Magn. Magn. Mater., 203 (1999), 135.
[38] BECKER K.D., Solid State Ionics, 141–142 (2001), 21.
[39] MULLER D.A., MILLS M.J., Mater. Sci. Eng. A, 260 (1999), 12.
[40] FIERRO G., JACONO M. LO, INVERSI M., DRAGONE R., PORTA P., Topics Catal., 10 (2000), 39.

Received 23 June 2006
Revised 29 September 2006

Materials Science-Poland, Vol. 25, No. 1, 2007

Changes of structural, optical and electrical properties of sol-gel derived ZnO films with their thickness

A. JAIN, P. SAGAR, R. M. MEHRA*

Department of Electronic Science, University of Delhi South Campus, New Delhi 21, India

Zinc oxide (ZnO) films having thickness in the range from 15 nm to 208 nm have been fabricated by the sol-gel technique by varying number of sequentially deposited layers. The structural, optical and electrical properties of ZnO films were investigated as a function of film thickness. The crystallinity and degree of orientation of the ZnO films were closely related to the film thickness. The textures of the films improved only at an optimum thickness. At lower thicknesses, the roughness of the film became very large and led to the presence of possible voids having porous microstructure. The absorption in UV region depended strongly on sequential layers and increased with the increase of film thickness. Films thinner than ca. 60 nm exhibit morphology and behaviour different from thicker ones. A marked increase in resistivity for thinner films can predominantly be attributed to surface scattering and the decrease in carrier concentration.

Key words: *sol-gel; ZnO*

1. Introduction

ZnO, a direct band gap semiconductor with the band gap of 3.37eV [1] and high exciton binding energy of 60 meV [2] has a variety of potential applications such as bulk acoustic and surface acoustic wave (SAW) devices [3, 4]. It is also a promising candidate for spintronics applications. ZnO films have low electric resistance and high transparency in the visible light. Several deposition techniques have been used to grow ZnO thin films, including sol-gel process [5], spray pyrolysis [6], molecular beam epitaxy (MBE) [7, 8], chemical vapour deposition (CVD) [9] and sputtering [10, 11]. In comparison with other techniques, the sol-gel technique has the advantage of being low cost and low substrate temperature deposition. Certain applications require ZnO films with some specific structure characteristics, orientation, stress relief, smooth surface and high packing density. In the present work, these characteristics are examined as a function of the thickness of the film. It has been observed that the crystallite size and the density of film increases when ZnO films deposited increase in

*Corresponding author, e-mail: rammehra2003@yahoo.com

thickness. The influences of thickness variation on the crystalline structure, surface morphology, optical and electrical properties of ZnO films have been investigated, with the aim to analyze the films growth mechanism.

Single crystalline substrates provide nucleation for the growth of ZnO, however in the case of amorphous substrates the first few layers of ZnO crystallites are developed, which act as nucleating centres for a further growth of the film. It has been reported that strong self-texture is effective in obtaining a highly oriented and single crystalline epitaxial growth [12]. If the lower layer is crystalline, it provides a nucleation step for a further crystallization of the upper layers and there could be a competition between upper layer and lower layer [13]. That may act as a substrate for ZnO film to be grown with a minimum lattice mismatch. A minimum thickness with less structural defects and impurity in the material may essentially be required to provide a good self texture for further growth of a good crystalline quality film.

2. Experimental

The solutions were prepared by dissolving zinc acetate, ($Zn(CH_3CO_2)_2 \cdot 2H_2O$, purity 99.5%) in anhydrous methanol. The obtained mixture was mixed ultrasonically for about two hours. The clear solutions were used for spin coating after 24 hours of aging on Corning glass (7059) substrates. The substrates were cleaned ultrasonically, first in acetone, and subsequently in methanol for 10 minutes each. They were further cleaned with ion exchanged distilled water for 20 minutes and kept in an oven at 80 °C for 30 minutes. The films were dried at 300 °C for 20 minutes each. This process was repeated several times to deposit films of the desired thickness. The films were annealed for one hour at temperature from 575 °C for decomposition and oxidation of the precursors. X-ray diffraction pattern of the films were recorded with a Philips PW 1830 diffractometer, using a monochromatized X-ray beam with nickel-filtered CuK_α radiation (λ = 1.5418 Å) in 2θ from 20° to 60°, with a 0.02 sample pitch. The thickness of the films was determined by a Dektak^{-3} ST surface profiler and was observed to vary in the range 0.015–0.21 μm for various films. The surface morphology of the films was analyzed based on atomic force microscopy (AFM) micrographs using an SPI 3700. Optical transmittance measurements were carried out using a Shimadzu UV-260 spectrophotometer in the range of 300–800 nm. The electrical sheet resistance was measured with the four-probe method.

3. Results and discussion

The X-ray diffractograms (Fig. 1) show that ZnO films of different thicknesses annealed at 575 °C are polycrystalline in nature with (002) plane in preferred mode. Figure 2 shows the increase of peak intensity and decrease of the full width of their half maxima (FWHM) as the thickness of ZnO film increases, since the peak intensity

and grain size are associated with the crystallinity of the film. Poor crystallinity in a thinner ZnO film could be associated with an incomplete growth of the crystallites as only few atomic layers of disordered atoms constitute the bulk of the film [14].

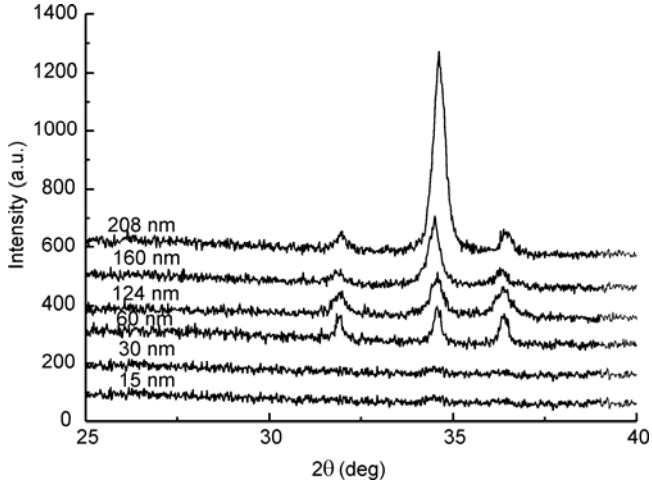

Fig. 1. X-ray diffraction patterns of ZnO films differing in thicknesses

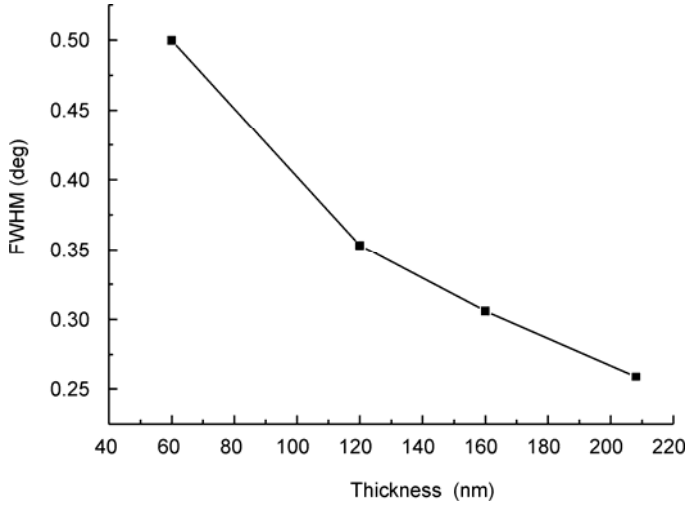

Fig. 2. Dependence of FWHM on the thickness of ZnO films

According to the mechanism of crystal growth [15, 16], the growing faces of crystallites correspond to the crystal shape at equilibrium and are determined by the orientation of the crystal. A growth competition can start among the neighbouring crystals according to their growth types (i.e., to their orientation). The faster growing crystals will grow over the slower growing ones. This competition is terminated when only crystals exhibiting the same type of crystal faces proceed to form the free surface.

This competitive crystal growth represents an orientation selection resulting in the competitive growth texture [17]. This was probably why the crystallinity was increased when ZnO film was thicker. The crystallite size has been estimated from the FWHM of (002) diffraction peak by the Scherrer relation [18]:

$$l = \frac{0.94\lambda}{B\cos\theta}$$

where λ is the wavelength of X-ray radiation θ is the Bragg angle of the (002) peak, B is the angular width of the (002) peak at a half of its maximum intensity (FWHM). The film thickness varying from 60 nm to 208 nm has the grain size of the crystallites between 16 nm to 32 nm.

3.1. Surface morphology

Figure 3 shows AFM the images of ZnO films with various thickness. The surface of ZnO films exhibited hillocks with island-like growth with the decrease of thickness at 15 nm. It indicated that there would be more defects existing in thinner films with varying grain size and orientation distributions.

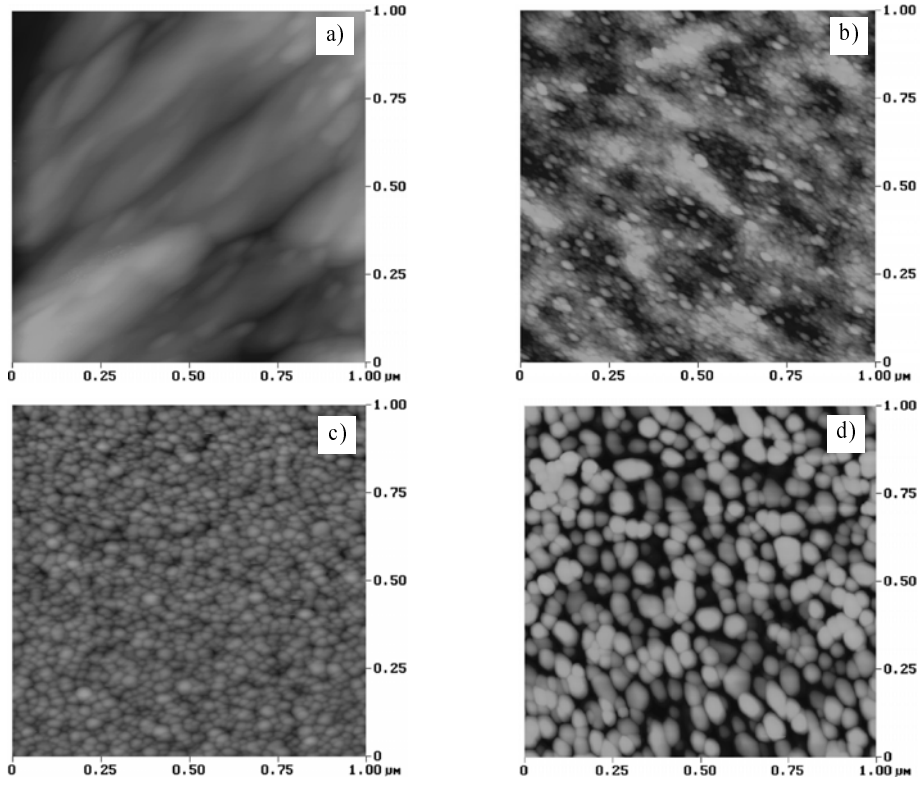

Fig. 3. AFM micrographs of ZnO films with various thicknesses:
a) 15 nm, b) 60 nm, c) 124 nm, d) 208 nm

Thinner films are observed to have smaller grains, non-uniform grain size and random orientation with poor degree of crystallinity. As the film thickness increases during deposition, the deeper layers of atoms are subjected to stronger interatomic forces and form a compact structure, whereas for thin films the atoms near the surface are subjected to a weaker interatomic force and thus form a spongy loose packed structure [19]. It is observed from the figure (3a) that film with a thickness of 15 nm showed no growth of grains and only hillocks are observed. The surface roughness of 38.8 nm was observed. Grains start developing at the thickness of 60 nm with the surface roughness decreased to 4.0 nm (Fig. 3a, b).

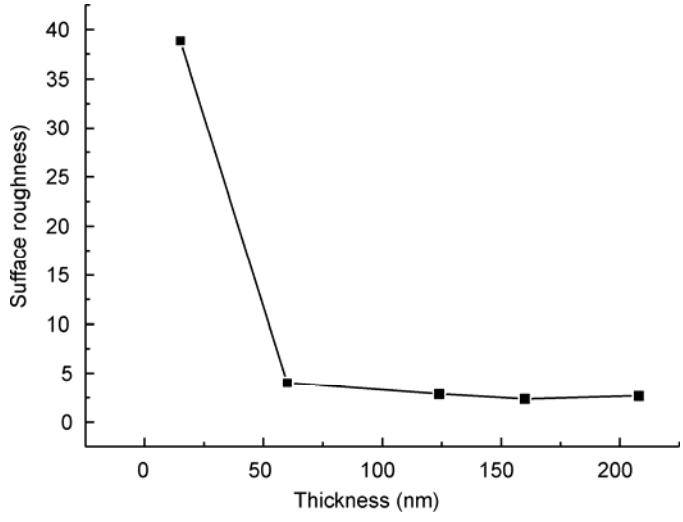

Fig. 4. Dependence of surface roughness on the thickness of ZnO films

The variation of the surface roughness is shown in Fig. 4. The drastic change in surface roughness is in conformity with the analysis of the growth of the film. This trend of growth continues with the further increase of thickness indicating the increase of grain sizes along with the decrease of surface roughness.

3.2. Optical properties

Figure 5 shows the UV–VIS–IR transmission spectra of ZnO films of different thicknesses. The optical transmission in the visible region was high (>80%) but it decreased substantially at short wavelengths near the ultraviolet range for films with different thickness. Generally, the visible transmission of film decreased with the increase of film thickness. However, the films 15 nm thick showed the lowest average visible transmission [20]. AFM pictures show clearly hillocks growth in films with thickness 15 nm. The surface morphology improved and structural defects decrease with increase in thickness, which is in agreement with the XRD analysis. The trans-

mission of the film was found to depend upon the quality of the film, which in turn depends upon the thickness of the film. With the increase of thickness probably oxygen vacancies VO^{++} increase which results in slight decrease of transmission.

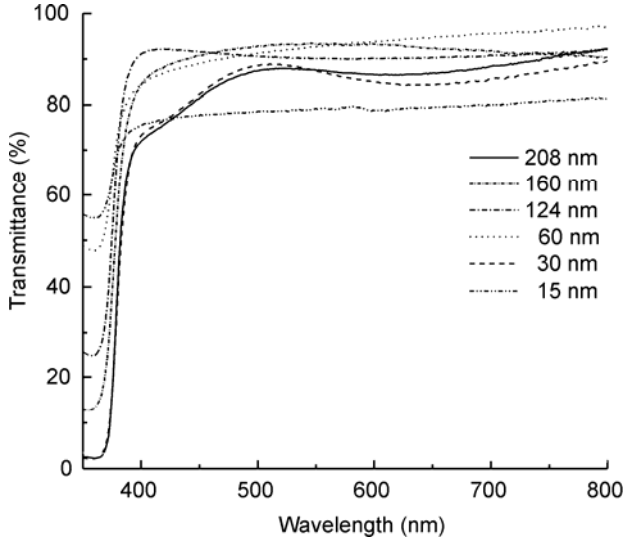

Fig. 5. Dependence of optical transmission on wavelength for ZnO films of various thicknesses

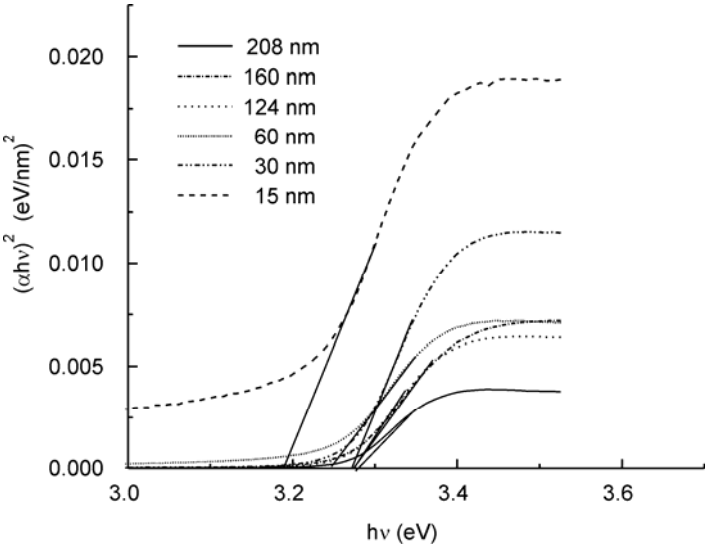

Fig. 6. The plot of $(\alpha h\nu)^2$ vs. $h\nu$ for ZnO film deposites from 15 nm to 208 nm thick

The band gap of the films was determined from the Tauc plots of $(\alpha hv)^2$ vs. photon energy. Figure 6 shows the $(\alpha hv)^2$ vs. photon energy curves of ZnO films with varying thickness.

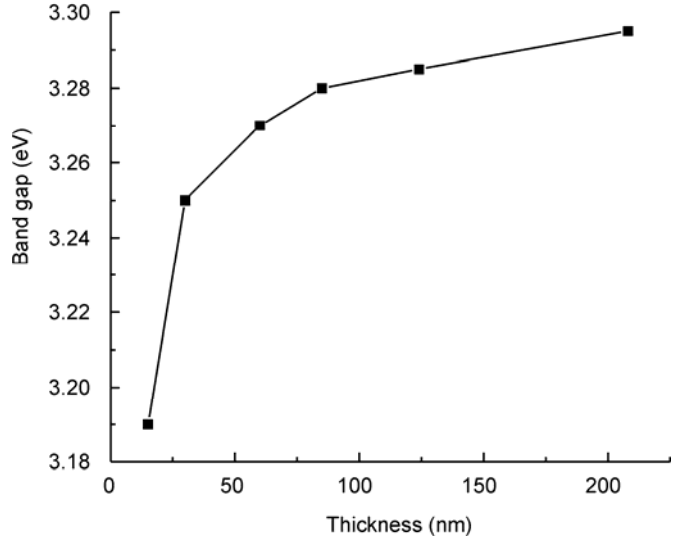

Fig. 7. Dependence of the band gap on thickness of ZnO films

Figure 7 shows the increase of optical band gap E_g from 3.19 eV to 3.27 eV for ZnO films with thicknesses varying from 15 nm to 60 nm, thereafter a slow increase to the value of 3.30 is observed for the thickness of 208 nm. The low energy band gap could be attributed to defects and impurities [21] such as interstitial zinc atoms. For films with thickness higher than 60 nm, the film grows with improvement in grain size which results in a little shift of the absorption edge.

The results suggest that the band gap of ZnO films does not depend significantly on the crystallographic orientation or degree of texturing. It is mainly affected by carrier concentration [22]. There is only a little change in the optical properties of ZnO films by varying the film thickness after the full growth of film at the thickness of more than 60 nm.

3.3. UV absorbance

Figure 8 shows the absorption spectra of ZnO samples with increasing thickness. It is observed that the increase of thickness results in higher absorption of radiation in the UV region. It is shown in Fig. (9) where the absorbance at 365 nm is plotted with the increase of thickness. Two distinct domains of absorption are observed. Apparently there is a critical film thickness ca. 60 nm, which seems to assure a good crystallinity of the film.

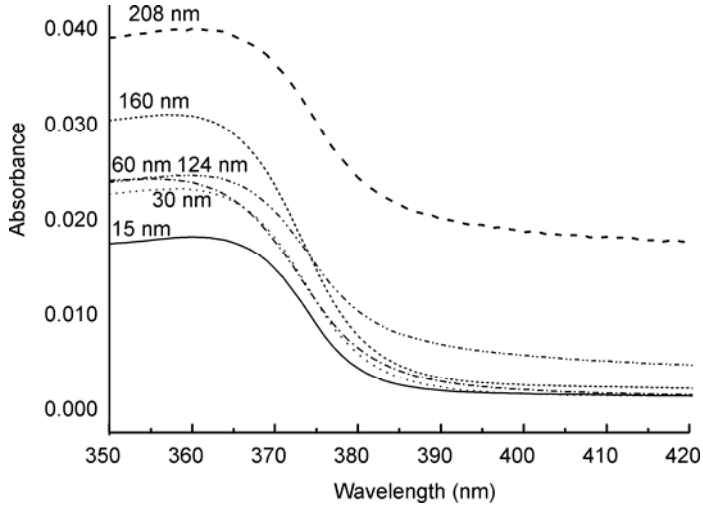

Fig. 8. Absorption spectra of ZnO films

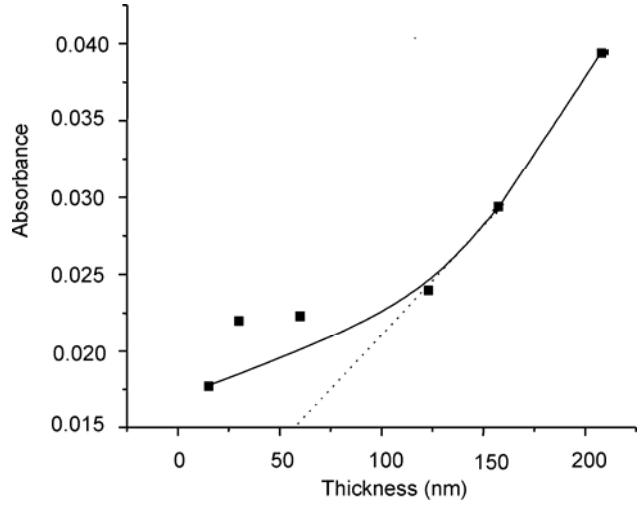

Fig. 9. Dependence of the absorbance of the excitonic band (at 365 nm) on thickness of ZnO films

3.4. The effect of thickness on resistivity of ZnO films

The variation of sheet resistance of ZnO films with different thickness and annealed at 575 °C is shown in Fig. 10. The sheet resistance decreases substantially with increase of thickness. A higher sheet resistance for thinner films could be attributed to surface scattering and the decrease in carrier concentration. For thinner films, more defects act as scattering centres which results in the formation of trapping states capable of trapping carriers and thereby immobilizing them. This reduces the number of

free carriers available for electrical conduction. Also after trapping the mobile carriers, the traps became electrically charged, creating a potential energy barrier, which impeded the motion of carriers from one crystallite to another, thereby reducing their mobility [23, 24]. It is observed that a very high sheet resistance was observed for a film thickness of 15 nm, which decreases, rapidly with the increase of thickness.

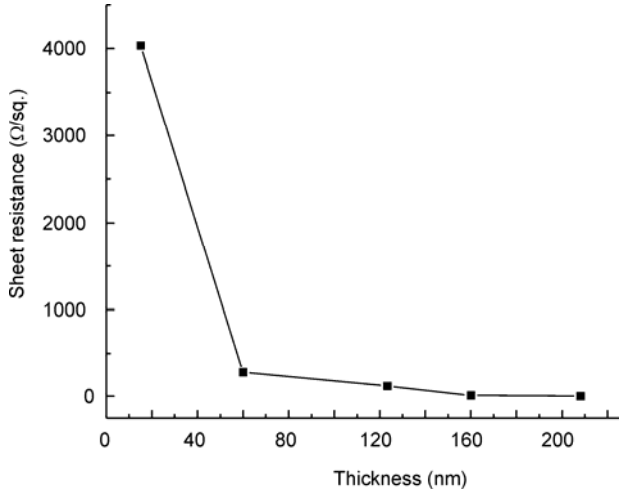

Fig. 10. Dependence of sheet resistance on the thickness of ZnO films

Sheet resistance R_{sh} is related to resistivity by the relation:

$$R_{sh} = \frac{\rho}{d}$$

It has been reported that the absorption edge shifts the Fermi level to a higher energy due to the Burstein–Moss (BM) effect [25]. The decrease in carrier concentrations for thinner films results in the increase of resistivity. The decrease in band gap for thinner films is due to lower carrier concentration in conformity with the BM shift given by the relation

$$\Delta E^{BM} = \left(\frac{\hbar^2}{2m^* e}\right)\left(3\pi^2 N\right)^{2/3}$$

where m^* is the effective mass of the electron and N is the carrier concentration.

4. Conclusion

ZnO films of varying thickness have been fabricated using the sol-gel process on a corning glass (7059) substrate. The structural, optical and electrical properties of the

ZnO films reveal two different zones of thickness. A critical minimum thickness of 60 nm ensures good crystallinity and low sheet resistance of the films. Incomplete growth of crystallites with structural defects was seen in films having thickness lower than 60 nm. Above the critical thickness of the film, no significant change in the band gap of ZnO is observed.

References

[1] PEARTON S.J., NORTON D.J., IP K., HEO Y.W., STEINER T., Progress Mater. Sci., 50 (2005), 293.
[2] JIMENEZ-GONZALEZ A.E., JOSE A. SOTO URUETA, SUAREZ-PARRA R., J. Cryst. Growth, 192 (1998), 430.
[3] JAGER S., SZYSZKA B., SZCZYRBOWSKI J., BRAUER G., Surf. Coatings Technol., 98 (1998), 1304.
[4] TANG Z.C., WONG G.K.L., YU .P, KAWASAKI M., OHTOMO A., KOINUMA H., SEGAWA Y., Appl. Phys. Lett.,72 (1998), 3270.
[5] SAGAR P., KUMAR M., MEHRA R.M., Thin Solid Films, 489 (2005), 94.
[6] BAIK D.G., CHO S.M., Thin Solid Films, 354 (1999), 227.
[7] FONS P., IWATA K., NIKI S., YAMADA A., MATSUBARA K., WATANABE M., J. Cryst. Growth, 209 (2000), 532.
[8] SAKURAI K., IWATA D., FUJITA S., FUJITA S., Jpn. J. Appl. Phys., Part 138 (1999), 2606.
[9] LIU Y., GORLA C.R., LIANG S., EMANETOGLU N., LU Y., SHEN H., WRABACK M., J. Electron. Mater., 29 (2000), 69.
[10] VOSSEN J.L., Phys. Thin Films, 9 (1977), 1.
[11] KARULKAR P.C., MC COY M.E., Thin Solid Films, 83 (1981), 259.
[12] FUJIMURA N., NISHIHARA T., GOTO S., XU J., ITO T., J. Cryst. Growth, 130 (1993), 269.
[13] OHYA Y., SAIKI H., TANAKA T., TAKAHASHI Y., J. Am. Ceram. Soc., 79 (1996), 825.
[14] SETO J.Y.W., J. Appl. Phys., 46 (1975), 5247.
[15] VAN DER DRIFT A., Philips Res. Rep., 22 (1967), 267.
[16] KNUYT G., QUAEYHAEGENS C., HAEN J.D., STALS L.M., Phys. Stat. Sol. B, 195 (1996), 179.
[17] BARNA P.B., ADAMIK M., Thin Solid Films, 317 (1998), 27.
[18] SAGALOWICZ L., FOX G.R., J. Mater. Res., 14 (1999), 1876.
[19] PARRAT I.G., Phys. Rev., 95 (1954), 359.
[20] SU-SHIA L., JOW-LAY H., DING-FWU L., Surf. Coatings Technol., 190 (2005) 372.
[21] DEMIRYONT H., NIETERING K.E., Sol. Energy Mater., 9 (1989), 79.
[22] TANG W., CAMERON D.C., Thin Solid Films, 238 (1994), 83.
[23] TASSIS D.H., DIMITRIADIS C.A., BRINI J., KAMARINOS G., BIRBAS A., J. Appl. Phys., 85, (1999) 4091.
[24] PAPAGEORGIOU D.G., EVANGELAKIS G.A., Surf. Sci. Lett., 461 (2000), 543.
[25] ANUBHA J., SAGAR P., MEHRA R.M., Solid State Electron., 50 (2006), 1420.

Received 23 June 2006
Revised 29 September 2006

Materials Science-Poland, Vol. 25, No. 1, 2007

Effect of dislocation density on the efficiency of multicrystalline silicon solar cells

Z. BENMOHAMED*, M. REMRAM

Département d'Electronique, Université Mentouri de Constantine, 25000, Algeria

The behaviour of structural defects is still one of the major problems in multicrystalline silicon. The properties of solar cells made from these materials are mainly determined by dislocations, grain boundaries and intragrain defect impurities such as oxygen and carbon. Interactions between dislocations and impurities are also an important factor influencing the minority carrier diffusion length and then multicrystalline solar cells performances. In this paper, the effect of dislocations on minority carrier diffusion length is analysed and discussed. We carried out the calculation on the cell efficiency of multicrystalline silicon solar cell obtained from wafers cut out of ingots grown by Polix of Photowatt and Sitix of Sumitomo. A comparison between solar cells efficiency for the two materials outlined above is presented. Performances of the cells are estimated according to the last technological processes developed. The analyses have also been carried out to optimize solar cell performances by combining the effect of a double antireflection coating and back surface field.

Key words: *multicrystalline silicon; efficiency; dislocation; impurity; antireflection coating*

1. Introduction

Multicrystalline silicon (mc-si) which can be produced by different techniques is a low-cost material for photovoltaic applications. It was shown that structural defects together with the impurities present in solar grade material directly influence its electrical properties and therefore solar cell performance [1, 2]. Impurities such as oxygen and carbon are of particular importance because of their complex interactions with structural defects which may modify their electrical activity and then affect considerably photovoltaic properties of mc-si solar cells.

In recent years, there has been a growing interest in large grained multicrystalline silicon solar cells obtained by several growth process such as wafers cast out of ingots supplied for Polix of Photowatt or Sitix of Sumitomo. Because of different growth

methods, the properties limiting dislocations can be present in different concentrations, structural defects can behave differently as well, and then the properties of solar cells produced from mc-si wafers show a significant variation [3]. The purpose of this work is to clarify a part of this variation; this may help to minimize the variation as much as possible, e.g., through an optimised ingot growth. Hence, the optimal solar cell fabrication processes have also to be developed and optimised individually.

The usual electrical and structural characterization techniques have been used, the minority carrier diffusion length was evaluated by steady state surface photovoltage (SPV) method, and the dislocation density was determined by selective etching.

PC1D simulator was used in order to calculate solar cells performances under standard illumination (AM1.5G, 100 mW/cm^2). The technological parameters were selected according to the recent development in solar cells fabrication.

2. Experimental procedures

In order to study the effect of structural and electrical parameters on the multicrystalline solar cells efficiency, we have used two series of P-type multicrystalline silicon wafers cut out of ingots grown respectively by Polix of Photowatt and Sitix of Sumitomo with the boron concentration of about 1×10^{16} cm^{-3}.

The two materials have been two side polished. The dislocation densities were determined by selective etching on polished surfaces, the etch pits were automatically counted by an image processing system.

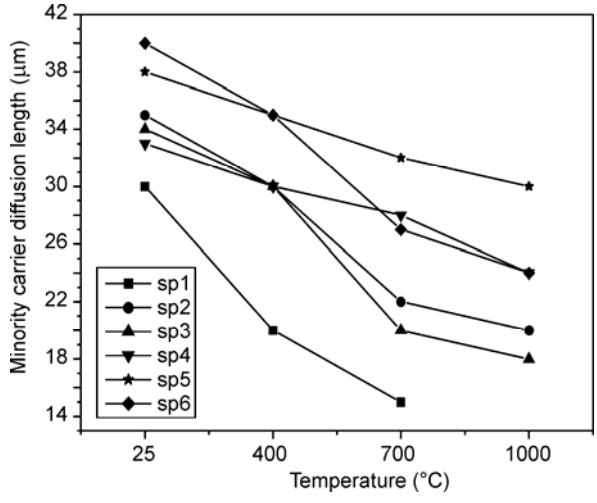

Fig. 1. Variation of minority-carrier diffusion length (μm) after RTP in Polix wafers in function of RTP temperature

The effective minority carrier diffusion length was evaluated by steady state surface photovoltage technique (SPV) [4, 5]. The effective minority carrier diffusion length for

Sitix samples was evaluated at room temperature and it varied between 53 μm and 82 μm [6]. The Polix samples were treated by rapid thermal processing (RTP) during 20 s in an FV4 furnace of JIPILEC France, with a cooling rate of 50 °C/s at a temperature range from 400 °C to 1000 °C. The SPV results after thermal treatment are shown in Fig. 1. Effective minority carrier diffusion length decreases when the temperature increases. We also note that at a given temperature the samples present different minority diffusion lengths; this is attributed to the position of wafers in ingots where the concentration of oxygen and carbon change from the top to the bottom [7]. The measured length is only an effective value, which is not trivially related to any real diffusion length. This effective value is lower than the true one, because of the recombination of minority charge carriers at the backside of samples [8].

3. Effect of the dislocation density on diffusion length

The variation of diffusion length versus dislocations density for the two types of materials in particular at room temperature is illustrated by Fig. 2. We notice that the diffusion length decrease when the dislocation density increases from $10^3\,cm^{-2}$ to $10^5\,cm^{-2}$ for the two series of wafers. Furthermore, the Sitix samples present diffusion length larger than the Polix samples. The degradation of minority diffusion length can be attributed to the presence of impurities (transitions metals, oxygen and carbon) and their segregation in the vicinity of dislocations. Thus the dislocation behaviour is influenced [9]. These have a direct consequence on the decreasing of minority-carrier diffusion length and their lifetime.

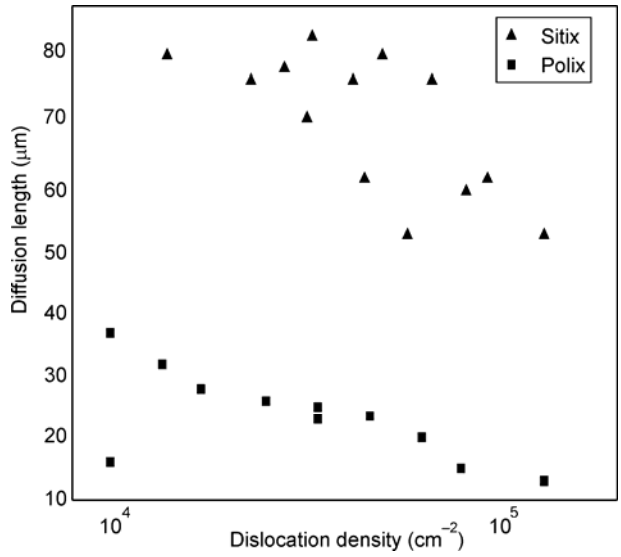

Fig. 2. Minority-carrier diffusion length versus dislocation density

Our results are in accordance with some mathematical models describing the diffusion length according to the structural parameters. Indeed, Yamaguchi et al. [10] described the minority carrier diffusion length with the equation:

$$\frac{1}{L^2} = \frac{1}{L_0^2} + \frac{1}{L_D^2} + \frac{1}{L_i^2} \tag{1}$$

where: L_0 is the bulk minority-carrier diffusion length. In addition to the effect of dislocations expressed by L_D, L_i describes the various possible interactions (grain boundaries dislocations, dislocation impurities) which can occur in material and deteriorate the minority carrier diffusion length.

We believe that the dislocation parameter remains limited to describe the carriers transport in multicrystalline silicon. However, such a phenomenon remains difficult to be quantified, considering the evolution of the unstable state of various interactions.

The results of electrical and structural characterization that we have obtained are used to calculate the efficiency of multicrystalline solar cells.

4. Simulation

The cell structure used to calculate the solar cell efficiency assumes an n^+pp^+ junction, the cell area is 1 cm^2 consisting of a thin n emitter region (0.15 μm) doped at $10^{20}\,cm^{-3}$, a P base region with the thickness of 20 μm and a 5μm thick p^+ layer serving as a back surface field (BSF); the latter being expected to play an important role under the condition $L_n >> d$. The doping of p and p^+ regions is fixed at $10^{16}\,cm^{-3}$ and $5\times10^{18}\,cm^{-3}$, respectively. PC1D simulator version 5.0 is used to calculate the solar cell efficiencies under standard illumination (AM1.5G, 100 mW/cm^2). The material parameters used in the calculation such as the electric permittivity, refractive index and absorption coefficient are the program default settings. No special light-trapping structure is used so that the internal reflectance was assumed to be 10%. The front and rear surface recombination velocities are set to be 100 cm/s and 500 cm/s, respectively.

5. Results and discussions

5.1. Effect of dislocation on the efficiency

Figures 3 and 4 show the evolution of multicrystalline silicon solar cells efficiency with the cell thickness as a function of dislocation density, elaborated by Sitix and Polix techniques, respectively. As expected, the increase of the dislocation density from $10^3\,cm^{-2}$ to $5\cdot10^5\,cm^{-2}$ reduces significantly the energetic efficiency. This degradation is more important for Polix solar cells compared to Sitix solar cells. Moreover for the two series of solar cells, there is an optimum cell thickness for energetic efficiency. For this result, a multicrystalline Sitix solar cells conversion efficiency of

16% is feasible. For Polix solar cells 13% is obtained even at a cell thickness of 20 μm if the dislocation density is less then 10^5 cm^{-2}.

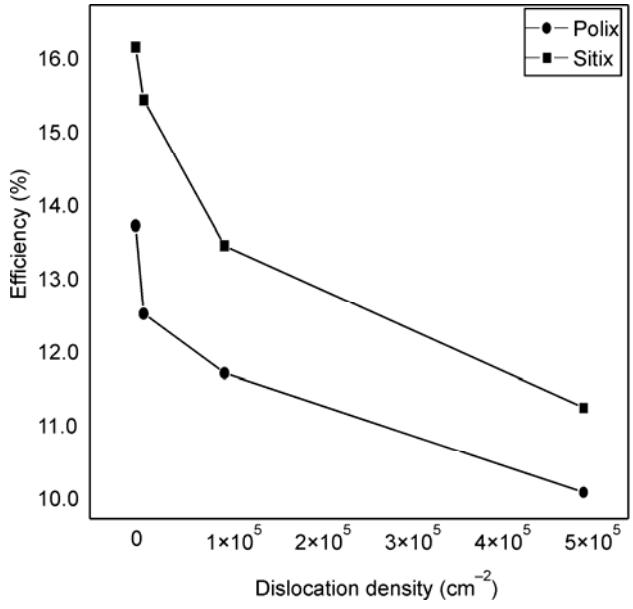

Fig. 3. Sitix solar cells conversion efficiency vs. dislocation density

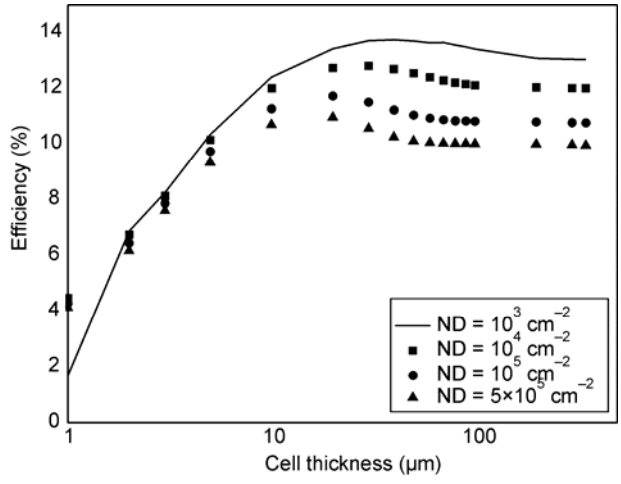

Fig. 4. Polix solar cells conversion efficiency vs. dislocation density

We also notice that energetic efficiency profile show different paces for the two series of samples. Indeed, one remarkable point is that when the dislocation density increases, the efficiency degradation is more pronounced for Sitix solar cells compared to Polix solar cells. One can assume, however, that impurities will diffuse to the

dislocation and decorate them. As a result, dislocations may have different recombination behaviours depending on the degree of decoration.

A comparison between solar cells efficiency for the two series of samples is illustrated by the Fig. 5. Variation efficiency between 11% and 16% is reached for multicrystalline silicon solar cells grown by Sitix, whereas that obtained for solar cells based of Polix samples vary from 10% to 13%.

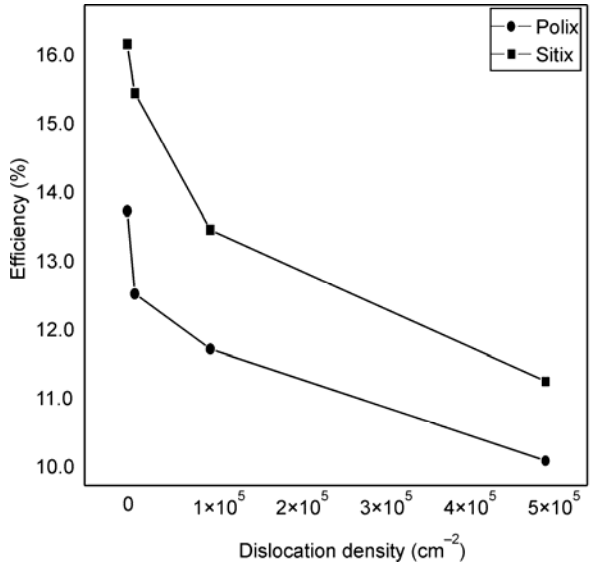

Fig. 5. Comparison of conversion efficiency for the two series of solar cells

We also notice that the efficiency obtained for Polix samples decreases little when the density of dislocation increases of two decades, compared to the Sitix samples where the efficiency variation is larger. That confirms the non-linearity of the mc-si solar cells efficiency versus the minority carrier diffusion length.

5.2. Effect of antireflection coating

The cell described in section 4 has a double antireflection coating, MgF_2 (106 nm) on a top of ZnS (56 nm) with the refractive index equal to 1.4 and 2.4 respectively; an analysis is made to identify the major areas for further improvements in solar cell properties. The results of simulation are summarized in Table 1.

An improvement in short-circuit current is observed. Short-circuit current increases from 23.5 mA/cm^2 to 31.18 mA/cm^2. This improvement is due to the reduction of optical losses from the front surface of the cell. Also it can be seen that further increase in solar cell efficiency can be reached by reducing recombination and reflection losses. An increase in diffusion length to 200 μm depends on further improvements in both growth material conditions and solar cell fabrication; with these factors improved, the efficiency of about 17.4% would be feasible for the Sitix solar cells.

Table 1. Results performance of areas improvement for Sitix solar cells

Structure	Performance		
	J_{sc} (mA/cm^2)	V_{oc} (V)	Efficiency (%)
n^+p	23.5	539.5	10.3
n^+pp^+	28.6	624.7	14.82
n^+pp^+ with MgF_2/ZnS	31.04	626.9	16.02
Improved L_n to 200 μm	31.18	672.6	17.49

6. Conclusion

In this study, we present and discuss the effect of dislocation density on electrical properties of multicrystalline silicon grown by Polix of Photowatt and Sitix of Sumitomo. The results show that the behaviour of the dislocations in both series of wafers differs. We assume that this is due to a different degree of contamination. Dislocations are not the major factor influencing electrical properties of material. Inactive impurities were already present in the grown material, in particular oxygen precipitates. The electrical activation of these impurities in an inhomogeneous distribution is also a principal source of deterioration of multicrystalline silicon solar cells efficiency. The effect of various impurities on the device performances is not completely analysed yet, but there is substantial evidence that these intragrain defects have to be taken into account. By a further optimisation of growth material and cell processes, high mc-si solar cells efficiency can be attained.

References

[1] MÖLLER H. J., FUNKE C., LAWERENZ A., RIEDEL S., WERNER M., Solar Energ. Mater. Solar Cells, 72 (2002), 403.
[2] BORJANOVIĆ V., JAKŠIĆ M., PASTOVIĆ Ž., PIVAC B., VLAHOVIĆ B., DUTTA J., JEČMENICA R., Solar Energ. Mater. Solar Cells, 72 (2002), 487.
[3] ACERBONI S., PIZZINI S., BINETTI S., ACCIARRI M., PICHAUD B., J. Appl. Phys., 76 (1994), 2703.
[4] CHIANG C-L., WAGNER S., IEEE Trans. Electr. Dev., ED-32 (1985), 1722.
[5] CHOO S.C., TAN L. S., Solid State Electr., 35 (1992), 269.
[6] IMAIZUMI M., ITO T., YAMAGUCHI M., J. Appl. Phys., 81 (1997), 7635.
[7] BENMOHAMED Z., REMRAM M., LAUGIER A., World Renewable Energy Network, 1–7 July, 2000, Brighton, UK.
[8] ELCHHMMER W., QUAI V.-T., SIFFERT P., J. Appl. Phys., 66, (1989), 3857.
[9] MÖLLER H.J., LONG L., WERNER M., YANG D., Phys. Stat. Sol. A, 171 (1999), 175.
[10] YAMAGUCHI M., AMANO C., J. Appl. Phys., 58 (1985), 3601.

Received 27 May 2006
Revised 30 November 2006